Science behind the hunt for Flight 370 *pp. 947 & 963*

Incentives for antibiotic innovation *p. 967*

Toward atomic magnetic memory *pp. 976 & 988*

Science

$10
30 MAY 2014
sciencemag.org

AAAS

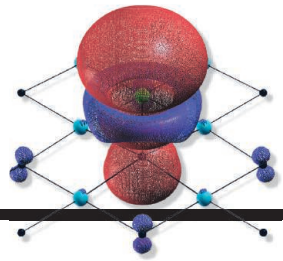


Inner life of the synapse

3D model yields realistic view of teeming proteins and organelles *p. 1023*

CONTENTS

30 MAY 2014 • VOLUME 344 • ISSUE 6187



976 & 988

Calculated valence spin density of a cobalt atom

NEWS

IN BRIEF

950 Roundup of the week's news

IN DEPTH

953 TIANANMEN'S BITTER LEGACY
The bloody crackdown 25 years ago left an indelible mark on China's research culture *By M. Hvistendahl*
▸ *SCIENCE* PODCAST

954 BRAIN PROJECT MEETS PHYSICS
Physicists provide a reality check for brain mappers *By E. Underwood*

955 PLAN TO INTERNATIONALIZE U.S. PROJECT MAY FACE HEADWIND
Washington may be reluctant to share physics facility on U.S. soil *By A. Cho*

957 PSYCHOLOGIST'S DEFENSE CHALLENGED
E-mails counter claimed location, timing of studies *By F. van Kolfschooten*

959 WHERE'S FRANCE CÓRDOVA? IN THE WASHINGTON HOT SEAT
New NSF director jumps into the frying pan served up by Congress *By J. Mervis*

960 VIEWS OF SCIENCE CLASH IN DEBATE OVER NSF BILL
Push for closer oversight of agency alarms university and science groups *By J. Mervis*

FEATURES

963 LOST AT SEA
As the hunt for the missing Malaysian jet grows more challenging, authorities are pondering how to avert future aviation vanishing acts *By D. Normile*
▸EDITORIAL P. 947

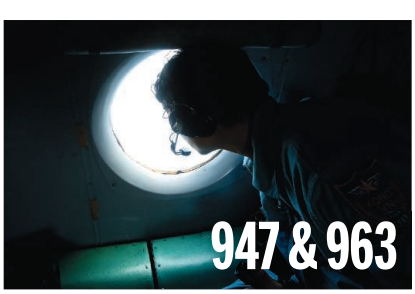
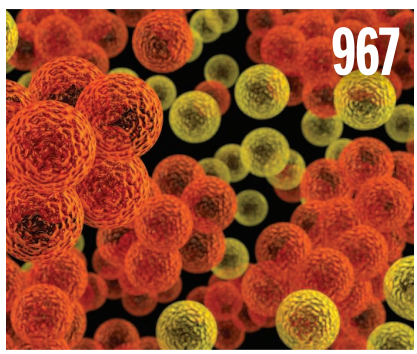


ILLUSTRATION: (BOTTOM RIGHT) MARC ROSENTHAL

INSIGHTS



PERSPECTIVES

967 TARGET SMALL FIRMS FOR ANTIBIOTIC INNOVATION
Once in clinical trials, antibiotics are more likely to survive than drugs in other classes *By T. J. Hwang* et al.

969 MAPPING BOND ORIENTATIONS WITH POLARIZED X-RAYS
Regions of bond order and disorder are revealed *By S. Lidin*
▸ REPORT P. 1013

970 CLUES FROM THE RESILIENT
Genetic information from individuals who do not succumb to disease may point to new therapies and ideas about wellness *By S. H. Friend and E. E. Schadt*

972 A BACTERIAL SEEK-AND-DESTROY SYSTEM FOR FOREIGN DNA
Bacterial argonaute proteins defend the cell against exogenous DNA *By J. Vogel*

974 HOW SULFUR BEATS IRON
Iron-reducing bacteria switch to sulfur reduction as their main energy source in alkaline environments
By M. W. Friedrich and K. W. Finster
▸ REPORT P. 1039

975 MANAGING THE SIDE EFFECTS OF INVASION CONTROL
Efforts to control invasive species must be adapted to avoid unintended damage to native species and ecosystems
By Y. M. Buckley and Y. Han
▸ REPORT P. 1028

976 HITTING THE LIMIT OF MAGNETIC ANISOTROPY
Enhancing the magnetic properties of adatoms provides a route toward atom-scale memory
By A. A. Khajetoorians and J. Wiebe
▸ RESEARCH ARTICLE P. 988

BOOKS *ET AL.*

978 FOUR FIELDS
By T. Dee, reviewed by S. Knapp

980 THE PERFECT 46
B. R. Bonowicz, director, reviewed by D. Greenbaum

LETTERS

981 RETRACTION
By M. McNutt

981 KILLER KIDNEY DISEASE COMMON IN SRI LANKA
By M. C. M. Iqbal and C. B. Dissanayake

981 INTOLERANCE EXTENDS BEYOND CARNIVORES
By K. J. Hockings et al.

981 TECHNICAL COMMENT ABSTRACTS

DEPARTMENTS

947 EDITORIAL
The hunt for MH370
By Marcia McNutt
▸ NEWS STORY P. 963

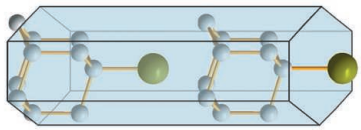
1054 WORKING LIFE
Winter is coming
By Christina Reed



Science Staff 944
AAAS News & Notes 982
New Products 1048
Science Careers 1049

Published by AAAS

CONTENTS



969 & 1013
Orientation of bromoadamantane in x-ray imaging

30 MAY 2014 • VOLUME 344 • ISSUE 6187

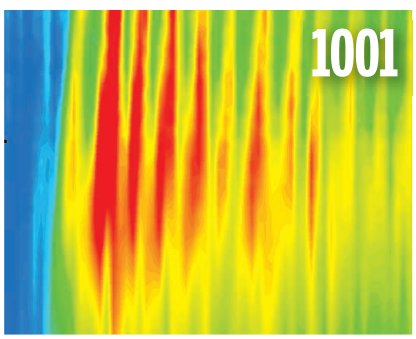
RESEARCH

IN BRIEF

984 From *Science* and other journals

REVIEW

987 BIODIVERSITY STATUS
The biodiversity of species and their rates of extinction, distribution, and protection
S. L. Pimm et al.
REVIEW SUMMARY; FOR FULL TEXT: HTTP://DX.DOI.ORG/10.1126/SCIENCE.1246752



RESEARCH ARTICLES

988 MOLECULAR MAGNETISM
Reaching the magnetic anisotropy limit of a 3*d* metal atom
I. G. Rau et al.
▸ PERSPECTIVE P. 976

992 ION CHANNEL STRUCTURE
Crystal structure of a heterotetrameric NMDA receptor ion channel
E. Karakas and M. Furakawa

REPORTS

998 CHILDHOOD DEVELOPMENT
Labor market returns to an early childhood stimulation intervention in Jamaica
P. Gertler et al.

1001 SOLAR CELLS
Coherent ultrafast charge transfer in an organic photovoltaic blend
S. M. Falke et al.

1005 WATER SPLITTING
Amorphous TiO_2 coatings stabilize Si, GaAs, and GaP photoanodes for efficient water oxidation
S. Hu et al.

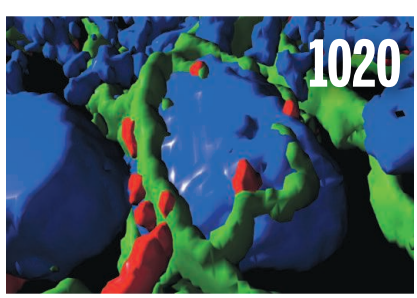
1009 WATER STRUCTURE
Vibrational spectral signature of the proton defect in the three-dimensional $H^+(H_2O)_{21}$ cluster
J. A. Fournier et al.

1013 IMAGING TECHNIQUES
X-ray birefringence imaging
B. A. Palmer et al.
▸ PERSPECTIVE P. 969

1016 MARINE BIOGEOGRAPHY
Quaternary coral reef refugia preserved fish diversity
L. Pellissier et al.

1020 NEURAL DEVELOPMENT
Retrograde semaphorin signaling regulates synapse elimination in the developing mouse brain
N. Uesaka et al.

1023 SYNAPSES
Composition of isolated synaptic boutons reveals the amounts of vesicle trafficking proteins
B. G. Wilhelm et al.



1028 CONSERVATION ECOLOGY
Optimal approaches for balancing invasive species eradication and endangered species management
A. Lampert et al.
▸ PERSPECTIVE P. 975

1031 CELLULAR DYNAMICS
High-resolution mapping of intracellular fluctuations using carbon nanotubes
N. Fakhri et al.

1035 STRUCTURAL BIOLOGY
Structures of PI4KIIIβ complexes show simultaneous recruitment of Rab11 and its effectors
J. E. Burke et al.

1039 SUBSURFACE MICROBES
Sulfur-mediated electron shuttling during bacterial iron reduction
T. M. Flynn et al.
▸ PERSPECTIVE P. 974

1042 TRANSCRIPTION
A pause sequence enriched at translation start sites drives transcription dynamics in vivo
M. H. Larson et al.

ON THE COVER



A realistic, molecular-scale view of a synapse, showing a few hundred thousand proteins. The synapse organization was measured by a combination of electron microscopy, quantitative biochemistry, and super-resolution microscopy. This three-dimensional computational model now enables a quantitative understanding of synaptic processes. See page 1023. *Image: Burkhard Rammner/Rizzoli Laboratory, University of Göttingen Medical Center*

PHOTO: (BOTTOM) MASANOBU KANO

Science (ISSN 0036-8075) is published weekly on Friday, except the last week in December, by the American Association for the Advancement of Science, 1200 New York Avenue, NW, Washington, DC 20005. Periodicals mail postage (publication No. 484460) paid at Washington, DC, and additional mailing offices. Copyright © 2014 by the American Association for the Advancement of Science. The title SCIENCE is a registered trademark of the AAAS. Domestic individual membership and subscription (51 issues): $153 ($74 allocated to subscription). Domestic institutional subscription (51 issues): $1282; Foreign postage extra: Mexico, Caribbean (surface mail): $55; other countries (air assist delivery): $85. First class, airmail, student, and emeritus rates on request. Canadian rates with GST available upon request, GST #1254 88122. Publications Mail Agreement Number 1069624. **Printed in the U.S.A.**
Change of address: Allow 4 weeks, giving old and new addresses and 8-digit account number. **Postmaster:** Send change of address to AAAS, P.O. Box 96178, Washington, DC 20090–6178. **Single-copy sales:** $10.00 current issue, $15.00 back issue prepaid includes surface postage; bulk rate on request. **Authorization to photocopy** material for internal or personal use under circumstances not falling withiin the fair use provisions of the Copyright Act is granted by AAAS to libraries and other users registered with the Copyright Clearance Center (CCC) Transactional Reporting Service, provided that $30.00 per article is paid directly to CCC, 222 Rosewood Drive, Danvers, MA 01923. The identification code for *Science* is 0036-8075. *Science* is indexed in the *Reader's Guide to Periodical Literature* and in several specialized indexes.

Published by AAAS

EDITORIAL

The hunt for MH370



Marcia McNutt is Editor-in-Chief of Science.

In a world that is increasingly connected, that grows smaller every day, and where so many human actions are exposed to prying eyes, it seems almost incomprehensible that the world's largest twinjet aircraft, with 239 passengers and crew, could vanish for more than 2 months. Determining the crash site of Malaysia Airlines Flight 370 (MH370) has become a scientific detective story, emerging through a combination of scientific technologies used to address problems for which they were never designed. The search for MH370 illustrates a humanitarian dividend from past investments in science as searchers attempt to bring closure to the families and friends of the victims of the tragedy.

MH370 went incommunicado on 8 March 2014. A single Inmarsat satellite exchanged six brief messages with the MH370 Aircraft Communications Addressing and Reporting System. Oceanographers and other mariners have relied on Inmarsat's system of geostationary telecommunications satellites in remote parts of the world's oceans for data and voice communication. Significantly, it is not a navigation system. From the Doppler effect, engineers calculated the plane's velocity relative to the satellite at each time interval, and the delay in the return signal gave them the distance of the aircraft from the satellite. The Doppler was key in choosing the southern over the northern route. Using additional information on the plane's range, they then triangulated to estimate the likely crash site to within 160 km (100 miles). This was the first-ever use of Inmarsat in this mode.

The search area is a remote part of the Indian Ocean. Planes searched for wreckage with no success; ships listened for pings as time ran out on the 30-day batteries sustaining the black boxes. Some promising signals were detected, but the area still to be searched is largely unexplored. The survey tool of choice was a Bluefin-21 autonomous underwater vehicle (AUV). Bluefin Robotics was spun out of the Massachusetts Institute of Technology's Sea Grant Lab. The Bluefin-21 vehicle inherited its distinct construction, gimbal-ducted propeller, mission-control software, and side-scan sonar payload from roots in academic research. Its deep-sea rating that enabled the MH370 response was initially driven by academic applications. The best available bathymetry to help the AUV avoid crashing into rough terrain as it scanned for the debris field of MH370 was assembled from a combination of very sparse ship sonar and satellite altimetry. Satellite altimeters, first launched nearly 40 years earlier to map the ocean surface, produced better maps of the seafloor than were available from shipboard echo-soundings alone, by using small-scale features in the marine geoid to estimate the shape of the seafloor. Scientists had been using these maps to better understand Earth beneath the ocean; now the map would help guide the AUV in a search area still needle-in-a-haystack large and more than 4000 m deep.



A New Zealand military plane searches for debris.

"We should use better technology to track what is too valuable to lose."

As of this writing, the search continues. In April 2011, a team from the Woods Hole Oceanographic Institution found the debris field from Air France Flight 447, which had crashed into the Atlantic Ocean 2 years before, after a week of searching with similar AUV technology,* bringing resolution to the families of the victims. Finding the black boxes is vital to avoiding similar incidents happening again. We hope for the same outcome for the MH370 search. But it took 2 years to narrow the search to the right part of the Atlantic. In both cases, the response could have been improved by filling known gaps in scientific understanding (see the News story on p. 963). For example, the resolution of the satellite-derived map guiding the Bluefin-21 is ±250 m vertical and 15 km horizontal. Relative to the plane's dimensions, the unknowns are serious. For comparison, the resolution of features on Mars is ±1 m vertical and 1 km horizontal. And knowing where to look saves precious time, whether one seeks a plane full of passengers or a truck full of Nigerian schoolgirls. We should use better technology to track what is too valuable to lose.

– Marcia McNutt

10.1126/science.1255963

*www.whoi.edu/page.do?pid=96017&tid=3622&cid=96189&c=2.

PHOTO: STACEY PENTLAND PHOTOGRAPHY; (INSET) AFP/GETTY IMAGES

Downloaded from www.sciencemag.org on May 30, 2014

Published by AAAS

> "Using vaccinators for these purposes is the moral equivalent of running guns in Red Cross ambulances—and the world rejected that many many years ago."
>
> **Stefano Bertozzi**, dean of public health at the University of California, Berkeley, responding to a White House vow that the CIA will stop using vaccination programs as cover for spying.

IN BRIEF

Toxic toad invades Madagascar



The Asian common toad has appeared in the island nation, threatening native fauna.

The imperiled fauna of Madagascar may face a deadly new threat—a highly toxic toad. In late March, Jonathan Kolby of James Cook University, Townsville, in Australia and other researchers caught six Asian common toads (*Duttaphrynus melanostictus*) near the seaport of Toamasina. The species is common in Southeast Asia, spread to Bali in 1958, and has since invaded other parts of Indonesia. The toads appear to be harming native wildlife in East Timor, like their relative the cane toad has done in Australia. The Asian toad has deadly chemical defenses similar to the cane toad. Because there are no native toads in Madagascar, predators such as mongooses, lemurs, and more than 50 species of snakes are at risk of poisoning. The voracious, fertile toad could also compete with native frogs for food. "This is the worst thing I've seen come along in a while," says Fred Kraus of the Bishop Museum in Honolulu. "It makes one's blood chilled." Writing in a letter to *Nature* this week, Kolby, Kraus, and 10 colleagues call for urgent eradication. Researchers are scouting around Toamasina to see how far the toad may have spread. "We hope that we've found it soon enough," Kolby says. "If it hasn't spread that far yet, then we've got hope."

AROUND THE WORLD

Less review for gene therapy

BETHESDA, MARYLAND | The National Institutes of Health (NIH) will no longer subject all proposed gene therapy clinical trials to review by the Recombinant DNA Advisory Committee (RAC), which has reviewed them since the late 1980s. As the field has matured, using gene therapy to treat several disorders, researchers argued that RAC review is redundant because gene therapy protocols are already reviewed by institutional ethics and biosafety boards and the U.S. Food and Drug Administration. In December 2013, an Institute of Medicine (IOM) panel agreed, recommending that NIH should continue to register trials but the RAC only needs to review protocols not evaluated by standard oversight bodies and that pose unusual risks—for example, ones that use a new vector. Last week, NIH Director Francis Collins announced that NIH has accepted these IOM recommendations. http://scim.ag/genether

Institut Pasteur under fire

PARIS | Contrary to press stories last week, the Institut Pasteur has not been closed or ordered to halt its research, says Pasteur Director-General Christian Bréchot. But Pasteur is struggling with a public relations fiasco, after the discovery earlier this year that it can't account for 2349 vials containing samples from the 2003 SARS outbreak. An independent panel found no risk to public health, but the issue led to three investigations and questions about the institute's safety procedures. On 21 May, the website Mediapart published fragments



Institut Pasteur was investigated after SARS virus samples went missing this year.

PHOTOS: (TOP TO BOTTOM) JONATHAN KOLBY; LUCA BORGHI/WIKIMEDIA COMMONS

Downloaded from www.sciencemag.org on May 30, 2014

Published by AAAS

from a leaked letter by two French Cabinet ministers addressed to government inspectors investigating the issue; the letter listed multiple apparent security problems at Pasteur. Bréchot says the institute is working to improve the way it handles dangerous agents. http://scim.ag/pastSARS

Funding agreement reached

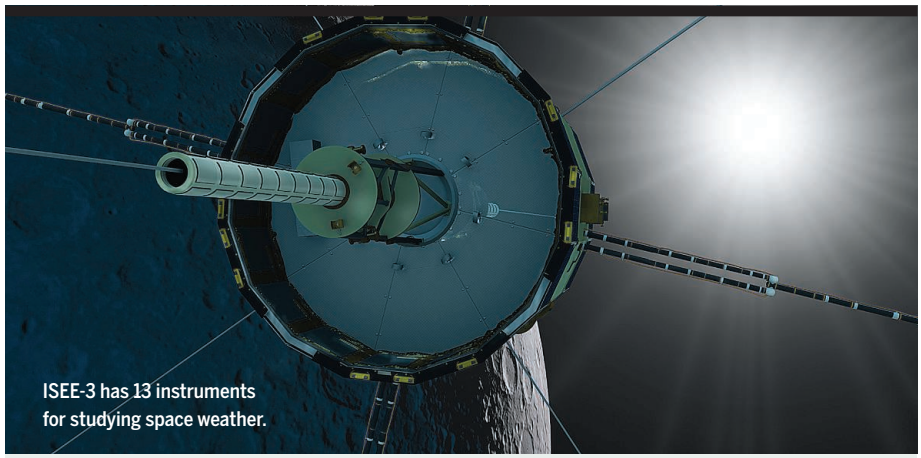
BERLIN | Financing for German science got a boost this week when politicians agreed on how to spend €6 billion slated for education over the next 4 years. Disagreements between the federal and state governments had delayed plans for distributing the money, promised in November. At a 26 May meeting between Angela Merkel and leaders of her party's coalition partners, the leaders agreed that the federal government would take over the country's financial aid program for university students, saving the states an additional €1.2 billion. In return, the states agreed to a change in the constitution that would allow the federal government to fund universities directly. Science leaders have lobbied for the change for several years, but the states have been reluctant to give up their control of education to the federal government. http://scim.ag/germanfund

Young inventor may seek asylum

LOS ANGELES, CALIFORNIA | A 17-year-old Egyptian inventor has refused to head home after competing in the Intel International Science and Engineering Fair, held 11 to 16 May in Los Angeles, California. Weeks before traveling to the United States, Abdullah Assem was arrested near Tahrir Square in Cairo, charged by police, and imprisoned for a little over a week for burning two vehicles and founding a group that attacked Egyptian security services in Assiut, says Assem's attorney, Farida Chetata of the Council on American-Islamic Relations. In a video interview with Al-Jazeera, Assem denied the charges and said he fears further incarceration if he returns to Egypt. A student at Dar Heraa Islamic Private School in Assiut, Assem joined 1700 finalists, aged 13 to 20 from over 70 countries, in vying for more than $5 million in awards and scholarships. He showcased a pair of wireless glasses that allows quadriplegic people to type using only eye movements.

Yelp reviews track illness

NEW YORK CITY | Taking citizen science to a new level, New Yorkers who used the online rating site Yelp to review restaurants between July 2012 and March 2013 also unwittingly helped the New York Department of Health and Mental Hygiene (DOHMH) hunt for outbreaks of foodborne disease. Using software developed at Columbia University, the DOHMH pilot project analyzed 294,000 reviews, searching for keywords such as "vomit" and "diarrhea." After flagging 893 reviews for further evaluation by an epidemiologist, DOHMH eventually interviewed 27 reviewers by phone—and identified three "previously unreported restaurant-related outbreaks" involving 16 people; in each case, they even identified the likely food culprit. The researchers described the unusual effort on 23 May in the U.S. Centers for Disease Control and Prevention's *Morbidity and Mortality Weekly Report*. But, they note, investigating reports of illness this way could require "considerable time and resources."



ISEE-3 has 13 instruments for studying space weather.

RANDOM SAMPLE

Space buffs to wake up 'zombie' probe

A group of citizen scientists are ready to wake up and recycle a long-unused NASA spacecraft. NASA launched the International Sun-Earth Explorer-3 (ISEE-3) in 1978 to study space weather, and it went on to study two comets. The mission ended in 1997, but the spacecraft kept broadcasting its location. On 23 May, the ISEE-3 Reboot Project, which has raised more than $150,000 in crowd-funding, tested its transmission equipment at the Arecibo radio telescope in Puerto Rico. As *Science* went to press, the group was waiting for final NASA permission to make first contact with the spacecraft, says Keith Cowing, a co-director of the project. "[NASA] left gas in the gas tank and the keys in the ignition," he says. Robert Farquhar, the 81-year-old original flight director for the ISEE-3 mission, believes that most of the spacecraft's 13 instruments should still be working. He wants to redirect the spacecraft to an encounter with comet 46P/Wirtanen in 2018.



Some foodborne disease came from raw fish.

NEWSMAKERS

Three Q's



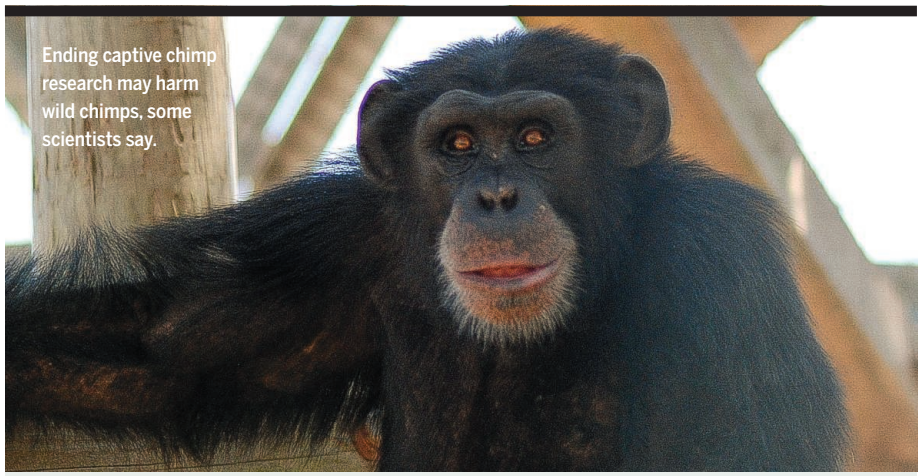
Earlier this month, the National Aquarium in Baltimore, Maryland, announced that it was considering moving its eight Atlantic bottlenose dolphins to a marine sanctuary (http://scim.ag/baltdolphins). The aquarium's CEO, **John Racanelli**, has wrestled with the ethics of keeping dolphins in captivity for decades.

Q: What got you thinking about the welfare of captive dolphins?

A: One of my first jobs was cleaning the dolphin tank at Marine World in San Francisco in the early 1970s. One of the dolphins died right after a show. I just

PHOTOS: (TOP TO BOTTOM) ISEE-3 REBOOT PROJECT; MARK MAXWELL; THINKSTOCK; NATIONAL AQUARIUM

Published by AAAS



Ending captive chimp research may harm wild chimps, some scientists say.

Ape researchers speak up for captive chimp studies

The U.S. government's recent push to stop "invasive" research with captive chimpanzees may overreach and cause the overall species harm. So argue ape researcher Peter Walsh of the University of Cambridge in the United Kingdom and colleagues in the 26 May online issue of the *Proceedings of the National Academy of Sciences*. The researchers tested a vaccine for the Ebola virus in chimpanzees at the New Iberia Research Center in Louisiana, aiming to protect wild chimps and gorillas from devastating outbreaks. But, Walsh and colleagues lament, "in an effort to pay back an ethical debt to captive chimpanzees, the U.S. Government is poised to renege on an even larger debt to wild chimpanzees," which were exported from Africa to create the captive colonies. The government should instead establish a captive chimp population dedicated solely to conservation research, the authors propose. Their study, which showed that the vaccine was safe and stimulated the immune system, was likely "the first conservation-related vaccine trial on captive chimpanzees" and, they note, "may be the last."

remember thinking, "She worked her whole life. She never got to retire."

Q: How has the National Aquarium changed its approach to dolphins?
A: In 1991, we were doing seven shows a day. Then, two baby dolphins died in 2011, and we stopped the shows. Today, the public can see the dolphins, but there's no music and no TV monitors. The dolphins have more time to just goof around.

Q: Will aquariums exist in the future?
A: I believe there will always be a place for aquaria. People find it fascinating to see a world they wouldn't see any other way. But when you start talking about higher order animals, the public gets uncomfortable seeing them in captivity.

Famed anthropologist dies

Emory University biological anthropologist **George Armelagos**, who helped found the field of paleopathology, died 15 May, 6 days after being diagnosed with pancreatic cancer. He continued to teach, mentor, and publish until his death at age 77. Armelagos, the son of Greek immigrants, was a graduate student in 1967 when he excavated Nubian human skeletons in Sudan dating back 10,000 years. Studying patterns of diet, disease, and death in these and other skeletons, he published a flurry of groundbreaking papers in paleopathology, including how changes in diet with the origin of agriculture influenced their health. He won many honors and was also known for his criticism of the concept of race. A much-loved mentor, many of his former students honored him in 2013 at a daylong session of the American Association of Physical Anthropologists.



Armelagos helped found the field of paleopathology.

PHOTOS: (TOP TO BOTTOM) JEREMY BREAUX, NEW IBERIA RESEARCH CENTER; SPECIAL COLLECTIONS AND UNIVERSITY ARCHIVES, UNIVERSITY OF MASSACHUSETTS AMHERST LIBRARIES

Published by AAAS

IN DEPTH



Alex Liu (holding banner) at Tiananmen Square in the spring of 1989.

SCIENCE IN CHINA

Tiananmen's bitter legacy

The bloody crackdown 25 years ago left an indelible mark on China's research culture

By **Mara Hvistendahl,** ***Shanghai, China***

As intellectuals gathered in Tiananmen Square in Beijing in the spring of 1989 to demand democratic reforms, a young Stanford University statistician, Alex Liu, was in China studying the small businesses then springing up in the wake of economic liberalization. Three years earlier, Liu had graduated from Peking University; now his alma mater had promised him a teaching post, and he had committed to moving back permanently after finishing his doctorate. But on 15 April, 5 days after Liu touched down in Beijing, the protests started. He dropped his project and joined the crowd in the square.

By the time the army opened fire on protesters on 3 and 4 June 1989, killing hundreds or possibly thousands, Liu had returned to the United States. But the Tiananmen crackdown changed the course of Liu's career and those of thousands of other scientists. It also warped science in China, say researchers inside and outside the country, contributing to problems it is now struggling to overcome. Tiananmen and its aftermath drove an exodus of talent and cemented a top-down research system that is prone to corruption. "It's just like the political system," says Bob He, a materials scientist who helped organize protests in the United States following the crackdown and is now director of innovation and business development at Bruker AXS in Madison.

The years leading up to the Tiananmen protests had been ones of unprecedented openness in China, with debates erupting over the relationship between scientific development and political liberalism. Scientists led by the late physicist Fang Lizhi, sometimes called China's Sakharov, and science historian Xu Liangying challenged Marxist versions of science and the utilitarian approach to research that had taken root with economic reforms. In February 1989, 42 prominent scholars signed an open letter to the Chinese government calling for the release of political prisoners—along with greater democracy. They also called for increased science funding, especially in basic research.


Staring down tanks at Tiananmen.

The scholars helped inspire a movement culminating that April, when thousands gathered in Beijing and other cities to mourn the death of Hu Yaobang, a liberal reformer who had been purged from China's leadership circle. Students occupied Tiananmen Square, demanding that the government uphold Hu's views. The government ultimately ordered martial law and condoned the bloody crackdown.

In the repression that ensued, the Chinese Academy of Social Sciences fired staff involved in the protests. Talented scholars like Fang fled China. Nascent efforts at building overseas ties faltered. In China, most mainland scientists fell silent, says sociologist Lun Zhang, a protest leader in the square. They "just returned to their offices and stayed out of anything related to society," says Zhang, who escaped to Hong Kong and then to France, where he now studies change in contemporary China at the University of Cergy-Pontoise in France. Meanwhile, thousands of top Chinese students who were studying abroad, the vast majority of them in the sciences, put off plans to return.

Many never did. In 1992, under pressure from Chinese students, President George H. W. Bush pushed the Chinese Student Protection Act through Congress, guaranteeing green cards to all Chinese nationals who had been in the United States between 5 June 1989 and 11 April 1990. The act was a "huge blow" to Chinese science, says David Zweig, a political scientist at the Hong Kong University of Science and Technology who researches Chinese returnees. Fully 54,000 people collected green cards under the new law, many of them scientists. Thousands more took advantage of similar provisions in Canada and Australia. The exodus "delayed China's science and technology dramatically—probably by 5 or 10 years," says He, who stayed in the United States instead of returning to China as initially planned.

Luring back that talent has been tricky, Zweig says. In the early 1990s, Chinese leader Deng Xiaoping urged overseas students to return, declaring that their previous "political attitude" didn't matter. By 2000, even some scientists who had been politically active after Tiananmen had been invited back, often for prominent positions in the

PHOTOS: (TOP TO BOTTOM) COURTESY OF YONG-CHUAN LIU; JEFF WIDENER/AP

Downloaded from www.sciencemag.org on May 30, 2014

Published by AAAS

country's booming research enterprise. They returned to a vastly different intellectual environment: one with far more money for research, but dominated by political connections and more intolerant of dissent—and still hindered by a top-down distribution of grants and accolades. "The ethos and culture of the domestic research system" took a hit after 1989, notes Richard Suttmeier, an expert on Sino-American science cooperation at the University of Oregon, Eugene. "It is hard to recover from that."

In surveys and interviews, overseas scientists tend to name the complex social relations shaping Chinese science as the key impediment to their return, Zweig says. "If you're not part of the inner network, if you're not part of the team of the director of the institute, you're not going to get grants," he says.

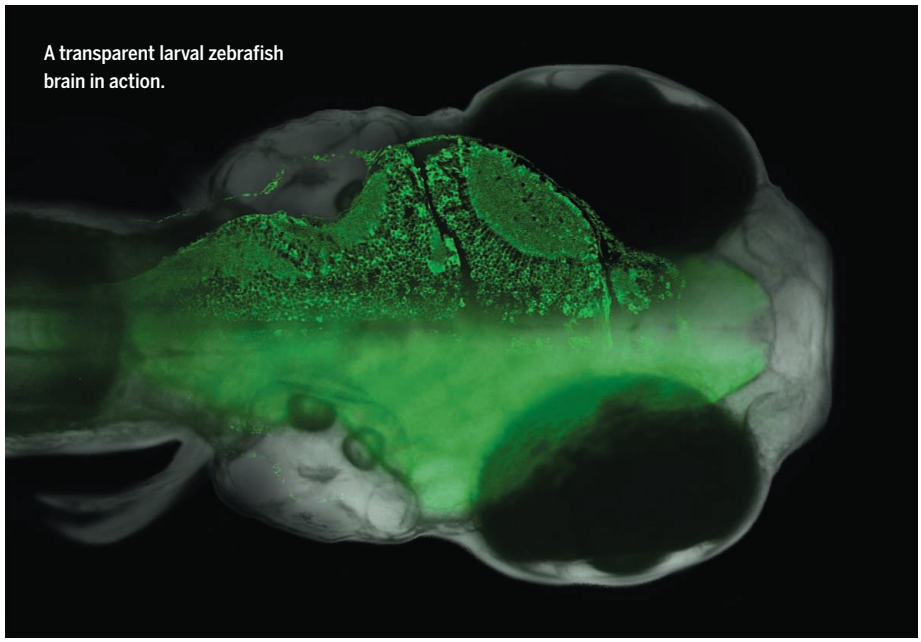
PODCAST

To hear a podcast with author Mara Hvistendahl, see http://scim.ag/pod_6187.

Returnees concur that fundamental cultural issues hamper Chinese science. One prominent scientist who was barred from China after 1989 for his political activities but eventually returned from the United States to head a lab on the mainland says that a rigid hierarchy and lack of openness thwart scientific debate. While the culture is gradually changing, he says, the top-down distribution of grants and a lack of investigator-initiated projects mean that "big investments are sometimes wasted." Young scholars are discouraged from contradicting their advisers, He adds. "If you have a higher position, people think you are more right."

Such shortcomings seem to hardly register with Chinese science officials, many of whom question why the government's outlays haven't yielded more breakthroughs—or netted the nation a Nobel Prize in science. To try to boost innovation, the government has stepped up efforts to bring overseas Chinese scientists back home. Foreign-born researchers are now wooed, too, under the Recruitment Program of Foreign Experts introduced in 2011. Some say that scientists brought in under such programs are helping change China's research culture—by instituting reforms within their labs and sitting on university committees dedicated to institutional change. China's science ministry has even consulted former dissidents for their thoughts on scientific reform.

But the recruitment drive misses the point, Zhang contends: "The most important question is not talent. It is the loss of vitality." In the wake of the Tiananmen crackdown, he says, Chinese intellectual life lost its edge. Without that, he notes, "They can train engineers and scientists, but the really original inventions won't come from China." ■



A transparent larval zebrafish brain in action.

PHOTO: NEWS & VIEWS/RESEARCH; *NATURE* **485** (24 MAY 2012) © 2012 MACMILLAN PUBLISHERS LIMITED/VALENTINA LYAU AND M. AHRENS *ET AL.* (2012), AND THE WELLCOME TRUST

NEUROSCIENCE

BRAIN project meets physics

Neuroscientists have some wild ideas for measuring brain activity. Physicists are providing a reality check

By **Emily Underwood**

Neuroscientists were over the moon in April 2013 when President Barack Obama announced a bold new initiative to study the human brain in action. But in their heady excitement, some may have forgotten to check the math in their first proposals. At least, that's the contention of a group of physicists, engineers, and neuroscientists meeting this week in Arlington, Virginia, to discuss which ideas are likely to succeed and which may fall flat.

Key to the success of the roughly $100 million Brain Research through Advancing Innovative Neurotechnologies (BRAIN) Initiative is crafting new tools or methods to measure neural activity either from inside or outside the brain. Unfortunately, some ideas "violated either a physical law or some very significant engineering constraint or biological constraint," says neurophysicist Partha Mitra of Cold Spring Harbor Laboratory in New York, who helped organize the meeting, sponsored by the National Science Foundation.

The goal is to have a realistic discussion of what the physical limits are, he says, so "scientists who want to make devices will not make crazy proposals," or, "if a proposal is crazy, one could recognize it as such" and look for other ways to make the idea work.

One such "fanciful" idea is to build nanosized radios that could snuggle up to individual neurons to record and transmit information about their activity, says physicist Peter Littlewood, director of Argonne National Laboratory in Lemont, Illinois. But any radio small enough to be injected into the brain without causing significant harm would not be able to transmit any information out through tissue and bone, he says. Make the devices any more powerful, he adds, and they'd likely cook the surrounding brain. Another aspiration that is likely doomed is to get microscopes that probe the brain with pulses of light to penetrate much further than they already do, Mitra says. A little more than 1 mm is possible, he adds, but even 1 cm is "out of the question, since the signal to background [noise] ratio decreases exponentially with depth."

But physicists and engineers shouldn't simply shoot down outlandish proposals—or gripe about the intrinsic messiness of the brain's biology. They should model themselves as "fancy technicians" who can help develop revolutionary tools, Littlewood says. There are precedents for such collaboration, he notes: He, Mitra, and their colleagues at Bell Labs, for ex-

Published by AAAS

ample, helped develop functional magnetic resonance imaging in the 1990s.

One area where physical scientists can help today is in fashioning small, strong, conductive wires that can record from many different neurons simultaneously, says neurophysicist David Kleinfeld of the University of California, San Diego. For decades, neuroscientists have relied largely on electrodes fashioned from fragile glass pipettes. But only a small number of these sensors will fit in a given brain region without disrupting connections between cells or killing them outright. Biophysicist Timothy Harris at the Janelia Farm Research Campus in Ashburn, Virginia, and others have had some success at making much smaller ones for fish and fly brains—some, made of silicon, are roughly 3 microns wide, about 25 times thinner than a human hair.

These probes are by no means the tiniest possible—polymer-coated carbon nanotubes, for example, can be 0.1 microns or smaller across and are highly conductive. Such thin wires tend to be very short and too flexible to get into the brain easily, however—when pushed, they simply buckle. One question Harris plans to pose at the meeting is whether the probes could be magnetized, then pulled, rather than pushed, into the brain with a powerful magnet.

Ultimately, researchers hope to measure neural activity inside the brain without poking wires into living tissue, and there, too, physics can help. Harris has his eye on light-sheet microscopy, which shines a plane of light across a living brain tissue, illuminating neurons engineered to fluoresce green or red when they are flooded by calcium during neuronal firing. Last year, neuroscientist Misha Ahrens and colleagues at Janelia Farm used this technique to produce the first "real" whole-brain activity map of a zebrafish larva, Harris says.

A larval zebrafish brain is 1000 times smaller than a mouse brain, however. It is also conveniently transparent, while mouse and human brain tissue scatter and blur light. Using the same optical techniques that astronomers employ to discern very faint or close-together stars with a telescope, researchers such as physicist Na Ji, also at Janelia Farm, have discovered ways to distinguish between hard-to-see neurons in murky brain tissue.

In preparation for the meeting, Mitra has brushed off an old copy of *Principles of Optics* by Emil Wolf and Max Born, one of the most venerable and difficult physics tomes. Getting back to basics, he hopes, will help him and his BRAIN project colleagues determine which rules must be followed to the letter, and which might be cleverly circumvented. ■

PARTICLE PHYSICS

Plan to internationalize U.S. project may face headwind

Washington may be reluctant to share control of a long-baseline neutrino experiment on U.S. soil

By **Adrian Cho**

It's a gamble that leading U.S. particle physicists say they must take: To finally get started on their next megaproject at the United States' sole particle physics lab, they want to make it an international collaboration—even if that means ceding direct control to a council of member nations. Doing so could open the way to an ambitious effort to study elusive particles called neutrinos and ensure the future of the Fermi National Accelerator Laboratory (Fermilab) in Batavia, Illinois. But the approach may not fly with Congress.

The recommendation comes from a draft road map for U.S. particle physics presented on 22 May to a federal advisory panel in Bethesda, Maryland. The report of the ad hoc Particle Physics Project Prioritization Panel (P5) strikes a decidedly more international tone than previous plans. It urges the government to "[p]ursue the most important opportunities wherever they are, and host unique, world-class facilities that engage the global scientific community."

"The case for proceeding this way is persuasive [because] collaboratively, we can address all the physics" originally envisioned for the Fermilab project, says Andrew Lankford, a particle physicist at the University of California, Irvine, and chair of the High Energy Physics Advisory Panel (HEPAP), the Department of Energy (DOE) and National Science Foundation panel that commissioned the report. "The question is, will the decision-makers in Washington appreciate it?"

P5 has followed the lead taken by European particle physicists last May, when they revised their long-term strategy. The European report suggested that Europe, the United States, and Japan share the field's biggest projects. Europe would continue to run the world's highest energy atom smasher, the 27-kilometer-long Large Hadron Collider (LHC) at the European particle physics laboratory, CERN, in Switzerland—which 2 years ago unearthed the long-sought Higgs boson. Europe might also contribute to a massive neutrino experiment, perhaps in the United States, and to the proposed International Linear Collider (ILC), a 30-kilometer electron-positron collider that would study the Higgs boson in great detail. Japanese physicists hope to host the ILC.

The P5 report calls for the United States to stay fully involved in the LHC and its planned upgrades. More than 1200 U.S. physicists now work on LHC experiments, about a third of the total. Similarly, if Japan goes forward with the ILC, the United States should join that collaboration—if money allows.

If Europe is willing to work on somebody else's neutrino experiment, the P5 report has one to offer: a so-called long-baseline neutrino facility. It would fire neutrinos 1300 kilometers to a gigantic detector filled with

Ups and downs

The proposed configuration of Fermilab's next neutrino experiment has fluctuated.

DATE	DETECTOR SIZE (KILOTONNES)	DEPTH (M)	COST
2009	300 water or >50 liquid argon	1480	—
2010	200 water or 33 liquid argon	1480	$990 million
2011	Combination of water and argon	1480	~$1.1 billion
March 2012	33 liquid argon	1480	$1.5 billion
August 2012	10 liquid argon	Surface	$789 million
Present	>40 liquid argon	1480	To be determined

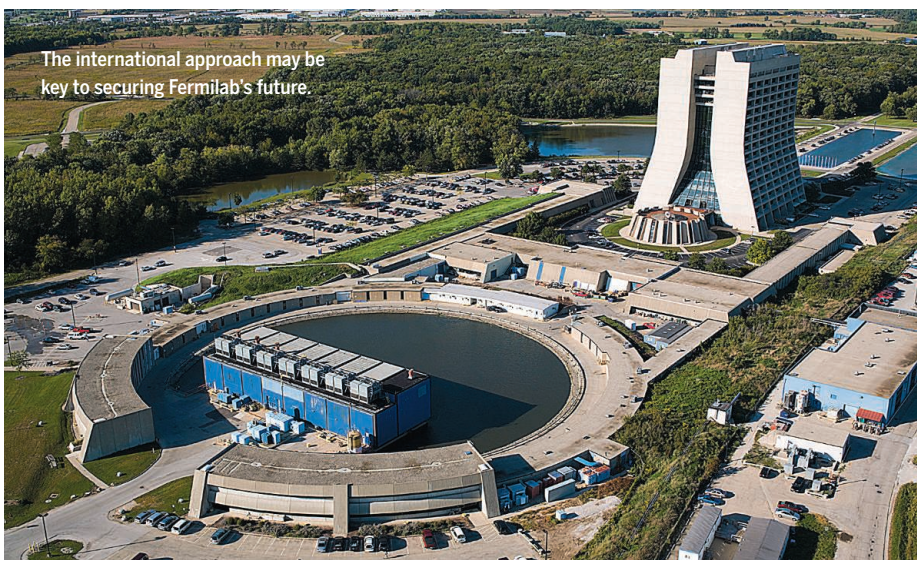
Source: *AIP Conf. Proc.* **1222**, 479 (2010), *Science* **330**, 904 (2010), Fermilab, DOE

Downloaded from www.sciencemag.org on May 30, 2014

Published by AAAS

40,000 tonnes of frigid liquid argon and set 1480 meters down in an abandoned gold mine in Lead, South Dakota. It would study how the "flavors" of neutrinos morph into one another as they zing along at near light speed. The experiment's main goal would be to spot an asymmetry between the behavior of neutrinos and antineutrinos that could help explain how the universe generated so much more matter than antimatter.

Fermilab researchers already had a plan for such a project, called the Long-Baseline Neutrino Experiment (LBNE). In 2012, Fermilab physicists presented a design for a neutrino detector filled with 34,000 tonnes of liquid argon in the mine. The underground detector also could have looked for signs that protons in the liquid argon decay—a key prediction of some theories—and spotted neutrinos from supernovas. But DOE officials balked at LBNE's $1.5 billion price tag. So, Fermilab physicists proposed a $789 million version with a detector less than one-third the size of the previous proposal, located at the surface. P5 now says researchers should scrap that attenuated plan and start over with a bigger international effort.



The international approach may be key to securing Fermilab's future.

That most likely means the project would have to answer to an international council like the one that governs CERN, says Fermilab Director Nigel Lockyer. "The U.S. government has to accept that it has to give up something in the way they normally do things," he says. Rolf Heuer, director-general of CERN, says such an arrangement would be very important for European physicists. "An international project is not one where I say what I'm going to do and you can do it, too," Heuer says. "It's one where the participants are on the same eye level."

That approach may be hard to sell to Congress, especially as it deals with huge cost overruns for the international fusion experiment ITER under construction in Cadarache, France. "The facility construction and day-to-day project management should stay in the hands of DOE," says a staffer with the Democratic majority in the Senate. "We don't want to repeat project management problems that have plagued ITER, and we don't want to overly complicate a billion-dollar-class science construction project."

However, James Siegrist, DOE's associate director for high-energy physics, says CERN's successful LHC collaboration can serve as a model for a U.S.-based project: "I'm pretty confident we can figure this out."

The P5 report also recommends increasing funding for smaller underground experiments to detect particles of dark matter. But it calls for an end to current R&D efforts to develop a collider that smashes muons, heavier unstable cousins of electrons, and several other projects.

Money could strain P5's global plan. P5 considered three budget scenarios: One in which DOE's particle physics budget, now $797 million, increases by a meager 5% over 10 years, one in which it increases by 17% over 10 years, and one in which it is unlimited. In the first two cases, the United States could contribute only R&D money and some hardware to the ILC.

If the United States doesn't play ball on the ILC, then Japan could opt for its own proposed neutrino experiment. "That's a challenge for the strategy," says HEPAP's Lankford, although he says the U.S. project might be able to go ahead without Japan.

DOE officials hope the plan will help unify the factious U.S. particle community. "It's the right fit for this global picture," Siegrist says. "So hopefully people will recognize that." ■

PHOTOS: (LEFT) REIDAR HAHN/FERMILAB; (RIGHT) HUMBOLDT-STIFTUNG/SVEN MÜLLER

SCIENTIFIC COMMUNITY



Jens Förster can't provide original data on studies.

Psychologist's defense challenged

E-mails counter claimed location, timing of studies

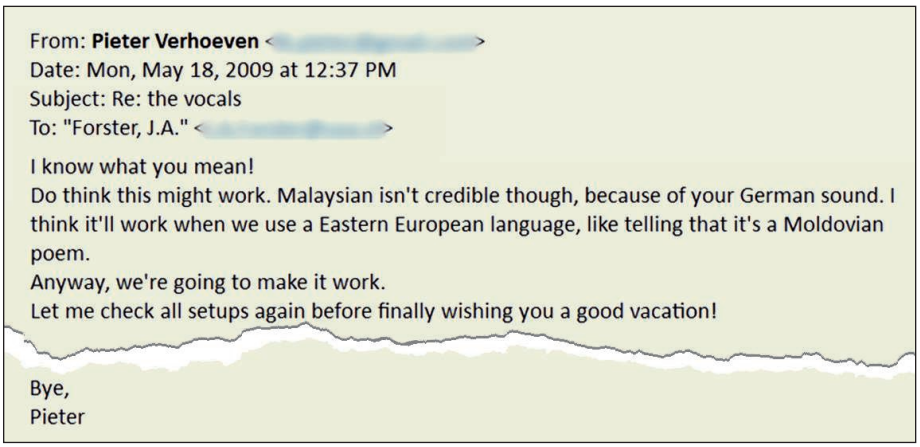
By **Frank van Kolfschooten**

With a once distinguished career, a €5 million grant, and a new professorship all hanging in the balance, social psychologist Jens Förster has vigorously fought back against recent charges that some of his results are so statistically improbable that they could only have resulted from data manipulation. But a key element of his defense has also exposed Förster, who recently resigned from the University of Amsterdam (UvA), to a new line of attack.

E-mails reviewed by *Science* call into question his assertion that some of the studies at the heart of the controversy were not conducted recently at UvA but were done much earlier in Germany over a decadelong period ending in 2008. In explaining certain puzzling aspects of the study subjects, and his inability to provide the original data files on them, Förster had said the studies took place long ago at another institution. The e-mails between Förster and a UvA colleague discuss how to conduct various aspects of some of those studies—yet the e-mails were sent in May 2009, undercutting Förster's timeline.

This perplexing saga began in 2012 when another psychologist expressed concern to UvA about unusually large effects that seemed improbably consistent, reported in 40 studies described in three papers. After participants had been "primed" by subtle stimuli, such as hearing poems, their scores

Published by AAAS



From: **Pieter Verhoeven** <[redacted]>
Date: Mon, May 18, 2009 at 12:37 PM
Subject: Re: the vocals
To: "Forster, J.A." <[redacted]>

I know what you mean!
Do think this might work. Malaysian isn't credible though, because of your German sound. I think it'll work when we use a Eastern European language, like telling that it's a Moldovian poem.
Anyway, we're going to make it work.
Let me check all setups again before finally wishing you a good vacation!

Bye,
Pieter

This 2009 e-mail between Jens Förster and his research assistant seemingly discusses plans for a study Förster says was already completed by 2008.

on a cognitive ability test rose significantly. The complaint sparked a UvA investigation that delved into the statistics of Förster's publications and found some "virtually impossible" results in papers published in 2009, 2011, and 2012, but did not conclude misconduct. A second inquiry, by the Netherlands' National Board for Research Integrity, did conclude that data had been manipulated in the 2012 paper published in *Social Psychological and Personality Science*, however. UvA has recommended that that paper be retracted, but Förster has not acceded.

In addition to questioning Förster's results, the person who filed the complaint had expressed skepticism about the recorded information on the study subjects, noting, for example, that the sex ratio of the participants was very different from that among students at UvA. The psychologist also found it suspicious that the 2012 paper and two others recorded not a single study dropout, out of more than 2200 participants across 40 experiments, and not a single participant who had guessed the purpose of the study—even though many of them were presumably psychology students at UvA.

In a 11 May posting on his website, Förster reiterated a previous denial of data manipulation and stressed that his challenger had made a key mistaken assumption—the studies documented in the 2011 and 2012 papers, Förster says, were conducted from 1999 to 2008 in Germany, mostly at Jacobs University Bremen, with the help of more than 150 co-workers. Förster further hinted that one of those people might have manufactured the exceptional results. "I can also not exclude the possibility that the data has been manipulated by someone involved in the data collection or data processing. … During the time of investigation I tried to figure out who could have done something inappropriate. However, I had to accept that there is no chance to trace this back; after all, the studies were run more than 7 years ago and I am not even entirely sure when, and I worked with too many people," he wrote.

> ***"I can only conclude we were still working on the exact design of the experiments in May 2009."***
>
> **Pieter Verhoeven**

In an earlier posting on 29 April, Förster wrote that he had thrown away the original questionnaires for the challenged studies when he moved to a much smaller office in Amsterdam. (In that posting, he did not note where the studies were done.) In his 11 May statement, Förster noted that he provided both investigations with processed data files, one of which contained questionnaire answers in German, which he says proves the experiments were performed in Germany and not in Amsterdam as had been assumed. Those files are time-stamped February 2013, however, according to Förster's challenger and a second source, who has access to the data files but does not want to be named.

Förster's accuser says the integrity committee of UvA should have asked for data files with a time stamp before September 2012, when the complaint was filed. He also says the UvA erred by not confiscating Förster's computer, as often happens in such investigations. (The whistleblower's identity is known to Förster, the university, and the national investigating body, but he agreed to talk to *Science* only if not named.)

The real challenge to Förster's timeline may lie in e-mails between him and Pieter Verhoeven, his research assistant at UvA from September 2008 to June 2009, who made the correspondence available to Förster's accuser. In it, the two discuss how to conduct what are evidently the same experiments Förster's blog declares were completed much earlier in Bremen. For instance, among the stimuli used are three unintelligible audio recordings, which the 2011 paper says were described to the subjects as "Moldavian" poems. In an 18 May 2009 e-mail, Verhoeven comes up with the idea to describe the poem that way, rather than as Malaysian, because the reader of the poem has a German accent.

In another e-mail, sent to Verhoeven on 13 May 2009, Förster reports having found "little boxes" at a home appliance store. "I'm optimistic that this will work," Förster writes. The 2012 and 2011 papers describe having study subjects touch an object "that consisted of four square plastic boxes."

Verhoeven has confirmed to *Science* that these e-mails discussing details of studies seemingly described in the 2011 and 2012 paper are genuine. "Reading back our correspondence 5 years later, I can only conclude we were still working on the exact design of the experiments in May 2009," says Verhoeven, now an interior designer in Amsterdam, who says he has no animosity toward Förster. He provided the e-mails only after Förster's accuser approached him.

Förster's accuser has also informed UvA that six more of his papers contain statistically improbable data. UvA, however, tells *Science* that it will take no action because there has been no filing of a "new, formal, and substantiated" complaint.

In lieu of any new investigation, colleagues are judging Förster themselves, often posting their views online. For example, psychologist Uri Simonsohn of the University of Pennsylvania, whose statistical analysis of the data published by psychologist Dirk Smeesters of Erasmus University Rotterdam exposed his scientific misconduct, joined with Leif Nelson of University of California, Berkeley, to analyze the 2012 paper. On 8 May on the blog datacolada.org, they describe conducting 100,000 data simulations and other statistical analyses to examine how likely the results are. "[W]e have a conceptual replication of 'these data are not real,' " they concluded.

Förster has not responded to *Science*'s multiple attempts to reach him. As the psychology community mulls the bewildering tale, he awaits word from Ruhr University Bochum, which has postponed plans for him to start a professorship endowed with €5 million in funding from the German Alexander von Humboldt Foundation. The university and the foundation now say they may not address the matter until October. ■

Frank van Kolfschooten is a freelance writer in Amsterdam and the author of two books on scientific misconduct.

Published by AAAS



PHOTO: MATTHEW RAKOLA PHOTOGRAPHY

INTERVIEW

Where's France Córdova? In the Washington hot seat

New NSF director jumps into the frying pan served up by Congress as it reviews agency programs

By **Jeffrey Mervis**

"Can you find Dr. Córdova?" asks a brightly colored cartoon poster slapped on bulletin boards and elevators throughout two buildings housing the National Science Foundation (NSF) in Arlington, Virginia. A picture taken from a *Where's Waldo?* children's book has a mug shot of France Córdova, the agency's new director, neatly hidden in a corner. Below is a message inviting employees to say "hello" to their new boss as she made an inaugural round of meet and greets earlier this month.

"It's an experiment," explains the 66-year-old astrophysicist, who on 31 March became NSF's 14th director. "And they are really surprised when I stop by."

Córdova believes that personal connections matter. That approach worked well for her when she was president of Purdue University in West Lafayette, Indiana, says Howard Zelaznik, a professor of kinesiology there and former chair of the university senate. "When she went away from the podium and spoke with faculty in an unscripted way, she was quite impressive," says Zelaznik, who is also an associate vice president for research. But, he adds, "she was less effective when she's in a public setting."

If Zelaznik is right, then Córdova may want to hang a Waldo poster on the fourth floor of the Rayburn House Office Building. That's where Representative Lamar Smith (R–TX), the chair of the science committee in the U.S. House of Representatives, has his office. For the past year, Smith—whose panel oversees NSF—has been vocally criticizing the agency for making "wasteful" grants and is pushing a controversial bill that would make substantive changes to NSF's policies (see p. 960). Córdova has arrived just as her agency is under political siege and academic researchers are rallying to its defense.

Figuring out how to keep NSF from being permanently scarred by the controversy is certainly Córdova's biggest and most pressing challenge. But it's not yet appropriate for her to speak out about it, she told *Science* during a 15 May interview in her 12th-floor office. "As you know, neither NSF nor the administration has stated a position on the bill. And so I don't really have a comment on it."

However, she believes that a positive outlook can make a difference. "I never focus on divisions. I focus on where people can come together," she explains. Members of Congress share her positive outlook, she adds. "There is no one I've met on either side of the aisle that wouldn't agree on the importance of science and technology, both now and in the future," she says.

Córdova's focus on common ground is consistent with her heritage. "My mother is Irish, my father was born in Mexico but his father was an American citizen, and his mother was Mexican," she says about her background. Raised in southern California, Córdova majored in English literature at Stanford University but was smitten by astrophysics after watching Neil Armstrong walk on the moon. Accepted for graduate work in physics at the California Institute of Technology, she earned her Ph.D. "by working hard and having that passion. And I think it matters a lot how much you throw yourself into something."

Her circuitous path has also shaped her perspective on attracting students into science and engineering and retaining them. "I'm trying to get rid of this metaphor of pipelines," she says. "I think our lives are filled with lots of disjointed pipelines. We go in one direction for a while, then we have an opportunity to go in a different direction. My own life shows that. It's unpredictable. We don't know what's going to happen."

Córdova's own career path began at Los Alamos National Laboratory and included 3 years as NASA's chief scientist during the Clinton administration. In 1996, she returned to academia, eventually becoming chancellor of the University of California, Riverside, before arriving at Purdue in 2007 (*Science*, 9 August 2013, p. 600).

This second stint in Washington—she has a 6-year term—is likely to test her ability to put a personal touch on what is one of the nation's most public science posts. What follows are excerpts from her interview with *Science* on her time at Purdue, her passions, and the many issues on her plate.

Q: Is there more that NSF can do to broaden participation in science by underrepresented groups?

A: I recently had a 2-day retreat with the ADs [associate directors], and I would say no subject garnered as much excitement as broadening participation. We have leverage through specific programs designed to foster development of faculty who are

Downloaded from www.sciencemag.org on May 30, 2014

Published by AAAS

hired. And to the extent NSF can encourage people to do more formal and informal education, we can inspire people who will become the next generation of faculty.

We have an untapped talent pool in this country of women and minority students. And some would argue that young men from disadvantaged communities would also be part of that pool. We are also looking at who will be the future legislators and journalists, and what they know about science.

Q: You took several belt-tightening steps at Purdue to offset severe state funding cuts. Should NSF be asking universities to do more to hold down costs?

A: The university community doesn't need NSF suggesting how to run its institutions. I am just so impressed with the people who step up to be presidents and chancellors of our universities and how responsive they are to all our concerns, social and economic and academic.

Q: Lawmakers and others have raised concerns about the high cost of NSF's temporary "rotators," academics who come into the agency for a few years to run programs. Should NSF think about using fewer of them?

A: The National Science Board has looked into rotators, and I think everyone really sees their value. As with any program, can we make it stronger? I'm sure we can. But the value of rotators is not in question. It's more about the money and time involved.

Q: What's the future of Innovation Corps [I-Corps], a new program to teach NSF grantees how to commercialize research?

A: I don't have a crystal ball about how much more we will put into the program. NSF's real strength is in seeding brilliant ideas. And we often look at who wants to come into that space, and then take it to the next level. Could that happen to I-Corps? It's a very exciting program, but I

Views of science clash in debate over NSF bill

By **Jeffrey Mervis**

Does the National Science Foundation (NSF) need a minor tuneup or a major overhaul? How lawmakers in Congress answer that question could have an impact on U.S. science that extends far beyond the $7 billion agency.

Congressional scrutiny of one of the federal government's most important engines of innovation reached a new intensity last week as the science committee of the U.S. House of Representatives wrangled over the extent to which NSF's practices need to be altered. The battleground was a controversial proposal called the Frontiers in Innovation, Research, Science, and Technology (FIRST) Act.

More than a year in the making, FIRST is designed to curb wasteful and unwise practices at the agency, according to the committee's chair, Representative Lamar Smith (R–TX). But university and science groups fiercely oppose the measure, and they received unusually energetic backing last week from the panel's Democrats. The clash underscores growing tensions within the committee over an agency that has traditionally enjoyed bipartisan support. It also highlights a broader policy and funding debate likely to grow fiercer as budgets tighten in an era of divided government.

"What's most troubling in the bill is the questioning of scientists and of science," says Michael Lubell, head of the Washington, D.C., office of the American Physical Society. "There seems to be a growing desire by some politicians to score points at the expense of the scientific community. You see it often with respect to climate change and evolution. Their attitude is that scientists come up with theories that keep changing, and that they can't be trusted."

At the heart of the FIRST fight are a set of provisions that Smith says are needed to make NSF more transparent and accountable, and ensure that only "high quality research receives taxpayer dollars." He and other Republicans have repeatedly criticized the agency for wasting millions of dollars on "questionable grants," particularly from its social and behavioral sciences directorate, "at the expense of higher priority research in fields like engineering, mathematics, computer science and biology." Those grants include funding for a play about climate change (see picture).

> ***"Having no bill emerge from Committee would be better than passing a bad bill."***
> **Representative Eddie Bernice Johnson**

To address that issue, the bill favors those "higher priority" disciplines and proposes a sharp cut in NSF spending on the social and behavioral sciences. It would also require NSF officials to certify that each of the agency's roughly 11,000 annual grants pass a six-point test for being "in the national interest." FIRST would also increase the penalties for scientists found guilty of misconduct, reduce the number of cited publications in grant proposals, and require applicants who have already won a grant to certify that they won't duplicate existing work with new funds.

A few provisions, including better coordination of all federal science education programs, have bipartisan backing, and they were adopted without debate last week. But most of the bill has sparked vocal opposition from NSF's governing board and scientists. And the panel's Democrats, after largely holding their fire in earlier stages of the bill-writing process, came out with guns blazing at the 21 May markup. Their critique of the bill was sprinkled with phrases like "unwise and irresponsible," "a recipe for disaster," and "a threat to continued U.S. leadership in science and technology."

FIRST reflects "a distrust of NSF" and "hostility toward science," charged the committee's top Democrat, Representative Eddie Bernice Johnson (TX), who also characterized it as "an opportunity lost." Her last criticism echoes the widespread feeling among the scientific community that the bill's negative tone, in the words of the Federation of American Societies for Experimental Biology, "fails to provide a long-range vision for the National Science Foundation (NSF) and other science agencies."

The differences aren't just over policy; money is an issue, too. The science committee has traditionally been sympathetic to pleas for increased federal investment in research and science education. But Smith's panel is proposing that NSF receive less money next year than

Published by AAAS

think we need to let it evolve.

Q: The science board recently issued a report warning that rules intended to prevent conflicts of interest might also inhibit university-industry interactions. Does NSF need to monitor more closely what is going on at universities?

A: I don't get into that space directly. We have a chief operating officer, Cora Marrett, who is the ultimate resolution person. But frankly, I think good practices and monitoring goes a long way. And it starts with the university making sure its policies are being implemented.

Q: Is requiring grant applicants to share the cost of proposed research a good way for applicants to show their commitment to the project, or does it discriminate against institutions with fewer resources?

A: It all depends on the program, whether you're talking about large centers or smaller efforts. There are many ways of engagement. Some are with industry, and others are with other universities or organizations.

Q: Do you think NSF's $200 million budget for new facilities is adequate and sustainable?

A: Presently, I think it is. That situation is always fluid. But I think things look healthy at the moment.

Q: What can NSF do to ensure that the cost of operating new facilities doesn't reduce funding for individual investigators?

A: In some disciplines, and astrophysics is one, it's hard to be a [principal investigator], even a theorist—just look at BICEP2—without a big telescope. It's hard to be an ocean researcher without a ship. So I think a little bit of the debate is not really looking at how researchers actually do their work. So we fund the facility, and then individuals say they have a great idea and want to use it. ■



PHOTO: RICHARD TERMINE

Republicans have criticized NSF's funding of *The Great Immensity*, a play about climate change that includes research data and interviews with scientists.

provided by the body's spending committee, which usually plays the miser. For the 2015 fiscal year that begins 1 October, FIRST would give the agency $7.28 billion, $127 million less than the House appropriations panel has already approved. Critics note that FIRST would also retroactively cut the current budget for the social sciences directorate by a whopping 28%, to $200 million; a pending amendment would lop off another $50 million in 2015.

Democrats expressed dismay at the moves. "I have voted for a balanced budget amendment and I understand the need to reduce overall federal spending, but I think it's just common sense to authorize what the appropriators say we can spend," said Representative Daniel Lipinski (D–IL). His amendment would raise FIRST's 2015 numbers to match those in the spending bill covering NSF and many other agencies.

Smith pointed out that FIRST would authorize $22 million more for NSF than the $7.26 billion that President Barack Obama has requested for the 2015 fiscal year. Anything higher would be irresponsible, say Republicans on the panel. Representative Mo Brooks (R–AL) blasted efforts to raise the overall 2015 numbers and restore funding for the social sciences. "I'm opposed to spending $127 million that we don't have and can't pay back," he said, citing the nation's massive debt. "Why are we borrowing money from China and jeopardizing our children's future to fund this type of research?"

In the end, Smith and his allies are likely to prevail on the controversial provisions in the bill because the panel's Democrats, being in the minority, simply don't have the votes to block them. The same calculus applies to the full House, the bill's next step once it clears the committee.

In the meantime, however, Democrats are taking solace from a procedural victory: Their demand for recorded votes on each amendment left Smith without time to complete the markup. "At the end of the day, having no bill emerge from Committee would be better than passing a bad bill," Johnson said in a press release the day after the hearing. The bill's opponents also think they have an ace in the hole: The Democrat-controlled Senate is unlikely to go along with the FIRST Act as it's now written.

Even if the FIRST Act doesn't become law, however, the issues it has raised won't be going away. Republicans are expected to control the House at least through 2016, and some analysts say they may also claim the Senate in the November elections. If that happens, Smith and other conservatives will probably have a more sympathetic audience in Congress for their argument that NSF—and perhaps other research funding agencies—are in need of widespread reform. ■

Published by AAAS

FEATURE



Lost at sea

As the hunt for the missing Malaysian jet grows more challenging, authorities are pondering how to avert future aviation vanishing acts

By **Dennis Normile**

The disappearance of Malaysia Airlines Flight 370 (MH370) in the early morning hours of 8 March has become one of the darkest riddles in aviation history. As the mystery stretches into its third month, the odds of finding wreckage—and closure for grieving relatives—are rapidly receding. The scientific lessons are sobering, too: The futile search for the jet, an overnight flight from Kuala Lumpur bound for Beijing that is thought to have gone down in a desolate stretch of the southern Indian Ocean, has exposed disconcerting gaps in knowledge of the deep sea, and in technologies for monitoring aircraft from afar.

The fleeting detection early last month of pings emanating from a patch of water some 1700 kilometers northwest of Perth, Australia, raised hopes that searchers had drawn a bead on the plane's flight data recorder and cockpit voice recorder—the black boxes. That clue didn't lead to any wreckage, and the pings soon ceased, possibly because recorder batteries are designed to last for only a month or so, or because the pings weren't from the stricken plane. A search of 4,638,670 square kilometers of ocean by 29 civilian and military aircraft and 14 ships has failed to turn up a single scrap of flotsam linked to the plane. "The search for this aircraft has been one of the most difficult ever undertaken anywhere in the world," said Warren Truss, Australia's deputy prime minister, at a 5 May press conference in Canberra.

As authorities lay plans for the next phase of the operation—what could be the widest ranging and most challenging seafloor search in history—they face a paucity of data: the largely uncharted bathymetry of the southern Indian Ocean's sea floor and the poorly understood dynamics of how sound travels deep underwater. Knowledge of the ocean floors is "vastly poorer than our knowledge of the topographies of Earth's Moon, Mars, and Venus," write Walter Smith and Karen Marks, geophysicists at the Laboratory for Satellite Altimetry of the U.S. National Oceanic and Atmospheric Administration in College Park, Maryland, in the 27 May issue of *Eos*.

A Vietnamese military official scans the South China Sea for signs of MH370 on 12 March.

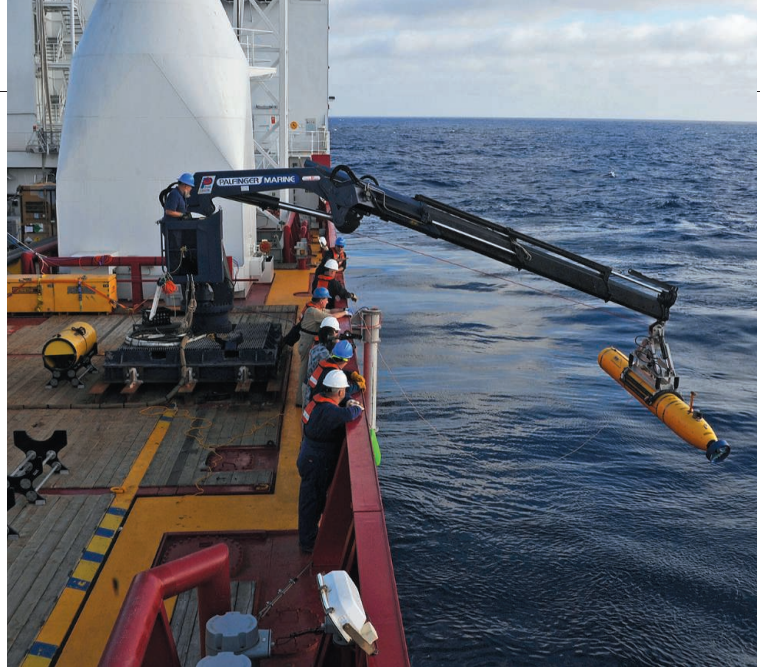
Then there's the sinking realization that MH370's black boxes may never be found, leaving investigators in the dark about what happened during the flight's last hours. That prospect has given new life to schemes for ensuring that ground stations can monitor flight data in real time, rather than only after a tragedy.

LIGHT AND RADIO WAVES, mainstays of imaging on land, don't travel far in seawater. So seafloor mappers must rely on sound: single-beam echo soundings gathered along a track directly beneath a ship or modern acoustic multibeam soundings, tied into GPS, which take in wide swaths of sea floor. Mappers can also infer bathymetry from satellite altimetry, which uses radar to measure bumps and depressions in

PHOTO: KHAM/REUTERS/CORBIS

Downloaded from www.sciencemag.org on May 30, 2014

Published by AAAS



An Australian navy vessel deploys the U.S. Navy's *Bluefin-21 Artemis* AUV, which has used side-scan sonar to scour 400 square kilometers of seabed in the search for MH370.

the sea surface reflecting the gravitational effect of water either piling up above submerged mountains or dipping above trenches. Multibeam soundings are the gold standard, but such mapping has been concentrated in coastal zones, along shipping lanes, and in regions harboring hydrocarbon or mineral deposits, says Erik van Sebille, an oceanographer at the University of New South Wales in Sydney, Australia.

Modern echo surveys have mostly ignored the southern Indian Ocean, where depths have mostly been estimated from satellite altimetry, Smith and Marks note in *Eos*. "Most seafloor features are very poorly resolved," they write. In the search area, the deepest spot is estimated to be over 7800 meters down. And no matter which ocean, the deeper you go, the less is known. The mean depth of the oceans is 4000 meters, "and we don't know anything about what happens at that depth or below," says Charitha Pattiaratchi, an oceanographer at the University of Western Australia in Perth.

One area of ignorance is how sound travels through the abyss. Sound waves move more slowly in colder water, and deep-ocean temperatures are not well known, Pattiaratchi says. The needs of submarines have driven most studies of sound propagation in the ocean, and subs rarely dive below 1000 meters. The resulting uncertainties may have stymied efforts to pinpoint the origin of the pings presumed to have come from MH370's black boxes.

Even if the search for the black boxes comes up empty, bathymetric readings and other data collected in the coming weeks might help avert a different kind of tragedy. Better bathymetry would allow for sharper modeling of tsunami propagation and more accurate tsunami warnings, Pattiaratchi says. It also "would help biologists immensely in predicting likely biodiversity hotspots … [and] dispersal of deep-sea fishes," says David Booth, a marine ecologist at the University of Technology, Sydney.

SURFACE SEARCHES MAY NOT HELP much in pinpointing the black boxes or the rest of the plane. Finding debris would confirm that it went down in the Indian Ocean; but given that nearly 3 months have passed, backtracking from a surface sighting to a likely crash site would be a difficult and imprecise exercise, van Sebille says. "The ocean is like a giant pinball machine, where if you just hit the ball slightly differently with a flipper you get a completely different trajectory," he says. In an experiment in the Southern Ocean, his team simultaneously dropped identical buoys off the port and starboard sides of a ship. Within weeks, some buoy pairs were hundreds of kilometers apart. Currents in the MH370 search area are weaker than those in the Southern Ocean, he says, "but there are a lot of eddies that mix things around."

An earlier flight that was lost at sea underscores the challenge. Air France Flight 447 (AF447) fell from the sky in the early hours of 1 June 2009 while en route from Rio de Janeiro to Paris. Debris and an oil slick were spotted from the air the following day, 650 kilometers off Brazil's coast. By 6 June, ships had begun recovering bodies, baggage, and plane pieces. But even though the ocean floor in the area had been mapped in great detail, it was nearly 2 years before REMUS 6000 autonomous underwater vehicles (AUVs) directed by a team from the Woods Hole Oceanographic Institution finally captured sonar images and pictures of wreckage in water nearly 4000 meters deep that proved to be from AF447.

Six handshakes, then silence

By **Daniel Clery**

How can air traffic controllers lose sight of a modern Boeing 777 while it flies thousands of kilometers? In the age of satellite communications and GPS, it shouldn't be hard to track an airliner's location over the ocean. But Malaysia Airlines Flight 370 (MH370) has pointed up holes in the technology and spurred discussions about improving it.

At present, commercial airliners are still mostly located in the sky using radar. While a plane is over or near land, "secondary" radar sends out coded pings and a plane's transponder answers with its own identifying signal. Contact with MH370 was lost in the early hours of 8 March over the Gulf of Thailand when its transponder mysteriously stopped operating. Seconds later, its transponder mysteriously stopped operating. It was still visible to conventional, uncoded radar as it turned west over Thai and Indonesian territory, but over the Indian Ocean it was out of range.

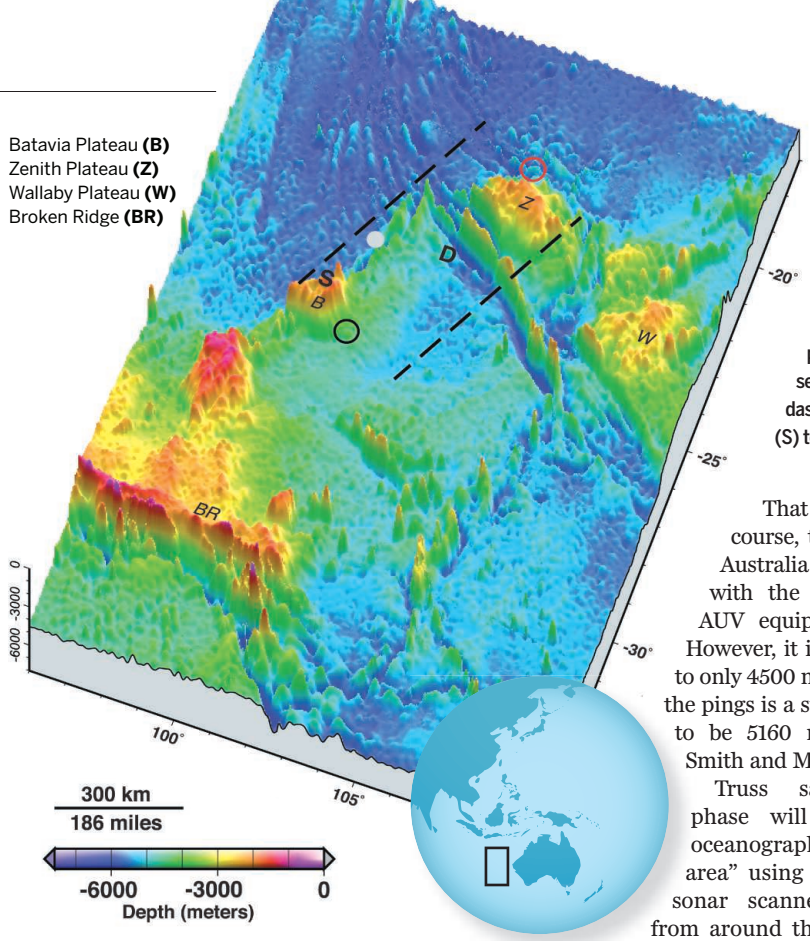
MH370 was also equipped with an advanced tracking system that should have kept close tabs on it wherever it was: Automatic Dependent Surveillance-Broadcast (ADS-B), which uses a GPS receiver to log the plane's position every second and transmits that data directly to ground receivers or via satellite. But it, too, stopped working, at the same time as the transponder.

The little information investigators have about the plane's course comes from a third transmitter, the Aircraft Communications Addressing and Reporting System (ACARS). This older technology automatically sends short digital messages to ground-based receivers or satellites, conveying routine data such as flight plans, weather information, and engine status. MH370's ACARS also stopped transmitting over the Gulf of Thailand—but it didn't fall completely silent.

If an ACARS station on the ground hasn't heard from an aircraft for awhile,

PHOTO: U.S. NAVY/FLICKR

Published by AAAS



Satellite measurements and old-fashioned echo soundings revealed the bathymetry of the sea floor in and around the MH370 search area in the southern Indian Ocean. Circles mark where pings were detected; depths in that search zone (roughly between the dashed lines) range from 1647 meters (S) to more than 7800 meters (D).

The loss or destruction of black boxes may be a rare event, but it is deeply troubling to aviation experts. Back in 2000, computer scientist Krishna Kavi and his doctoral student Mohamed Aborizka at the University of North Texas, Denton, proposed a "glass box," a system for continual streaming of flight data via satellite to make information available to investigators as soon as something goes awry. But the cost of downloading so much data from the roughly 30,000 airliners in service deterred the industry. "Unless regulators demand it, airlines won't do it," Kavi says.

One company, however, did develop something similar. FLYHT Aerospace Solutions of Calgary, Canada, sells satellite communications quipment to airlines and provides a service that automatically starts streaming black box data to the ground if something unexpected happens to a plane, like an unannounced deviation from the flight path. Only a small fraction of flights, though, have used the system since it was unveiled in 2005.

Regulators and the industry took more notice of such systems following AF447's loss. French aviation authorities set up a working group on flight data recovery, which concluded that flight data streaming could reduce the search area for a loss at sea to a radius of 4 nautical miles. "There was a lot of study work after AF447," says David Coiley, a vice president at the satellite communications company Inmarsat in London. "But industry didn't follow through." The sticking point, he says, was figuring out what trigger would give you enough time to get the data downloaded. "The technology exists, it's just a matter of finding a practical and affordable way to implement it," Coiley says.

That will come far too late, of course, to aid the hunt for MH370. Australia is continuing to search with the U.S. Navy's *Bluefin-21*, an AUV equipped with side-scan sonar. However, it is designed to operate down to only 4500 meters; the likeliest source of the pings is a stretch of sea floor estimated to be 5160 meters deep, according to Smith and Marks.

Truss said the search's next phase will involve "more detailed oceanographic mapping of the search area" using equipment such as towed sonar scanners and AUVs borrowed from around the world. "It will require a significant effort for us to understand the ocean floor in that area," he said.

With no debris, an uncertain flight path, and scant knowledge of the sea floor in the southern Indian Ocean, the search for MH370 is "unprecedented compared to other plane crashes," said acting Malaysia Transport Minister Hishammuddin Hussein at the 5 May press conference. "We've got very little to work on." ■

With reporting by Daniel Clery.

it sends a ping to find out if the plane is operating and in range. The aircraft's ACARS sends an automatic acknowledgement; the exchange is known as a handshake. While MH370 was otherwise silent, it carried out six hourly handshakes, which allowed investigators to conclude that it had crashed in the southern Indian Ocean.

ACARS handshakes don't carry precise location data, but following MH370's disappearance, the satellite communications company Inmarsat performed additional analyses. All the handshakes traveled via the Inmarsat-3 F1 geostationary satellite over the Indian Ocean. By measuring the time for the ping to travel to the plane and bounce back, Inmarsat analysts could calculate the distance between satellite and plane. And by measuring the Doppler shift of the ping's frequency, they could tell how fast the plane was traveling toward or away from the satellite.

Inmarsat gleaned further detail about MH370's flight path from Doppler shifts caused by movement of the satellite. The satellite's position has decayed and it now orbits around a fixed point on the equator. This movement shifts the ping frequency—an effect that investigators could subtract from the measured Doppler shift to constrain the plane's course.

Within a few years, such sleuthing shouldn't be necessary. A pair of systems under development—the Next Generation Air Transportation System in the United States and Single European Sky in Europe—will make it mandatory for every aircraft to carry an ADS-B transmitter, and it will become the primary method of locating planes. More precise position information should allow planes to fly closer together, permitting more direct routing and fewer delays.

Aircraft will be required to have ADS-B by the end of this decade. But MH370 has made better tracking over oceans a priority, and earlier this month the International Civil Aviation Organization convened a meeting to find ways to implement something sooner. The body received many proposals from industry for ways to track aircraft, and it set up a task force to evaluate them and make recommendations by September. ■

PHOTO: SMITH *ET AL.*, *EOS, TRANSACTIONS, AMERICAN GEOPHYSICAL UNION* **95**, 21 (27 MAY) © AGU; (INSET) EDWARD GRAJEDA/ISTOCKPHOTO.COM

Published by AAAS

INSIGHTS

Accuracy in movie science and designer genomes *p. 978*

Argonautes defend cells against foreign DNA *p. 980*



PERSPECTIVES

DRUG DEVELOPMENT

Target small firms for antibiotic innovation

Once in clinical trials, antibiotics are more likely to survive than drugs in other classes

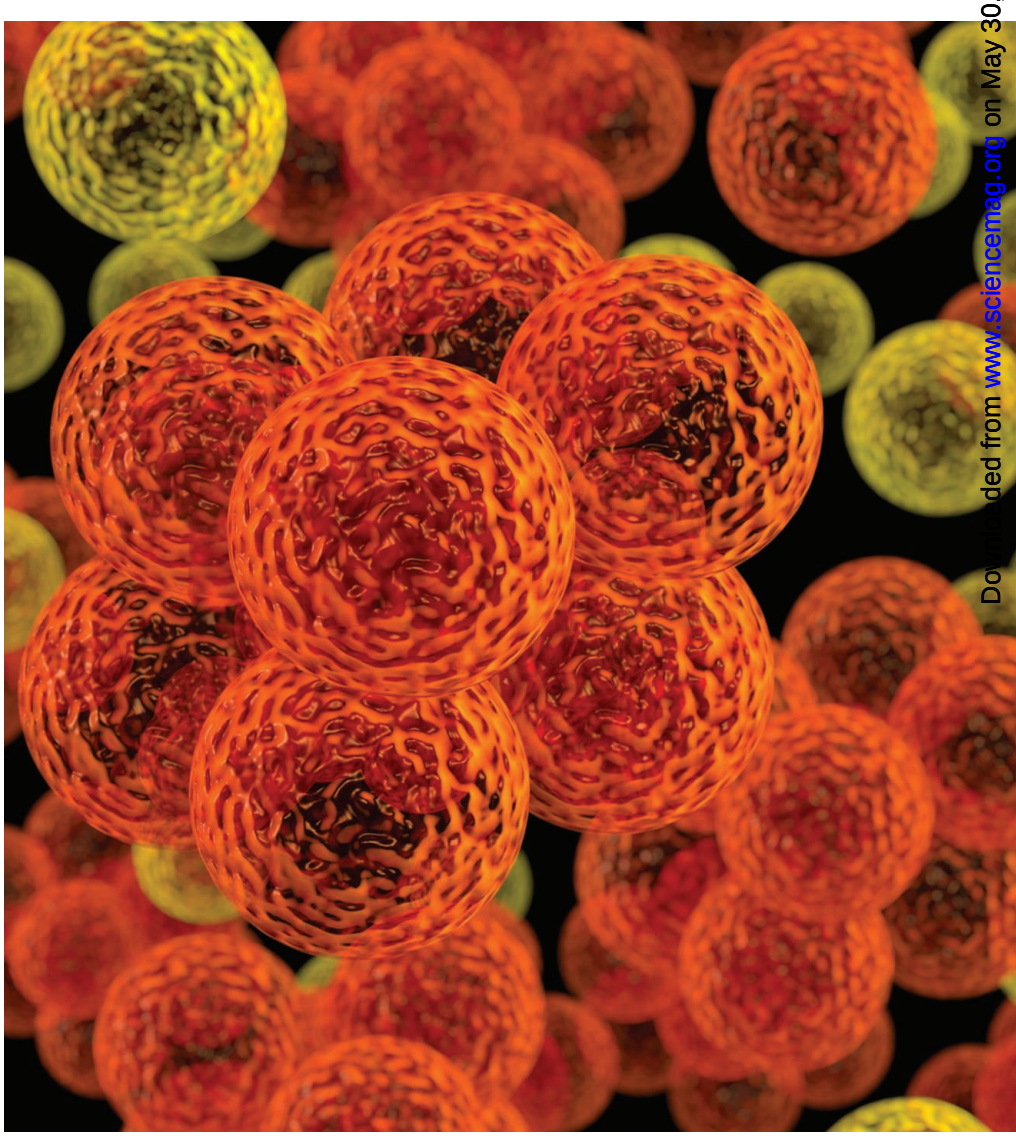
By **Thomas J. Hwang**[1,3*†], **Daniel Carpenter**[1,2], **Aaron S. Kesselheim**[3†]

Antibiotics are an indispensable part of modern medicine. Yet, since the first β-lactam, aminoglycoside, macrolide, tetracycline, and fluoroquinolone classes of antibiotics were discovered and approved from 1940 to 1980, few antibiotics with novel mechanisms of action have been developed (*1*). At the same time, antibiotic resistance has been on the rise (see photo). Ensuring appropriate use, or stewardship, of antibiotics is critical to ensure that antibiotics retain their effectiveness against pathogens. In addition, the need for new classes of antibiotics has seen increasing international attention. To inform ongoing policy debates, we characterize trends in antibiotic research and development (R&D) over the past two decades.

POLICY

In 2012, the United States passed legislation that granted five additional years of market exclusivity to sponsors of newly approved antibiotics, during which time no other companies can legally market the drug. The U.S. Congress is considering the Antibiotic Development to Advance Patient Treatment Act of 2013 (ADAPT Act), which would create a pathway for accelerated regulatory approval for antibiotics intended to be used in limited and specific patient populations. The goal of the Act is to decrease the duration of antibiotic premarket clinical trials and Food and Drug Administration review by curtailing the size and scope of certain phase 2 or 3 trials (*2*).

However, there is limited empirical evidence to help policy-makers evaluate which proposed incentives for antibiotic development will be most effective. One prevailing view is that the antibiotic development

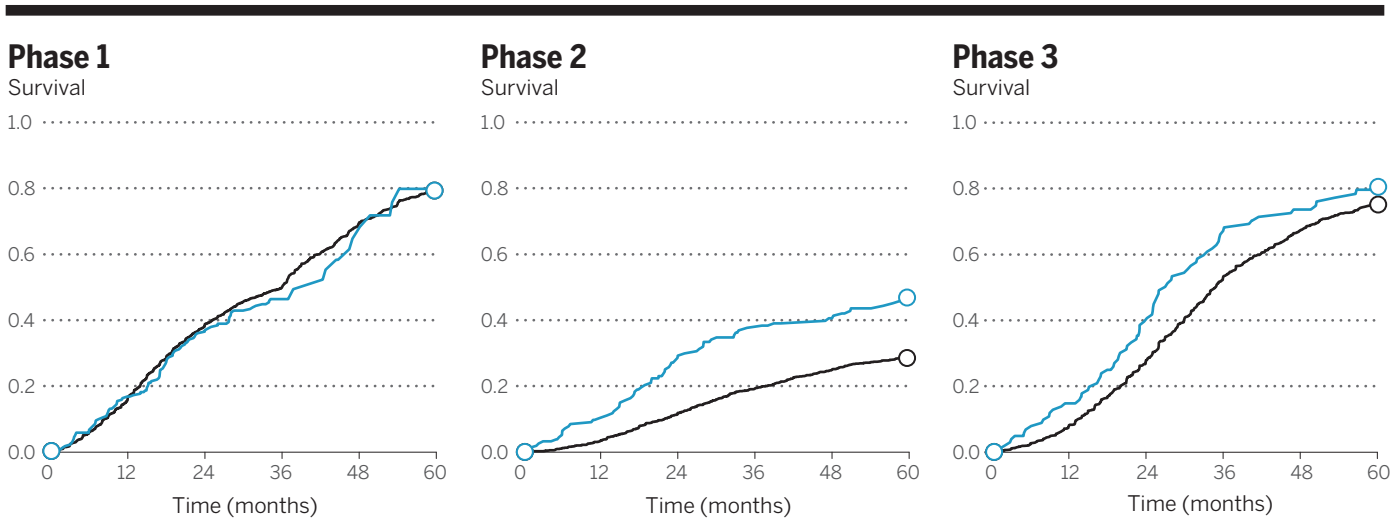


Cocci bacteria. Three-dimensional rendering of cocci bacteria, which include species such as methicillin-resistant *Staphylococcus aureus* (MRSA) and *Neisseria gonorrhoeae*. The rising public health toll of infections caused by multidrug-resistant bacteria demands greater focus on policies for developing new antibiotics with unique mechanisms of action.

PHOTO: KNORRE/THINKSTOCK

Downloaded from www.sciencemag.org on May 30, 2014

Published by AAAS



Success in clinical trials. Antibiotics (blue) were 43% more likely than other drugs (black) to survive in phase 2 clinical trials and 17% more likely to survive in phase 3. There was no significant difference in survival rates in phase 1. Higher values on the cumulative survival distribution curves indicate greater cumulative probability of survival. Event-time ratios (ETRs) compare the rates of survival between groups. Phase 1: ETR = 1.10; 95% confidence interval [CI]: 0.89–1.36; $P = 0.37$. Phase 2: ETR = 0.57, 95% CI: 0.43–0.76, $P < 0.001$. Phase 3: ETR = 0.83, 95% CI: 0.68–0.99; $P = 0.007$. See SM.

deficit is partly a result of an exodus of companies from R&D in this field (*3*). However, prior studies of antibiotic R&D have relied on drug approvals, which only occur after years of R&D effort, and reviews of the development pipelines of large companies, which may offer an incomplete picture of global R&D (*4*).

CHANGING LANDSCAPE OF R&D. We merged compound-by-compound data from Pharmaprojects (Informa Plc., London, UK) and market data from EvaluatePharma (Evaluate Group Ltd., London, UK) [see supplementary materials (SM) for full details on data and analyses] (*5*). This database captured 4715 drugs that entered phase 1 testing (the first formal clinical trial stage) between 1990 and 2012, of which 312 (7%) were primarily indicated as antibiotics.

We found that small and medium-sized companies (SMCs), defined as companies with gross revenues less than U.S. $1 billion, which accounted for less than 30% of all antibiotic clinical trials in 1990, accounted for 60% in 2012. We also investigated the survival rates of antibiotics as compared to other drugs, defined as the probability of entry into the subsequent clinical trial phase (i.e., from phase 1 to phase 2 and from phase 2 to phase 3) or regulatory filing. We fit our data to accelerated failure time models, controlling for time, market size, firm size, and other covariates. Antibiotics were more likely to survive in phase 2 and 3, compared with nonantibiotic drugs (see the chart). (Fig. 2) There was no difference in phase 1.

Some have suggested that antibiotics' higher likelihood of success in clinical trials may be a consequence of greater regulatory certainty (*6*). Antibiotic trials also enroll fewer patients, on average, than those for other types of drugs (*7*), meaning that they can be less costly and burdensome to conduct.

PARADIGMS FOR ANTIBIOTIC INNOVATION. To incentivize antibiotic R&D, policy-makers have focused on marketing exclusivity and regulation. Our data suggest that policy solutions should instead help SMCs and increase the overall number of investigational antibiotic candidates. Interventions that meet these criteria include R&D tax credits targeted at SMCs, public-private partnerships (PPPs) for antibiotic discovery and development, and funding for basic research.

R&D tax credits. Extensions in market exclusivity such as those recently enacted by Congress affect revenue streams in the distant future. By contrast, R&D tax credits, which allow companies to avoid paying taxes on monies invested in R&D, are immediately borne by firms, allowing them to re-invest and reallocate some amount of those savings into additional R&D. Such a credit would have statutory precedent: The 1983 Orphan Drug Act established a 50% tax credit on certain R&D activities for companies developing drugs for rare diseases. That credit has been linked to commercial success and viability of small companies pursuing drugs for rare diseases. Making these tax credits refundable would provide most benefit to early-stage companies that have not yet incurred federal income tax liabilities, because they could be entitled to a payment from the government if the credits reduced the amount of tax owed to less than zero.

Public-private partnerships. Our analysis indicates that antibiotics are more likely to succeed in clinical trials than other drugs. Instead of seeking to improve the probability of success through a regulatory solution, new policies would have greater impact if they raised the number of new antibiotics entering clinical trials. One approach to accomplish this goal arose in 2013, when the United States and the European Union (EU) announced strategic partnerships between government and industry to foster antibiotic drug discovery. The U.S. Department of Health and Human Services' Biomedical Advanced Research and Development Authority (BARDA) awarded its first contract, worth up to $200 million over 5 years, to GlaxoSmithKline to manage a portfolio of antibiotic candidates. In parallel, the European Innovative Medicines Initiative (IMI), announced €225 million (c. U.S. $310 million) in funding for the development of new antibiotics.

Such PPPs offer the possibility of bringing investigational antibiotics into trials that pharmaceutical manufacturers may not have pursued on their own by reducing the risks and costs of R&D. This model was used in the case of the first disease-modifying drug for cystic fibrosis (ivacaftor), which

[1]Faculty of Arts and Sciences, Harvard University, Cambridge, MA 02138, USA. [2]Radcliffe Institute for Advanced Study, Harvard University, Cambridge, MA 02138, USA. [3]Program on Regulation, Therapeutics, and Law (PORTAL), Division of Pharmacoepidemiology and Pharmacoeconomics, Department of Medicine, Brigham and Women's Hospital and Harvard Medical School, Boston, MA 02115, USA. *Present address: The Blackstone Group, London W1J5AL, UK. †Corresponding author. E-mail: tjhwang@post.harvard.edu (T.J.H.); akesselheim@partners.org (A.S.K.)

Published by AAAS

arose from a risk-sharing arrangement between Vertex Pharmaceuticals and the Cystic Fibrosis Foundation, and has been successful in other contexts (e.g., multidrug-resistant tuberculosis and malaria).

Funding for basic research. Infectious diseases account for ~5% of the U.S. National Institutes of Health (NIH)'s research funding. One study estimated that a 10% increase in disease-specific funding by NIH yielded a 4.5% increase in the number of related drugs entering clinical testing (*8*). Given the possible national security threat from multidrug-resistant infections, the U.S. Department of Defense would represent a logical additional source for increased support. Bolstering public funding for basic research would increase the pool of knowledge and new experimental therapies, as well as speed development of riskier therapeutic modalities, such as targeted biologics stimulating an immune response to pathogens and therapeutic vaccines.

Conserving antibiotic resources through stewardship could be achieved through renewed public health efforts to reduce inappropriate prescribing and overconsumption of antibiotics by humans and in agriculture. One way to foster antibiotic conservation may involve "delinkage," separating the funding of antibiotic R&D investments from volume-driven drug sales (*9*). New policies should help ensure adequate reward for antibiotic R&D, as well as for all institutions that contribute to the societal need to conserve these life-saving drugs for future generations. ■

REFERENCES AND NOTES

1. A. Coates, Y. Hu, R. Bax, C. Page, *Nat. Rev. Drug Discov.* **1**, 895 (2002).
2. J. H. Rex *et al.*, *Lancet Infect. Dis.* **13**, 269 (2013).
3. S. J. Projan, *Curr. Opin. Microbiol.* **6**, 427 (2003).
4. H. W. Boucher *et al.*, *Clin. Infect. Dis.* **56**, 1685 (2013).
5. T. J. Hwang, *PLOS ONE* **8**, e71966 (2013).
6. J. A. DiMasi *et al.*, *Clin. Pharmacol. Ther.* **87**, 272 (2010).
7. N. S. Downing *et al.*, *JAMA* **311**, 368 (2014).
8. M. E. Blume-Kohout, *J. Policy Anal. Manage.* **31**, 641 (2012).
9. D. Holmes, *Nat. Med.* **20**, 320 (2014).

ACKNOWLEDGMENTS

This research was supported by grants (to T.J.H.) from the Interfaculty Initiative in Health Policy (Cordiero Fellowship) and Center for American Political Studies, both at Harvard University. A.S.K. is supported by the Greenwall Faculty Scholarship, a Harvard Program in Therapeutic Science Ignition Award, and the Robert Wood Johnson Investigator Award in Health Policy Research. We thank J. M. Franklin for helpful comments. The content is solely the responsibility of the authors. The funders had no role in study design, manuscript drafting, or decision to publish. The authors declare no conflicts of interest.

SUPPLEMENTARY MATERIALS

www.sciencemag.org/content/344/6187/967/suppl/DC1

10.1126/science.1251419

IMAGING TECHNIQUES

Mapping bond orientations with polarized x-rays

Regions of bond order and disorder are revealed

By **Sven Lidin**

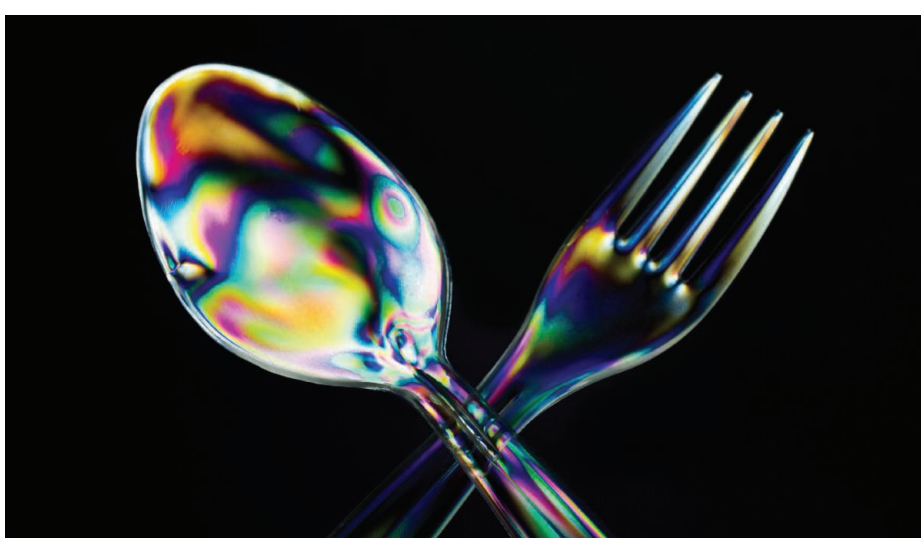
Good sunglasses eliminate glare because their surfaces have filters that pass only vertically polarized visible light. Reflected light from outdoor horizontal surfaces (a wet street or snow-covered ground) is horizontally polarized, and the crossed filter blocks this light. Many other interactions of light with materials depend on polarization. A birefringent material is an optically active substance that has a refractive index that depends on the polarization and propagation direction of light relative to the crystallographic axes of the material. Such a material can rotate the polarization direction of the incident light, and this effect can be used for identification of crystals in polarized light microscopy. On page 1013 of this issue, Palmer *et al.* (*1*) use an analog of this method that exploits the shorter wavelength of x-rays to identify regions of order and disorder on a smaller scale, the orientation of bonds in a crystal.

Light passing through crossed polarizing filters is effectively extinguished, but a birefringent crystal placed between crossed polarizers rotates the direction of polarization so that it can pass through the second filter. This method may be used to identify crystals that are birefringent, such as the urate salt crystals associated with gout. Stress can create local regions in materials that are birefringent. Crystals can be examined for imperfections, and even noncrystalline plastics can show stressed regions (see the figure).

Most x-rays used for diffraction experiments are polarized because the monochromators that select the wavelength are essentially x-ray mirrors. The polarization, like optical glare, is normally a nuisance that is dealt with in a footnote of the experiment; "the data were corrected for polarization effects." Indeed, that x-ray birefringence may introduce errors into intensity measurements and compromise comparisons between measurements at different wavelengths has been pointed out (*2*).

Palmer *et al.* show that polarization of x-rays can also be put to good use. Although the interaction of a crystal with visible light is a collective phenomenon that reflects the symmetry properties of the entire crystal, the energy of the x-ray beam can be tuned to coincide with the absorption edge of a particular element. The interaction between

Department of Polymer and Materials Chemistry, Lund University, Sweden. E-mail: sven.lidin@chem.lu.se



Lighting up under stress. Polarized light microscopy can provide a simple way to identify regions of stress in a material. A clear polymer spoon and fork show regions where internal stress aligns the otherwise disordered polymer molecules. These regions become birefringent; the colors result from variations in the stress. Palmer *et al.* exploited a birefingent effect in the x-ray region to map ordering and disordering of bond orientation in host-guest crystals.

PHOTO: ETOAKIN/ISTOCKPHOTO

Published by AAAS

the x-ray beam and the crystal will be completely dominated by the local geometry of the chosen element. Bromine has a conveniently placed absorption edge accessible for many synchrotron beam lines and distinct from those of lighter elements. Also, bromine tends to form bonds to just one of the carbon atoms in organic compounds and represents the ideal probe.

The thiourea inclusion systems used by Palmer *et al.* are well known for their structural diversity. The correlation between the thiourea host network and the included guest molecules is often strongly temperature dependent (*3*), and the guest bromocyclohexane is no exception. The high-temperature form of the compound (*4*) features an effectively orientationally disordered guest, in that this phase shows no x-ray birefringence. The disorder creates an isotropic environment around the bromine atoms, but the overall structure is still optically active and displays the typical cyclic behavior with respect to transparency to polarized light.

In previous studies of x-ray birefringence (*5*, *6*), a small probe was used that allowed the intensity of transmitted light to be measured. However, this approach would make mapping impractical because it would require scanning the entire specimen for each orientation. Palmer *et al.* used a wide beam that illuminated the entire sample and created a map simply by using a detector with good spatial resolution. In the ordered low-temperature phase, the Br–C bonds are antiparallel, and the crystals show birefringence with respect to both x-rays and visible light. Ordering of the bromocyclohexane resulted in domain formation. These domains were directly visible as light and dark regions in the x-ray birefringence images.

The work of Palmer *et al.* provides proof-of-principle for the use of x-ray birefringence imaging, both as a way of mapping local order and as an element-specific probe in partially disordered structures. The technique may be used to address the whole specimen simultaneously. This capability opens the way for many interesting applications, perhaps the most alluring being the possibility of studying domain boundary dynamics in real time. ■

REFERENCES

1. B. A. Palmer *et al.*, *Science* **344**, 1013 (2014).
2. D. Templeton, L. Templeton, *Phys. Rev. B* **40**, 6505 (1989).
3. K. D. M. Harries, *Chem. Soc. Rev.* **26**, 279 (1997).
4. T. Ishibashi, M. Machida, N. Koyano, *J. Korean Phys. Soc.* **46**, 228 (2004).
5. B. A. Palmer, A. Morte-Ródenas, B. M. Kariuki, K. D. M. Harris, S. P. Collins, *J. Phys. Chem. Lett.* **2**, 2346 (2011).
6. Y. Joly, S. P. Collins, S. Grenier, H. C. N. Tolentino, De M. Santis, *Phys. Rev. B* **86**, 220101(R) (2012).

10.1126/science.1254902

TRANSLATIONAL GENOMICS

Clues from the resilient

Genetic information from individuals who do not succumb to disease may point to new therapies and ideas about wellness

By **Stephen H. Friend**[1,2] *and* **Eric E. Schadt**[2]

The genetics approach to uncovering the causes of disease has focused mainly on finding the underlying primary mutations, with diseased individuals playing the leading role in this discovery. But as health care begins to focus more on preventive therapies, an emphasis on understanding how individuals remain healthy—"resilient" to disease—may provide insights into disease pathogenesis and new treatments. This view underlies "The Resilience Project" (www.resilienceproject.me), an effort to search broadly for these apparently healthy people (see the photo). There are, indeed, individuals whose genetics indicate exceptionally high risk of disease, yet they never show any signs of the disorder. What are the genetic and environmental factors that buffer disease for them? How can such information be gathered and harnessed most efficiently and effectively?



Talk the talk. "The Resilience Project" is described in a Technology, Entertainment, Design (TED) conference. See www.ted.com/talks/2004.

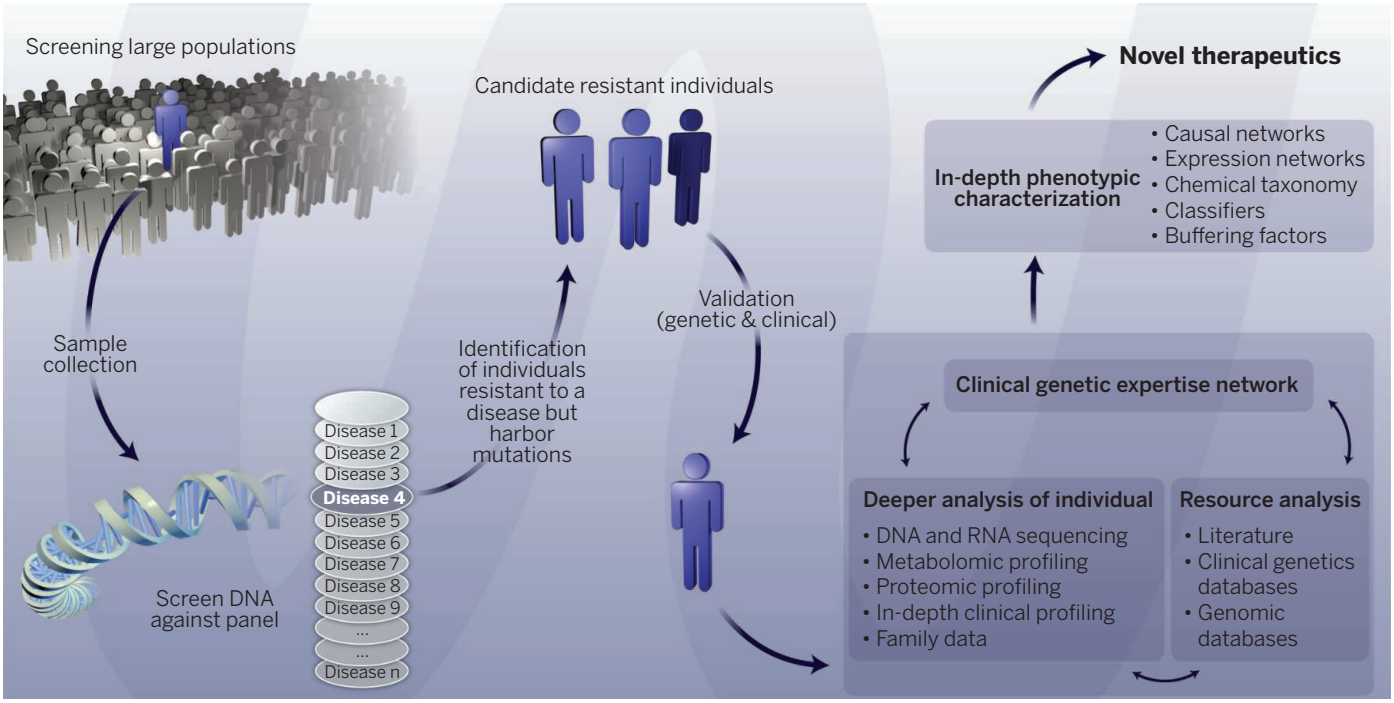
For 127 catastrophic Mendelian diseases (those caused by a single gene such as cystic fibrosis and ataxia-telangiectasia), there are presently 164 genes harboring 685 known recurrent variants that are highly penetrant and causal for deleterious traits, most typically manifesting in individuals before the age of 18 (*1*). More generally, thousands of variants spanning many hundreds of genes have now been associated with common diseases ranging from inflammatory bowel disease, rheumatoid arthritis, type 1 diabetes, and cancer, to Alzheimer's disease, schizophrenia, and asthma (*2*). Yet, despite this wealth of discoveries, few gene variants have translated directly into diagnostic predictors of disease risk and severity or into therapeutic interventions. For common diseases, the observed small effect sizes of individual gene variants limit diagnostic potential, and given that most variants identified have an unclear function, how to target the corresponding gene for therapeutic intervention is typically unclear. For rarer Mendelian disorders, although genetics directly implicate a specific gene in a disease, a majority of such cases relate to loss-of-function mutations. Designing small molecules to fix the corresponding broken protein has proven difficult. Compounds are effective in some cases, such as potentiators of mutant (loss-of-function) forms of the cystic fibrosis transmembrane conductance regulator in patients (*3*). However, substantial challenges remain in delivering functional versions of the aberrant proteins to specific cell types at the right time to treat or prevent disease.

The prominent role of second-site mutations and environmental factors that enable resistance to (or buffer against) disease traits has been well established in a multitude of model organisms from yeast to mice (*4*–*7*). Screening for second-site mutations in "resilient" individuals that prevent disease-causing alleles from manifesting their effects could identify targets to which drugs would be designed to disrupt their function, as opposed to targeting the disease-causing gene directly. Genetic studies examining seemingly healthy people have revealed, for example, rare mutations in chemokine (C-C motif) receptor type 5 (the co-receptor for human immunodeficiency virus) that block HIV infection (*8*), and secondary mutations in fetal globin genes that modify the severity of sickle cell disease by buffering primary mutations in β-globin genes (*9*). Even among common diseases, examples of protective alleles are growing, such as mutations in the gene encoding the enzyme proprotein con-

[1]*Sage Bionetworks, Seattle, WA, 98109 USA;* [2] *Icahn School of Medicine at Mount Sinai, Department of Genetics and Genomic Sciences and the Icahn Institute for Genomics and Multiscale Biology, New York, NY 10029, USA. E-mail: friend@sagebase.org; eric.schadt@exchange.mssm.edu*

PHOTO: JAMES DUNCAN DAVIDSON/TED

Published by AAAS



The search. A scheme to identify new treatments for disease is shown that begins with screening large populations of seemingly healthy people for disease-associated variations in their genomes. Once validated, multiple dimensions of data on a resilient individual would be combined with existing knowledge and clinical genetic expertise to generate an in-depth characterization that could point to new ways to suppress a disease trait.

vertase subtilisin/kexin type 9 (*PCSK9*) (*10*) and the gene encoding zinc transporter 8 (*ZNT8*) (*11*). These are striking examples of mutations that confer strong protective effects against cardiovascular disease and diabetes, respectively. Importantly, studies highlighting cases in which disease-causing mutations fail to result in disease (*12*) and rare individuals carrying disease modifiers are identified in extended families segregating disease (*13*) raises the question: Could more general worldwide searches across all childhood diseases be undertaken to find evidence for resilience factors, be they genetic or environmental?

A search of individuals older than 40 years of age for highly penetrant alleles in genes that cause catastrophic disease in children (with severe phenotypes that typically manifest before 18 years of age) is consistent with classical genetic study designs in which individuals with extreme phenotypes are analyzed because they are more likely to be homogeneous, and the extreme phenotypes are more likely explained by a smaller number of loci or environmental factors with big effect sizes. The identification of resilient individuals is thus much less ambiguous. This is opposed to identifying mutations that may have a relatively high carrier frequency in the population but far lower penetrance. The trade-off for this clarity is the need to sample many individuals, which requires systematic screening across general populations and diverse regions of the globe.

Given the ability to sequence hundreds of samples simultaneously, it is now within reach to screen a million individuals for relatively low cost (tens of dollars per individual) and in a short period of time (less than a year). The challenge will be to decipher which of the hundreds of candidate second site mutations or environmental factors may be responsible for the buffering against disease. The power to resolve the buffering effect statistically will be very low as the number of candidates expected to be identified will be relatively small. However, recent studies successfully combined biochemical, molecular, and genetic pathway and network analysis tools to identify individuals with rare genomic variants that suppress a disease phenotype. For example, one recent study sequenced the genomes of a small number of positive responders to a drug administered in a clinical trial; by combining multiple types of data, the study identified the basis for the responders' sensitivity to the drug (*14*). Such tools have further validated these "positive outliers" and have led to personalized treatments. Technologies to investigate environmental factors, probe epigenetic phenomena, profile microbes, differentiate and manipulate induced pluripotent stem cells, and directly edit genomes are now advanced enough to decipher the extremely complex mechanisms of buffering human genetic variations.

The scale required in a resilience study can only be supported by the sharing of data and ideas among collaborators that operate in a large network spanning a large scope of disciplines and knowledge. Critical to such a network are clinical genetics experts who could rapidly filter through candidate resilient individuals to validate their genetic status, rule out what may be common explanations such as mosaicism, and ultimately identify factors that enable resistance. The Online Metabolic and Molecular Bases of Inherited Disease reference offers a potential model of clinical experts who study individual genes responsible for rare disorders and can assess the clinical and primary gene defects. A version of this model that covers a broad range of diseases could facilitate the kinds of connections required to elucidate the complexity of resilience to a given disease.

Obtaining informed consent from 1 million individuals in such a study could not be done in a traditional way, but would need to be done electronically. What would be their motivation? Low risk and potentially high reward. Enabling participants to assess whether they can serve as an "unexpected hero" to others who are afflicted with catastrophic disease could be personally inspiring. There is also low risk in that this strategy minimizes the likelihood of conveying future risk of disease to participants. Collecting and processing patient samples in a highly automated way would be necessary, but direct to consumer genomic companies and lab testing companies have demonstrated that efficient, large-scale sample acquisition and

Published by AAAS

processing can be done routinely. Given that the study would only report individuals with resistance to disease, not generalized risks of disorders across spectrums of disease, both the regulatory and ethical requirements would be reduced.

A resilience project (see the figure) approach helps shift thinking on treating disease. Rather than developing therapies that modify symptoms or the consequences of inherited diseases, a systematic search for resilience factors will change the focus in ways that prevent or modify the course of diseases. This should initially be easier for single-gene Mendelian childhood diseases, but emerging network approaches that define clusters of genes that drive a disease (such as diabetes, cancer, and Alzheimer's disease) could eventually be amenable to this strategy.

The resilience approach (see the figure) can well complement emerging efforts to follow well individuals longitudinally (*15*) and to identify and characterize human "knockouts" (people lacking specific genes) (*16*, *17*) by more rapidly targeting (in a large number of individuals and at relatively low cost) a specific set of genes that harbor what are thought to be completely penetrant mutations that cause catastrophic disease, to find people who should have gotten sick, but did not. Achieving the greatest degree of success across all of these types of efforts will require collating and making publicly accessible the data collected in each study. The focus on genetic and environmental factors that offer protection against disease as opposed to putting you at risk for disease may also help engage a public that is more participatory in sharing their insights and data to help others. ■

REFERENCES AND NOTES

1. P. D. Stenson *et al.*, *Curr. Protoc. Bioinformatics*, Chapter 1: Unit 1.13 (2012).
2. D. Welter *et al.*, *Nucleic Acids Res.* **42**, D1001 (2014).
3. B. W. Ramsey *et al.*, *N. Engl. J. Med.* **365**, 1663 (2011).
4. J. L. Hartman 4th, *Proc. Natl. Acad. Sci. U.S.A.* **104**, 11700 (2007).
5. J. L. Hartman 4th *et al.*, *Science* **291**, 1001 (2001).
6. J. L. Hartman 4th, N. P. Tippery, *Genome Biol.* **5**, R49 (2004).
7. R. J. Louie *et al.*, *Genome Med.* **4**, 103 (2012).
8. P. R. Gorry *et al.*, *Lancet* **359**, 1832 (2002).
9. G. Galarneau *et al.*, *Nat. Genet.* **42**, 1049 (2010).
10. J. Cohen *et al.*, *Nat. Genet.* **37**, 161 (2005).
11. J. Flannick *et al.*, *Nat. Genet.* **46**, 357 (2014).
12. D. N. Cooper *et al.*, *Hum. Genet.* **132**, 1077 (2013).
13. P. R. Sosnay *et al.*, *Nat. Genet.* **45**, 1160 (2013).
14. G. Iyer *et al.*, *Science* **338**, 221 (2012).
15. L. Hood, N. D. Price, *Sci. Transl. Med.* **6**, 225ed5 (2014).
16. J. Kaiser, *Science* **344**, 687 (2014).
17. www.borninbradord.nhs.uk/studies/129/StudyDetails/british-autozygosity-population-study

ACKNOWLEDGMENTS

S.H. F. is a principal investigator of The Resilience Project (www.resilienceproject.me).

10.1126/science.1255648

BIOCHEMISTRY

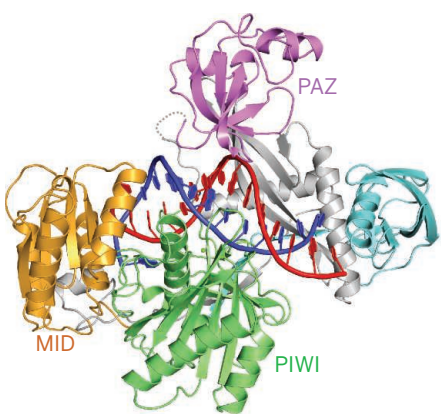
A bacterial seek-and-destroy system for foreign DNA

Bacterial argonaute proteins defend the cell against exogenous DNA

By **Jörg Vogel**

Argonaute proteins have emerged as the key effectors in virtually all eukaryotic small RNA–mediated gene silencing pathways (*1*). Central to all their activities is their association with the small guide RNAs that allow them to recognize through sequence complementarity, and in some cases also cleave, cellular transcripts.

Curiously, Argonaute-like proteins are also encoded by many bacteria and archaea (*2*) (see the first figure), which apparently do not have RNA interference (RNAi)–based silencing systems. Hints about possible functions came from the Argonaute of the bacterium *Aquifex aeolicus*, which showed a preference for a small DNA rather than an RNA guide in transcript cleavage assays (*3*). Yet subsequent structural work with eukaryotic Argonautes continued to bolster the RNA guide–RNA target model (*4*), and eclipsed research into the putative alternative functions of their odd prokaryotic cousins.



Structure of the *T. thermophilus* Argonaute protein bound to guide DNA and target DNA, according to (*7*).

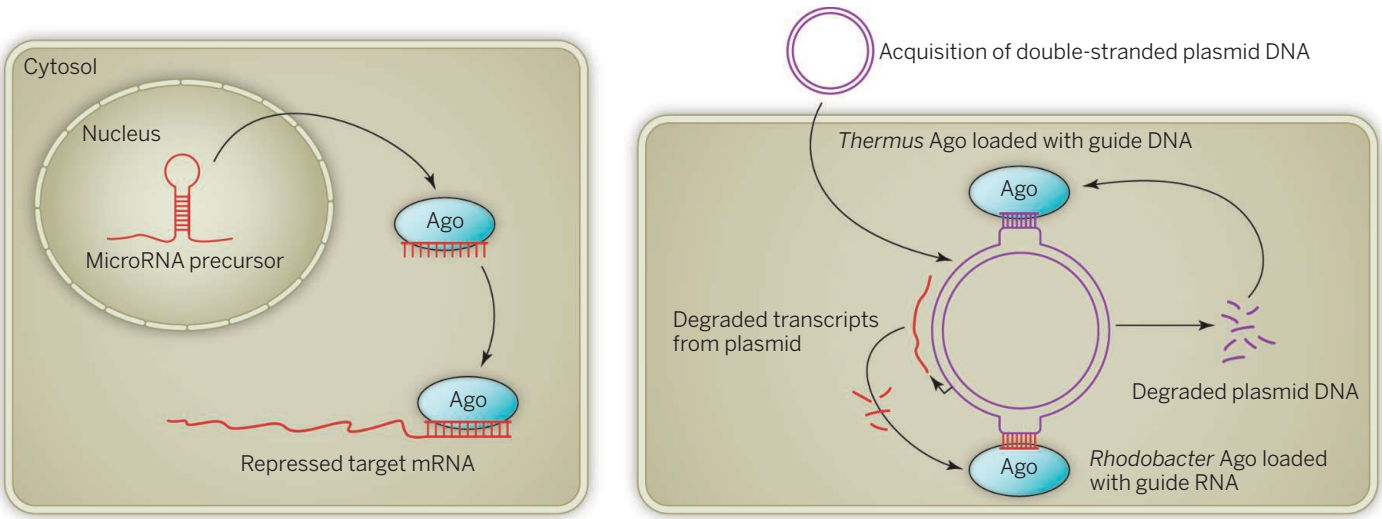
This situation has now been rectified by two recent studies, from Olovnikov *et al.* (*5*) and Swarts *et al.* (*6*), that have discovered a novel Argonaute target in microbes: foreign DNA. Analyzing the nucleic acids bound to the Argonautes of the unrelated bacteria *Rhodobacter sphaeroides* (*5*) and *Thermus thermophilus* (*6*), both groups observed a strong enrichment of short DNA fragments from plasmids, common extrachromosomal elements that can easily be transferred between bacteria. Physiologically, these bacterial Argonautes were shown by both teams to restrict the acquisition and maintenance of new plasmids, which suggests that they may function as a general surveillance system to protect their host bacteria from parasitic DNA. Indeed, regions of foreign DNA in the chromosome (such as transposons and prophage genes) also seem to be selectively targeted. As such, the Argonautes of *R. sphaeroides* and *T. thermophilus* add to a growing list of mechanisms—ranging from restriction modification enzymes to the recently discovered CRISPR/Cas systems—that collectively help bacteria to fend off unwanted or invasive DNA. Intriguingly, because the appearance of these bacterial Argonautes likely predated their eukaryotic counterparts, genome defense against invading DNA may constitute an ancient function of Argonautes that preceded their recruitment to RNA-based gene silencing.

Things become more complex when considering the details of the underlying mechanism of the two bacterial Argonautes (see the second figure). The *R. sphaeroides* protein (RsAgo) (*5*) associates with two classes of nucleic acids: a class of 15- to 19-nucleotide RNAs that originate from many cellular transcripts, and a class of 22- to 24-nucleotide single-stranded DNAs that display complementarity to the small RNAs. Analysis of these fragments both in *R. sphaeroides* and upon expression of RsAgo in the heterologous host *Escherichia coli* suggest that the small RNAs, perhaps originating from degraded mRNAs, act as guides for RsAgo (they have a strong bias for U at the first position, like the guide RNAs of some eukaryotic Argonautes), and the small DNAs are the remnants of cleaved targets. How the cleavage occurs is unclear; RsAgo is inactive as a slicing nuclease because critical residues are mutated (*5*), and a suitable in vitro assay to validate the

RNA Biology Group, Institute for Molecular Infection Biology, University of Würzburg, D-97080 Würzburg, Germany. E-mail: joerg.vogel@uni-wuerzburg.de

ILLUSTRATION: COURTESY OF YANLI WANG

Published by AAAS



RNA versus DNA targets. (**Left**) Eukaryotic Argonaute (Ago) is loaded with guide RNA (here, microRNA) in the cytosol and uses it to recognize a target mRNA for repression of protein synthesis at the posttranscriptional level. (**Right**) Bacterial Argonautes target exogenous plasmid DNA. Depending on the protein, two models are proposed. The *Thermus thermophilus* protein recruits small guide DNAs from degraded plasmid DNA to recognize and cleave the same plasmid sequence. The *Rhodobacter sphaeroides* protein is proposed to use RNA guides that derive from degraded plasmid transcripts to promote cleavage of the plasmid DNA by an unknown nuclease.

eukaryotic-like use of small guide RNAs by this bacterial Argonaute is lacking.

Swarts *et al*., studying the *T. thermophilus* Argonaute (TtAgo), arrive at a different model for its mode of action. TtAgo expressed in *E. coli* also associates with both small RNAs and DNAs. However, Swarts *et al.* dismiss the small RNAs as potential guides for several reasons: They are too heterogeneous in size, they lack the 5′ phosphate group that anchors RNA guides in other Argonaute proteins, and they purify with both the wild type and a nuclease active-site mutant of TtAgo. By contrast, the small DNAs, which form two populations (respectively, 15 nucleotides and 13 to 25 nucleotides in length), exhibit guide-like characteristics: They carry 5′ phosphates and do not purify with the mutant TtAgo. Furthermore, plasmid DNA cleavage can be reconstituted in the test tube with purified Ago and synthetic small guide DNAs, but not with RNA of the same sequence. Thus, although the mechanism and target of TtAgo in its natural host are yet to be established, biochemistry validates it as a programmable DNA-guided DNA endonuclease—a property that receives independent support from crystal structures of ternary TtAgo complexes with DNA guide and target (*7*).

It will be exciting to see whether the different mechanistic models proposed for these two bacterial Argonaute proteins reflect a hidden diversity among the prokaryotic homologs, similar to the diverse functions and mechanisms of their eukaryotic counterparts. There may yet be a role for bacterial Argonaute proteins in RNA-guided posttranscriptional regulation, which in prokaryotes has been the domain of the protein Hfq and its associated small RNAs (*8*). A protein with an Argonaute-like MID domain affects gene regulation in rhizobia (*9*), and the CRISPR-derived Cas9 protein, which also targets foreign DNA, was recently found to regulate mRNAs in pathogenic *Franciscella* bacteria (*10*), illustrating how microbes recruit genome defense factors for RNA regulation.

Many questions remain to be answered concerning the DNA targeting by RsAgo and TtAgo. How are the RNA or DNA guides generated, and what would be the advantage of DNA over RNAs? Both studies establish plasmid DNA as a preferred target. It might simply be that plasmids, which are both highly replicated and transcribed, produce more DNA that is available for cleavage (*5*). Alternatively, a yet unknown priming mechanism may attract the Argonautes to a plasmid-specific replication intermediate or topology. DNA supercoiling does seem to play a role, as suggested by the in vitro cleavage experiments with TtAgo (*6*). When it comes to potential targets in the chromosome, the bacteria must have ways to prevent their genome from being constantly nicked or cleaved by their own Argonaute proteins. Of note, bacteria silence foreign DNA on the transcriptional level by protein H-NS (*11*), which, similarly to TtAgo (*6*), preferentially binds to AT-rich sequences that often mark xenogeneic DNA. Thus, Argonautes might be an altruistic fail-safe mechanism coming into play when newly acquired DNA fails to be dealt with by H-NS.

There are practical implications, too. Given that DNA molecules are generally more stable than RNA, the programmable DNA-guided DNA endonuclease TtAgo could complement the CRISPR/Cas9 genome editing system, which has to be programmed with small guide RNAs (*12*). Microbiologists, too, may benefit: Many bacteria remain difficult to manipulate because of poor transformability with DNA, but getting rid of Argonaute could make life a little easier. In fact, the Argonaute-deficient *T. thermophilus* strain that first hinted at the protein's function was a previously described mutant with enhanced transformability (*13*). Thus, we may be in for more surprises with bacterial Argonautes. ■

ILLUSTRATION: ADAPTED BY P. HUEY/*SCIENCE*

REFERENCES

1. G. Meister, *Nat. Rev. Genet.* **14**, 447 (2013).
2. K. S. Makarova, Y. I. Wolf, J. van der Oost, E. V. Koonin, *Biol. Direct* **4**, 29 (2009).
3. Y. R. Yuan *et al.*, *Mol. Cell* **19**, 405 (2005).
4. C. D. Kuhn, L. Joshua-Tor, *Trends Biochem. Sci.* **38**, 263 (2013).
5. I. Olovnikov, K. Chan, R. Sachidanandam, D. K. Newman, A. A. Aravin, *Mol. Cell* **51**, 594 (2013).
6. D. C. Swarts *et al.*, *Nature* **507**, 258 (2014).
7. G. Sheng *et al.*, *Proc. Natl. Acad. Sci. U.S.A.* **111**, 652 (2014).
8. J. Vogel, B. F. Luisi, *Nat. Rev. Microbiol.* **9**, 578 (2011).
9. S. P. Pandey, B. K. Minesinger, J. Kumar, G. C. Walker, *Nucleic Acids Res.* **39**, 4691 (2011).
10. T. R. Sampson, S. D. Saroj, A. C. Llewellyn, Y. L. Tzeng, D. S. Weiss, *Nature* **497**, 254 (2013).
11. W. W. Navarre, M. McClelland, S. J. Libby, F. C. Fang, *Genes Dev.* **21**, 1456 (2007).
12. E. Charpentier, J. A. Doudna, *Nature* **495**, 50 (2013).
13. S. T. Gregory, A. E. Dahlberg, *FEMS Microbiol. Lett.* **289**, 187 (2008).

10.1126/science.1252962

Published by AAAS

GEOCHEMISTRY

How sulfur beats iron

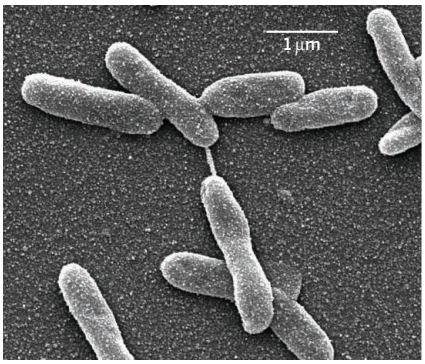
Iron-reducing bacteria switch to sulfur reduction as their main energy source in alkaline environments

By **Michael W. Friedrich**[1] *and* **Kai W. Finster**[2]

Betting on several metabolic horses may be a sound evolutionary strategy for microbes, helping to increase their chance of survival in an ever-changing environment. For example, many microbes can use a variety of electron acceptors to conserve energy. This feature allows them to respond when environmental conditions are changing, for example, when oxygen becomes depleted in aquatic environments. On page 1039 of this issue, Flynn *et al.* (*1*) show how iron-reducing bacteria can switch to sulfur reduction when the environment is too alkaline for iron reduction.

Electron acceptors such as nitrate, iron(III) oxide, sulfate, and carbon dioxide (CO_2) differ in how much energy they allow the microorganism to conserve (*2*). For example, iron(III) oxide provides microorganisms with more energy than does elemental sulfur, provided that they use the same electron donor. This simple thermodynamic regulation holds true as long as organisms operate at neutral pH (pH 7). Flynn *et al.* now investigate the relation between environmental pH and the energy yields of iron and elemental sulfur reduction, both of which are of ecological importance in aquifers.

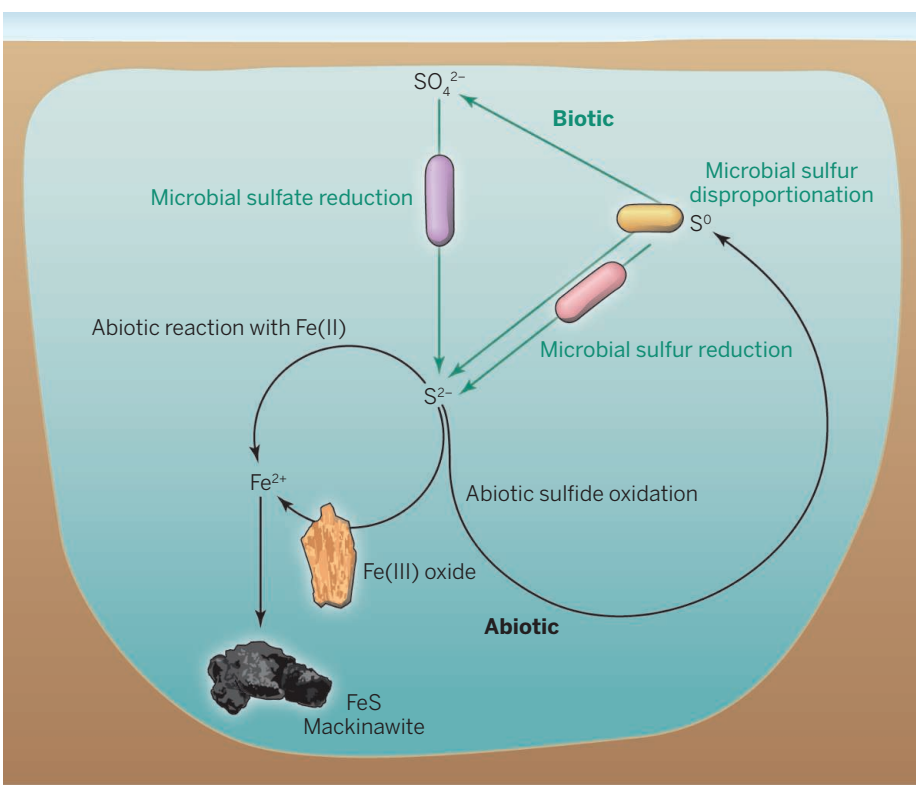
The energy available to microorganisms strongly depends on the chemistry of the metabolic reaction. In the case of the iron(III) oxide goethite as electron acceptor, 16 moles of protons are required to oxidize one mole of formate to CO_2. At low to neutral pH, the proton concentration is sufficiently high for this reaction to proceed, but at pH 9, few free protons are available for microorganisms that thrive by iron(III) reduction. In contrast, formate oxidation coupled to sulfur reduction releases protons. Flynn *et al.* show that sulfur reduction with formate as electron donor is energetically favorable at pH 9, whereas goethite reduction is not.



Versatile bug. The iron-reducing microbe *Shewanella oneidensis* strain MR-1 can switch to sulfur reduction under alkaline conditions or when no Fe(III) oxide is present at neutral pH.

These theoretical results are supported by studies on metal and sulfur reduction with *Shewanella oneidensis* strain MR-1 (see the figure) (*3*). However, it is tricky to distinguish between microbially driven iron reduction and sulfur reduction because sulfide can also react directly with Fe(III). With the help of a *S. oneidensis* mutant that lacks a sulfur reductase, Flynn *et al.* show that microbial sulfur reduction to sulfide is essential for iron(III) reduction at pH 9, because iron reduction is largely driven by abiotic reduction with sulfide. The reaction of sulfide with iron(III) conceals the formation of sulfide, effectively recycling sulfur for multiple rounds of microbial reduction. Thus, a microbially catalyzed hidden or "cryptic" sulfur cycle (see the image) operates at alkaline pH. In alkaline aquifers, sulfur-reducing bacteria require a source of sulfur. The frequently co-occurring sulfate-reducing bacteria produce sulfide, from which sulfur is formed by abiotic reaction with iron(III) oxide (*4*).

The cryptic cycling of sulfur includes numerous biotic and abiotic reactions. For example, in the oxygen minimum zone off the coast of northern Chile, microbially catalyzed oxidation of sulfide with nitrate as electron acceptor drives the formation of sulfate with little or no accumulation of sulfide (*5*). In marine sediments of Aarhus Bay and the Black Sea, microbial sulfate reduction can be fueled by downward diffusing sulfide that originates from sulfate-driven anaerobic methane oxidation (*6*, *7*). Here, the sulfide is chemically oxidized by buried reactive iron(III) oxides, compa-



Cryptic sulfur cycling in alkaline aquifers. Microbial (green) and abiotic reactions (black) are linked at alkaline pH. Flynn *et al.* now show that some iron-reducing bacteria maintain a sulfur-reducing metabolic pathway, helping them to survive under alkaline conditions.

[1]*Department of Biology/Chemistry and MARUM–Center for Marine Environmental Sciences, University of Bremen, 28359 Bremen, Germany.* [2]*Department of Bioscience, Aarhus University, Ny Munkegaard 116, 8000 Aarhus C, Denmark. E-mail: michael.friedrich@uni-bremen.de*

ILLUSTRATION: P. HUEY/*SCIENCE*; IMAGE: C. FISCHER, R. S. ARVIDSON, A. LÜTTKE/UNIVERSITY OF BREMEN

Published by AAAS

rable to the sulfur cycling under alkaline conditions reported by Flynn *et al.*

In alkaline environments such as groundwater aquifers, iron(III)-reducing microorganisms apparently have an ecological advantage when equipped with the ability for sulfur reduction. Flynn *et al.* argue that both traits could have coevolved in one microorganism in the alkaline ocean cradle of early Earth. However, these early oceans might have been acidic (*8*, *9*). Moreover, iron reduction would not have evolved in a solely alkaline world, where the reaction is unfavorable. The presence of multiple respiratory pathways in one microorganism provides flexibility to changing environmental conditions. The maintenance of both iron and sulfur reduction pathways implies that iron-reducing microorganisms are exposed to fluctuations in electron acceptor availability.

The work of Flynn *et al.* provides an intriguing explanation for how iron-reducing bacteria can thrive in alkaline environments. Some iron reducers have, in addition, the capability to use sulfur disproportionation, the fermentation of sulfur to sulfide and sulfate (*10*). In fact, sulfur disproportionation also becomes more favorable with alkaline pH and has been shown to occur at pH 10 in cultures isolated from a soda lake (*11*). Sulfur-reducing and sulfur-disproportionating bacteria are, thus, likely to compete for sulfur as a common substrate, especially in carbon-poor aquifers, because sulfur disproportionation is independent of organic carbon substrates. In the future, it will be important to dissect the quantitative role of these intertwined reactions of the sulfur and iron cycle and the bacteria involved in the environment. ■

REFERENCES AND NOTES

1. T. M. Flynn, E. J. O'Loughlin, B. Mishra, T. DiChristina, K. M. Kemner, *Science* **344**, 1039 (2014).
2. D. R. Lovley, S. Goodwin, *Geochim. Cosmochim. Acta* **52**, 2993 (1988).
3. J. K. Fredrickson *et al.*, *Nat. Rev. Microbiol.* **6**, 592 (2008).
4. T. M. Flynn *et al.*, *BMC Microbiol.* **13**, 146 (2013).
5. D. E. Canfield *et al.*, *Science* **330**, 1375 (2010).
6. L. Holmkvist, T. G. Ferdelman, B. B. Jorgensen, *Geochim. Cosmochim. Acta* **75**, 3581 (2011).
7. L. Holmkvist *et al.*, *Deep Sea Res. Part I Oceanogr. Res. Pap.* **58**, 493 (2011).
8. D. L. Pini, *in Lectures in Astrobiology Vol. I*, M. Gargaud *et al.*, Eds. (Springer, Berlin/Heidelberg, 2005), pp. 83-112.
9. M. J. Russell *et al.*, *Astrobiol.* **14**, 308 (2014).
10. D. E. Holmes, D. R. Bond, D. R. Lovley, *Appl. Environ. Microbiol.* **70**, 1234 (2004).
11. A. Poser *et al.*, *Extremophiles* **17**, 1003 (2013).

ACKNOWLEDGMENTS

We thank C. Fischer, R. S. Arvidson, and A. Lüttke (University of Bremen) for providing the high-resolution field emission scanning electron microscopy image of *Shewanella oneidensis* MR-1.

10.1126/science.1255442

ECOLOGY

Managing the side effects of invasion control

Efforts to control invasive species must be adapted to avoid unintended damage to native species and ecosystems

By **Yvonne M. Buckley**[1,2] *and* **Yi Han**[2]

Invasive species can threaten the conservation of biodiversity and natural resources and incur considerable economic losses. Invasive species management programs therefore aim to reverse or mitigate the impacts of invasion, but these programs can have severe negative impacts on native species and ecosystems (*1*, *2*), because invasive species integrate into their new ecosystems and can assume ecological functions previously carried out by native species. Indirect effects of management are likely to become more common as existing invaders form new interactions and new species continue to be introduced. On page 1028 of this issue, Lampert *et al.* report an optimal management model that shows how invasive species control can be combined with other ecosystem goals (*3*).

Rapid removal of an invasive plant is important for reducing its population, preventing further spread, and helping to ultimately attain eradication. However, rapid removal can lead to problems if native species use the invader as a resource. The program aiming to eradicate an invasive cordgrass species (a hybrid between the invasive *Spartina alterniflora* and the native *S. foliosa*) in San Francisco Bay was proceeding quickly and effectively (see the figure) when scientists noticed declines in an endangered bird, the California clapper rail, which nests in invasive hybrid *Spartina*. The control program for invasive hybrid *Spartina* was temporarily halted, leaving 8% of the originally infested area still containing the invader. The bird also nests in native *Spartina*, but the native



PHOTO: LEN BLUMIN

Different perceptions. The California clapper rail, an endangered bird species, sees no difference between a patch of invasive *Spartina* and a patch of native *Spartina*, laying eggs in either habitat. However, ecosystem managers view them very differently, aiming to eradicate the invasive grass and to encourage regrowth of the native one. Lampert *et al.* now report a model that takes undesired side effects of invader removal into account.

Published by AAAS

plant was slow to recover after removal of the invader (*3*). How can the clapper rail population be protected while preventing the remaining invasive hybrid *Spartina* population from recolonizing the bay?

To determine the best management strategy for such a situation, Lampert *et al.* constructed a model that constrains the side effects of hybrid *Spartina* management on the clapper rail. The model combines invader removal with the restoration of the native habitat to replace the beneficial function of the invader. The time scale of the management program is therefore controlled by the rate of recovery of the native and its ability to replace the habitat lost through invader removal.

"How can the clapper rail population be protected while preventing the remaining invasive hybrid Spartina population from recolonizing the bay?"

Removal of invaders can have various negative impacts on nontarget species and ecosystems (*4*). Native fruit-eating birds, bats, and mammals can incorporate invasive species in their diets (*5*), presenting conservation conflicts when removal of the resource has an impact on the native consumers. Removal of an invasive predator can lead to overabundance of prey (*2*) or increased populations of other damaging predators (*6*). Such nontarget effects of invader management are commonly recognized (*7*, *8*) but are rarely incorporated into optimal management models and are even more rarely assessed in terms of costs (*3*).

When management of an invader is in conflict with other conservation goals, there are three main options: to continue to manage the impacts of the invader and accept the collateral damage; abandon the management effort and accept the invader impacts; or seek a compromise management strategy that allows both goals to be attained. Several studies have highlighted the importance of assessing or predicting negative effects of invader removal and have recommended the integration of invasive species management with broader ecosystem goals (*4*), but few management plans have successfully resolved these conflicts.

This gap between theory and practice is difficult to bridge for several reasons. The complexity and uncertainty of species interactions makes it hard to predict the potential negative impacts of invader removal (*9*). Population reduction of the invader is often used as the sole criterion for judging the success of invasive species management, and time and resource constraints often limit follow-up monitoring and restoration efforts (*10*). Another important barrier to an ecosystem-based management approach is the lack of common valuation systems (currencies) that sum and compare the management costs, damages, and benefits (*11*).

Lampert *et al.* were able to combine the monetary costs of eradication, restoration, and the damages incurred by invasive hybrid *Spartina* with a constraint on the total amount of clapper rail habitat required to find an optimal management strategy. In other systems, however, it can be difficult to determine the costs of impact, and how reversible those costs are with invader removal (*12*). The costs of the side effects of management actions can also be difficult to assess and quantify. In these cases, it may be appropriate to use evaluation approaches that do not require conversion of different units of measurement into a single currency (*11*).

There are often large uncertainties in predicting the responses of managed systems. These uncertainties hinder the accurate identification of conservation conflicts and thus the optimization of solutions. We will never be able to predict all risks of environmental management, but the risks of not acting at all may be more serious. Tools like those constructed by Lampert *et al.* are crucial for reconciling the increasing number of conflicts likely to occur. ■

[1]School of Natural Sciences and Trinity Centre for Biodiversity Research, Department of Zoology, Trinity College, University of Dublin, Dublin 2, Ireland. [2]ARC Center of Excellence for Environmental Decisions, School of Biological Sciences, University of Queensland, Queensland 4072, Australia. E-mail: buckleyy@tcd.ie

REFERENCES

1. M. J. Rinella, B. D. Maxwell, P. K. Fay, T. Weaver, R. L. Sheley, *Ecol. Appl.* **19**, 155 (2009).
2. D. M. Bergstrom *et al.*, *J. Appl. Ecol.* **46**, 73 (2009).
3. A. Lampert, A. Hastings, E. D. Grosholz, S. L. Jardine, J. N. Sanchirico, *Science* **344**, 1028 (2014).
4. E. S. Zavaleta *et al.*, *Trends Ecol. Evol.* **16**, 454 (2001).
5. Y. M. Buckley *et al.*, *J. Appl. Ecol.* **43**, 848 (2006).
6. M. J. Rayner, M. E. Hauber, M. J. Imber, R. K. Stamp, M. N. Clout, *Proc. Natl. Acad. Sci. U.S.A.* **104**, 20862 (2007).
7. S. V. Fowler, Q. Paynter, S. Dodd, R. Groenteman, *J. Appl. Ecol.* **49**, 307 (2012).
8. J. Firn, A. P. N. House, Y. M. Buckley, *J. Appl. Ecol.* **47**, 96 (2010).
9. B. Raymond, J. McInnes, J. M. Dambacher, S. Way, D. M. Bergstrom, *J. Appl. Ecol.* **48**, 181 (2011).
10. A. M. Reid, L. Morin, P. O. Downey, K. French, J. G. Virtue, *Biol. Conserv.* **142**, 2342 (2009).
11. I. Grechi *et al.*, *Agric. Syst.* **125**, 1 (2014).
12. H. Yokomizo, H. P. Possingham, M. B. Thomas, Y. M. Buckley, *Ecol. Appl.* **19**, 376 (2009).

10.1126/science.1254662

PHYSICS

Hitting the limit of magnetic anisotropy

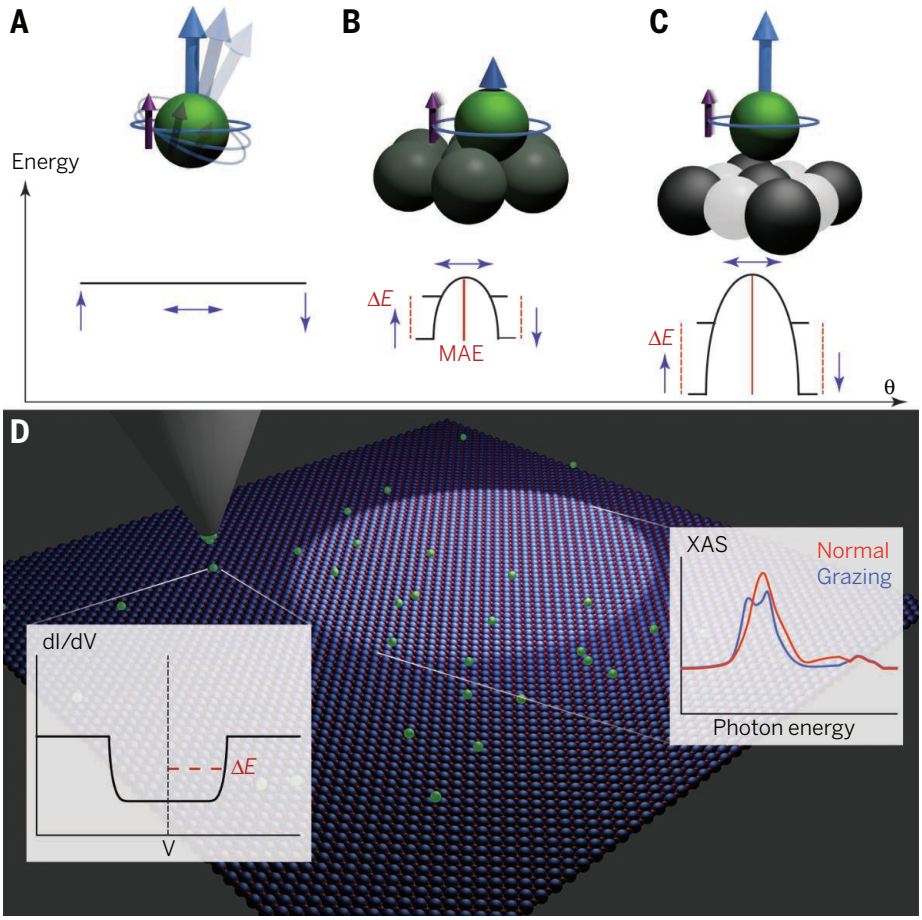
Enhancing the magnetic properties of adatoms provides a route toward atom-scale memory

By **Alexander Ako Khajetoorians** *and* **Jens Wiebe**

Single magnetic atoms adsorbed on surfaces, or so-called adatoms, provide a viable ground for realizing information storage and processing at ultimate length scales (*1*–*3*). Such concepts hinge on the magnetic anisotropy energy (MAE), which energetically favors a preferential spatial orientation of the adatom's magnetic moment m, where m is the sum of coupled spin and orbital momenta. Unlike for a free atom, where m can rotate freely in any direction without energy cost (see the figure, panel A, MAE = 0), large MAE (panel B, MAE ≠ 0) enables m to maintain a fixed orientation for a sufficient amount of time. For stable and robust magnetic memory storage, large values of MAE are desirable. On page 988 of this issue, Rau *et al.* (*4*) show that a suitable choice of substrate and adatom pairing can result in the further enhancement of MAE, thus providing a possible route toward realizing information storage at the atomic scale.

MAE originates from the so-called ligand field, which is the electrostatic energy generated by the shape of the orbitals of both the adatom and the neighboring substrate atoms, and which breaks the degeneracy of the atomic levels producing the magnetic moment. This energy landscape, combined with spin-orbit coupling (SOC), which locks the spin moment to the orbital moment, generates the resultant MAE. One crucial hurdle toward stabilizing a single adatom is to maximize the MAE, thus protecting m from thermal fluctuations. Consequently, the three important ingredients for large MAE are a large SOC energy, a large orbital moment, and a strong ligand field. The first condition can be maximized by a proper choice of adatom species. Unfortunately, the

Published by AAAS



Atomically controlled magnetism. Orbital (blue arrow) and spin (purple arrow) moments, and the corresponding MAE for (**A**) a free Co atom, (**B**) a Co adatom on a Pt(111) surface, and (**C**) a Co adatom on an MgO surface. The zero-field splitting energy ΔE is a measure of the MAE. (**D**) Atomic spin detection techniques based on SP-STS and XAS.

other two are usually inversely correlated to each other (i.e., a strong ligand field typically quenches the orbital moment).

In 2003, experiments using x-ray adsorption spectroscopy (XAS) and x-ray magnetic circular dichroism (XMCD) showed that Co adatoms on a platinum(111) metallic surface (see the figure, panel B) exhibited a MAE of 10 meV resulting from strong SOC and an incomplete quenching of the orbital moment (*5*). With the advancement of single-atom spin detection (see the figure, panel D) based on inelastic scanning tunneling spectroscopy (ISTS) (*6*, *7*) and spin-polarized STS (SP-STS) (*8*, *9*), it was revealed that even in the presence of large MAE, both single Fe and Co adatoms do not exhibit magnetic stability, even at extremely low temperatures. Although the insufficient MAE is one reason for this instability, strong interactions of m with the underlying metallic substrate electrons further destabilize m by spin-flip scattering. Therefore, questions remained whether the MAE could be further enhanced by a choice of substrate that supports a large adatom orbital moment, but at the same time provides a sufficiently strong ligand field, and that limits the coupling of m to the substrate.

Rau *et al.* show that these challenges can be solved by placing a Co adatom on a thin insulating MgO film (see the figure, panel C). Because of the particular symmetry of the Co adatom on top of an oxygen atom, there is a strong ligand field that keeps particular degeneracies of the Co orbitals. As a result, the orbital moment retains its free atom value and the MAE is pushed toward the SOC limit of the free Co atom of about 60 meV.

Probing the magnetic excitations of the Co adatom with ISTS (see the figure, panel D), Rau *et al.* show that the energy needed to excite the Co adatom is ~58 meV. These observations are corroborated by measurements in a magnetic field that confirm the magnetic nature of the excitation. Because ISTS yields little information about the magnetization dynamics of the Co adatom, Rau *et al.* also apply SP-STS based on a pump-probe scheme (*7*) to probe the relaxation time of the excited Co adatom. They find that the time for the magnetic moment to relax to the ground state after excitation over the anisotropy barrier is 0.2 ms, by far the largest lifetime seen for a *3d* transition metal atom on any surface. The insulating MgO film evidently decouples the Co moment from interacting with the underlying electron bath.

To gain deeper insight into the orbital configuration that drives the gigantic MAE, and to determine m of the Co adatom, Rau *et al.* used XAS and XMCD, which are extremely sensitive to the magnetic orientation and orbital configuration of the Co adatom. Such experiments were quantitatively compared to ligand field theory simulations and ab initio calculations, which can precisely determine the multiplet energies of the Co adatom and nicely reproduce the XAS spectra. These results corroborate the STS experiments illustrating that m strongly favors an out-of-plane orientation with a gigantic MAE. The work of Rau *et al.* presents the first application of all established atomic spin detection techniques, combined with insights from state-of-the-art calculations, to unravel the magnetic properties of an adatom.

Although the MAE reported by Rau *et al.* is record breaking, the observation that the Co adatom still fluctuates on a time scale of hundreds of microseconds certainly places in doubt its feasibility for information storage. Therefore, it is important to ascertain whether such fluctuations are weaker for other adatoms, like Fe, and whether such behavior can be preserved on metallic surfaces. One promising route would be to expand such studies to rare earth metal adatoms or to study whether atomic alloys formed between rare earth and *3d* transition metal adatoms can lead to stability. Finally, the viability of single-atom information technology will hinge on the coupling of such single adatoms to arrays that form bits (*2*, *3*) or logic elements (*1*), and on a minimally disturbing input and readout, leaving room for a bunch of further challenging investigations. ■

Institute of Applied Physics, Hamburg University, 20355 Hamburg, Germany. E-mail: akhajeto@physnet.uni-hamburg.de,; jwiebe@physnet.uni-hamburg.de

REFERENCES

1. A. A. Khajetoorians, J. Wiebe, B. Chilian, R. Wiesendanger, *Science* **332**, 1062 (2011).
2. S. Loth, S. Baumann, C. P. Lutz, D. M. Eigler, A. J. Heinrich, *Science* **335**, 196 (2012).
3. A. A. Khajetoorians *et al.*, *Science* **339**, 55 (2013).
4. I. G. Rau *et al.*, *Science* **344**, 988 (2014).
5. P. Gambardella *et al.*, *Science* **300**, 1130 (2003).
6. A. J. Heinrich, J. A. Gupta, C. P. Lutz, D. M. Eigler, *Science* **306**, 466 (2004).
7. S. Loth, M. Etzkorn, C. P. Lutz, D. M. Eigler, A. J. Heinrich, *Science* **329**, 1628 (2010).
8. J. Wiebe, L. Zhou, R. Wiesendanger, *J. Phys. D* **44**, 464009 (2011).
9. A. A. Khajetoorians *et al.*, *Phys. Rev. Lett.* **106**, 037205 (2011).

10.1126/science.1254402

Published by AAAS

BOOKS *ET AL.*

HUMANS AND NATURE

Fields of dreams

By **Sandra Knapp**

In a simple construct, writer and nature lover Tim Dee shows how our landscapes profoundly affect who and what we are. His at-times poetic paean to human-altered landscapes in Britain, Ukraine, Zambia, and the United States explores the meaning of the relationship between humans and the world they have altered, created, and in large part seemingly destroyed. Baba Dioum, the Senegalese conservationist, noted, "In the end, we will conserve only what we love, we will love only what we understand, and we will understand only what we have been taught." Dee, however, shows clearly that teaching isn't all that matters—actually experiencing makes a big difference as well. In these days when school field trips are curtailed and natural history teaching is on the wane, *Four Fields* offers a plea for a closer look at nature, not in a scientific sense, but from the heart.

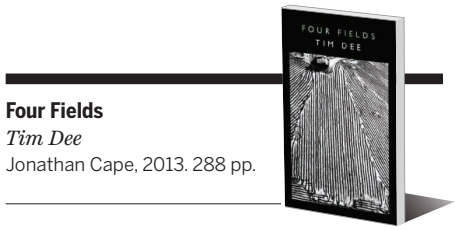


Field of reeds, Wicken Fen, Cambridgeshire.

Woven through with literary and historical references, the book takes readers on a journey from the fens of East Anglia (much altered by an almost continuous loop of people's practices), to the wild grasslands of eastern Africa (inhabited by people since humans evolved), to the sterile fields around Chernobyl (where nature has been put on hold), to the rolling hills of Custer's Last Stand (drenched in blood from a changing way of life): four fields of grass, exhibiting four very different stories of human interactions with landscapes. With great subtlety Dee introduces another theme of four into the story, the passing of the seasons in his own personal field, a fen in Norfolk. His journey, and ours, comes to an end as he notes, "There are no right angles in the seasons, but there are corners and there came a day one late August when I could see round one on the fen and watch the year turning." Dee writes with an honesty that is both refreshing and astonishing—his starting point is that "much of my happiness has come from being outside," something all field biologists have in common.

Much of what we today know about ecosystems is built upon the observations of our predecessors, such as Leonard Blomefield, a 19th century naturalist who kept (he called himself his works' keeper, not its author) a meticulous record of the happenings in the Norfolk fens between 1820 and 1831. Blomefield recorded first blossom, cessation of blackbird song, the sight of the last swifts, everything. Dee reckons that a walk with him would have been "like walking with a recording angel who could channel the song of the earth." The fens—low, flat, flooded areas in East Anglia—are an extraordinary habitat, one long subject to alteration by people. They have been drained, planted, flooded, and mined for peat. More recently, one in particular, Wicken Fen, has been preserved as it might have been before human interference. But Wicken Fen shows how such interference is in fact part of the natural way of things in the fens: left to itself, trees invade and destroy its open grassy boggy character. So management is necessary; human hands have been part of this landscape for so long that without them, it would not exist.

The reviewer is at the Department of Life Sciences, Natural History Museum, Cromwell Road, London SW7 5BD, UK. E-mail: s.knapp@nhm.ac.uk



Four Fields
Tim Dee
Jonathan Cape, 2013. 288 pp.

We often think of human alteration of habitats as a peculiarly European, Old World sort of thing. But humans have been almost everywhere—the "terra preta" (black earth) of apparently virgin Amazon forests is a signature of past human activity. We are a part of the diversity of life on Earth and have had an effect everywhere, not just in fields.

Dee's four fields, and the many side journeys that he makes along the way through the year, all reveal different ways in which people have interacted with the land: The grasslands of Custer's Last Stand in Montana now farmed by descendants of those who defeated him and the eeriness of the dead land around the Chernobyl reactor in Ukraine both reflect the essentially ephemeral nature of humans and of nature itself. Both are ever-changing, and sometimes the obvious is not easy to see.

For a bird enthusiast, Dee is remarkably observant about other organisms. His praise and understanding of John Ray's compendium of the plants of the Cambridge (England) area written in the 18th century are both accurate and inspiring. In fact, the breadth of knowledge he displays about not only natural history but also literature and history could well be intimidating. I haven't read many books that refer to, among many others, Darwin, Tolstoy, Keats, Dante, and Shakespeare or whose author doesn't "know any sexier lines in literature" than those from Milton's *Paradise Lost* that describe the "last day of creation when animals crawl out of the soil into life." But just relax and relish the ride.

Four Fields is an intensely personal book about our interactions with the world around us. Dee reminds us that truly seeing requires more than a glance; careful observation takes time. He also reminds us that the landscapes we inhabit are dynamic—much managed by humans but always changing over time, through seasons, and among places. Above all, his book reminds us that there is much to celebrate in the seemingly ordinary. Nature is endlessly fascinating and will well reward those who take the time to observe the world around them and to see themselves as part of it.

10.1126/science.1253651

PHOTO: PAUL WAKEFIELD/NATIONAL TRUST PHOTOLIBRARY/ALAMY

Downloaded from www.sciencemag.org on May 30, 2014

Published by AAAS

FILM: BIOETHICS

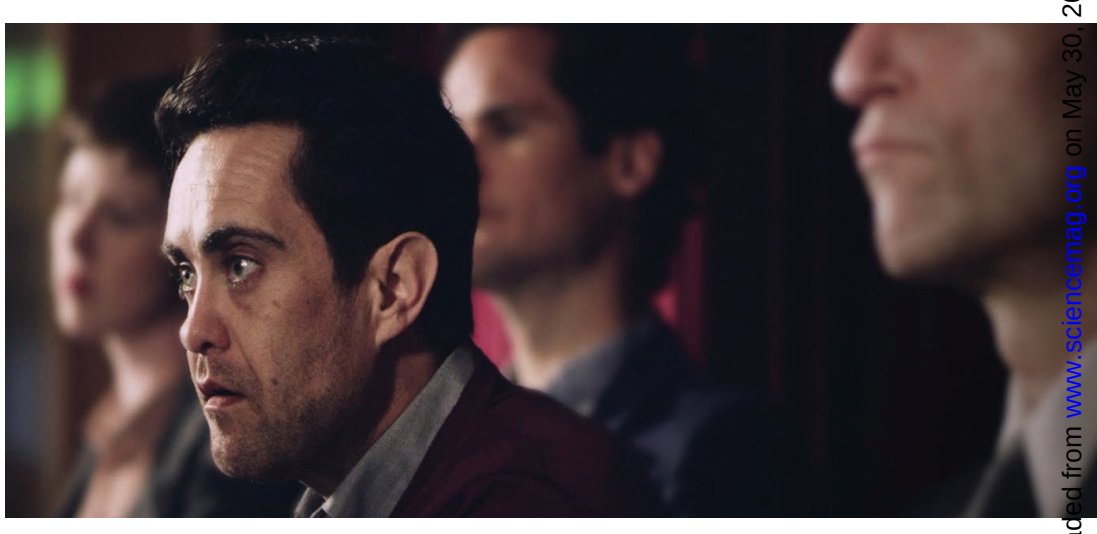
The importance of authentic science on screen

By **Dov Greenbaum**

The Perfect 46
Brett Ryan Bonowicz director
Clindar/Sneak Attack, 2014; 97 minutes

Writer-director-producer Brett Ryan Bonowicz begins *The Perfect 46* with a disclaimer: "This film is scientifically authentic. It is only one step ahead of present reality." To Bonowicz's credit, he seems to have gone to great lengths to make sure that the technology presented in this movie, unlike most thrillers with science in a supporting role, is more science than fiction.

(Spoilers ahead.) Less dystopian than *Gattaca*, and ostensibly more contemporary, the film presents a nonlinear narrative—revolving around a home invasion—that chronicles the rise and fall of the eponymous company and its founder (expertly played by Whit Hertford). The company, whose name alludes to 46 disease-free chromosomes, told customers that its proprietary algorithms provided a means for "assessing you and your partner's genomes and determining your likelihood for a child with diseases caused by your genes." It also claimed to be able to help pair "individuals with their ideal genetic partner for children" (*1*).



The company's meteoric rise is mirrored by its rapid fall after a glitch in the algorithm results in the birth of a number of babies afflicted with Tay-Sachs disease (TSD). The irony will not be lost on viewers who recognize Tay-Sachs screening as one of the earliest success stories of real-life genetic screening for potential couples: an effort that began in the 1970s now includes a wider spectrum of genetic disorders (*2*) and has reduced the birth rate of TSD babies in the Ashkenazi Jewish community by at least 90% (*3*).

The film's disclaimer notwithstanding, Bonowicz does take some literary liberties in the movie's science. His tale ignores, for example, the probability of persistent carriers due to opposing selective pressures (*4*–*6*) and our enduring inability to accurately predict non-Mendelian, epigenetic, complex multigene, and environmentally interrelated diseases. In addition, the film provides only a narrow view of the relevant science, eschewing introducing mitigating and related technologies, such as preimplantation genetic diagnosis or personalized medicine. That, however, may reflect a laudable effort to not complicate, misrepresent, or dumb down the science for the general audience.

Movies can be a touchstone for complicated issues in society, providing easily accessible signposts in discussions of complex topics. Accepting such a role for cinema, one could argue that some filmmakers may have a responsibility to not misrepresent the facts—whether scientific, historical, or from some other field—especially if there exists some likelihood that audiences will perceive them as reality or even a probable reality.

Concerns with accurate representation go way beyond simply mangling scientific theories at the water cooler. Good science in film can inspire innovation and promote participation in scientific endeavors. Controversial or bad science can, intentionally or otherwise, excessively influence conventional wisdom, public policy, legal outcomes, and even the direction and funding of research (*7*).

Scientifically accurate film can be also be a powerful tool for teaching (*8*). Audiences perceive high-quality movies as authentic and believable, and as such, often more engaging in classrooms than hard-to-relate-to hypotheticals. *The Perfect 46* raises a number of timely and relevant bioethical subjects while admirably allowing viewers to form their own opinions on them. These include eugenics, playing God, the role of regulatory oversight (particularly as it relates to direct-to-consumer genetics), control of knowledge, issues of privacy and accountability, the possibility that governments may have access to an entire population's genomic data, and concerns regarding the worried well and their cyberchondriac counterparts.

Hollywood has shown an interest in making the science in movies more scientifically accurate (*9*). Given the impact movies can have on culture and society, scientists should take advantage of this attention. The American Humane Association has long monitored movies and films, noting their approval with the "no animals were harmed" disclaimer in the final credits (*10*). Perhaps scientific societies should consider implementing something similar. There are programs [e.g., (*11*)] to help filmmakers present science (and scientists) more accurately. Should we go further and set up some program to review films and forewarn moviegoers?

The reviewer is at Molecular Biophysics and Biochemistry, Yale School of Medicine, 255 Whitney Avenue, New Haven, CT 06511, USA. E-mail: dov.greenbaum@yale.edu

REFERENCES AND NOTES

1. http://theperfect46.com.
2. H. Curd *et al.*, *J. Commun. Genet.* **5**, 139 (2014).
3. A. Schneider *et al.*, *Am. J. Med. Genet. A* **149A**, 2444 (2009).
4. B. Spyropoulos, *Nature* **331**, 666 (1988).
5. M. Aidoo *et al.*, *Lancet* **359**, 1311 (2002).
6. In some instances, carrier incidence has fallen as a result of genetic screenings (*12*).
7. D. Greenbaum, *Vanderbilt J. Entertain. Technol. Law* **11**, 249 (2009).
8. H. Colt, S. Quadrelli, L. Friedman, Eds., *The Picture of Health: Medical Ethics and the Movies* (Oxford Univ. Press, Oxford, 2011).
9. "A ticket to Tinseltown," *Science* **304**, 1241 (2004).
10. www.americanhumane.org/animals/programs/no-animals-were-harmed.
11. www.scienceandentertainmentexchange.org.
12. A. R. Kyrri *et al.*, *Meoglobin* **37**, 435 (2013).

10.1126/science.1255500

PHOTO: CLINDAR/SNEAK ATTACK

Downloaded from www.sciencemag.org on May 30, 2014

Published by AAAS

LETTERS

Edited by ***Jennifer Sills***

Retraction

SCIENCE HAS RECEIVED the results of the University of California, Riverside Committee on Privilege and Tenure's investigation of the papers published in *Science* by Professor Frank Sauer and colleagues, "TAF1 activates transcription by phosphorylation of serine 33 in histone H2B" (*1*) and "Noncoding RNAs of trithorax response elements recruit *Drosophila* Ash1 to Ultrabithorax" (*2*).

For the 2004 Report (*1*), the Committee's findings can be summarized as follows: Lanes 3 and 4 in Fig. 1B were replicated from a figure in another paper (*3*). There was manipulation of gel images that constituted data falsification and fabrication in Fig. 2C; Fig. 3, B and C; Fig. 4, B and D; and panel A in fig. S5C. For the 2006 Research Article (*2*), the Committee's findings can be summarized as follows: In Fig 6C, there was replication of the same image in two panels that constitutes data falsification. There was manipulation of gel images that constituted data falsification and fabrication in Fig. 4D; Fig. 6, A and B; and fig. S5A.

The Committee concluded that the image manipulations described above constituted a significant departure from the accepted practices of Dr. Sauer's research community. Therefore, the data, results, and conclusions in the papers are clearly not reliable. *Science* is hereby retracting the papers, at the request of University of California, Riverside and Dr. Sauer. The Committee determined that Dr. Sauer was the sole individual responsible for producing the figures.

Marcia McNutt
Editor-in-Chief

REFERENCES

1. T. Maile *et al.*, *Science* **304**, 1010 (2004).
2. T. Sanchez-Elsner *et al.*, *Science* **311**, 1118 (2006).
3. C. Beisel *et al.*, *Nature* **419**, 857 (2002).

CKDu in Sri Lanka

CHRONIC KIDNEY DISEASE of unknown cause (CKDu), seen in Central America ("Mesoamerica's mystery killer," J. Cohen, News Focus, 11 April, p. 143), has also been prevalent in Sri Lanka since the 1990s. As in Central America, those affected are predominantly male rice farmers toiling under dry, dehydrating conditions.

A recent cross-sectional study concluded that the likely culprit is chronic exposure to low levels of Cd and As through the food chain and to pesticides, along with other predisposing factors (e.g., selenium deficiency) (*1*). An unequivocal cause-and-effect explanation has remained elusive and, as in the Americas, many contributing factors have been studied, including heavy metals, pesticides, hard water, cyanotoxins, and water fluoride content (*2*, *3*).

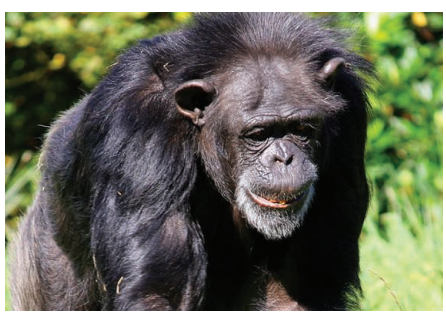
CKDu is a recent phenomenon, whereas rice farming has taken place since ancient times in these regions without apparent health concerns. Recent changes include climate, food habits, and social lifestyle. Perhaps we should discard the conventional search for mechanistic explanations and instead take a holistic approach focusing on the environmental changes and social lifestyle of the affected communities.

M. C. M. Iqbal* *and* ***C. B. Dissanayake***

Institute of Fundamental Studies, Hantana Road, Kandy, Sri Lanka.
*Corresponding author. E-mail: mcmif2003@yahoo.com

REFERENCES

1. N. Jayatilake *et al.*, *BMC Nephrol.* **14**, 180 (2013).
2. R. Chandrajith *et al.*, *Environ. Geochem. Health* **33**, 267 (2011).
3. C. B. Dissanayake, *Geol. Soc. London Spec. Pub.* **113**, 131 (1996).



Perceived threat. Fear complicates conservation.

PHOTO: BARDROCK/WIKIMEDIA COMMONS

Fear beyond predators

IN THEIR PERSPECTIVE, "Tolerance for predatory wildlife" (2 May, p. 476), A. Treves and J. Bruskotter argue that when examining reasons for intolerance of and intention to kill predators, social factors (such as peer group norms and government-sanctioned predator killings) are more important than conventionally held views (such as measured or perceived threats to livelihoods). The authors use case studies on jaguars, wolves, lions, and bears to convincingly support their argument.

With increased anthropogenic disturbance, species not traditionally viewed as predatory may respond increasingly aggressively toward people. Although attacks are rare, concerns about sharing landscapes with great apes may be motivated more by fear of physical aggression than other more common causes of provocation such as threats to livelihoods (i.e., crop damage). As with carnivores, tolerance by local people toward these large-bodied mammals is affected by deep-rooted social beliefs that can influence outcomes, including retaliatory killings.

People's tolerance of wildlife can change quickly in response to shifting economic, demographic, and political conditions. To understand the potential for sustainable human-wildlife coexistence, human social change must be considered alongside changing wildlife behavior in response to human activities and across contexts (such as crop feeding, livestock depredation, and attacks on people) and species. To disentangle such complexities, conservation science must encourage collaborations between social and biological scientists.

Kimberley J. Hockings,[1,2]*
Matthew R. McLennan,[1] Catherine Hill[1]

[1]Social Sciences, Oxford Brookes University, Oxford, OX3 0BP, UK. [2]Centre for Research in Anthropology (CRIA), Lisbon, 1069-061, Portugal.
*Corresponding author.
E-mail: khockings@brookes.ac.uk

TECHNICAL COMMENT ABSTRACTS

Comment on "High-resolution global maps of 21st-century forest cover change"

Robert Tropek, Ondřej Sedláček, Jan Beck, Petr Keil, Zuzana Musilová, Irena Šímová, David Storch

Hansen *et al.* (Reports, 15 November 2013, p. 850) published a high-resolution global forest map with detailed information on local forest loss and gain. We show that their product does not distinguish tropical forests from plantations and even herbaceous crops, which leads to a substantial underestimate of forest loss and compromises its value for local policy decisions.

Full text at http://dx.doi.org/10.1126/science.1248753

Response to Comment on "High-resolution global maps of 21st-century forest cover change"

M. Hansen, P. Potapov, B. Margono, S. Stehman, S. Turubanova, A. Tyukavina

Tropek *et al.* critique the Hansen *et al.* global forest loss paper in terms of its utility and accuracy. Both criticisms suffer from a miscomprehension of the definition of forest employed as well as the requirements of product validation. Utility of the product is enhanced through its integration with forest type, carbon stock, protected area status, and other ancillary data.

Full text at http://dx.doi.org/10.1126/science.1248817

Downloaded from www.sciencemag.org on May 30, 2014

Published by AAAS



Vigilance required. Big data can benefit society, but protecting privacy and fairness is critical, said White House counselor John Podesta.

Big data, big questions

Can researchers capitalize on "big data" without sacrificing individuals' privacy?

By **Kathy Wren**

Patterns lurking within massive data sets—such as those collected via smartphone apps, online retail sites, or clinical trials—can yield important insights into scientific questions, according to a report released by the White House on 1 May. But the sharing of this data leaves many vulnerable to privacy invasions and discrimination in areas such as housing, health care and employment.

The report's authors, led by White House counselor John Podesta, call for a number of measures that would enhance privacy protection for consumers, students, patients, and others, such as resurrecting the consumer privacy bill of rights that President Obama proposed 2 years ago. A complementary report on big data's technical dimensions, produced by the President's Council of Advisors on Science and Technology (PCAST), concludes that technical measures alone are not sufficient for protecting privacy, and recommends that policy should focus more on how big data is used and less on how it is collected and analyzed.

Raising these issues "isn't an indictment of the technology or the methods themselves. Our aim, really, should be to maximize the benefits of big data while minimizing risks to privacy and other values," said Podesta, presenting his group's findings at the AAAS Forum on Science & Technology Policy on 2 May. The 2-day event drew over 400 people to discuss a wide range of topics at the intersection of science, technology, and policy.

Several federal programs focused on big data have launched or expanded in recent years, a notable trend considering that U.S. spending on R&D overall has dropped by $24 billion in constant dollars over the last 4 years, according to Matthew Hourihan, director of the R&D Budget Analysis Program at AAAS. In 2012 the White House kicked off a $200-million "big data initiative" spanning six federal departments and agencies. The president's FY 2015 budget would fund several related programs, including the National Institutes of Health's "Big Data 2 Knowledge" (BD2K) initiative and the Department of Energy's Advanced Scientific Computing Research program.

Pharmaceutical companies that amass huge datasets during their clinical trials are also rethinking their approach to data sharing. Access to this information has historically been limited to company researchers, their collaborators, and regulatory agencies like the FDA. But last year, two industry trade groups, the Pharmaceutical Research and Manufacturers of America and the European Federation of Pharmaceutical Industries and Associations, issued a set of joint guidelines for sharing data more broadly with patients, researchers, and the public.

"We're living in a brave new world where data is a commodity and access to data is an expectation," said Ariella Kelman, group medical director at Genentech, speaking at a Forum session on reproducibility in science.

The Roche Group, which owns Genentech, is now making the data sets from its clinical trials—vast quantities of information including the measurements made during every patient visit—available upon request to outside researchers. Kelman outlined several basic principles that underlie Roche's approach to data sharing: respect for patients and the role of regulatory authorities and commitment to innovation and scientific progress.

PHOTO: AAAS/CARLA SCHAFFER

Downloaded from www.sciencemag.org on May 30, 2014

Published by AAAS

"There are some risks with the broader sharing of complex data," she acknowledged, citing the possibility of privacy breaches, frivolous lawsuits, or benefits to competitors. But, the company has taken rigorous measures to de-identify the patient data, and ultimately, she said, the opportunity to optimize patient benefits, gain public trust, and align with industry trends will make this effort worthwhile.

Despite the forward momentum for big data, multiple speakers at the Forum also described how funding pressures would stifle other areas of science and technology. President Obama's proposed R&D budget for 2015 is a modest $136.5 billion, a 0.7% increase above 2014. But that does not match the 1.7% rate of inflation. The proposal falls within the spending caps set by the Murray-Ryan budget deal from last December. It also requests an additional $5.3 billion in R&D spending for an "Opportunity, Growth and Security Initiative," but this is unlikely to be approved, according to Hourihan. "It's very much a treading water kind of budget," he said.

Others noted that some countries have dramatically increased their R&D spending; for example China's national R&D investment has roughly tripled in the 21st century. The resulting "innovation deficit" in the United States has serious implications for economic competitiveness and national security, said Hunter Rawlings, president of the Association of American Universities.

Plenary speaker John Holdren, who is President Obama's top science adviser, maintained that even though the federal funding for R&D "is not what we'd like it to be," science and technology are still high priorities in the White House. He also expressed concern over the Frontiers in Innovation, Research, Science, and Technology (FIRST) authorization bill proposed by Representative Lamar Smith (R–TX), which would reshape the National Science Foundation's peer-reviewed grant-making system. Holdren noted that other countries are trying to replicate the NSF's successful approach. "To try to fix what is not broken at NSF would risk eroding a cornerstone of American science and engineering excellence," he said.

Screeners needed for journalism awards
Volunteer scientists in the Washington, D.C. area are needed to review the scientific accuracy of entries in the AAAS Kavli Science Journalism Awards competition. Please contact Katharine Zambon (kzambon@aaas.org).

New grants bring STEM volunteers to schools

By **Kat Zambon**

The AAAS National STEM Volunteer Program has awarded seven grants of approximately $12,000 each to nonprofit organizations working with AAAS members, to build collaborations between STEM professionals and K-12 students and teachers. The grantees will work in classrooms and after school, and many of the programs will focus on outreach to communities that have been historically underrepresented in the science fields.

The grant winners include: University of New England Center for Excellence in Neuroscience and Marine Science; Salk Institute for Biological Studies New Frontiers in Science Education Program; University of Georgia REFOCUS Program; University of Colorado-Denver Young Hands in Science Program; University of Washington Institute of Science and Math Education; University of Wisconsin Young Science Scholars; and Rochester Institute of Technology Insight Lab for Science Outreach and Learning Research.

The ambitious new program will help educators prepare their students for testing under the Next Generation Science Standards and the Common Core Standards, which emphasize problem-solving and research skills.

"Our diverse membership puts AAAS in a unique position to connect STEM professionals with middle and high school students," said Alan I. Leshner, AAAS chief executive officer and executive publisher of the journal *Science*. "The National STEM Volunteer Program will also help us build a network of volunteers who can help students understand the practice of STEM in formal and informal settings."

Volunteers for the program may include retired and current STEM professionals as well as STEM graduate students and postdocs. Potential partners include school districts, universities, federally funded research and development centers, science museums, federal labs, and STEM professional organizations. Learn more about the program and this year's grantees at www.aaas.org/JzH.



Satellites show hospital damage in Syria

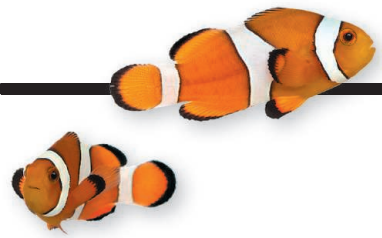
Satellite images analyzed in a new AAAS report have confirmed substantial war-related damage to several medical facilities in Syria. By 16 July 2012, Amal Hospital in Homs was completely destroyed (red box), as were many buildings in the surrounding neighborhood (arrows). The AAAS Geospatial Technologies and Human Rights Project report was requested by Physicians for Human Rights, which is documenting reports of attacks on medical care in Syria.

COORDINATES: 34.7357627 N, 36.7089954 E. IMAGE ©2014, DIGITALGLOBE, NEXTVIEW LICENSE/ANALYSIS AAAS

Published by AAAS

RESEARCH

Ancient reefs protected diverse fish from past climate changes *p. 1016*



IN *SCIENCE* JOURNALS

Edited by **Stella Hurtley**



Endangered California clapper rail.

CONSERVATION ECOLOGY

Conservation vs. eradication

What's an ecologist to do when an endangered bird lives in an invasive grass? Ecosystems are complicated networks, with one species relying on another, and managing one species in isolation may damage other members of a community. Lampert *et al*. (see the Perspective by Buckley and Han) looked at the conflict between eradicating a damaging invasive grass species and protecting an endangered bird species that uses the grass as its home. The most effective management and restoration approach focused not on eradicating the invasive grass as quickly as possible but on making changes slowly enough that the birds could adapt. This approach may prove useful in other situations in which active restoration conflicts with other conservation goals. — AMS

Science, this issue p. 1028; see also p. 975

CHILDHOOD DEVELOPMENT

Help as hungry children helps young adults

Supporters of early childhood interventions follow the rule "better early than late," but so far there's been limited evidence that the rule applies to disadvantaged children in developing countries. Gertler *et al.* looked at the earnings of young adults in Jamaica, 20 years after, as toddlers, they were given 2 years of help from community health workers. The earnings of the treatment group caught up to those of a comparison group of well-fed children, but the control group of undernourished children that did not receive the health worker visits has lagged behind. — GJC

Science, this issue p. 998

CANCER

Fighting cancer needs more of the right T cells

In immunotherapy that helps the body's fight against cancer, antibodies that block the cell surface protein CTLA-4 (cytotoxic T lymphocyte–associated antigen-4) entice the immune system to enter the ring. Cha *et al.* used next-generation sequencing to show that blocking CTLA-4 in cancer sufferers drives change among T cells, so that the population becomes active against a different collection of targets. However, increasing T cell diversity is not the whole story—after treatment, the patients with more favorable clinical outcomes were able to maintain certain preexisting abundant T cells, whereas poorly responding patients lost these cells. Thus, although CTLA-4 blockade induces T cell repertoire diversification, it may actually be the maintenance of particular vigorous T cell clones that helps the antitumor immune response. — AC

Sci. Transl. Med. **6**, 238ra70 (2014).

WATER SPLITTING

Keeping semiconductors safe from harm

Solar cells harvest the energy of sunlight to create electricity, but electricity is hard to store. Solar cells could also be used to make hydrogen from water, which can be stored as a fuel. Separating water into hydrogen and oxygen, however, presents challenges, especially if this is done directly by illuminating the anode that oxides water. Under the acidic or alkaline conditions needed for practical devices, semiconducting anode materials corrode during operation. Hu *et al.* now show that amorphous titanium dioxide coatings can protect semiconductors from alkaline corrosion while still allowing light through. — PDS

Science, this issue p. 1005

INTERFERON SIGNALING

A way to build a better interferon?

Type I interferons stimulate an antiviral response during infections, but they also prevent immune cells from proliferating.

Downloaded from www.sciencemag.org on May 30, 2014

PHOTOS: (TOP TO BOTTOM) © LIFE ON WHITE/ALAMY; ROBERT CLARK

Published by AAAS

This effect complicates the use of interferons in patients, because the body needs greater numbers of immune cells to fight viruses effectively. Interferons activate two distinct sets of genes: one for the antiviral response and the other to block immune cells from proliferating. Levin *et al.* engineered an interferon called IFN-1ant that prevented other forms of interferon from binding to the interferon receptor. At certain doses, IFN-1ant activated the genes required for antiviral immunity without activating the genes that keep immune cells from proliferating. — JFF

Sci. Signal. **7**, ra50 (2014).

SUBSURFACE MICROBES

How bacteria manage to breathe on rust

In the absence of oxygen, anaerobic bacteria turn to other chemical compounds during respiration. This can be helpful in detoxifying heavy-metal pollution. Flynn *et al.* (see the Perspective by Friedrich and Finster) found that alkaline conditions prevent a detoxifying bug—*Shewanella oneidensis*—from using enzymes to reduce rust-like minerals. Instead, the bacteria reduce elemental sulfur compounds, generating hydrogen sulfide that reduces the iron indirectly. This interplay between anoxic biogeochemical cycles may explain why some anaerobic bacteria contain the genetic machinery necessary to reduce multiple compounds besides oxygen. — NW

Science, this issue p. 1039; see also p. 974

SYNAPSES

High-definition view of the synapse

Individual neurons communicate with one another via their synapses, so to understand the nervous system, we need to understand in detail how the synapses are organized. Wilhelm *et al.* present a quantitative molecular-scale image of the "average" synapse populated with realistic renditions of each of the protein components that contribute to the inner workings of neurons. — SMH

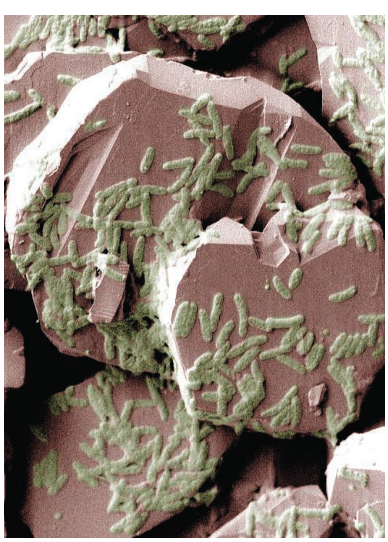
Science, this issue p. 1023

MOLECULAR MAGNETISM

Maximizing atomic magnetic memory

A study of the magnetic response of cobalt atoms adsorbed on oxide surfaces may lead to much denser storage of data. In hard drives, data are stored as magnetic bits; the magnetic field pointing up or down corresponds to storing a zero or a one. The smallest bit possible would be a single atom, but the magnetism of a single atom —its spin— has to be stabilized by interactions with heavy elements or surfaces through an effect called spin-orbit coupling. Rau *et al.* (see the Perspective by Khajetoorians and Wiebe) built a model system in pursuit of single-atom bits—cobalt atoms adsorbed on magnesium oxide. At temperatures approaching absolute zero, the stabilization of the spin's magnetic direction reached the maximum that is theoretically possible. — PDS

Science, this issue p. 988; see also p. 976



The detoxifying bug *Shewanella oneidensis* (green) growing on crystals of hematite (brown).

PHOTOS: (TOP TO BOTTOM) M. CARVALHO *ET AL.*, *PLOS ONE* **9** (5 MAY 2014); EMSL/FLICKR

IN OTHER JOURNALS

Edited by **Kristen Mueller** *and* **Jesse Smith**



Insects chewing leaves in the forest

PLANT ECOLOGY

Ancient leaves tattle on insects

Paleoentomologists have long estimated past levels of insect diversity by counting different types of leaf damage in fossils—but they've had little evidence of whether leaf damage is, in fact, a good proxy for insect diversity. Carvalho *et al*. examined the canopies of 24 tree species in modern tropical forests to assess the level of insect damage and identify the types of insects associated with the observed damage. The number of insect species collected from the forests correlated positively with the different types of leaf damage seen on leaves fed to these insects in the laboratory. The findings support the practice of extrapolating from fossils of chewed leaves to the diversity of the ancient chewers. — LMZ

PLOS One **9**, 94950 (2014).

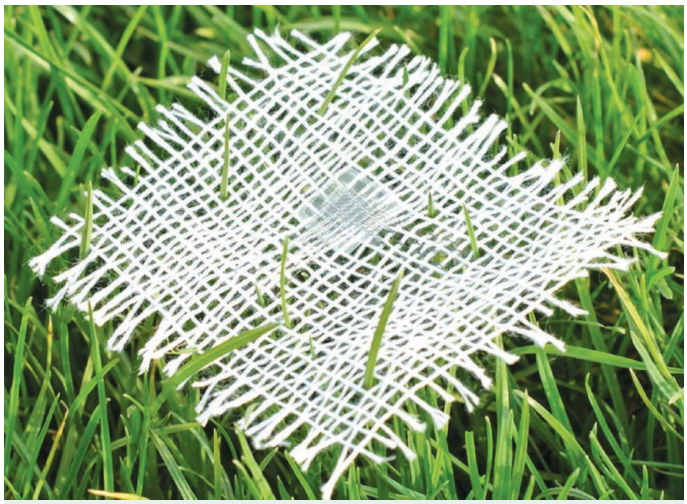
AGING

Tracking down a tonic for a long life

Scientists may not yet have found the fountain of youth, but Ye *et al*. now report on a screen for drugs that can extend life span in the worm *Caenorhabditis elegans*. Starting with a collection of over 1200 drugs that have or are suspected to have activity in human cells, they identified nearly 60 compounds that extended life span up to 43%. Many of the compounds targeted proteins that function in signaling pathways between cells, such as hormone or neurotransmitter receptors, particularly those for adrenaline and noradrenaline, serotonin, dopamine, histamine, and serotonin. Given that humans and worms share some aging mechanisms, these results may help bypass the time and expense of similar studies in mammals. — LBR

Aging Cell **13**, 206 (2014).

Published by AAAS



A solar cell textile integrated in a fabric.

MATERIALS SCIENCE

Weaving solar energy into fabrics

Imagine a sweatshirt that charges your cell phone or a sail that powers a ship's radio. To bring solar-powered fabric closer to reality, Pan *et al.* modified the standard design of a dye-sensitized solar cell by sandwiching the dye and electrolyte between two flexible electrodes. Earlier approaches twisted the electrodes together into cylinders. Instead, Pan *et al.* stacked grids of titanium dioxide–coated titanium wires and carbon nanotube fibers, making it easier to connect multiple cells. With a solid-state electrolyte, the cells lost less than 6% of their efficiency over 300 hours of operation in air. As a proof of principle, the authors used several woven cells connected in series to power a red light–emitting diode. — JSY

Angew. Chem. Int. Ed. **53**, 10.1002/anie.201402561 (2014).

EDUCATION

Making business students science-savvy

What happens when science pedagogy goes to business school? Future business leaders become knowledgeable about the latest developments in renewable-energy technology. Rodgers engaged undergraduate business management students in developing their business skills while learning about renewable-energy technologies by having them take a basic course on energy sources and prepare a "rocket pitch"—a short presentation designed to recruit investors. Rodgers also had the students research and design a new environmental technology project. The experience exposed them to primary sources and immersed them in debate about which energy source would be an ideal investment for the future. The approach, Rodgers found, prepared the business students to use scientific knowledge in their future business decisions. — MM

J. Coll. Sci. Teach. **43**, 28 (2014).

CANCER

Serendipity rules in cancer therapy

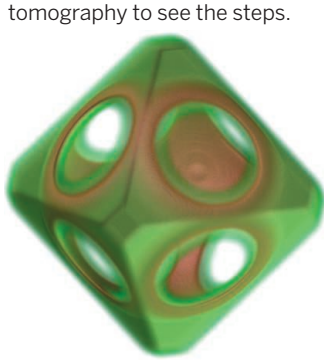
While testing cancer drugs in a mouse model of a deadly blood cancer, multiple myeloma, Shortt *et al*. made a startling discovery: On its own, an inert solvent commonly used as a drug delivery vehicle can halt the cancer's growth. The researchers noticed that control mice treated with *N*-methyl-2-pyrrolidone (NMP) survived longer than control mice treated with other drug delivery vehicles. Further analyses of NMP in cultured cells and live mice confirmed the solvent's anti-myeloma activity. NMP shares certain mechanistic similarities with other promising drug candidates for myeloma that were discovered in more traditional ways. Plans for phase 1 clinical trials are under way. — PAK

Cell Rep. **7**, 10.1016/j.celrep.2014.04.008 (2014).

CHEMISTRY

Nanoparticle transformations in 3D

When silver nanocubes react with gold ions, they combine into hollow-frame octohedral structures. Now Goris *et al.* have imaged the process with electron tomography and x-ray element mapping to see how it happens. Goris *et al.* reacted silver nanocubes with $HAuCl_4$ and found that three silver atoms were oxidized for every gold atom consumed. They removed a series of samples at different points in the reaction and used three-dimensional (3D) tomography to see the steps.



A golden nanoparticle framework.

First, a pinhole opens up in one facet. Next, all the facets open up. Then the vertices flatten to become new facets, until finally only an octahedral wire frame structure remains. The analysis also revealed that a protective gold layer surrounded the initial pinhole and forced the reaction of silver from the interior of the nanocube. — PDS

Nano Lett. 10.1021/nl500593j (2014).

PHYSICS

Stretching graphene to switch it off

Graphene, which is made up of a single layer of carbon atoms arranged in a honeycomb pattern, has remarkable mechanical and electrical properties, but conducts electricity almost too well. Therefore, researchers are looking for ways to switch off graphene devices more easily. It is known that graphene sometimes develops electronic states in which it doesn't conduct electricity when it is placed on hexagonal boron nitride (hBN), another honeycomb-structured material. Woods *et al.* now have found that graphene stretches and adapts locally to the underlying hBN lattice so that the atoms of the two lattices lie on top of each other, as long as the angle of orientation of the graphene layer with respect to hBN is not too great. The matched areas probably contribute to the nonconducting states through the homogeneity of their electronic properties. — JS

Nat. Phys. 10.1038/nphys2954 (2014).

OCEANOGRAPHY

Arctic sea ice traps floating plastic

Scientists are all too familiar with microplastics—tiny polymer beads, fibers, or fragments—in ocean eddies or near coastlines. But currents, it turns out, also carry them to the Arctic. Obbard *et al*. melted and filtered parts of four Arctic sea-ice cores, analyzing the remaining particles' chemistry. They found rayon, as well as polyester, nylon, and other synthetic polymers. As Arctic ice freezes, the researchers argue, it traps floating microplastics, accumulating hundreds of particles per cubic meter: three orders of magnitude larger than some counts of particles in the Pacific Garbage Patch. And melting sea ice, they note, could release more than 1 trillion pieces of plastic to the ocean in the next decade. — EH

Earth's Future 10.1002/2014EF000240 (2014).

PHOTOS: (TOP TO BOTTOM) S. PAN *ET AL. ANGEWANDTE CHEMIE INTERNATIONAL EDITION* **53** (30 APRIL 2014) © 2014 WILEY-VCH VERLAG GMBH & CO. KGAA, WEINHEIM; B. GORIS *ET AL., NANO LETTERS* (5 MAY 2014) © 2014 AMERICAN CHEMICAL SOCIETY

Published by AAAS

ONLINE IN *SCIENCE*

Edited by **Stella Hurtley**

BIODIVERSITY STATUS

Maintaining biodiversity: From here to eternity?

There has been substantial recent progress in determining the distributions and identity of vulnerable species, and in understanding how (and where) human activity is leading to extinctions. Pimm *et al.* review the current state of knowledge and ask what the future rates of species extinction will be, how well protected areas will slow extinction rates, and how the remaining gaps in knowledge might be filled. — AMS

Science, this issue p. 987

SOLAR CELLS

Pull, pull, pulling electrons along

Organic photovoltaics operate by transferring charge from a light-absorbing donor material to a nearby acceptor. Falke *et al.* show that molecular vibrations smooth the way for this charge transfer to proceed. A combination of ultrafast spectroscopy and theoretical simulations revealed an oscillatory signal in a model donor/acceptor blend that implicates carbon-carbon bond stretching in concert with the electronic transition. This vibrational/electronic, or vibronic, process maintains a quantum-mechanical phase relationship that guides the charge more rapidly and directly than an incoherent migration from donor to acceptor. — JSY

Science, this issue p. 1001

WATER STRUCTURE

Blackjack water cluster detected

Spectroscopy of protonated water clusters has played a pivotal role in elucidating the molecular arrangement of acid solutions. Whereas bulk liquids manifest broad spectral features, the cluster bands tend to be sharper. The 21-membered water cluster has for decades inspired particular interest on account of its stability and its place in the transition from two-dimensional to three-dimensional hydrogen-bonding network motifs, but the spectral signature of its bound proton has proved elusive. Fournier *et al.* have now detected this long-sought vibrational feature by applying an innovative ion cooling technique. — JSY

Science, this issue p. 1009

IMAGING TECHNIQUES

A close-up view of carbon-bromide bonds

Polarizing filters are widely used in optical microscopy to highlight a range of material properties that cause optical path boundaries or birefringence in a material. Palmer *et al*. (see the Perspective by Lidin) developed an analog method for x-ray microscopy using linearly polarized x-ray beams and an area detector inside a synchrotron. The technique revealed the orientation of the C-Br bonds within crystalline materials. — MSL

Science, this issue p. 1013; see also p. 969

MARINE BIOGEOGRAPHY

Ancient reefs provided fishy refuges

Climate fluctuations have occurred repeatedly in Earth's history, and so there is much to be learned from examining the responses of past systems. Pellessier *et al.* reconstructed paleoenvironments over the past 3 million years from sediment cores collected across coral reef systems to explore the impacts of past conditions on reef fish diversity. Coral reefs survived in the Indo-Australian regions during times of otherwise extensive habitat loss. These robust reefs can explain much of the diversity found in present-day reef fish species. — SNV

Science, this issue p. 1016

NEURAL DEVELOPMENT

Making and breaking neuronal synapses

As the brain develops, early synapse formation is exuberant and haphazard. But as development progresses, connections are refined into functional networks. In that process, many synapses get eliminated. Uesaka *et al*. now show that molecules already known for axon guidance are functional later on when they regulate the synaptic pruning needed to refine the circuits connected during axon guidance. — PJH

Science, this issue p. 1020

CELLULAR DYNAMICS

Motors stirring within the living cell

Cytoskeletal dynamics is key to cellular function. At very short time scales, thermal motions probably dominate, whereas on time scales from minutes to hours, motor-protein-12–based directed transport is dominant. But what about the times in between? Fakhri *et al*. tracked kinesin molecules labeled with carbon nanotubes and monitored their motion in living cells for milliseconds to hours. The kinesins motored along microtubule tracks, but sometimes moved more randomly as the tracks themselves were moved by active, larger-scale cell movements. This active "stirring" of the cytoplasm may play a role in nonspecific transport. — VV

Science, this issue p. 1031

STRUCTURAL BIOLOGY

How to recruit membrane trafficking machinery

PI4KIIIβ is a lipid kinase that underlies Golgi function and is enlisted in biological responses that require rapid delivery of membrane vesicles, such as during the extensive membrane remodeling that occurs at the end of cell division. Burke *et al.* determined the structure of PI4KIIIβ in a complex with the membrane trafficking GTPase Rab11a. The way in which the proteins interact gives PI4KIIIβ the ability to simultaneously recruit Rab11a and its effectors on specific membranes. — SMH

Science, this issue p. 1035

TRANSCRIPTION

Transcription takes a pause to consider

A short sequence in DNA causes RNA polymerase (RNAP) to pause at thousands of previously undocumented locations in the genome. Larson *et al.* mapped these pause sites at single-nucleotide resolution in vivo in actively growing bacteria. Transcriptional pausing can be critical for the regulation of gene expression, by allowing RNA folding events and in the recruitment of other transcription factors. — GR

Science, this issue p. 1042

ION CHANNEL STRUCTURE

Intact NMDA receptor structure revealed

For brains to develop and form memories, a signal must be transmitted from one neuron to the next. Glutamate is an important neurotransmitter that excites the receiving nerve cell by binding to an ion channel called an *N*-Methyl-D-Aspartate (NMDA) receptor. This activates the NMDA receptors, causing calcium ions to flood in, triggering signal transduction. Either under- or overactivation can result in a variety of neurological disorders and diseases. Karakas and Furukawa describe the crystal structure of an intact NMDA receptor composed of four separate subunits. — VV

Science, this issue p. 992

Published by AAAS

REVIEW SUMMARY

BIODIVERSITY STATUS

The biodiversity of species and their rates of extinction, distribution, and protection

S. L. Pimm,* C. N. Jenkins, R. Abell, T. M. Brooks, J. L. Gittleman, L. N. Joppa, P. H. Raven, C. M. Roberts, J. O. Sexton

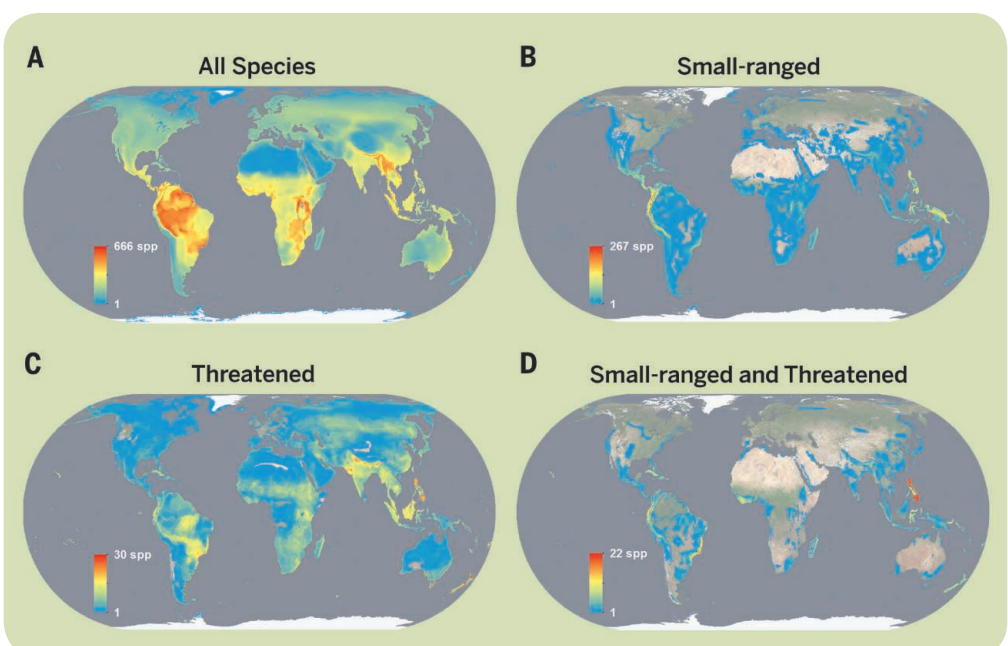
BACKGROUND: A principal function of the Intergovernmental Science-Policy Platform on Biodiversity and Ecosystem Services (IPBES) is to "perform regular and timely assessments of knowledge on biodiversity." In December 2013, its second plenary session approved a program to begin a global assessment in 2015. The Convention on Biological Diversity (CBD) and five other biodiversity-related conventions have adopted IPBES as their science-policy interface, so these assessments will be important in evaluating progress towards the CBD's Aichi Targets of the Strategic Plan for Biodiversity 2011–2020. As a contribution toward such assessment, we review the biodiversity of eukaryote species and their extinction rates, distributions, and protection. We document what we know, how it likely differs from what we do not, and how these differences affect biodiversity statistics. Interestingly, several targets explicitly mention "known species"—a strong, if implicit, statement of incomplete knowledge. We start by asking how many species are known and how many remain undescribed. We then consider by how much human actions inflate extinction rates. Much depends on where species are, because different biomes contain different numbers of species of different susceptibilities. Biomes also suffer different levels of damage and have unequal levels of protection. How extinction rates will change depends on how and where threats expand and whether greater protection counters them.

ADVANCES: Recent studies have clarified where the most vulnerable species live, where and how humanity changes the planet, and how this drives extinctions. These data are increasingly accessible, bringing greater transparency to science and governance. Taxonomic catalogs of plants, terrestrial vertebrates, freshwater fish, and some marine taxa are sufficient to assess their status and the limitations of our knowledge. Most species are undescribed, however. The species we know best have large geographical ranges and are often common within them. Most known species have small ranges, however, and such species are typically newer discoveries. The numbers of known species with very small ranges are increasing quickly, even in well-known taxa. They are geographically concentrated and are disproportionately likely to be threatened or already extinct. We expect unknown species to share these characteristics. Current rates of extinction are about 1000 times the background rate of extinction. These are higher than previously estimated and likely still underestimated. Future rates will depend on many factors and are poised to increase. Finally, although there has been rapid progress in developing protected areas, such efforts are not ecologically representative, nor do they optimally protect biodiversity.

ON OUR WEBSITE

Read the full article at http://dx.doi.org/10.1126/science.1246752

OUTLOOK: Progress on assessing biodiversity will emerge from continued expansion of the many recently created online databases, combining them with new global data sources on changing land and ocean use and with increasingly crowdsourced data on species' distributions. Examples of practical conservation that follow from using combined data in Colombia and Brazil can be found at www.savingspecies.org and www.youtube.com/watch?v=R3zjeJW2NVk.



Different visualizations of species biodiversity. (**A**) The distributions of 9927 bird species. (**B**) The 4964 species with smaller than the median geographical range size. (**C**) The 1308 species assessed as threatened with a high risk of extinction by BirdLife International for the Red List of Threatened Species of the International Union for Conservation of Nature. (**D**) The 1080 threatened species with less than the median range size. (D) provides a strong geographical focus on where local conservation actions can have the greatest global impact. Additional biodiversity maps are available at www.biodiversitymapping.org.

The list of author affiliations is available in the full article online.
*Corresponding author. E-mail: stuartpimm@me.com
Cite this article as S. L. Pimm *et al.*, *Science* 344, 1246752 (2014). DOI: 10.1126/science.1246752

Published by AAAS

REVIEW

BIODIVERSITY STATUS

The biodiversity of species and their rates of extinction, distribution, and protection

S. L. Pimm,[1]* C. N. Jenkins,[2] R. Abell,[3]† T. M. Brooks,[4] J. L. Gittleman,[5] L. N. Joppa,[6] P. H. Raven,[7] C. M. Roberts,[8] J. O. Sexton[9]

Recent studies clarify where the most vulnerable species live, where and how humanity changes the planet, and how this drives extinctions. We assess key statistics about species, their distribution, and their status. Most are undescribed. Those we know best have large geographical ranges and are often common within them. Most known species have small ranges. The numbers of small-ranged species are increasing quickly, even in well-known taxa. They are geographically concentrated and are disproportionately likely to be threatened or already extinct. Current rates of extinction are about 1000 times the likely background rate of extinction. Future rates depend on many factors and are poised to increase. Although there has been rapid progress in developing protected areas, such efforts are not ecologically representative, nor do they optimally protect biodiversity.

One of the four functions of the Intergovernmental Science-Policy Platform on Biodiversity and Ecosystem Services (IPBES) is to "perform regular and timely assessments of knowledge on biodiversity" (*1*). In December 2013, its second plenary session approved starting global and regional assessments in 2015 (*1*). The Convention on Biological Diversity (CBD) and five other biodiversity-related conventions have adopted IPBES as their science-policy interface, so these assessments will be important in evaluating progress toward the CBD's Aichi Targets of the Strategic Plan for Biodiversity 2011–2020 (*2*). They will necessarily follow the definitions of biodiversity by the CBD introduced by Norse *et al.* (*3*) as spanning genetic, species, and ecosystem levels of ecological organization. As a contribution, we review the biodiversity of eukaryote species and their extinction rates, distributions, and protection.

Interestingly, several targets explicitly mention "known species"—a strong, if implicit statement of incomplete knowledge. So how many eukaryote species are there (*4*)? For land plants, there are 298,900 accepted species' names, 477,601 synonyms, and 263,925 names unresolved (*5*). Because the accepted names among those resolved is 38%, it seems reasonable to predict that the same proportion of unresolved names will eventually be accepted. This yields another ~100,000 species for a total estimate of 400,000 species (*5*). Models predict 15% more to be discovered (*6*), so the total number of species of land plants should be >450,000 species, many more than are conventionally assumed to exist.

For animals, recent overviews attest to the question's difficulty. About 1.9 million species are described (*7*); the great majority are not. Costello *et al.* (*8*) estimate 5 ± 3 million species, Mora *et al.* (*9*) 8.7 ± 1.3 million, and Chapman (*7*) 11 million. Raven and Yeates (*10*) estimate 5 to 6 million species of insects alone, whereas Scheffers *et al.* (*11*) think uncertainties in insect and fungi numbers make a plausible range impossible. Estimates for marine species include 2.2 ± 0.18 million (*9*), and Appeltans *et al.* estimate 0.7 to 1.0 million species, with 226,000 described and another 70,000 in collections awaiting description (*12*).

Concerns about biodiversity arise because present extinction rates are exceptionally high. Consequently, we first compare current extinction rates to those before human actions elevated them. Vulnerable species are geographically concentrated, so we next consider the biogeography of species extinction. Given taxonomic incompleteness, we consider how undescribed species differ from described species in their geographical range sizes, distributions, and risks of extinction. To understand whether species extinction rates will increase or decrease, we review how and where threats are expanding and whether greater protection may counter them. We conclude by reviewing prospects for progress in understanding the key lacunae in current knowledge.

Background Rates of Species Extinction

Given the uncertainties in species numbers and that only a few percent of species are assessed for their extinction risk (*13*), we express extinction rates as fractions of species going extinct over time—extinctions per million species-years (E/MSY) (*14*)—rather than as absolute numbers. For recent extinctions, we follow cohorts from the dates of their scientific description (*15*). This excludes species, such as the dodo, that went extinct before description. For example, taxonomists described 1230 species of birds after 1900, and 13 of them are now extinct or possibly extinct. This cohort accumulated 98,334 species-years—meaning that an average species has been known for 80 years. The extinction rate is $(13/98{,}334) \times 10^6 = 132$ E/MSY.

The more difficult question asks how we can compare such estimates to those in the absence of human actions—i.e., the background rate of extinction. Three lines of evidence suggest that an earlier statement (*14*) of a "benchmark" rate of 1 (E/MSY) is too high.

First, the fossil record provides direct evidence of background rates, but it is coarse in time, space, and taxonomic level, dealing as it does mostly with genera (*16*). Many species are in monotypic genera, whereas those in polytypic genera often share the same vulnerabilities to extinction (*17*), so extinction rates of species and genera should be broadly similar. Alroy found Cenozoic mammals to have 0.165 extinctions of genera per million genera-years (*18*). Harnik *et al.* (*19*) calculated the fractions of species going extinct over different intervals. Converting these to their corresponding rates yields values for the past few million years of 0.06 genera extinctions per million genera-years for cetaceans, 0.04 for marine carnivores, and, for a variety of marine invertebrates, between the values of 0.001 (brachiopods) and 0.01 (echinoids).

Second, molecular-based phylogenies cover many taxa and environments, providing an appealing alternative to the fossil record's shortcomings. A simple model of the observed increase in the number of species S_t in a phylogenetic clade over time, t, is $S_t = S_0 \exp[(\lambda - \mu) \times t]$, where λ and μ are the speciation and extinction rates. In practice, λ and μ may vary in complex ways. Estimating the average diversification rate, $\lambda - \mu$, requires only modest data. Whether one can separate extinction from speciation rates by using species numbers over time is controversial (*20*, *21*) and an area of active research that requires carefully chosen data to avoid potential biases. With the simple model, the logarithm of the number of lineages [lineages through time (LTT)] should increase linearly over time, with slope $\lambda - \mu$, but with an important qualification. In the limit of the present day, the most recent taxa have not yet had time to become extinct. The LTT curve

[1]Nicholas School of the Environment, Duke University, Box 90328, Durham, NC 27708, USA. [2]Instituto de Pesquisas Ecológicas, Rodovia Dom Pedro I, km 47, Caixa Postal 47, Nazaré Paulista SP, 12960-000, Brazil. [3]Post Office Box 402 Haverford, PA 19041, USA. [4]International Union for Conservation of Nature, IUCN, 28 Rue Mauverney, CH-1196 Gland, Switzerland. [5]Odum School of Ecology, University of Georgia, Athens, GA 30602, USA. [6]Microsoft Research, 21 Station Road, Cambridge, CB1 2FB, UK. [7]Missouri Botanical Garden, Post Office Box 299, St. Louis, MO 63166–0299, USA. [8]Environment Department, University of York, York, YO10 5DD, UK. [9]Global Land Cover Facility, Department of Geographical Sciences, University of Maryland, College Park, MD, 20742, USA.
*Corresponding author. E-mail: stuartpimm@me.com †Authors after the second are in alphabetical order.

should be concave, and its slope should approach λ (20, 21). This allows separate estimation of speciation and extinction rates.

Unfortunately, in the many studies McPeek (22) compiled, 80% of the LLT curves were convex, whence μ = 0. If currently recognized subspecies were to be considered as species, then a greater fraction of the LTT curves might be concave, making μ > 0. This suggests that taxonomic opinion plays a confounding role and one not easily resolved, whatever the underlying statistical models. The critical question is how large an extinction rate can go undetected by these methods. Generally, if it were large, then concave curves would predominate, but that falls short of providing quantification.

Third, data on net diversification, λ − μ, are widely available. Plants (23) have median diversification rates of 0.06 new species per species per million years, birds 0.15 (24), various chordates 0.2 (22), arthropods 0.17, (22), and mammals 0.07 (22). The rates for individual clades are only exceptionally >1. Valente *et al*. (25) specifically looked for exceptionally high rates, finding them >1 for the genus *Dianthus* (carnations, Caryophyllaceae), Andean *Lupinus* (lupins, Fabaceae), *Zosterops* (white-eyes, Zosteropidae), and cichlids in East African lakes.

There is no evidence for widespread, recent, but prehuman declines in diversity across most taxa, so extinction rates must be generally less than diversification rates. This matches the conclusion from phylogenetic studies that do not detect high extinction rates relative to speciation rates, and both lines of evidence are compatible with the fossil data. This suggests that 0.1 E/MSY is an order-of-magnitude estimate of the background rate of extinction.

Current Rates of Species Extinction

The International Union for Conservation of Nature (IUCN), in its Red List of Threatened Species, assesses species' extinction risk as Least Concern, Near-Threatened, three progressively escalating categories of Threatened species (Vulnerable, Endangered, and Critically Endangered), and Extinct (13). By March 2014, IUCN had assessed 71,576 mostly terrestrial and freshwater species: 860 were extinct or extinct in the wild; 21,286 were threatened, with 4286 deemed critically endangered (13). The percentages of threatened terrestrial species ran from 13% (birds) to 41% (amphibians and gymnosperms) (13). For freshwater taxa (26), threat levels span 23% (mammals and fishes) to 39% (reptiles).

Efforts are expanding the limited data from oceans for which only 2% of species are assessed compared with 3.6% of all known species (27). Peters *et al*. (28) assessed the snail genus *Conus*, Carpenter *et al*. (29) corals, and Dulvy *et al*. (30) 1041 shark and ray species. Overall, some 6041 marine species have sufficient data to assess risk: 16% are threatened and 9% near-threatened, most by overexploitation, habitat loss, and climate change (13).

The direct method of estimating extinction rates tracks changing status over time. Most changes in IUCN Red List categories result from improved knowledge, so the calculation of the Red List Index measures the aggregate extinction risk of all species in a given group, removing such nongenuine changes (31). Hoffmann *et al*. (32) showed that, on average, 52 of 22,000 species of mammals, birds, and amphibians moved one Red List category closer to extinction each year. If the probability of change between any two adjacent Red List categories were identical, this would yield an extinction rate of 450 E/MSY. The probability is lower for the transition from critically endangered to extinct (33), however, perhaps because the former receive disproportionate conservation attention.

Extinction rates from cohort analyses average about 100 E/MSY (Table 1). Local rates from regions can be much higher: 305 E/MSY for fish in North American rivers and lakes (34), 954 E/MSY for the region's freshwater gastropods (35), and likely >1000 E/MSY for cichlid fishes in Africa's Lake Victoria (36)

Studies of modern extinction rates typically do not address the rate of generic extinctions, but direct comparisons to fossils are possible. For mammals, the rate is ~100 extinctions of genera per million genera years (13) and ~60 extinctions for birds (13, 37).

How does incomplete taxonomic knowledge affect these estimates? Given that many species are still undescribed and many species with small ranges are recent discoveries, these numbers are surely underestimates. Many species will have gone or be going extinct before description (8, 15). Extinction rates of species described after 1900 are considerably higher than those described before, reflecting their greater rarity (Table 1). Moreover, a greater fraction of recently described species are critically endangered (Table 1). Rates of extinction and proportions of threatened species thus increase with improved knowledge. This warns us that estimates of recent extinction rates based on poorly known taxa (such as insects) may be substantial underestimates because many rare species are undescribed.

In sum, present extinction rates of ~100 E/MSY and the strong suspicion that these rates miss extinctions even for well-known taxa, and certainly for poorer known ones, means present extinction rates are likely a thousand times higher than the background rate of 0.1 E/MSY.

The Biogeography of Global Species Extinction

Human actions have eliminated top predators and other large-bodied species across most continents (38), and oceans are massively depleted of predatory fish (39). For example, African savannah ecosystems once covered ~13.5 million km^2. Only ~1 million km^2 now have lions, and much less area has viable populations of them (40). Recognizing the importance of such regional extirpations, we concentrate on the irreversible global species extinctions and now consider where they will occur.

General patterns—"laws" (41)—describe species' geographical distributions. First, small geographical ranges dominate. Gaston (42) suggests a lognormal distribution, although many taxa have more small-ranged species than even that skewed distribution (Fig. 1). In Fig. 1, 25% of most taxa have ranges $<10^5$ km^2 and, for amphibians, $<10^3$ km^2.

These sizes substantially overestimate actual ranges. Figure 1 assumes that, for plants, the presence in one of the 369 regions of the World Checklist of Selected Plant Families (WCSPF) (43) means the species occurs throughout the entire region. Similar, Fig. 1 assumes that the *Conus* species occur throughout the ocean within their geographical limits. These outer boundaries of the estimated ranges are too large. Of course, species are further limited to specific habitats within the outer boundaries of their ranges (44, 45).

A second law is that small-ranged species are generally locally scarcer than widespread ones (41). Combined, these two laws have consequences. First, unsurprisingly, taxonomists generally describe widespread and locally abundant species before small-ranged and locally scarce ones (46). Even for well-known vertebrates, taxonomists described over half the species in Brazil with ranges <20,000 km^2 after 1975 (47).

Second, since the majority of species are undescribed, one expects that samples from previously unexplored regions would contain a preponderance of them. Indeed, the fraction of undescribed species should provide estimates of how many species there are in total (11, 12). In practice, small

Table 1. Extinction rates calculated by cohort analysis and fractions of species that are critically endangered (CR). Data from (13, 37, 50, 51). Bird species thought to be "possibly extinct" are counted as extinctions.

When described	Species	Extinctions	Species-years	Extinction rate	CR	% CR
			Birds			
Before 1900	8922	89	1,812,897	49	123	1.4
1900 to present	1230	13	98,334	132	60	4.9
			Amphibians			
Before 1900	1437	14	212,348	66	37	2.6
1900 to present	4972	22	206,187	107	483	9.7
			Mammals			
Before 1900	2983	36	500,252	72	70	2.3
1900 to present	2523	43	176,858	243	126	5.0

samples across dispersed locations include widespread, common species and few rare ones. For example, in samples across ~6 million km^2 of Amazonian lowlands, a mere 227 species accounted for half the individual trees, suggesting that the Amazon might be floristically quite homogeneous. However, the samples contained 4962 known tree species, and many that could not be identified (*48*). The Amazon might contain as many as 16,000 species (*48*). Only accumulating species lists while quantifying sampling effort can provide compelling estimates of how diversity varies geographically and thus how many total species there are.

Uncertainties about where species are may be more limiting than not knowing how many species there are. The IUCN maps 43,000 species (*13*). Almost half are amphibians, birds, and mammals. The most common—but least informative map for conservation—is of species richness. Widely distributed species dominate these maps, whereas the majority of species with small ranges are almost invisible (fig. S1). An essential accompaniment maps out small-ranged species, such as the richness of species with less than the median range size (*49*) or, for coarsely defined regions, those endemic to each region. Figures 2 to 5 provide examples for mammals and amphibians (*13*, *50*, *51*), flowering plants (*43*), freshwater fish (*52*), and marine snails of the genus *Conus* (*28*). Supplementary materials provide details (*53*). There are similar maps for 845 reef-building coral species (*29*), coastal fish, various marine predators, and invertebrates (*54*, *55*).

Where there are the most species, one might expect the most species of all range sizes—large and small alike. Surprisingly, species with small ranges are geographically concentrated. The highest numbers of bird species live in the lowland Amazon, whereas small-ranged species concentrate in the Andes (fig. S1). Although mapped at a much coarser scale, freshwater fish also often attain their highest diversities in large rivers flowing through forests. A striking exception is the high numbers in East African rift lakes (Fig. 4). The Philippines have the greatest number of *Conus* species; the concentrations of small-ranged species are elsewhere (Fig. 5). Other marine taxa are similar (*55*).

Many past extinctions have been on islands, but current patterns of threat are geographically much broader (*49*, *56*). Rare species—either widespread but scarce (such as top predators and other large-bodied animals) or with small geographical ranges and so often locally scarce (*41*)—dominate the lists. Species with small ranges are disproportionately more likely to be threatened than those with larger ones (*49*, *57*). Interestingly, for a given range size, a smaller fraction of island species are threatened than for those on continents, likely because island species are locally more abundant (*49*).

Concentrations of threatened species more closely match concentrations of small-ranged species than they do total species numbers and so are more informative about where currently threatened species live and where species may become threatened in the future (*49*, *50*) (Fig. 2 and fig. S1).

Myers *et al.* (*58*) made the vital and separate point that habitat destruction is greatest where the highest concentrations of small-ranged species live. As it were, small-ranged species are born vulnerable and then have the greater threats thrust upon them. Myers *et al.*'s hotspot definition combines a minimum number of small-ranged plant species and sufficiently high habitat loss.

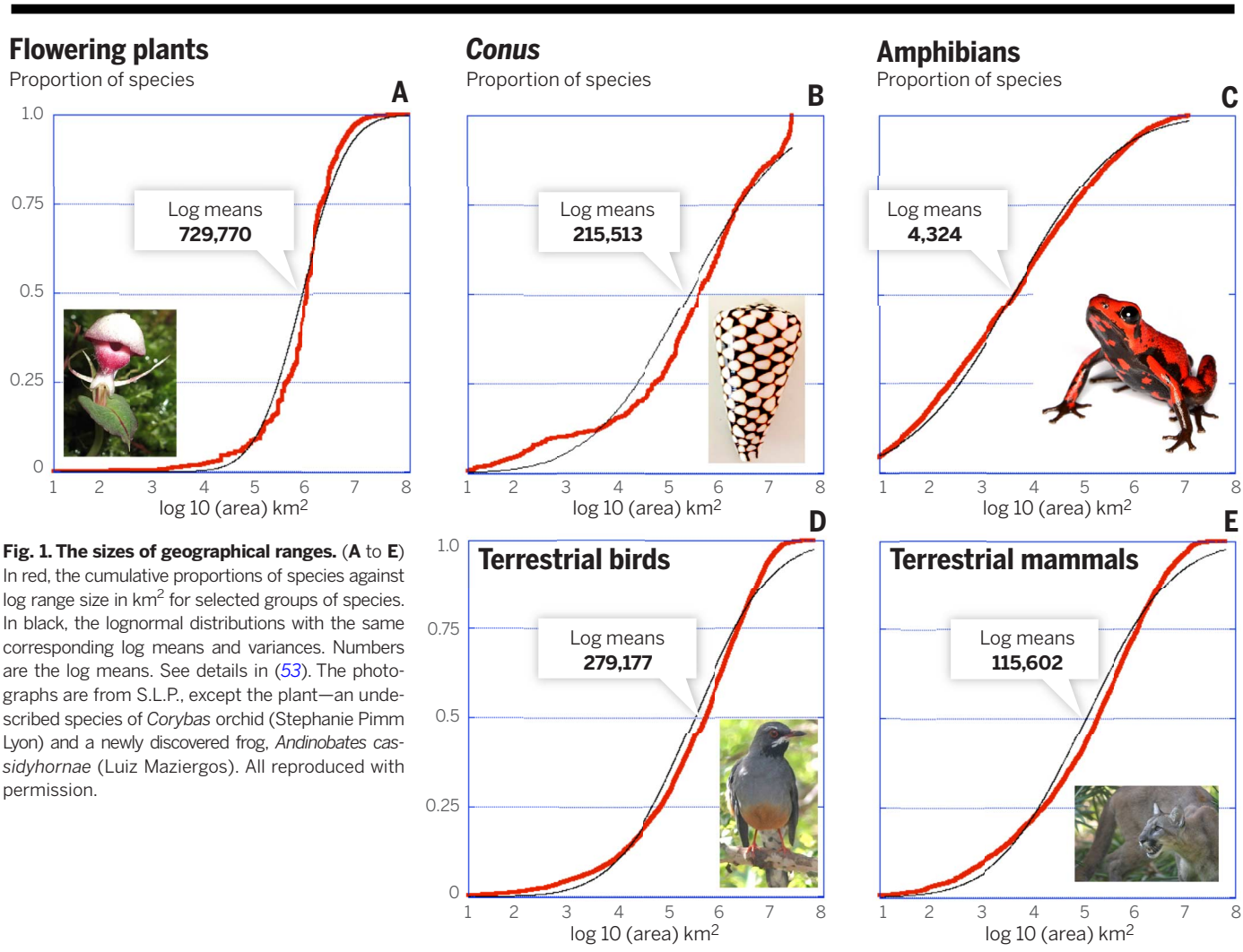


Fig. 1. The sizes of geographical ranges. (**A** to **E**) In red, the cumulative proportions of species against log range size in km^2 for selected groups of species. In black, the lognormal distributions with the same corresponding log means and variances. Numbers are the log means. See details in (*53*). The photographs are from S.L.P., except the plant—an undescribed species of *Corybas* orchid (Stephanie Pimm Lyon) and a newly discovered frog, *Andinobates cassidyhornae* (Luiz Maziergos). All reproduced with permission.

Quantitative data from the WCSPF (43) have clarified these areas (59).

Future Rates of Species Extinction

The overarching driver of species extinction is human population growth and increasing per capita consumption. How long these trends continue—where and at what rate—will dominate the scenarios of species extinction and challenge efforts to protect biodiversity.

Before the last decade, most applications developed extinction scenarios from simple assumptions of land use change as a primary driver of biodiversity loss, employing the species-area relationship (14). For example, Pimm and Raven (60) projected 18% extinction by 2100 due to deforestation to date in tropical forest hotspots and 40% extinction if these regions retained natural habitat only in currently protected areas.

Until recently, these scenarios were the only empirically validated models. The validations focused on vertebrates, globally (61) or regionally: eastern United States (62), South American Atlantic Forest (63), and insular Southeast Asia (64). There was excellent correspondence between the numbers of species predicted to go extinct and those that did (62) or, for more recent deforestation, with those threatened (61, 63, 64). There are discussions about the underlying theory of such estimates (65). Nonetheless, when one counts all the extinctions likely to follow deforestation (66), these estimates are conservative. Theory predicts that many more extinctions are possible with severe habitat fragmentation (67), as observations confirm (68).

Pereira *et al.*'s review of projected future extinctions (69) classified and compared various models. Strikingly, the six sets of projections predicted a hundred-fold range of extinction rates. This emerged from the different drivers considered (land use change, climate change, or both), model approaches, taxonomic coverage, and geographic scale. Given this range, there is an urgent need for validation of projections against documented extinctions to date. Few studies attempt this. Here, we consider the prospects for such validation with newly available data that can reduce the uncertainties.

Climate disruption will cause species extinctions, but the range of estimates is large. Thomas *et al.* (70) estimated that 15 to 37% of various taxa would be committed to extinction by 2050 for a mid-range warming scenario. Specific studies for birds estimated that >400 species of land birds out of 8750 studied (4.6%) would experience a range reduction greater than 50% by year 2050 (71). For Western Hemisphere land birds, intermediate extinction estimates based on projected climate-induced changes in current distributions ranged from 1.3% (1.1°C warming) to 30% (6.4°C warming) of the 3349 species studied (72). A global assessment of expected warming-induced range contractions estimated that 184 to 327 montane bird species (out of 1009) would lose >50% of their range and result in range sizes of <20,000 km^2 (73).

Cheung *et al.* (74) used a global climate model to predict range shifts, extinction, and invasion intensities based on ocean warming up to 2050 for 1066 species of exploited marine fish and invertebrates. They predicted that poleward range movements would lead to species' extinctions from tropical and subpolar latitudes of 4 and 7% respectively, with mostly range readjustments in between. They attribute the lower extinction probabilities than on land (70) to greater freedom of movement in the sea. Enclosed seas, like the Mediterranean, could trap clusters of endemic species against insurmountable barriers (75). Nor did they consider any other potential extinction drivers, such as ocean acidification (76), overfishing (30), or the inability of sessile species—such as brooding corals—to move.

On land, the effects of climate disruption remain unclear for several reasons. A key uncertainty is whether climate disruption and habitat destruction harm overlapping sets of species or broadly different ones—and they may act synergistically. Climate disruption seems to be an added threat (77). Some studies explicitly combine species-area projections of species loss to incorporate climate change as a driver, via models of changing global vegetation (78), and suggest that 12% of species will become extinct. Other studies estimate that 7 to 24% of plant species (79) will become extinct. The impacts

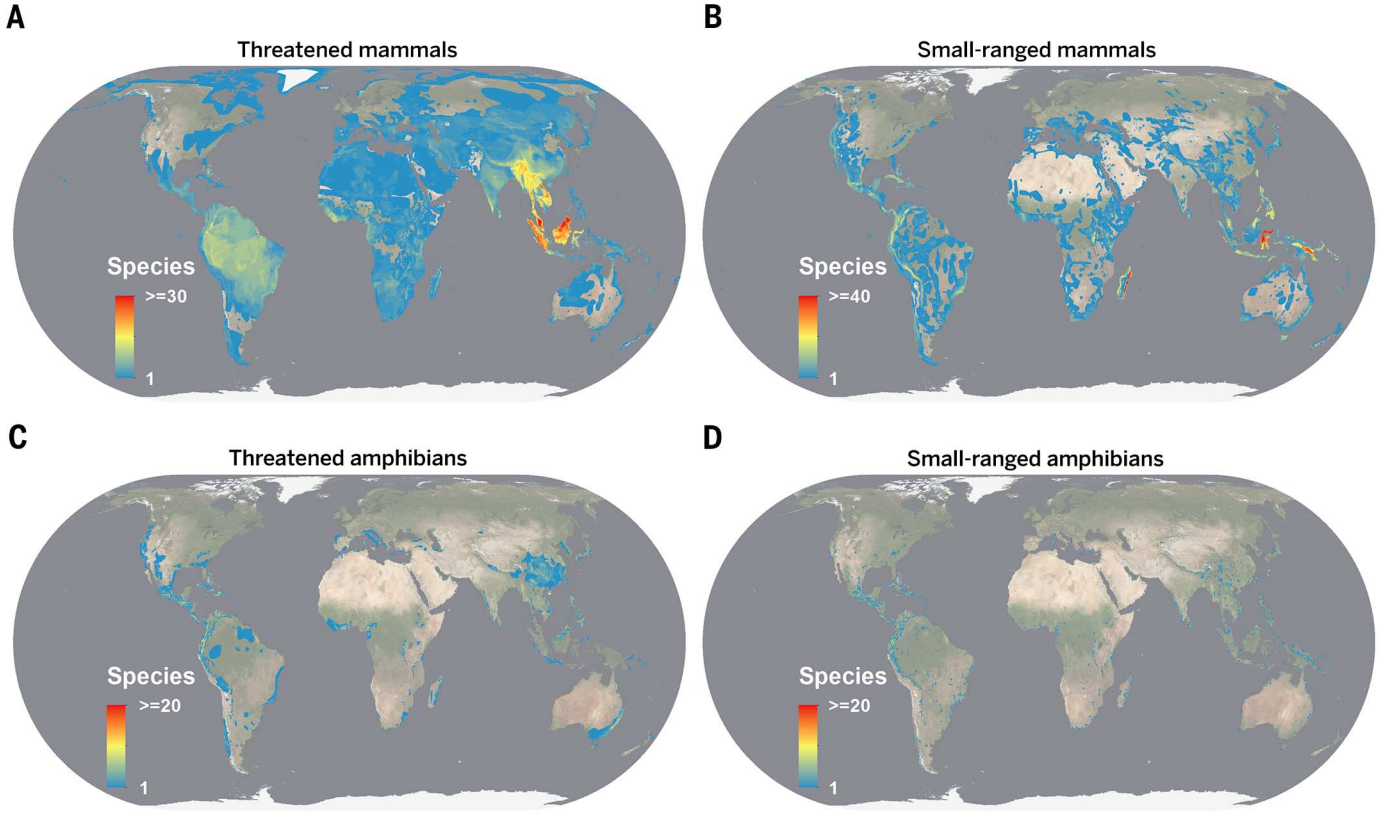


Fig. 2. Fine-scale patterns of terrestrial vertebrate diversity. (**A**) The numbers of threatened mammal species and (**B**) those with ranges smaller than the median range size. (**C**) and (**D**) show the corresponding maps for amphibians. See details in (53).

of climate disruption are complex. A meta-analysis compared 188 predicted with 130 observed climate change responses and suggested that 10 to 14% of species would become extinct (*80*). Moreover, the interactions of environmental drivers with intrinsic biological traits (e.g., geographic range, body size, and reproductive rate) indicate that species' responses to increased human population density will become increasingly uncertain (*81*).

Another uncertainty is that none of Pereira *et al.*'s (*69*) models assessed population viability and habitat suitability. Rather, they take indirect approaches, such as some fraction of their present range, as in (*70*). Approaches incorporating viability provide strong empirical foundations for estimating extinction risk (*82*). Some regional studies have employed them, however, including a study of South African Proteaceae (*83*).

Above all, there are few empirical tests. The above methods assume species moving poleward, to higher elevations, or to deeper depths to remain in their climate envelopes. Using fortuitous repeats of surveys done decades ago, diverse studies find substantial lags in upslope movements for plants (*84*), insects (*85*), and birds (*86*). These question the fate of species now living outside past climate envelopes. Furthermore, the few studies that consider predictions of changing geographical ranges from the past to the present and then calibrate them against present ranges do not always find compelling matches (*87*).

For freshwater species, direct and indirect habitat modification, including pollution (*88*) and the already extensive and continuing fragmentation and flow regulation of rivers (*89*), are clearly major drivers of extinction, especially for species with limited dispersal abilities. Existing alterations to freshwater systems may already have compromised species' viability to the extent that no level of future protection might prevent extinction (*90*).

Introduced species, including diseases, are a major cause of extinctions and the main cause of recent bird extinctions (*37*). Some 10% of plant species are endemic to islands small enough for introduced herbivores to be a major threat (*59*). We know of no estimates of extinction rates from introduced species. Such extinctions can unfold quickly and unpredictably, as the destruction of Guam's endemic avifauna by an introduced snake (*91*) and the destruction and possible extinction, primarily by the Nile perch, of as many as 200 Lake Victoria haplochromine cichlids demonstrate (*36*).

In sum, there are few empirically tested predictions of future extinctions. Typical scenarios consider what can be predicted—extinctions from deforestation or climate disruption—but not potentially important processes—disease, introduced species, or hydrological changes—that one cannot easily model.

How Will Protection Slow Extinction Rates?

Among the many uncertainties in projecting future extinction rates, a particularly important one is the effect that conservation actions might have in reducing them (*92*). For instance, the rate at which mammals, birds, and amphibians have slid toward extinction over the past four decades would have been 20% higher were it not for conservation efforts (*32*).

The destruction of natural habitats is the major threat to species (*13*). Thus, protected areas, while diverse and differing substantially in their purposes and levels of protection (*93*), are essential to reducing extinctions. Aichi Target 11 seeks the protection of >17% "ecologically representative" terrestrial and freshwater ecosystems and >10% of coastal and marine ecosystems (*2*), whereas CBD's Global Strategy for Plant Conservation (GSPC) Target 4 seeks >15% of "each ecological region or vegetation type" (*94*).

In 2009, 12.9% of the total land area was under some legal protection, up from <4% in 1985 (*95*). Protected areas are biased toward areas where there is little human pressure (*96*). Coverage varies between 4% and 25% protection of 14 major terrestrial biomes (*96*). Of the world's 821 terrestrial ecoregions, half had <10% of their area protected (*96*).

How well these areas capture species within their boundaries now and in the future is an essential input to predict future extinction rates (*50*, *60*). Rodrigues *et al.* (*97*) analyzed threatened mammal, bird, amphibian, and turtle ranges combined with the World Database on Protected Areas (*93*). Overall, 27% of threatened amphibians, 20% of threatened birds, 14% of threatened mammals, and 10% of threatened turtles live outside protected areas. Subsequent analyses have set targets for representation scaled in inverse proportion to range size (*98*)—for example, 100% representation for species with ranges <1000 km^2, 10% representation for ranges >250,000 km^2, and a linear interpolation for species in between. Only ~46% of birds, ~39% of mammals, and ~19% of amphibians reach or exceed their targets (*98*).

These global gap analyses are vulnerable to commission errors—species appearing to occur when they do not—resulting from the overlay of the coarse-resolution species maps with the high-resolution protected area boundaries (*99*). These can generate a false sense of security:

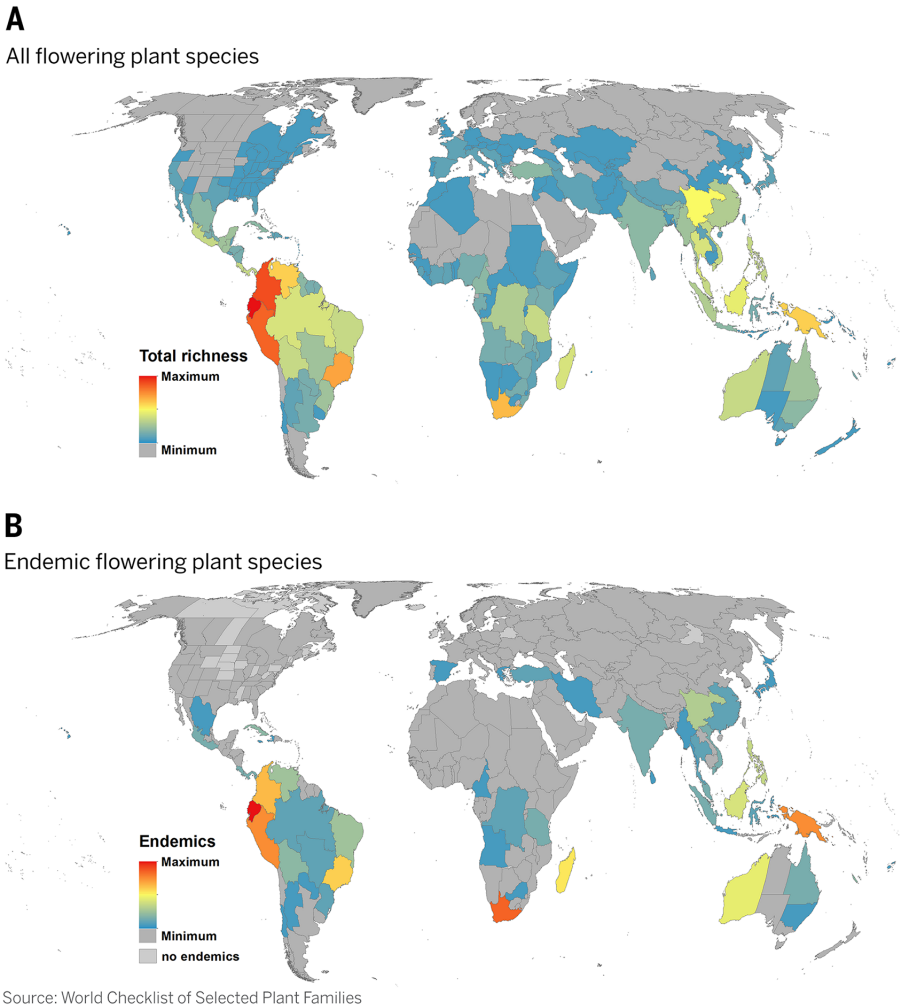


Fig. 3. Relative numbers of flowering plant species in the different regions used by the World Checklist of Selected Plant Families (*43*). (**A**) All species and (**B**) endemic species. See details in (*53*).

Species thought safely represented may be going extinct. Alternative approaches that accept higher omission errors, although less efficient, are less problematic. Thus, for birds, protected areas cover only 49% of sites documented to hold the entire population of at least one highly threatened species (*56*) and only 51% of globally important sites for birds (*100*).

Do protected areas work? Certainly, some fail completely: Even large national parks in West Africa have lost lions and many of their prey (*40*). For freshwater species populations, occurrence within reserves is no guarantee of protection, given external threats like flow modification and lack of explicit reserve management to meet freshwater objectives (*101*). Protected forests generally retain their forest cover (*102*), have far fewer anthropogenic fires than unprotected areas (*103*), and do not attract higher than expected human population growth to their perimeters (*104*). Most studies do not assess plant and animal populations directly, and remaining habitats are often too small, or too heavily exploited, to retain all of their species (*105*). Those that do track species reveal that protected areas deliver substantial outcomes for preventing extinctions. Globally, species with >50% of the sites of particular importance for them protected are sliding toward extinction only half as rapidly as those with <50% of their important sites protected (*100*).

Ocean protection lags behind that on land. A 2013 assessment (*106*) reported ~10,000 marine protected areas (MPAs) covering 2.3% of the oceans. Aichi Target 11 admits "other effective area-based conservation measures," so this assessment included large fishery management zones closed to certain fishing gears, including some in New England, Florida, and New Zealand. These were not established for biodiversity conservation and, in the New Zealand case, were proposed by the deep-sea fishing industry, avoiding places important for fishing (*106*). A more conservative assessment (*107*) estimates 1.8% global coverage.

As on land, marine protected area coverage is uneven. Reserves are often absent where threats to biodiversity are highest, such as fishing grounds and oil and gas leases. Beyond the 200 nautical mile limits of national jurisdiction, 0.17% of open waters are protected, compared with 8% of continental shelves (*106*). Coastal coral reefs are the best protected, with 18.7% within protected areas by 2006 (*108*). Only 2% were in MPAs considered to be of adequate size, management, level of protection, and connectivity, however. Moves to establish large and remote sites as MPAs, such as the U.K.'s British Indian Ocean Territory, have contributed strongly to recent growth in protection, suggesting that the Aichi target of 10% coverage may be attainable (*109*). Marine protected areas that are no-take, well-enforced, old, large, and isolated by deep water or sand are disproportionately successful in retaining their species (*110*).

Aichi Target 11 seeks protection of 17% of terrestrial lands (*2*), whereas the GSPC seeks to protect 60% of plant species (*94*). Are both targets possible simultaneously? The concentration of small-ranged species is such that were land protected efficiently to capture biodiversity, the 17% so selected would encompass part of the ranges of 81% of plant species and all the ranges of 67% (*59*). How might the prediction that 15% more plant species are currently undescribed change these selections? Joppa *et al.* (*111*) used rates of species' description corrected for taxonomic effort and predicted that undescribed species will be in the known concentrations of species with small ranges, leaving current priorities unchanged.

These plant priorities match those for terrestrial vertebrates. Some 89% of bird species, 80% of amphibians, and 74% of mammals live within these plant priority areas (*59*). Percentages for species with ranges smaller than the median are 88%, 82%, and 73%, respectively (*59*). With updated data, these results capture Myers *et al.*'s (*58*) observation that conserving a large fraction of species is possible in limited areas if authorities choose protected areas cognizant of what species they contain (*112*). Areas of high freshwater fish diversity match some areas of high terrestrial diversity, but such congruence cannot be assumed: Exceptions include the high-diversity freshwater systems of the Ganges and Mekong deltas (*113*) (Fig. 4.) Moreover, protecting freshwater species will require managing landscapes and water use beyond reserves' fence lines and well into larger catchments (*101*).

What We Know, What We Do Not, and How to Fix the Gaps

We know enough to see that our ignorance about species' numbers, distributions, and status strongly affects key biodiversity statistics. Two examples illustrate the consequences. First, ~20% of known plants are thought threatened (*114*). Adding the predicted 15% of undescribed species—almost all will be rare and in places with extensive habitat loss (*36*)—suggests that 30% of plant species are threatened (*6*). Climate disruption threatens additional species.

Second, only 6.5% of the 632 *Conus* species are threatened. Another 14% are "Data Deficient"—there is insufficient information to assess their status, typically because they are rare and have small geographical ranges (*28*). Were better knowledge to deem them threatened, the map of where threatened species occur would change substantially (Fig. 5). Investment in extending

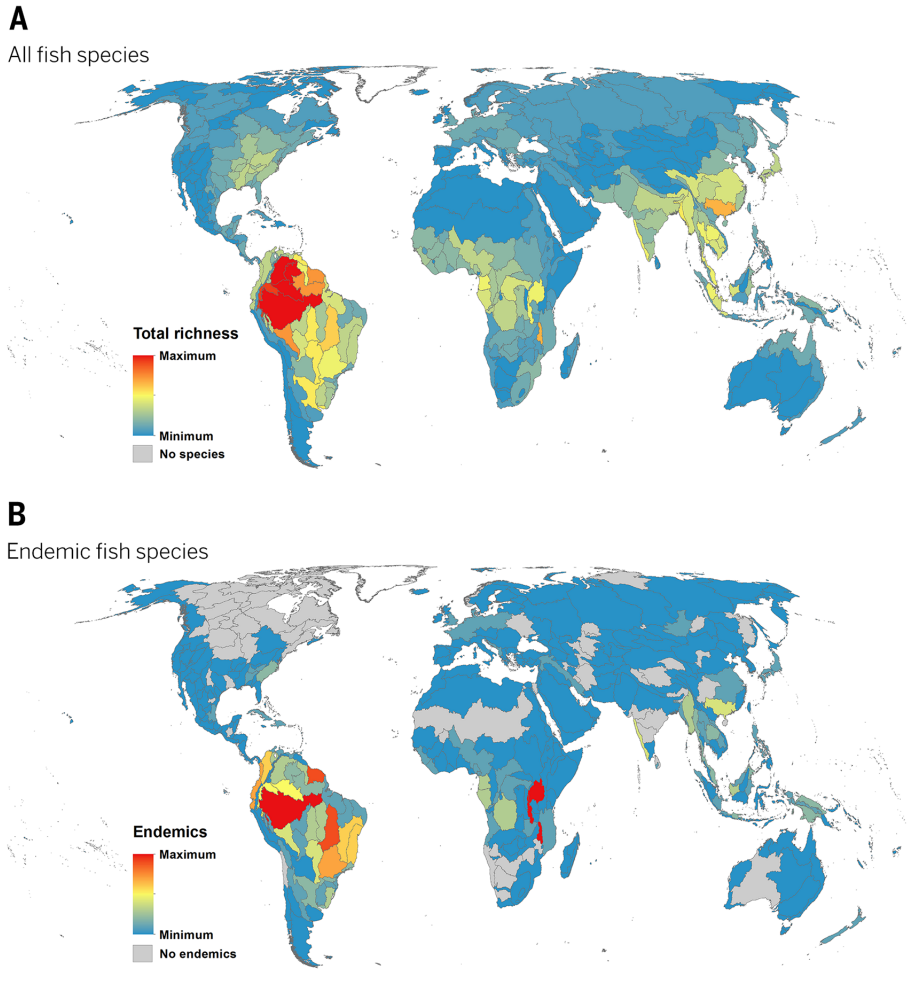


Fig. 4. Relative numbers of freshwater fish species in the different freshwater ecoregions (*52*). (**A**) All species and (**B**) endemic species. See details in (*53*).

the coverage of the IUCN Red List to its target of 160,000 species assessments is a priority (*115*).

What is the progress toward getting better knowledge, and what are the prospects for continued improvements? Aichi Target 19 calls for data to be "widely shared." Recent online efforts toward this goal include the Global Biodiversity Information Facility (GBIF) (*116*), with 420 million records and 1.45 million species' and subspecies' names, and the Ocean Biogeographic Information System (*117*), with 38 million records of 115,000 species. Species 2000 seeks to create a validated checklist of all species, and the Tree of Life (*118*) and TimeTree (*119*) provide phylogenetic relationships.

Communities of taxonomists now address the tedious but vital issue of synonymy and placing their lists and taxonomic decisions into the public domain. Large databases include the World Register of Marine Species (*120*), which has checked 95% of 221,000 marine species, and FishBase, with 32,700 species of fish (*121*). WCSPF (*43*) has currently assessed ~110,000 plant species (*5*).

New technologies help. Genetic barcoding (*122*) offers the potential to identify animal species quickly for US$1 per sample from a small, but unique, DNA sequence. Barcoding for plants is slightly more difficult. For the great majority of unknown species in animal taxa with few taxonomic specialists, this will surely become the predominant method of discovering new species. It raises the controversial idea that many species may become known by a number derived from barcoding and not—or not only—from conventional descriptions (*123*). The potential to find new species and untangle clusters of cryptic species (*124*) is also being realized. Less appreciated is that cost-effective barcoding by batches of species is now possible. Powerful new statistical methods (*125*) estimate how many species may be present in an area and how these overlap with other samples from increasing sampling efforts. Combined with batch barcoding, there is the promise of rigorous estimates of what fractions of undescribed species are present in poorly sampled areas—the most direct way of estimating how many species there are.

Even for species that are mapped, substantial uncertainties remain. The highest apparent numbers of vertebrate species in South America (fig. S1) are close to research centers, as are many GBIF records. The most important consequence of having a public species' range map is that it challenges observers to confirm or amend it.

Although GBIF (*116*) is the repository for information into which other sources feed, the diversity of those sources merits comment. They include professional organizations, such as Tropicos (*126*), with 4.2 million specimens. The fastest growth in understanding species' distributions comes from large numbers of amateurs. Birdwatchers are most numerous: eBird (*127*) became an international depository in 2010 and already has >100,000 observers and >100 million observations. It permits fine-scale mapping and month-by-month changes in distribution. Such wealth of data skews broad biodiversity assessments (*128*), motivating efforts for less popular taxa.

To be useful, observations require identifications, and identifying organisms requires training and skill. Recent advances in photo-sharing technology and social networking provide new opportunities. Apps like iNaturalist (*129*) allow division of labor between amateur observers uploading mystery field observations from smartphones and skilled identifiers who later catalog these observations from the photos provided. Cooperation between amateurs and experts now produces high volumes of quality data for diverse taxa. iNaturalist has already logged over half a million records and become the preferred app for incorporating crowd-sourced data into national biodiversity surveys in Mexico and elsewhere. The Reef Life Survey is generating similar advances for marine biodiversity (*130*).

Crowd-sourced data, especially when including data on sampling effort, provide substantial opportunities to monitor a broad range of species over time and across broad geographical areas—exactly the requirements needed to assess the various scenarios for future extinction.

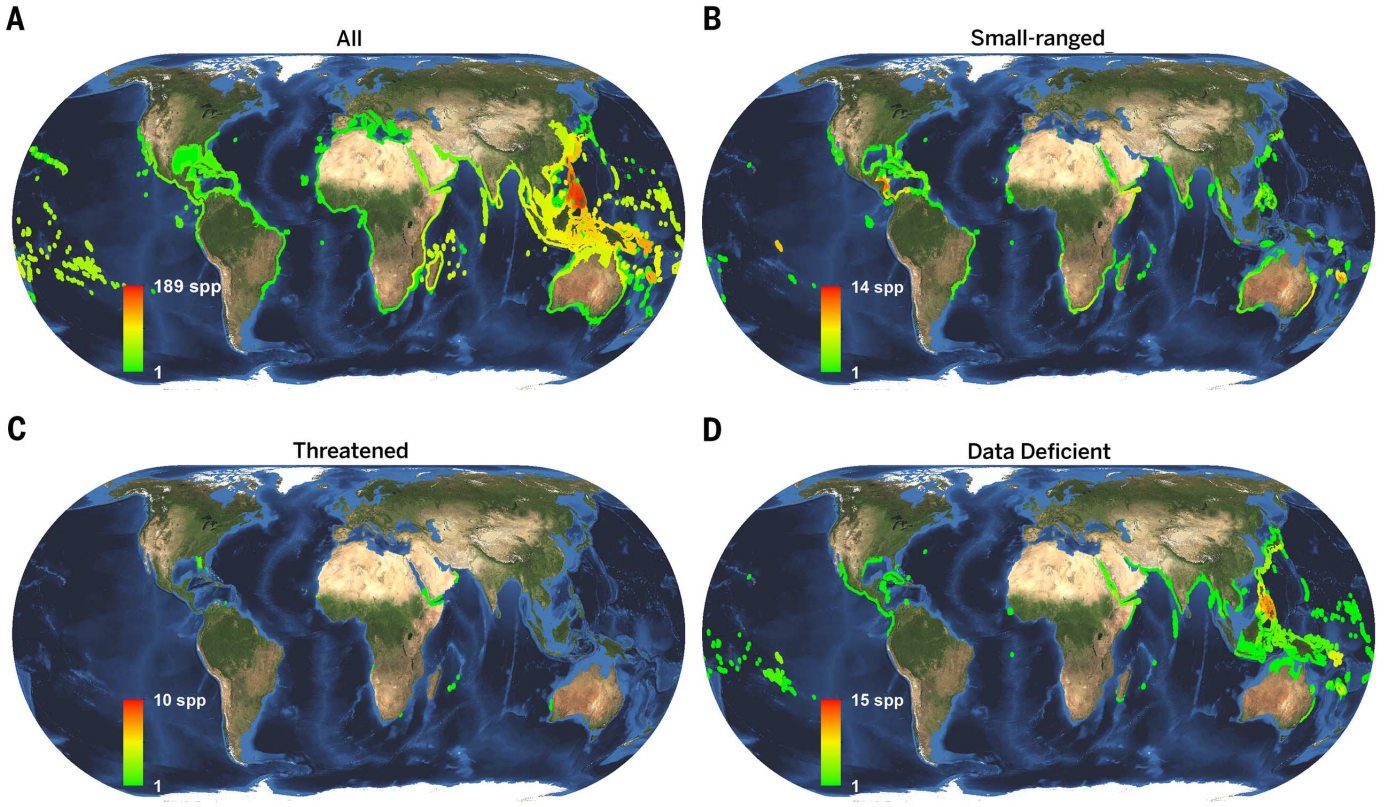


Fig. 5. The distribution of species in the marine snail genus *Conus*. (**A**) The numbers of all species; (**B**) those with ranges smaller than the median range size; (**C**) those threatened; and (**D**) data-deficient species for which there is insufficient data to assess their status. Figure S2 provides a detail of the Cape Verde islands, where a large number of small-ranged species live. The terrestrial background is shown in approximately true color to show the distribution of forests (dark green) and drylands (buff) and oceanic bathymetry (darker colors mean deeper water). See details in (*53*).

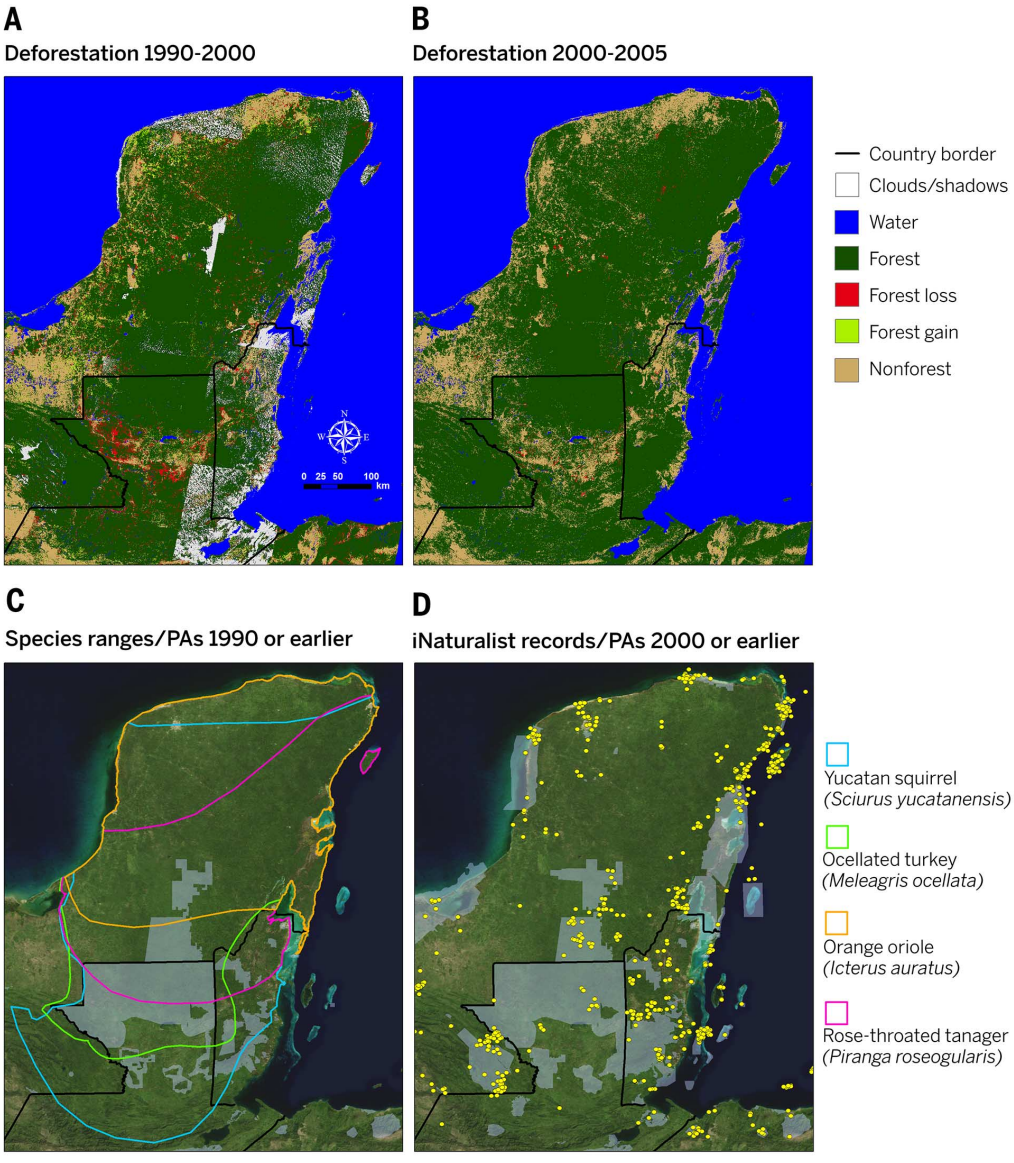


Fig. 6. Combining databases to assess the changing status of biodiversity. Maps (**A**) and (**B**) show land cover change in the Yucatan peninsula of Central America. Forest-cover data for 2000 to 2005 available at www.landcover.org/data/landsatFCC. Although protected areas increased over time, there was extensive deforestation in lowland Guatemala from 1990 to 2000 (shown in red), some of it in protected areas. Forest loss slowed from 2000 to 2005. (**C**) Deforestation has reduced and fragmented the ranges of four exemplar species endemic to the Yucatan. (**D**) All iNaturalist records from this area. See details in (*53*).

The numbers and kinds of online databases have increased dramatically in recent years and will continue to do so. Global estimates of land cover from remote sensing [e.g., (*131*)] diversified with the 2009 opening of the U.S. Geological Survey Landsat archive and subsequent efforts to collect and calibrate global repositories of Landsat images going back to the early 1970s (*132*, *133*).

Even more promising is combining data sources. Studies now permit detailed assessments of the current status of species by trimming available range maps using remotely sensed estimates of elevation and remaining habitats (*134*) and connecting directly to metapopulation models of fragmented ranges (*45*). Figure 6 provides an example of the extent to which species' ranges have been lost and fragmented by deforestation—and when this happened. It also shows where forest remains outside of protected areas, how it has been lost from within them, and the potential of crowd-sourced data to monitor species' distributions.

Combining such sources anticipates an ability to assess biodiversity continuously and provide a template onto which crowd-sourced data could validate predictions of changing species' distributions. Global biodiversity monitoring can now move to combining databases of increasing scope and certainty at regular intervals. These coming advances will increasingly enable scientists and policy-makers to understand the status, trends, and threats to Earth's biodiversity and to act accordingly to protect it.

REFERENCES AND NOTES

1. Intergovernmental Platform on Biodiversity and Ecosystem Services (2014); http://www.ipbes.net/images/documents/IPBES_1_12_En.pdf.
2. Strategic Plan for Biodiversity 2011–2020 (2014); http://www.cbd.int/sp/targets/.
3. E. A. Norse *et al.*, *Conserving Biological Diversity in our National Forests* (Wilderness Society, Washington, 1986).
4. R. M. May, How many species are there on Earth? *Science* **241**, 1441–1449 (1988). doi: 10.1126/science.241.4872.1441; pmid: 17790039
5. A. J. Paton, From working list to online flora of all known plants: Looking forward with hindsight 1. *Ann. Mo. Bot. Gard.* **99**, 206–213 (2013). doi: 10.3417/2011115
6. L. N. Joppa, D. L. Roberts, S. L. Pimm, How many species of flowering plants are there? *Proc. Biol. Sci.* **278**, 554–559 (2011). doi: 10.1098/rspb.2010.1004; pmid: 20610425
7. A. D. Chapman, *Numbers of Living Species in Australia and the World* (Biodiversity Information Services, Toowoomba, Australia, 2009).
8. M. J. Costello, R. M. May, N. E. Stork, Can we name Earth's species before they go extinct? *Science* **339**, 413–416 (2013). doi: 10.1126/science.1230318; pmid: 23349283
9. C. Mora, D. P. Tittensor, S. Adl, A. G. B. Simpson, B. Worm, How many species are there on Earth and in the ocean? *PLOS Biol.* **9**, e1001127 (2011). doi: 10.1371/journal.pbio.1001127; pmid: 21886479
10. P. H. Raven, D. K. Yeates, Australian biodiversity: threats for the present, opportunities for the future. *Aust. J. Entomol.* **46**, 177–187 (2007). doi: 10.1111/j.1440-6055.2007.00601.x
11. B. R. Scheffers, L. N. Joppa, S. L. Pimm, W. F. Laurance, What we know and don't know about Earth's missing biodiversity. *Trends Ecol. Evol.* **27**, 501–510 (2012). doi: 10.1016/j.tree.2012.05.008; pmid: 22784409
12. W. Appeltans *et al.*, The magnitude of global marine species diversity. *Curr. Biol.* **22**, 2189–2202 (2012). doi: 10.1016/j.cub.2012.09.036; pmid: 23159596
13. International Union for the Conservation of Nature (2014); http://www.iucnredlist.org..
14. S. L. Pimm, G. J. Russell, J. L. Gittleman, T. M. Brooks, The future of biodiversity. *Science* **269**, 347–350 (1995). doi: 10.1126/science.269.5222.347; pmid: 17841251
15. S. Pimm, P. Raven, A. Peterson, Ç. H. Şekercioğlu, P. R. Ehrlich, Human impacts on the rates of recent, present, and future bird extinctions. *Proc. Natl. Acad. Sci. U.S.A.* **103**, 10941–10946 (2006). doi: 10.1073/pnas.0604181103; pmid: 16829570
16. A. D. Barnosky *et al.*, Has the Earth's sixth mass extinction already arrived? *Nature* **471**, 51–57 (2011). doi: 10.1038/nature09678; pmid: 21368823
17. G. J. Russell, T. M. Brooks, M. M. McKinney, C. G. Anderson, Present and future taxonomic selectivity in bird and mammal extinctions. *Conserv. Biol.* **12**, 1365–1376 (1998). doi: 10.1046/j.1523-1739.1998.96332.x
18. J. Alroy, Constant extinction, constrained diversification, and uncoordinated stasis in North American mammals. *Palaeogeogr. Palaeoclimatol. Palaeoecol.* **127**, 285–311 (1996). doi: 10.1016/S0031-0182(96)00100-9
19. P. G. Harnik *et al.*, Extinctions in ancient and modern seas. *Trends Ecol. Evol.* **27**, 608–617 (2012). doi: 10.1016/j.tree.2012.07.010; pmid: 22889500
20. S. Nee, E. C. Holmes, R. M. May, P. H. Harvey, Extinction rates can be estimated from molecular phylogenies. *Philos. Trans. R. Soc. London Ser. B* **344**, 77–82 (1994). doi: 10.1098/rstb.1994.0054; pmid: 8878259

21. D. L. Rabosky, Extinction rates should not be estimated from molecular phylogenies. *Evolution* **64**, 1816–1824 (2010). doi: 10.1111/j.1558-5646.2009.00926.x; pmid: 20030708
22. M. A. McPeek, The ecological dynamics of clade diversification and community assembly. *Am. Nat.* **172**, E270–E284 (2008). doi: 10.1086/593137; pmid: 18851684
23. M. M. Ferrer, S. V. Good, Self-sterility in flowering plants: preventing self-fertilization increases family diversification rates. *Ann. Bot.* **110**, 535–553 (2012). doi: 10.1093/aob/mcs124; pmid: 22684683
24. A. B. Phillimore, T. D. Price, Density-dependent cladogenesis in birds. *PLOS Biol.* **6**, e71 (2008). doi: 10.1371/journal.pbio.0060071; pmid: 18366256
25. L. M. Valente, V. Savolainen, P. Vargas, Unparalleled rates of species diversification in Europe. *Proc. Biol. Sci.* **277**, 1489–1496 (2010). doi: 10.1098/rspb.2009.2163; pmid: 20106850
26. B. Collen *et al*., Global patterns of freshwater species diversity, threat and endemism. *Glob. Ecol. Biogeogr.* **23**, 40–51 (2014). doi: 10.1111/geb.12096
27. Global Marine Species Assessment (2014); http://www.sci.odu.edu/gmsa/index.html.
28. H. Peters, B. C. O'Leary, J. P. Hawkins, K. E. Carpenter, C. M. Roberts, *Conus*: First comprehensive conservation Red List assessment of a marine gastropod mollusc genus. *PLOS ONE* **8**, e83353 (2013). doi: 10.1371/journal.pone.0083353; pmid: 24376693
29. K. E. Carpenter *et al*., One-third of reef-building corals face elevated extinction risk from climate change and local impacts. *Science* **321**, 560–563 (2008). doi: 10.1126/science.1159196; pmid: 18653892
30. N. K. Dulvy *et al*., Extinction risk and conservation of the world's sharks and rays. *eLife* **3**, e00590–e00590 (2014). doi: 10.7554/eLife.00590; pmid: 24448405
31. S. H. M. Butchart *et al*., Measuring global trends in the status of biodiversity: Red List indices for birds. *PLOS Biol.* **2**, e383 (2004). doi: 10.1371/journal.pbio.0020383; pmid: 15510230
32. M. Hoffmann *et al*., The impact of conservation on the status of the world's vertebrates. *Science* **330**, 1503–1509 (2010). doi: 10.1126/science.1194442; pmid: 20978281
33. M. L. Brooke *et al*., Rates of movement of threatened bird species between IUCN Red List categories and toward extinction. *Conserv. Biol.* **22**, 417–427 (2008). doi: 10.1111/j.1523-1739.2008.00905.x; pmid: 18402584
34. N. M. Burkhead, Extinction rates in North American freshwater fishes, 1900-2010. *Bioscience* **62**, 798–808 (2012). doi: 10.1525/bio.2012.62.9.5
35. P. D. Johnson *et al*., Conservation status of freshwater gastropods of Canada and the United States. *Fisheries (Bethesda, Md.)* **38**, 247–282 (2013). doi: 10.1080/03632415.2013.785396
36. F. Witte *et al*., The destruction of an endemic species flock: Quantitative data on the decline of the haplochromine cichlids of Lake Victoria. *Environ. Biol. Fishes* **34**, 1–28 (1992). doi: 10.1007/BF00004782
37. Birdlife International (2014); http://www.birdlife.org.
38. G. Ceballos, P. R. Ehrlich, Mammal population losses and the extinction crisis. *Science* **296**, 904–907 (2002). doi: 10.1126/science.1069349; pmid: 11988573
39. R. A. Myers, B. Worm, Rapid worldwide depletion of predatory fish communities. *Nature* **423**, 280–283 (2003). doi: 10.1038/nature01610; pmid: 12748640
40. J. Riggio *et al*., The size of savannah Africa: A lion's (*Panthera leo*) view. *Biodivers. Conserv.* **22**, 17–35 (2013). doi: 10.1007/s10531-012-0381-4
41. S. Pimm, C. Jenkins, Extinctions and the practice of preventing them. *Conservation Biology for All* **1**, 181–199 (2010). doi: 10.1093/acprof:oso/9780199554232.003.0011
42. K. J. Gaston, Species-range-size distributions: patterns, mechanisms and implications. *Trends Ecol. Evol.* **11**, 197–201 (1996). doi: 10.1016/0169-5347(96)10027-6; pmid: 21237808
43. World Checklist of Selected Plant Families (2014). Facilitated by the Royal Botanic Gardens, Kew; http://apps.kew.org/wcsp/.
44. M. Almeida-Gomes, M. L. Lorini, C. F. D. Rocha, M. V. Vieira, Underestimation of extinction threat to stream-dwelling amphibians due to lack of consideration of narrow area of occupancy. *Conserv. Biol.* **28**, 616–619 (2014). doi: 10.1111/cobi.12196; pmid: 24372858
45. J. K. Schnell, G. M. Harris, S. L. Pimm, G. J. Russell, Quantitative analysis of forest fragmentation in the Atlantic Forest reveals more threatened bird species than the current Red List. *PLOS ONE* **8**, e65357 (2013). doi: 10.1371/journal.pone.0065357; pmid: 23734248
46. B. Collen, A. Purvis, J. Gittleman, Biological correlates of description date in carnivores and primates. *Glob. Ecol. Biogeogr.* **13**, 459–467 (2004). doi: 10.1111/j.1466-822X.2004.00121.x
47. S. Pimm, C. Jenkins, L. Joppa, D. Roberts, G. Russell, How many endangered species remain to be discovered in brazil? *Natureza Conservação* **8**, 71–77 (2010). doi: 10.4322/natcon.00801011
48. H. ter Steege *et al*., Hyperdominance in the Amazonian tree flora. *Science* **342**, 1243092 (2013). doi: 10.1126/science.1243092; pmid: 24136971
49. L. L. Manne, T. M. Brooks, S. L. Pimm, Relative risk of extinction of passerine birds on continents and islands. *Nature* **399**, 258–261 (1999). doi: 10.1038/20436
50. J. Schipper *et al*., The status of the world's land and marine mammals: Diversity, threat, and knowledge. *Science* **322**, 225–230 (2008). doi: 10.1126/science.1165115; pmid: 18845749
51. S. N. Stuart *et al*., Status and trends of amphibian declines and extinctions worldwide. *Science* **306**, 1783–1786 (2004). doi: 10.1126/science.1103538; pmid: 15486254
52. R. Abell *et al*., Freshwater ecoregions of the world: A new map of biogeographic units for freshwater biodiversity conservation. *Bioscience* **58**, 403–414 (2008). doi: 10.1641/B580507
53. Materials and methods are available as supplementary materials on *Science* Online.
54. D. P. Tittensor *et al*., Global patterns and predictors of marine biodiversity across taxa. *Nature* **466**, 1098–1101 (2010). doi: 10.1038/nature09329; pmid: 20668450
55. C. M. Roberts *et al*., Marine biodiversity hotspots and conservation priorities for tropical reefs. *Science* **295**, 1280–1284 (2002). doi: 10.1126/science.1067728; pmid: 11847338
56. T. H. Ricketts *et al*., Pinpointing and preventing imminent extinctions. *Proc. Natl. Acad. Sci. U.S.A.* **102**, 18497–18501 (2005). doi: 10.1073/pnas.0509060102; pmid: 16344485
57. M. Cardillo *et al*., The predictability of extinction: Biological and external correlates of decline in mammals. *Proc. Biol. Sci.* **275**, 1441–1448 (2008). doi: 10.1098/rspb.2008.0179; pmid: 18367443
58. N. Myers, R. A. Mittermeier, C. G. Mittermeier, G. A. B. da Fonseca, J. Kent, Biodiversity hotspots for conservation priorities. *Nature* **403**, 853–858 (2000). doi: 10.1038/35002501; pmid: 10706275
59. L. N. Joppa, P. Visconti, C. N. Jenkins, S. L. Pimm, Achieving the convention on biological diversity's goals for plant conservation. *Science* **341**, 1100–1103 (2013). doi: 10.1126/science.1241706; pmid: 24009391
60. S. L. Pimm, P. Raven, Biodiversity: Extinction by numbers. *Nature* **403**, 843–845 (2000). doi: 10.1038/35002708; pmid: 10706267
61. T. M. Brooks *et al*., Habitat loss and extinction in the hotspots of biodiversity. *Conserv. Biol.* **16**, 909–923 (2002). doi: 10.1046/j.1523-1739.2002.00530.x
62. S. L. Pimm, R. A. Askins, Forest losses predict bird extinctions in eastern North America. *Proc. Natl. Acad. Sci. U.S.A.* **92**, 9343–9347 (1995). doi: 10.1073/pnas.92.20.9343; pmid: 11607581
63. T. Brooks, A. Balmford, Atlantic forest extinctions. *Nature* **380**, 115 (1996). doi: 10.1038/380115a0
64. T. M. Brooks, S. L. Pimm, N. J. Collar, Deforestation predicts the number of threatened birds in insular Southeast Asia. *Conserv. Biol.* **11**, 382–394 (1997). doi: 10.1046/j.1523-1739.1997.95493.x
65. S. L. Pimm, T. Brooks, Conservation: Forest fragments, facts, and fallacies. *Curr. Biol.* **23**, R1098–R1101 (2013). doi: 10.1016/j.cub.2013.10.024; pmid: 24355786
66. T. M. Brooks, Extinctions: Consider all species. *Nature* **474**, 284–284 (2011). doi: 10.1038/474284b; pmid: 21677730
67. I. Hanski, G. A. Zurita, M. I. Bellocq, J. Rybicki, Species-fragmented area relationship. *Proc. Natl. Acad. Sci. U.S.A.* **110**, 12715–12720 (2013). doi: 10.1073/pnas.1311491110; pmid: 23858440
68. L. Gibson *et al*., Near-complete extinction of native small mammal fauna 25 years after forest fragmentation. *Science* **341**, 1508–1510 (2013). doi: 10.1126/science.1240495; pmid: 24072921
69. H. M. Pereira *et al*., Scenarios for global biodiversity in the 21st century. *Science* **330**, 1496–1501 (2010). doi: 10.1126/science.1196624; pmid: 20978282
70. C. D. Thomas *et al*., Extinction risk from climate change. *Nature* **427**, 145–148 (2004). doi: 10.1038/nature02121; pmid: 14712274
71. W. Jetz, D. S. Wilcove, A. P. Dobson, Projected impacts of climate and land-use change on the global diversity of birds. *PLOS Biol.* **5**, e157 (2007). doi: 10.1371/journal.pbio.0050157; pmid: 17550306
72. C. H. Sekercioglu, S. H. Schneider, J. P. Fay, S. R. Loarie, Climate change, elevational range shifts, and bird extinctions. *Conserv. Biol.* **22**, 140–150 (2008). doi: 10.1111/j.1523-1739.2007.00852.x; pmid: 18254859
73. F. A. La Sorte, W. Jetz, Avian distributions under climate change: Towards improved projections. *J. Exp. Biol.* **213**, 862–869 (2010). doi: 10.1242/jeb.038356; pmid: 20190111
74. W. W. Cheung *et al*., Projecting global marine biodiversity impacts under climate change scenarios. *Fish Fish.* **10**, 235–251 (2009). doi: 10.1111/j.1467-2979.2008.00315.x
75. F. Ben Rais Lasram *et al*., The Mediterranean Sea as a 'cul-de-sac'for endemic fishes facing climate change. *Glob. Change Biol.* **16**, 3233–3245 (2010). doi: 10.1111/j.1365-2486.2010.02224.x
76. L. M. Parker *et al*., Predicting the response of molluscs to the impact of ocean acidification. *Biology* **2**, 651–692 (2013). doi: 10.3390/biology2020651
77. S. L. Pimm, Biodiversity: Climate change or habitat loss—Which will kill more species? *Curr. Biol.* **18**, R117–R119 (2008). doi: 10.1016/j.cub.2007.11.055; pmid: 18269905
78. J. R. Malcolm, C. Liu, R. P. Neilson, L. Hansen, L. Hannah, Global warming and extinctions of endemic species from biodiversity hotspots. *Conserv. Biol.* **20**, 538–548 (2006). doi: 10.1111/j.1523-1739.2006.00364.x; pmid: 16903114
79. D. P. van Vuuren, O. E. Sala, H. M. Pereira, The future of vascular plant diversity under four global scenarios. *Ecol. Soc.* **11**, 25–42 (2006).
80. I. M. Maclean, R. J. Wilson, Recent ecological responses to climate change support predictions of high extinction risk. *Proc. Natl. Acad. Sci. U.S.A.* **108**, 12337–12342 (2011). doi: 10.1073/pnas.1017352108; pmid: 21746924
81. M. Cardillo, G. M. Mace, J. L. Gittleman, A. Purvis, Latent extinction risk and the future battlegrounds of mammal conservation. *Proc. Natl. Acad. Sci. U.S.A.* **103**, 4157–4161 (2006). doi: 10.1073/pnas.0510541103; pmid: 16537501
82. B. W. Brook *et al*., Predictive accuracy of population viability analysis in conservation biology. *Nature* **404**, 385–387 (2000). doi: 10.1038/35006050; pmid: 10746724
83. B. Bomhard *et al*., Potential impacts of future land use and climate change on the Red List status of the Proteaceae in the Cape Floristic Region, South Africa. *Glob. Change Biol.* **11**, 1452–1468 (2005). doi: 10.1111/j.1365-2486.2005.00997.x
84. K. J. Feeley *et al*., Upslope migration of Andean trees. *J. Biogeogr.* **38**, 783–791 (2011). doi: 10.1111/j.1365-2699.2010.02444.x
85. I.-C. Chen *et al*., Elevation increases in moth assemblages over 42 years on a tropical mountain. *Proc. Natl. Acad. Sci. U.S.A.* **106**, 1479–1483 (2009). doi: 10.1073/pnas.0809320106; pmid: 19164573
86. G. Forero-Medina, J. Terborgh, S. J. Socolar, S. L. Pimm, Elevational ranges of birds on a tropical montane gradient lag behind warming temperatures. *PLOS ONE* **6**, e28535 (2011). doi: 10.1371/journal.pone.0028535; pmid: 22163309
87. M. B. Araújo, C. Rahbek, Ecology. How does climate change affect biodiversity? *Science* **313**, 1396–1397 (2006). doi: 10.1126/science.1131758; pmid: 16959994
88. I. J. Harrison, M. L. Stiassny, in *Extinctions in Near Time*. R. D. E. MacPhee, Ed. (Springer, New York 1999), pp. 271–331.
89. C. Nilsson, C. A. Reidy, M. Dynesius, C. Revenga, Fragmentation and flow regulation of the world's large river systems. *Science* **308**, 405–408 (2005). doi: 10.1126/science.1107887; pmid: 15831757
90. D. L. Strayer, D. Dudgeon, Freshwater biodiversity conservation: Recent progress and future challenges. *J. N. Am. Benthol. Soc.* **29**, 344–358 (2010). doi: 10.1899/08-171.1
91. J. A. Savidge, Extinction of an island forest avifauna by an introduced snake. *Ecology* **68**, 660–668 (1987). doi: 10.2307/1938471
92. A. Waldron *et al*., Targeting global conservation funding to limit immediate biodiversity declines. *Proc. Natl. Acad. Sci. U.S.A.* **110**, 12144–12148 (2013). doi: 10.1073/pnas.1221370110; pmid: 23818619
93. IUCN and UNEP, The World Database on Protected Areas (WDPA) (*United Nations Environment Programme* World Conservation Monitoring Centre, Cambridge, UK, 2014). http://www.protectedplanet.net.
94. Global Strategy for Plant Conservation, http://www.cbd.int/gspc/targets.shtml.

95. C. N. Jenkins, L. Joppa, Expansion of the global terrestrial protected area system. *Biol. Conserv.* **142**, 2166–2174 (2009). doi: 10.1016/j.biocon.2009.04.016
96. L. N. Joppa, A. Pfaff, High and far: Biases in the location of protected areas. *PLOS ONE* **4**, e8273 (2009). doi: 10.1371/journal.pone.0008273; pmid: 20011603
97. A. S. L. Rodrigues *et al*., Effectiveness of the global protected area network in representing species diversity. *Nature* **428**, 640–643 (2004). doi: 10.1038/nature02422; pmid: 15071592
98. L. Cantú-Salazar, C. D. L. Orme, P. C. Rasmussen, T. M. Blackburn, K. J. Gaston, The performance of the global protected area system in capturing vertebrate geographic ranges. *Biodivers. Conserv.* **22**, 1033–1047 (2013). doi: 10.1007/s10531-013-0467-7
99. C. Rondinini, K. A. Wilson, L. Boitani, H. Grantham, H. P. Possingham, Tradeoffs of different types of species occurrence data for use in systematic conservation planning. *Ecol. Lett.* **9**, 1136–1145 (2006). doi: 10.1111/j.1461-0248.2006.00970.x; pmid: 16972877
100. S. H. M. Butchart *et al*., Protecting important sites for biodiversity contributes to meeting global conservation targets. *PLOS ONE* **7**, e32529 (2012). doi: 10.1371/journal.pone.0032529; pmid: 22457717
101. B. C. Chessman, Do protected areas benefit freshwater species? A broad-scale assessment for fish in Australia's Murray–Darling Basin. *J. Appl. Ecol.* **50**, 969–976 (2013). doi: 10.1111/1365-2664.12104
102. L. N. Joppa, S. R. Loarie, S. L. Pimm, On the protection of "protected areas". *Proc. Natl. Acad. Sci. U.S.A.* **105**, 6673–6678 (2008). doi: 10.1073/pnas.0802471105; pmid: 18451028
103. J. M. Adeney, N. L. Christensen, S. L. Pimm, Reserves protect against deforestation fires in the Amazon. *PLOS ONE* **4**, e5014 (2009). doi: 10.1371/journal.pone.0005014; pmid: 19352423
104. L. N. Joppa, S. R. Loarie, S. L. Pimm, On population growth near protected areas. *PLOS ONE* **4**, e4279 (2009). doi: 10.1371/journal.pone.0004279; pmid: 19169358
105. D. S. Wilkie, E. L. Bennett, C. A. Peres, A. A. Cunningham, The empty forest revisited. *Ann. N. Y. Acad. Sci.* **1223**, 120–128 (2011). doi: 10.1111/j.1749-6632.2010.05908.x; pmid: 21449969
106. M. Spalding, I. Meliane, A. Milam, C. Fitzgerald, L. Hale, Protecting marine spaces: Global targets and changing approaches. *Ocean Yearb.* **27**, 213–248 (2013). doi: 10.1163/22116001-90000160
107. MPAtlas, http://www.MPAtlas.com.
108. C. Mora *et al*., Coral reefs and the global network of Marine Protected Areas. *Science* **312**, 1750–1751 (2006). doi: 10.1126/science.1125295; pmid: 16794065
109. R. J. Toonen *et al*., One size does not fit all: The emerging frontier in large-scale marine conservation. *Mar. Pollut. Bull.* **77**, 7–10 (2013). doi: 10.1016/j.marpolbul.2013.10.039; pmid: 24246654
110. G. J. Edgar *et al*., Global conservation outcomes depend on marine protected areas with five key features. *Nature* **506**, 216–220 (2014). doi: 10.1038/nature13022; pmid: 24499817
111. L. N. Joppa, D. L. Roberts, N. Myers, S. L. Pimm, Biodiversity hotspots house most undiscovered plant species. *Proc. Natl. Acad. Sci. U.S.A.* **108**, 13171–13176 (2011). doi: 10.1073/pnas.1109389108; pmid: 21730155
112. A. Pino-Del-Carpio, A. H. Ariño, A. Villarroya, J. Puig, R. Miranda, The biodiversity data knowledge gap: Assessing information loss in the management of Biosphere Reserves. *Biol. Conserv.* (2013). doi: 10.1016/j.biocon.2013.11.020
113. R. Abell *et al*., Concordance of freshwater and terrestrial biodiversity. *Conserv. Lett.* **4**, 127–136 (2011). doi: 10.1111/j.1755-263X.2010.00153.x
114. N. Brummitt, S. P. Bachman, J. Moat, Applications of the IUCN Red List: Towards a global barometer for plant diversity. *Endanger. Species Res.* **6**, 127–135 (2008). doi: 10.3354/esr00135
115. S. N. Stuart, E. O. Wilson, J. A. McNeely, R. A. Mittermeier, J. P. Rodríguez, The barometer of life. *Science* **328**, 177 (2010). doi: 10.1126/science.1188606; pmid: 20378803
116. Global Biodiversity Information Facility (2014); http://www.gbif.org.
117. The Ocean Biogeographic Information System, Intergovernmental Oceanographic Commission of UNESCO (2014); http://www.iobis.org.
118. Tree of Life (2014); http://www.tolweb.org/tree/phylogeny.html.
119. TimeTree (2014); http://www.timetree.org.
120. World Register of Marine Species (2014); http://www.marinespecies.org.
121. Fishbase (2014); http://www.fishbase.org.
122. P. D. Hebert, A. Cywinska, S. L. Ball, J. R. deWaard, Biological identifications through DNA barcodes. *Proc. Biol. Sci.* **270**, 313–321 (2003). doi: 10.1098/rspb.2002.2218; pmid: 12614582
123. S. Ratnasingham, P. D. Hebert, A DNA-based registry for all animal species: The barcode index number (BIN) system. *PLOS ONE* **8**, e66213 (2013). doi: 10.1371/journal.pone.0066213; pmid: 23861743
124. P. D. N. Hebert, E. H. Penton, J. M. Burns, D. H. Janzen, W. Hallwachs, Ten species in one: DNA barcoding reveals cryptic species in the neotropical skipper butterfly *Astraptes fulgerator*. *Proc. Natl. Acad. Sci. U.S.A.* **101**, 14812–14817 (2004). doi: 10.1073/pnas.0406166101; pmid: 15465915
125. A. Chao, R. L. Chazdon, R. K. Colwell, T. J. Shen, A new statistical approach for assessing similarity of species composition with incidence and abundance data. *Ecol. Lett.* **8**, 148–159 (2005). doi: 10.1111/j.1461-0248.2004.00707.x
126. TROPICOS (2014); http://www.tropicos.org.
127. eBird (2014); http://www.ebird.org.
128. S. Gaiji *et al*., Content assessment of the primary biodiversity data published through GBIF network: Status, challenges and potentials. *Biodiversity Informatics* **8**, 94–172 (2013).
129. iNaturalist (2014); http://www.inaturalist.org.
130. Reef Life Survey (2014); http://reeflifesurvey.com.
131. J. O. Sexton *et al*., Global, 30-m resolution continuous fields of tree cover: Landsat-based rescaling of MODIS vegetation continuous fields with lidar-based estimates of error. *Int. J. Digit. Earth* **6**, 427–448 (2013). doi: 10.1080/17538947.2013.786146
132. J. R. Townshend *et al*., Global characterization and monitoring of forest cover using Landsat data: Opportunities and challenges. *Int. J. Digit. Earth* **5**, 373–397 (2012). doi: 10.1080/17538947.2012.713190
133. J. O. Sexton, D. L. Urban, M. J. Donohue, C. Song, Long-term land cover dynamics by multi-temporal classification across the Landsat-5 record. *Remote Sens. Environ.* **128**, 246–258 (2013). doi: 10.1016/j.rse.2012.10.010
134. G. Harris, S. L. Pimm, Range size and extinction risk in forest birds. *Conserv. Biol.* **22**, 163–171 (2008). doi: 10.1111/j.1523-1739.2007.00798.x; pmid: 18254861

ACKNOWLEDGMENTS

We thank A. Ariño, J. A. Drake, M. A. Fisher, S. Loarie, E. Norse, and P. R. Stephens for comments. The original data for this paper are in public archives from BirdLife International (*37*), IUCN (*13*), WCSPF (*43*), and the World Conservation Monitoring Centre (*94*). We thank those responsible for access to them and especially the many professionals and amateurs who collected them. NASA's Making Earth System Data Records for Use in Research Environments (MEaSUREs) (NNH06ZDA001N) and Land Cover and Land Use Change (NNH07ZDA001N-LCLUC) programs provided forest cover data. We thank the World Checklist of Selected Plant Families. The Brazilian agency CAPES, through the Ciência Sem Fronteiras program, supports C.N.J. M. Thieme, P. Petry, and C. Revenga co-led the synthesis of the freshwater fish data. Additional biodiversity maps are at www.biodiversitymapping.org.

SUPPLEMENTARY MATERIALS

www.sciencemag.org/content/344/6187/1246752/suppl/DC1
Materials and Methods
Figs. S1 and S2
References (*135*, *136*)

10.1126/science.1246752

RESEARCH ARTICLES

MOLECULAR MAGNETISM

Reaching the magnetic anisotropy limit of a 3*d* metal atom

Ileana G. Rau,[1]* Susanne Baumann,[1,2]* Stefano Rusponi,[3] Fabio Donati,[3] Sebastian Stepanow,[4] Luca Gragnaniello,[3] Jan Dreiser,[3,5] Cinthia Piamonteze,[5] Frithjof Nolting,[5] Shruba Gangopadhyay,[1] Oliver R. Albertini,[1,6] Roger M. Macfarlane,[1] Christopher P. Lutz,[1] Barbara A. Jones,[1] Pietro Gambardella,[4]† Andreas J. Heinrich,[1]† Harald Brune[3]†

Designing systems with large magnetic anisotropy is critical to realize nanoscopic magnets. Thus far, the magnetic anisotropy energy per atom in single-molecule magnets and ferromagnetic films remains typically one to two orders of magnitude below the theoretical limit imposed by the atomic spin-orbit interaction. We realized the maximum magnetic anisotropy for a 3*d* transition metal atom by coordinating a single Co atom to the O site of an MgO(100) surface. Scanning tunneling spectroscopy reveals a record-high zero-field splitting of 58 millielectron volts as well as slow relaxation of the Co atom's magnetization. This striking behavior originates from the dominating axial ligand field at the O adsorption site, which leads to out-of-plane uniaxial anisotropy while preserving the gas-phase orbital moment of Co, as observed with x-ray magnetic circular dichroism.

Magnetic anisotropy (MA) provides directionality and stability to magnetization. Strategies to scale up the MA of ferromagnetic 3*d* metals have relied on introducing heavy elements within or next to the ferromagnet in order to enhance the spin-orbit coupling energy. Rare-earth transition-metal alloys, such as TbCoFe (*1*), and binary multilayers, such as Co/Pt and Co/Pd (*2*), are used as magnetic recording materials because of their large perpendicular MA (*3*). Recent experiments, however, have shown that Co and Fe thin films deposited on metallic oxides such as AlO_x and MgO present MA energies on the order of 1 meV/atom (*4*, *5*), which is similar to that of Co/Pt interfaces but driven by the electronic hybridization between the metal 3*d* and O 2*p* orbitals (*6*, *7*). Perpendicular magnetic tunnel junctions, including CoFeB/MgO layers, are being intensively investigated for nonvolatile MRAM (magnetic random access memory) applications (*5*, *8*, *9*), in which the lateral dimensions of a magnetic bit approach 20 nm (*10*).

A fundamental constraint to the downscaling of magnetic devices is the total amount of MA energy that can be induced in the storage layer, which limits its thermal stability factor and influences the rate of magnetization switching (*11*). As the dimensions of a magnetic bit shrink to the atomic scale, quantum-mechanical excitation and relaxation effects, which greatly affect the magnetization, can come into play. We explore the limit of how much MA can be stored in an atom and for how long it can retain a given spin state in a model system of a single Co atom bound to an MgO layer. We show that this "bit" achieves the maximum possible MA energy for a 3*d* metal. This MA limit is ~60 meV, set by the atomic spin-orbit coupling strength times the unquenched orbital angular momentum. We measured spin relaxation times on the order of 200 μs at 0.6 K and show that the rate-limiting relaxation step for a Co atom is determined by the mixing of excited spin states into the ground state induced by nonaxial ligand field components.

Magnetic Anisotropy in Quantum Systems

The microscopic origin of MA is the combined effect of the anisotropy in the atom's orbital angular momentum (**L**), together with the interaction between **L** and the atom's spin angular momentum (**S**). This interaction is given by $H_{SOC} = \lambda \mathbf{L}\cdot\mathbf{S}$, where λ is the atomic spin-orbit coupling parameter. In solids and molecules, **L** tends to align along specific symmetry directions, set by the spatial dependence of the ligand field. The strength of the MA is defined here by the so-called zero-field splitting (ZFS) (*12*), which is the energy difference between the electronic ground state and the first excited state that has its spin pointing in a different direction with respect to the ground state, in the absence of an external field. For spin-flip transitions that leave **L** unchanged, the ZFS is thus proportional to λL, where λ is ~−22 meV for Co (*13*). However, in most magnetic compounds the orbital moment magnitude *L* is either quenched or strongly diminished by ligand field (*14*) and hybridization (*15*) effects, leading to MA energies on the order of 0.01 meV/atom in bulk magnets and up to ~1 meV/atom in thin films (*16*) and nanostructures (*17*). Achieving large ZFS

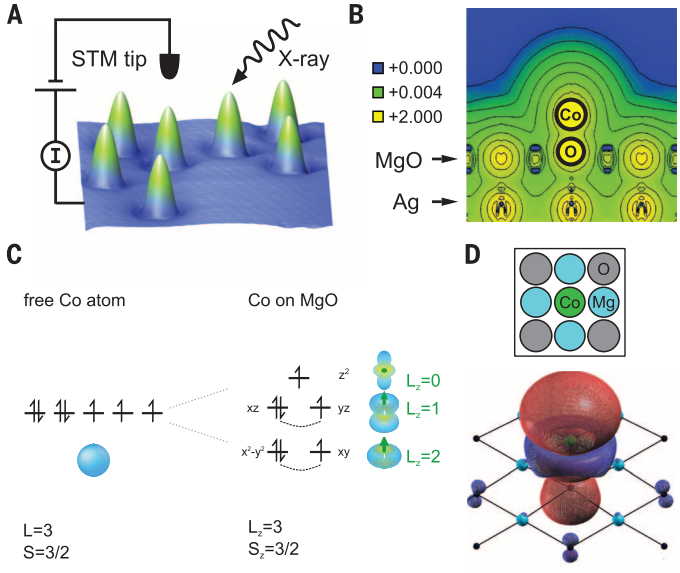


Fig. 1. Co on MgO films. (**A**) Constant current STM image of seven Co atoms on 1 ML of MgO on Ag(100) at T = 1.2 K (10 pA, 50 mV, 7.5 nm × 7.5 nm). Shown are schematic diagrams of STM (left) and XAS (right). (**B**) DFT-calculated structure and valence electron charge density of one Co atom atop an O atom in 1 ML MgO on Ag(100). Charge density color scale is in atomic units. (**C**) Schematic model of the orbital occupancy of Co in a free atom (left), in its ^4F term (L = 3, S = 3/2), and Co on the MgO surface (right). The orbital moment is preserved along the easy-axis of the Co in this cylindrical ligand field (L_Z = 3, S_Z = 3/2). (**D**) Top view of ball model of the atomic structure (top) and DFT calculation of the Co atom spin density of the valence electrons (bottom). Oblique view shows contours of constant positive (red) and negative (blue) spin polarization.

[1]IBM Almaden Research Center, 650 Harry Road, San Jose, CA 95120, USA. [2]Department of Physics, University of Basel, Klingelbergstrasse 82, CH-4056 Basel, Switzerland. [3]Institute of Condensed Matter Physics, Ecole Polytechnique Fédérale de Lausanne (EPFL), Station 3, CH-1015 Lausanne, Switzerland. [4]Department of Materials, Eidgenössische Technische Hochschule (ETH) Zürich, Hönggerbergring 64, CH-8093 Zürich, Switzerland. [5]Swiss Light Source, Paul Scherrer Institute, CH-5232 Villigen PSI, Switzerland. [6]Department of Physics, Georgetown University, 3700 O Street NW, Washington, DC 20057, USA.
*These authors contributed equally to this work. †Corresponding author. E-mail: andreash@us.ibm.com (A.J.H.); pietro.gambardella@mat.ethz.ch (P.G.); harald.brune@epfl.ch (H.B.)

in transition metals requires somehow breaking the spatial symmetry of the atomic wavefunctions without quenching the orbital magnetization. The most promising strategy to preserve the large L of a free atom and induce uniaxial anisotropy is to use low-coordination geometries, as shown for atoms deposited on the threefold coordinated sites of a (111) surface (*18*, *19*) and molecular complexes and crystals with two-coordinate metal species (*20*–*24*). This strategy, if specific conditions are met, can be brought to its limit by coordinating one magnetic atom to a single substrate atom.

We achieved this extreme by using cobalt, which has $L = 3$, the highest in the transition metal series, and a thin film of MgO as a substrate with a onefold ("atop") coordinated site for adsorbed transition metal atoms (*25*). Co atoms were deposited on a single MgO layer grown on Ag(100) (*26*–*28*). They appear as protrusions that are 0.15 ± 0.02 nm high when imaged with scanning tunneling microscopy (STM) (Fig. 1A). The preferred binding site, determined with density functional theory (DFT), is on top of oxygen (Fig. 1B) (*26*) with four Mg atoms as neighbors, resulting in C_{4v} symmetry. Despite the presence of these four Mg atoms, the spin density of the valence electrons of the Co is rotationally symmetric around z (effectively $C_{\infty v}$) (Fig. 1D). This axial coordination can preserve the orbital moment of the free atom along the vertical axis but quench it in-plane (Fig. 1C). The DFT density of states of the Co d-levels (Fig. 2) shows that the interaction with the Mg atoms is weak and the Co $d_{x^2-y^2}$, d_{xy} orbitals remain largely degenerate. The dominant bond is between the out-of-plane d orbitals of Co and p orbitals of O, resulting in an uniaxial ligand field along z. DFT calculations further indicate that the Co atom is charge-neutral and has spin magnitude S = 1.39 ± 0.05.

Measurement of the ZFS with STM

We used inelastic electron tunneling spectroscopy (IETS) (*19*, *29*–*32*) to probe the quantum spin states of the Co atoms (*26*). In such a measurement, electrons tunneling from the STM tip may transfer energy and angular momentum to a magnetic atom and induce spin-flip excitations above a threshold voltage. The IETS spectrum of a Co atom on 1 monolayer (ML) MgO at 0.6 K is shown in Fig. 3A. We observed a sudden stepwise increase in conductance at ±57.7 mV, symmetric around zero bias, as expected for an inelastic excitation. The dI/dV step is magnetic in origin and splits into two in an applied magnetic field (Fig. 3, B and C). For ease of discussion, we begin by approximating the magnetic state of the Co atom as an S = 3/2 system with uniaxial anisotropy (later in the paper, we will include the effects of configuration mixing and the presence of large orbital moment). We assign these excitations to transitions between the ground (S_z = ±3/2, labeled as states 0 and 1 in Fig. 3D) and excited states (S_z = ±1/2, states 2 and 3). At zero field, the states 0 and 1, as well as 2 and 3, are degenerate and yield identical excitation voltages ($V_{02} = V_{13}$). The two steps shift in accord with Zeeman energies, with the 0 → 2 step shifting up and the 1 → 3 shifting down in energy with increasing magnetic field, to yield a well-resolved splitting of 1.8 ± 0.2 meV at 6 T.

The IETS measurements reveal a remarkable ZFS of 57.7 meV between ground and excited states. The ZFS is much larger than the typical values of several millielectron volts reported before for single atoms on surfaces (*19*, *30*–*33*), which indicates an exceptionally high MA for Co on MgO. Moreover, the presence of the V_{13} step, in addition to the V_{02} step, at finite magnetic field is surprising because at low temperature ($k_BT << eV_{01}$, where k_B is the Boltzmann constant and T is temperature) and low applied voltage ($V_{bias} < V_{02}$) one would expect only state 0 (the ground state) to be occupied for an appreciable fraction of the time. The observation of the 1 → 3 transition for Co on MgO is an indication that the excited state 1 has a lifetime above 1 ns (the mean tunneling time between electrons at the measured currents).

Electronic Structure Probed with X-ray Absorption Spectroscopy

To understand the large energy and time scales revealed by the IETS measurements, we performed x-ray absorption spectroscopy (XAS) of isolated Co atoms deposited on 2 to 4 MLs of MgO on Ag(100). By measuring the excitation cross-section for 2p to 3d transitions, L-edge x-ray absorption spectra provide a probe of the bonding and the magnetic properties of transition metal ions (*34*) that is highly complementary to IETS. Spectra acquired at the L_3 Co edge with circularly polarized light are shown in Fig. 4A (*26*). The XAS lineshape differs from that of Co atoms adsorbed on metal substrates (*18*, *35*) as well as from typical CoO phases (*36*), showing that the bonding of Co is specific to the MgO surface. The x-ray magnetic circular dichroism (XMCD) intensity measured at normal incidence is larger than at grazing incidence (Fig. 4B),

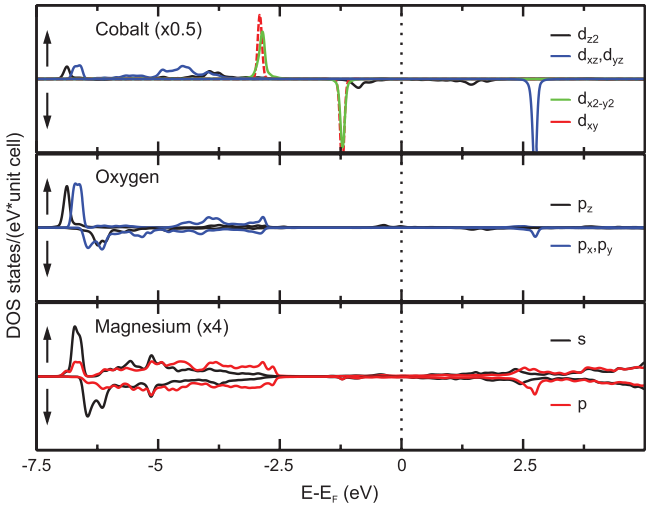


Fig. 2. DFT spin-resolved partial density of states of the Co, O, and Mg levels. The figure shows the large ligand field splitting induced by O ligation for the out-of-plane orbitals and also shows the degeneracy between the Co (d_{xz},d_{yz}) and (d_{xy},d_{x2-y2}) orbitals. Large overlap between the Co d_{z2} and O p_z as well as d_{xz}, d_{yz} and p_x, p_y orbitals indicates hybridization between Co and O, whereas no Co-Mg overlap is visible.

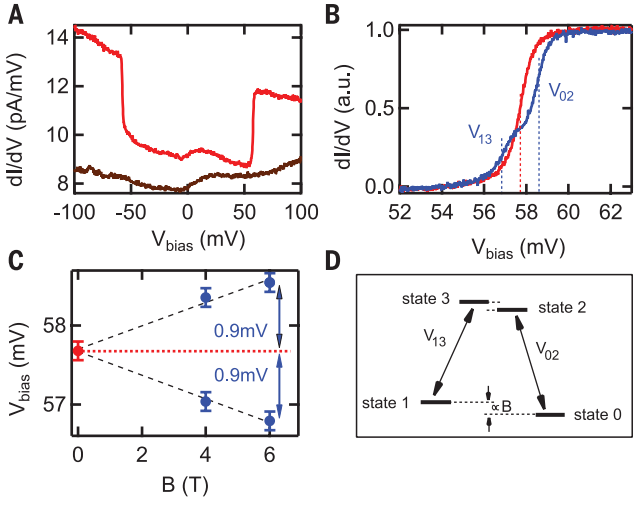


Fig. 3. Magnetic excitations measured in STM at T = 0.6 K. (**A**) Differential conductance spectrum (dI/dV). The tip is positioned above a Co atom on 1 ML MgO on Ag(100) (red) and bare MgO (brown). (**B**) Expanded view of the steps near 58 mV for 0 T (red) and 6 T (blue) (tip height setpoint 5 nA, 100 mV). (**C**) The step position as a function of magnetic field, showing the field-induced splitting. Only one step is resolvable at 0 T (red point). Dashed lines are linear fits to the data points. (**D**) Schematic energy level diagram. The states are labeled in order of increasing energy from 0 to 3. The arrows V_{02} and V_{13} indicate the transitions measured in IETS.

which implies that the Co magnetic moment has an out-of-plane easy axis. The XMCD spectra reveal a large orbital-to-effective spin moment ratio, in the range of 0.9 to 1.2, which indicates that L is very large on this surface. A discussion of the XMCD sum rule analysis (*37*, *38*) and technical challenges related to x-ray–induced desorption on thin insulating films (*39*) is reported in (*26*).

To determine the electronic ground state and the structure of the lowest lying magnetic states, we simulated the x-ray experimental results using multiplet ligand field theory (*34*). The multiplet calculations include charge transfer (σ-donation) via the d_{z^2} orbital and take into account the mixing between d^7 and $d^8\underline{l}$ configurations, where $\underline{l}$ describes a ligand hole on the O site. As shown in Fig. 4, A and B, there is excellent agreement between the simulated and experimental XAS and XMCD. The resulting d-shell occupancy is 7.44 electrons, which is in good agreement with the DFT results [7.27 electrons in a Löwdin analysis (*26*, *40*)]. The evolution of the calculated Co states as a function of ligand field splitting and spin-orbit interaction is shown in Fig. 4D [the complete energy diagram is provided in fig. S3 (*26*)]. The lowest energy level (Fig. 4D, left edge) is an octuplet (blue) with $L_z = \pm 3 \otimes S_z = \pm 1.25$, $S_z = \pm 0.42$, where the spin moment is slightly less than the free atom value of $S = 3/2$ because of mixing of the ground state ^4F and ^3F terms of the d^7 and d^8 configurations, respectively.

Origin of the ZFS

The electronic states of Co after including all interactions—namely, ligand field, spin-obit coupling, and external magnetic field—are shown on the right side of Fig. 4D. What is most unusual about the resulting spin doublet ground state is that it is composed of a mixture of states dominated by $L_z = \pm 3$ and thus has an orbital moment near the free atom limit. Unlike previous reports, such a large L for a surface-adsorbed transition metal atom was observed here because the ligand field is essentially uniaxial [it does not lift the degeneracy between the (d_{xz}, d_{yz}) or between the ($d_{x^2-y^2}$, d_{xy}) orbitals], and both d^7 and d^8 configurations have the same orbital multiplicity so that configuration mixing—which takes place here, as it does on most substrates—does not reduce the magnitude of L.

The substantial orbital contribution can also be seen in the magnetization measured by XMCD as a function of applied field, which indicates a local moment of ~$6\mu_B$ per atom (Fig. 4C) (where μ_B is the Bohr magneton). This result is in agreement with the magnetization $\mu_z = \langle L_z \rangle + \langle 2S_z \rangle$ calculated by using the wave functions and energy levels obtained from the multiplet simulations (Fig. 4C, solid black line). Both experimental and theoretical curves saturate very fast, as expected for strong MA. At low magnetic fields, the measured values remain above the calculated values (Fig. 4C, inset), which could be the result of slow relaxation effects or induced magnetic moment contributions from the substrate atoms.

The multiplet energy diagram in Fig. 4D, derived from the model fit to the XAS data, provides a detailed interpretation of the IETS spectra. The calculated energy separation between the ground-state spin doublet (states 0 and 1) and the first excited spin doublet (states 2 and 3) at zero field is 55 meV, which closely matches the energy of the conductance step ($V_{02} = V_{13} = 57.7$ mV) measured with IETS (*26*). This level of agreement between XAS and IETS is remarkable considering that these are independent experiments that take place at radically different energy scales (hundreds of electron volts for the x-ray measurements as compared with millielectron volts for IETS).

The multiplet results establish that the separation of the first two spin doublets at 0 T is the ZFS seen in IETS spectra and explain its magnitude. The key is the nearly unquenched orbital moment of the lowest energy levels, which allows the $S_z = \pm 3/2$ states to be split maximally from the $S_z = \pm 1/2$ states by the spin-orbit interaction. In this case, the ZFS is equal to $\lambda L\, \Delta S_z$, which for

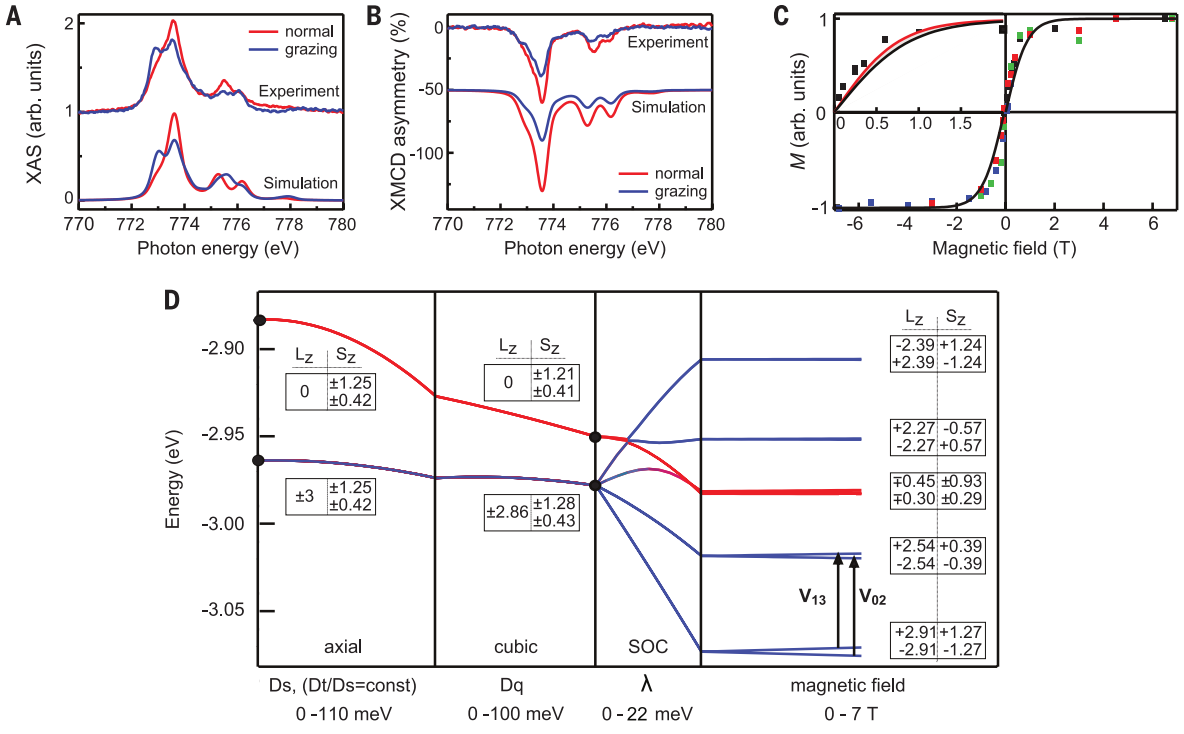


Fig. 4. XMCD measurements and multiplet calculations. (**A**) Experimental and simulated x-ray absorption spectra of Co/MgO/Ag(100) at normal (θ = 0°) and grazing (θ = 60°) incidence recorded over the L_3 Co edge at T = 3.5 K and B = 6.8 T. The Co coverage is 0.03 ML. The spectra are the sum of positive and negative circular polarization, ($I^+ + I^-$). (**B**) XMCD spectra ($I^- - I^+$). The XMCD intensity is given as percentage of the total absorption signal shown in (A). (**C**) Out-of-plane magnetization versus field at 3.5 K measured by XMCD after saturating the sample at 6.8 T (black, red, and green squares) and −6.8 T (blue) at each point. Different colors refer to different samples. The solid line represents the expectation value of $\langle L_z \rangle + \langle 2S_z \rangle \approx 6\mu_B$ at 3.5 K. The inset (top left quadrant) compares fits between 3 (red curve) and 3.5 K (black). (**D**) Lowest energy levels obtained with the multiplet calculations as a function of ligand field, spin-orbit coupling, and applied magnetic field. The color code of the energy levels highlights the different orbital symmetry of the states: blue for E and red for B_2. The two transitions seen in IETS are indicated by arrows.

Co (with $L = 3$ and $\Delta S_z = 1$) gives $\lambda L \approx 60$ meV, reaching up to the full magnitude of the spin-orbit coupling energy intrinsic to a Co atom. This value is much higher than usually observed for transition metal systems, in which **L** arises as a perturbative effect because of spin-orbit coupling, and the ZFS has a second-order dependence on λ^2 (*41*, *42*).

Spin Lifetime Measurements

The ZFS defines the energy for the lowest-order process required to surmount the barrier that separates 0 and 1, the states with large and opposite magnetic moments. Our experiments are at low temperature (k_BT << ZFS), which effectively suppresses thermal excitations of the magnetic moment over the MA energy barrier. These conditions offer the possibility to probe in detail nonthermal magnetization reversal mechanisms that become important when a magnet is scaled to atomic dimensions. In the case of magnetic atoms placed near electrodes (here, the Ag substrate and STM tip), spin relaxation can occur through $\Delta S_z = \pm 1$ transitions induced by electrons from these electrodes that scatter off the magnetic atom and either tunnel across the junction or return to the original electrode (*43*). These scattering processes result in quantum tunneling of the magnetization (*44*, *45*). These mechanisms are extremely sensitive to the local environment, such as the electronic density of states of the substrate and distortions of the ligand field surrounding the magnetic adsorbates (*45*).

We now focus on measurements of the spin lifetime as a probe of the nonthermal decay mechanisms. The relaxation time T_1 of excited spin states can be measured with spin-polarized STM with a pump-probe scheme (*33*). The current in a spin-polarized tunnel junction sensitively depends on the relative alignment of tip and sample spins (*46*). Thus, the tunnel current with the atom in the ground state is generally different from the current in an excited state. Sufficiently large pump pulses put the atom into excited spin states, from which it eventually decays back to the ground state. This decay was monitored with a probe pulse. Such a pump-probe measurement is shown in Fig. 5A with an exponentially changing current, yielding a lifetime $T_1 = 232 \pm 17$ μs at 1 T. To determine which state is giving the long lifetime signals observed here, we measured the amplitude of the pump-probe signal as a function of pump voltage (Fig. 5, B and C), which shows an onset of the signal at 59 ± 2 meV (Fig. 5B) and another sharp onset at 1.9 ± 0.1 meV (Fig. 5C). The first threshold is in good agreement with V_{02} and indicates when state 1 can be reached via state 2. The 1.9-meV threshold corresponds to the direct excitation $0 \rightarrow 1$, which is in agreement with $V_{01} = 2(L_Z + 2S_Z)\mu_B B$ calculated from the multiplet model at 3 T, demonstrating that we are measuring the lifetime of state 1. This Zeeman splitting yields a total magnetic moment of $5.5 \pm 0.3\mu_B$, which matches the magnetic moment determined from the XMCD measurements (Fig. 4C) (*47*), including the large orbital moment. The relaxation time remains independent of pump voltage, and we conclude that the measured T_1 is always that of state 1; the other states decay too quickly to be observed.

It is surprising that the pump signal is detectable for pump voltages below V_{02} because the ZFS is large, and quantum tunneling of the magnetization is forbidden in odd half-integer spin systems in the absence of a transverse magnetic field. However, the multiplet analysis shows that the weak distortion of the symmetry caused by the interaction of the Co with the Mg atoms mixes states from higher multiplets, mostly with $|0,\pm1/2\rangle$ character (Fig. 4D, in red), with the lowest states $|\pm3,\pm3/2\rangle$. Although this mixing is small (on the order of 4%) and does not change the total moments substantially, it allows the coupling of states 0 and 1 by a $\Delta S_z = \pm 1$ spin-flip transition between their $|0,-1/2\rangle$ and $|0,+1/2\rangle$ components, which can explain the observed quantum tunneling induced via substrate electrons. In addition, Co has a nuclear spin $I = 7/2$, which may facilitate otherwise prohibited electron spin relaxation. Tunneling of the magnetization because of hyperfine coupling could explain the lack of remanence in the magnetization curve measured with XMCD. However, the hyperfine coupling is usually effective at low fields (*48*) and is unlikely to be the cause of the spin relaxation observed for pump-probe experiments at $B \geq 1$ T.

The spin lifetime of Co/MgO is much lower than that reported for electrons bound to shallow donors in Si (*49*) as well as that reported for Ho atoms on Pt (*19*), both exceeding a few minutes at cryogenic temperatures. However, it is very large for a transition metal atom, for which typical T_1 times are on the order of 100 ns on insulating substrates (*33*) and 100 fs on metals (*31*). This difference can be attributed to the MgO layer serving two separate purposes. First, because the binding site symmetry preserves the orbital moment, state 0 and 1 are decoupled from each other not only by the large change in spin S_z, but also by the large change in L_z. Second, even a single MgO layer is very efficient in reducing the decay of the excited state by scattering with substrate electrons. This scattering rate could be tuned by increasing the number of MgO monolayers, while still being able to electrically probe the magnetic states. Furthermore, the presence of the STM tip imposes a limit on the lifetime, and the measured 200 μs value sets a lower bound on the intrinsic T_1 of Co atoms on this surface.

Discussion

This work elucidates the interplay between the MA, spin, and orbital degrees of freedom in systems at the border of free atoms and the solid state and highlights the atomistic limits on the miniaturization of magnetic systems. Additionally, this system realizes the single-atom analog of magnetic tunnel junctions based on perpendicular CoFeB/MgO layers. As such, it provides microscopic understanding of materials with strong perpendicular MA, which are required for further downscaling of spintronic devices (*9*, *10*). Our measurements of ZFS and spin relaxation time demonstrate the advantages and impediments intrinsic to size reduction in such materials. Despite the very large MA, the strong coupling of *d*-electrons to the environment makes the spin lifetime of transition metal atoms very sensitive to perturbations caused by the ligand field and scattering from conduction electrons. Nonetheless, the large energy and time scales measured in this experiment indicate that relatively long-lived quantum states are possible for single Co atoms on MgO surfaces. Judging from the knowledge accumulated on magnetic tunnel junctions and this work, Co/MgO and possibly Fe/MgO represent a very favorable combination for the miniaturization of magnetic devices beyond the present technological limits.

On a more fundamental note, our results show that the combination of IETS and XAS is extremely powerful to describe the many-body interactions that determine the spin and the

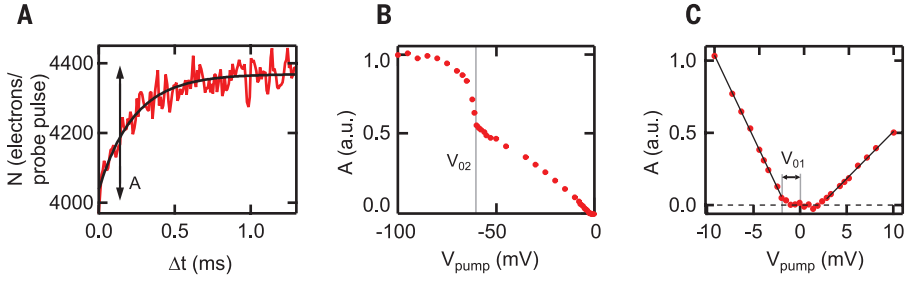


Fig. 5. Relaxation time and excitation threshold of Co at $T = 0.6$ K. (**A**) Pump-probe measurement of the excited state relaxation time at $B = 1$ T showing tunnel current as a function of delay time. The exponential fit (black line) yields $T_1 = 232 \pm 17$ μs. The data are taken with the tip height setpoint at I_{set} = 10 pA and V_{set} = 100 mV. The pulse sequence parameters are V_{pump} = 90 mV, V_{probe} = 20 mV. (**B** and **C**) Pump-probe signal amplitude at $B = 3$ T as a function of pump voltage. For signal-to-noise reasons, the setpoint is I_{set} = 500 pA and V_{set} = 100 mV, which corresponds to the tip 0.2 nm closer to the atom than in (A). This gives $T_1 = 7.6 \pm 0.1$ μs (*26*). The vertical line at −59 mV in (B) shows the transition seen in d*I*/d*V* spectra. (C) The pump-probe amplitude for a smaller range of pump voltages. Linear fits (black lines) extrapolate to -2 ± 0.1 mV and $+1.8 \pm 0.2$ mV at zero amplitude. Error bars are comparable with symbol size.

orbital degrees of freedom of magnetic atoms on surfaces, going beyond the spin Hamiltonian description successfully used in previous STM studies of nanosized magnetic structures (*19*, *30*, *32*, *33*). Aside from a consistent description of the electronic and magnetic ground state, the role of nonthermal spin relaxation mechanisms can be determined based on independent input obtained through the multiplet analysis of the x-ray spectra and pump-probe measurements.

REFERENCES AND NOTES

1. W. Meiklejohn, *Proc. IEEE* **74**, 1570–1581 (1986).
2. P. Carcia, *J. Appl. Phys.* **63**, 5066 (1988).
3. S. Khizroev, D. Litvinov, *Perpendicular Magnetic Recording* (Kluwer Academic Publishers, New York, 2004).
4. S. Monso *et al.*, *Appl. Phys. Lett.* **80**, 4157 (2002).
5. S. Ikeda *et al.*, *Nat. Mater.* **9**, 721–724 (2010).
6. A. Manchon *et al.*, *J. Appl. Phys.* **104**, 043914 (2008).
7. H. X. Yang *et al.*, *Phys. Rev. B* **84**, 054401 (2011).
8. M. Cubukcu *et al.*, *Appl. Phys. Lett.* **104**, 042406 (2014).
9. S. Ikeda *et al.*, *SPIN* **02**, 1240003 (2012).
10. M. Gajek *et al.*, *Appl. Phys. Lett.* **100**, 132408 (2012).
11. J. Z. Sun, *Phys. Rev. B* **62**, 570–578 (2000).
12. Magnetic anisotropy is often defined as a classical energy barrier, or as the energy needed to orient the magnetization perpendicular to the easy-axis. Our temperature was too low to observe Arrhenius behavior because nonthermal processes dominate the relaxation in the range of temperatures accessed. Additionally, studies of quantum magnets sometimes infer a barrier using DS^2 or DJ^2, but these are applicable only for pure-spin or pure-*J* systems. Consequently, we use the ZFS as definition of the MA.
13. M. Blume, R. E. Watson, *Proc. R. Soc. Lond. A Math. Phys. Sci.* **270**, 127–143 (1962).
14. J. van Vleck, *The Theory of Electric and Magnetic Susceptibilities* (Oxford Univ. Press, Oxford, 1966).
15. O. Eriksson, B. Johansson, R. C. Albers, A. M. Boring, M. S. S. Brooks, *Phys. Rev. B* **42**, 2707–2710 (1990).
16. D. Weller *et al.*, *Phys. Rev. Lett.* **75**, 3752–3755 (1995).
17. P. Gambardella *et al.*, *Nature* **416**, 301–304 (2002).
18. P. Gambardella *et al.*, *Science* **300**, 1130–1133 (2003).
19. T. Miyamachi *et al.*, *Nature* **503**, 242–246 (2013).
20. A. M. Bryan, W. A. Merrill, W. M. Reiff, J. C. Fettinger, P. P. Power, *Inorg. Chem.* **51**, 3366–3373 (2012).
21. J. M. Zadrozny *et al.*, *Nat. Chem.* **5**, 577–581 (2013).
22. J. D. Rinehart, J. R. Long, *Chem. Sci.* **2**, 2078 (2011).
23. J. Klatyk *et al.*, *Phys. Rev. Lett.* **88**, 207202 (2002).
24. A. Jesche *et al.*, *Nat. Commun.* **5**, 3333 (2014).
25. K. Neyman, C. Inntam, V. Nasluzov, R. Kosarev, N. Rösch, *Appl. Phys., A Mater. Sci. Process.* **78**, 823–828 (2004).
26. Materials and methods are available as supplementary materials on *Science* Online.
27. S. Schintke *et al.*, *Phys. Rev. Lett.* **87**, 276801 (2001).
28. S. Baumann, I. G. Rau, S. Loth, C. P. Lutz, A. J. Heinrich, *ACS Nano* **8**, 1739–1744 (2014).
29. A. J. Heinrich, J. A. Gupta, C. P. Lutz, D. M. Eigler, *Science* **306**, 466–469 (2004).
30. C. F. Hirjibehedin *et al.*, *Science* **317**, 1199–1203 (2007).
31. A. A. Khajetoorians *et al.*, *Phys. Rev. Lett.* **106**, 037205 (2011).
32. F. Donati *et al.*, *Phys. Rev. Lett.* **111**, 236801 (2013).
33. S. Loth, M. Etzkorn, C. P. Lutz, D. M. Eigler, A. J. Heinrich, *Science* **329**, 1628–1630 (2010).
34. F. de Groot, *Chem. Rev.* **101**, 1779–1808 (2001).
35. P. Gambardella *et al.*, *Phys. Rev. Lett.* **88**, 047202 (2002).
36. F. M. F. de Groot *et al.*, *J. Phys. Condens. Matter* **5**, 2277–2288 (1993).
37. B. T. Thole, P. Carra, F. Sette, G. van der Laan, *Phys. Rev. Lett.* **68**, 1943–1946 (1992).
38. P. Carra, B. T. Thole, M. Altarelli, X. Wang, *Phys. Rev. Lett.* **70**, 694–697 (1993).
39. A. Lehnert *et al.*, *Phys. Rev. B* **81**, 104430 (2010).
40. P.-O. Löwdin, *Phys. Rev.* **97**, 1474–1489 (1955).
41. B. McGarvey, in *Electron Spin Resonance of Transition-Metal Complexes, Transition Metal Chemistry*, vol. 3, R. L. Carlin, Ed. (Marcel Dekker, New York, 1966).
42. P. Bruno, *Phys. Rev. B* **39**, 865–868 (1989).
43. J.-P. Gauyacq, N. Lorente, F. D. Novaes, *Prog. Surf. Sci.* **87**, 63–107 (2012).
44. L. Thomas *et al.*, *Nature* **383**, 145–147 (1996).
45. D. Gatteschi, R. Sessoli, J. Villain, *Molecular Nanomagnets* (Oxford Univ. Press, Oxford, 2006).
46. R. Wiesendanger, *Rev. Mod. Phys.* **81**, 1495–1550 (2009).
47. The quantum mechanical description of the energy levels derived from the multiplet calculation indicates that *J* is not a good quantum number. Therefore, we use the Zeeman energy $(L_Z + 2S_Z)\mu_B B$ instead of a description based on the Landé g-factor.
48. R. Giraud, W. Wernsdorfer, A. M. Tkachuk, D. Mailly, B. Barbara, *Phys. Rev. Lett.* **87**, 057203 (2001).
49. G. Feher, E. A. Gere, *Phys. Rev.* **114**, 1245–1256 (1959).

ACKNOWLEDGMENTS

S.S. and P.G. acknowledge support from the Swiss Competence Centre for Materials Science and Technology (CCMX). J.D. acknowledges funding by an Ambizione grant of the Swiss National Science Foundation. I.G.R., S.B., C.P.L., and A.J.H. thank B. Melior for expert technical assistance. C.P.L and A.J.H. thank the Office of Naval Research for financial support. S.G., O.R.A., and B.A.J. thank the National Energy Research Scientific Computing Center (NERSC) for computational resources. O.R.A. was supported by the National Science Foundation under grant DMR-1006605. B.A.J. thanks the Aspen Center for Physics and National Science Foundation grant 1066293 for hospitality while doing the calculations which appear in this paper. We thank A. Cavallin for helping in developing the Igor code used to analyze the XAS spectra. I.G.R., S.B., R.M.M., C.P.L., and A.J.H. performed the STM experiments and data analysis. S.G., O.R.A., and B.A.J. carried out the DFT calculations. S.R., F.D., L.G., S.B., J.D., C.P., and F.N. carried out the XMCD experiments. F.D., S.R., S.S., and P.G. analyzed the XMCD data. S.S. wrote the multiplet calculation code and performed the simulations. All authors discussed the results and participated in writing the manuscript. A.J.H., P.G., and H.B. initiated and directed this research. The authors declare that they have no competing financial interests.

SUPPLEMENTARY MATERIALS

www.sciencemag.org/content/344/6187/988/suppl/DC1
Materials and Methods
Figs. S1 to S7
Table S1
References (*50*–*58*)

3 March 2014; accepted 21 April 2014
Published online 8 May 2014;
10.1126/science.1252841

ION CHANNEL STRUCTURE

Crystal structure of a heterotetrameric NMDA receptor ion channel

Erkan Karakas and Hiro Furukawa*

***N*-Methyl-D-aspartate (NMDA) receptors belong to the family of ionotropic glutamate receptors, which mediate most excitatory synaptic transmission in mammalian brains. Calcium permeation triggered by activation of NMDA receptors is the pivotal event for initiation of neuronal plasticity. Here, we show the crystal structure of the intact heterotetrameric GluN1-GluN2B NMDA receptor ion channel at 4 angstroms. The NMDA receptors are arranged as a dimer of GluN1-GluN2B heterodimers with the twofold symmetry axis running through the entire molecule composed of an amino terminal domain (ATD), a ligand-binding domain (LBD), and a transmembrane domain (TMD). The ATD and LBD are much more highly packed in the NMDA receptors than non-NMDA receptors, which may explain why ATD regulates ion channel activity in NMDA receptors but not in non-NMDA receptors.**

Brain development and function rely on neuronal communication at a specialized junction called the synapse. In response to an action potential, neurotransmitters are released from the presynapse and activate ionotropic and metabotropic receptors at the postsynapse to generate a postsynaptic potential. Such synaptic transmission is a basis for experience-dependent changes in neuronal circuits. The majority of excitatory neurotransmission in the human brain is mediated by transmission of a simple amino acid, L-glutamate (*1*), which activates metabotropic and ionotropic glutamate receptors (mGluRs and iGluRs, respectively). iGluRs are ligand-gated ion channels that comprise three major families, α-amino-3-hydroxy-5-methyl-4-isoxazole propionic acid (AMPA) (GluA1-4), kainate (GluK1-5), and *N*-Methyl-D-aspartate (NMDA) receptors (GluN1, GluN2A-D, and GluN3A-B). Non-NMDA receptors can form functional homotetramers that respond only to L-glutamate. In contrast, NMDA receptors are obligatory heterotetramers mainly composed of two copies each of GluN1 and GluN2, which activate upon concurrent binding of glycine or D-serine to GluN1 and L-glutamate to GluN2 and relief of a magnesium block of the ion channel pore by membrane depolarization (*2*). Opening of NMDA receptor channels results in an influx of calcium ions that triggers signal transduction cascades that control the strength of neural connectivity or neuroplasticity. Hyper- or hypo-activation of NMDA receptors is implicated in neurological disorders and diseases including Alzheimer's

Cold Spring Harbor Laboratory, W. M. Keck Structural Biology Laboratory, One Bungtown Road, Cold Spring Harbor, NY 11724, USA.
***Corresponding author. E-mail: furukawa@cshl.edu**

disease, Parkinson's disease, depression, schizophrenia, and ischemic injuries associated with stroke (*3*).

The NMDA receptor subunits, like other iGluR subunits, contain modular domains that are responsible for controlling distinct functions. In NMDA receptors, an amino terminal domain (ATD) contributes to control of ion channel open probability and deactivation speeds (*4*–*6*) and contains binding sites for subtype-specific allosteric modulator compounds, including zinc (GluN2A and 2B), ifenprodil (GluN2B), and polyamines (GluN2B) (*7*–*9*). A ligand-binding domain (LBD) binds agonists and antagonists to control ion channel opening. A transmembrane domain (TMD) forms the heterotetrameric ion channel. A carboxyl terminal domain (CTD) associates with postsynaptic density proteins, which in turn facilitates intracellular signaling pivotal for neuroplasticity. In non-NMDA receptors, the ATD does not regulate ion channel activity, the LBD binds only one agonist, L-glutamate, and the TMD forms an ion channel pore with no voltage-sensing capacity and with substantially less calcium permeability than NMDA receptors. The much shorter CTD interacts with postsynaptic proteins that are distinct from the NMDA receptor–associating proteins. Thus, despite being categorized in the same iGluR family, non-NMDA receptors and NMDA receptors have clear differences in basic ion channel physiology and pharmacology. The only crystal structure of an intact iGluR is the homotetrameric GluA2 AMPA receptor bound to an antagonist (*10*). In NMDA receptor families, structural information has been limited to that of isolated ATD (*7*, *8*, *11*) and LBD (*12*–*15*) extracellular domains. Thus, the modes of subunit and domain arrangement of intact heterotetrameric NMDA receptors have remained enigmatic. Moreover, the structure-function relation of NMDA receptors has been difficult to dissect because functions such as ATD-mediated allosteric regulation, ligand-induced gating, and ion permeability occur in the context of heterotetramers and involve intersubunit and interdomain interactions. Thus, to facilitate understanding of complex functions in NMDA receptors, we sought to capture the pattern of intersubunit and interdomain arrangement by crystallographic studies on the intact heterotetrameric GluN1a-GluN2B NMDA receptor ion channel.

Production and Structural Study of Heterotetrameric NMDA Receptors

NMDA receptors are obligatory heterotetramers composed of two copies each of GluN1 and GluN2. Structural studies of heteromultimeric eukaryotic membrane proteins from a recombinant source have been hindered by difficulties in properly assembling multiple membrane proteins in recombinant expression host cells. After extensive exploration of expression methods, we succeeded in obtaining homogeneously assembled heterotetrameric NMDA receptors by expressing modified GluN1-4a and GluN2B subunits (GluN1a-GluN2B$_{cryst}$) (figs. S1 to S4, see supplementary methods) in *Sf*9 insect cells using a recombinant baculovirus containing both of those subunits under the heat shock promoter Hsp70 from *Drosophila melanogaster*. Expression under conventional late promoters such as P10 and polyhedrin promoters hampers proper heteromeric assembly of the NMDA receptor subunits (fig. S2). The GluN1a/GluN2B$_{cryst}$ construct forms an ion channel that is opened upon glycine and L-glutamate application and allosterically regulated by ifenprodil and polyamines similarly to the wild-type receptor (figs. S5 and S6). GluN1a-GluN2B$_{cryst}$ was crystallized in the presence of a GluN1 agonist, glycine; a GluN2 agonist, L-glutamate; and an ATD-binding allosteric inhibitor, ifenprodil. The structure was initially solved at 5.7 Å by molecular replacement using the extracellular domain structures as search probes (supplementary methods). Overall the extracellular domains of the receptor were well resolved, and electron density for the TMD was of sufficient quality to conclude that TMD helices of GluN1a-GluN2B$_{cryst}$ receptor are arranged similarly to those of GluA2 (fig. S7) (*10*). To improve the x-ray diffraction quality, we stabilized the heterotetramer by forming disulfide cross-links between subunits (fig. S1). On the basis of the 5.7 Å structure, we engineered a GluN2B mutation in which cysteine replaced serine at position 214 (Ser214Cys) (*16*) to form a disulfide bond between the ATDs of two GluN2B subunits and pairs of mutations, the GluN1a Thr561Cys-Phe810Cys and GluN2B Asp557Cys-Ile815Cys, to tether the M1 helices to the M4 helices of the neighboring subunit at the TMD. The disulfide cross-linked mutant receptor (GluN1a-GluN2B$_{crystx}$) is trapped in an inhibited state, which could be unlocked by application of reducing agents (fig. S6). The cross-linking improved the diffraction limit to better than 4 Å, which resulted in electron density sufficient to build most of the GluN1a-GluN2B NMDA receptor including the entire extracellular domains; TMD; linkers between ATD and LBD and between LBD and TMD—except some residues in the cytoplasmic loops (GluN1a 583–604, 617–622, and 834–847, and GluN2B 570–601, 616–629, and 841–852), in the loop connecting the LBD to the TMD (GluN2B 541–548 and 803–806), and in the extracellular loops (GluN1a 95–104 and 442–444 and GluN2B 440–450) (Fig. 1 and figs. S3 and S4). The model for the TMD was built using GluA2 TMD as a guide, and residue assignment was verified using selenomethionine labeling (fig. S8 and table S1) and electron density for aromatic residues and cross-link sites. Even though structural refinement was conducted using the most advanced refinement methods for treating low-resolution data (*17*, *18*), we suggest cautious interpretation of our structural model at the TMD, because there is some level of positional uncertainty intrinsic to a 4 Å model. No significant difference in the architecture between GluN1a-GluN2B$_{cryst}$ and

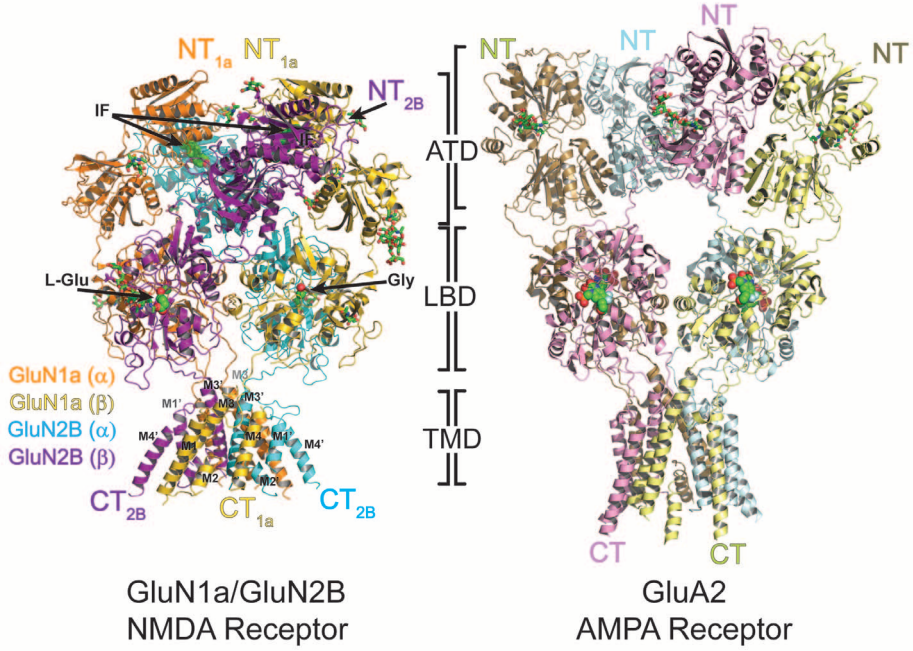


Fig. 1. Overall structure of heterotetrameric GluN1a-GluN2B NMDA receptor and comparison with GluA2 AMPA receptor. Overall structures of GluN1a-GluN2B NMDA receptor (left) and GluA2 AMPA receptor (right) [Protein Data Bank (PDB) ID: 3KG2]. Both structures are placed so that the tetramers of both receptors are in the similar orientation at the LBD layer. GluN1a and GluN2B subunits, labeled as GluN1a (α), GluN1a (β), GluN2B (α), GluN2B (β) are colored in orange, yellow, cyan, and purple, respectively. The amino (NT) and carboxy (CT) termini are located on top and bottom, respectively. Ifenprodil (IF), located at the GluN1a-GluN2B ATD heterodimer interfaces, and agonists, glycine (Gly) and L-glutamate (L-Glu), lodged at the LBD clamshells, are shown in green spheres. N-glycosylation chains are shown in green sticks.

GluN1a-GluN2B$_{crystx}$ was observed, which demonstrated that disulfide cross-linking of the subunits did not alter the overall structure.

Overall Structure

The GluN1a-GluN2B NMDA receptor bound to glycine, L-glutamate, and ifenprodil is shaped like a hot-air balloon where the balloon and basket correspond to the extracellular domains and the TMD, respectively (Fig. 1). There is a clear boundary between the layers of LBD and TMD, whereas the ATD and LBD appear as a single unit. The GluN1a and GluN2B subunits assemble as the staggered GluN1-GluN2-GluN1-GluN2 (1-2-1-2) heterotetramer in every domain as previously predicted (*10*, *19*, *20*) (Figs. 1 and 2). The GluN1a-GluN2B ATD and LBD heterodimers are similar to isolated GluN1b-GluN2B ATD complexed to ifenprodil [root mean square deviation (RMSD) of 0.9 Å] (*8*) and isolated GluN1-GluN2A LBD complexed to glycine and L-glutamate (RMSD 1.1 Å) (*12*). Observed electron density for glycine, L-glutamate, and ifenprodil supports the view that the structure represents the allosterically inhibited state (fig. S9). The assembly of the NMDA receptor tetramer as a dimer-of-dimers at the extracellular region is similar to the organization of the GluA2 AMPA receptor (*10*, *21*) and likely of other iGluR members. Despite the similarity in the pattern of tetrameric arrangement, the overall shape of the GluN1a-GluN2B NMDA receptor is distinct from that of the "Y"-shaped GluA2 AMPA receptor (Fig. 1) (*10*). This is attributed to tight packing of the ATD and LBD in GluN1a-GluN2B NMDA receptors. In contrast, ATD and LBD interact minimally in GluA2 AMPA receptors.

Organization of GluN1 and GluN2B Subunits

There are two key features in the pattern of subunit arrangement. First, pseudo-symmetry mismatch is present between the extracellular region

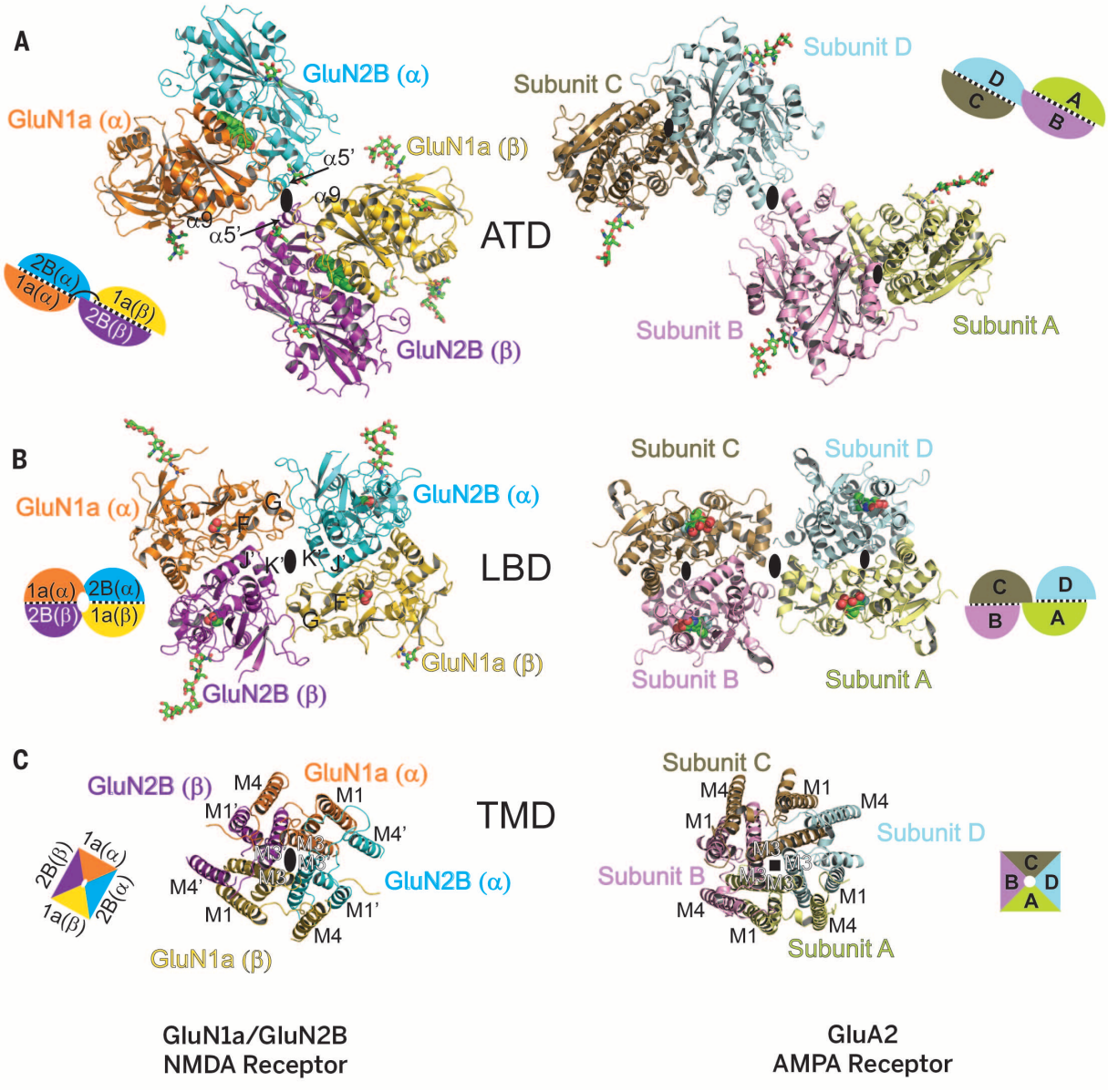


Fig. 2. Domain-by-domain structural comparison of heteromeric GluN1a-GluN2B NMDA receptors and homomeric GluA2 AMPA receptor. Structures of ATD (**A**), LBD (**B**), and TMD (**C**) viewed from the top of the receptors. All of the domains are assembled around the overall twofold axis (large black oval) in GluN1a-GluN2B heterotetramers (left). In GluA2 homotetramers (right), the local twofold axis (small black oval) runs within the ATD and LBD dimers, a twofold axis (large black oval) runs between the ATD and LBD dimers, and the fourfold axis (black square) runs in the center of the TMD. Schematic figures next to the structures represent subunit organization at each domain, where subunits with black dots in between represent dimer pairs. Ifenprodil, glycine, L-glutamate, and ZK200775 are shown in spheres. N-glycosylation chains are shown as green sticks.

and the TMD. The GluN1a and GluN2B subunits are arranged in a 1-2-1-2 orientation with two-fold symmetry between the two GluN1a-GluN2B heterodimers in the ATD and LBD, but with pseudo-fourfold symmetry in the TMD (Fig. 2). A similar subunit arrangement is observed in the GluA2 homotetrameric structure that has two-fold symmetries within and between homodimers of the ATD and LBD and fourfold symmetry in the TMD (*10*), which indicates that symmetry mismatch may be common to iGluR structures. The second important feature is swapping of dimer pairs between the ATD and LBD layers (Fig. 2, A and B). In the ATD layer, heterodimer pairs assemble as GluN1a (α)–GluN2B (α) and GluN1 (β)–GluN2B (β), whereas in the LBD layer, they assemble as GluN1a (α)–GluN2B (β) and GluN1 (β)–GluN2B (α) (Fig. 2, A and B). A similar pattern of domain swapping is also observed in the homotetrameric GluA2 AMPA receptor, where subunits assemble as a dimer of A-B and C-D homodimers at the ATD and as a dimer of A-D and B-C dimers at the LBD (Fig. 2, A and B) (*10*). Overall the conformations of GluN1a and GluN2B subunits approximately correspond to those of A-C and B-D subunits in the GluA2 AMPA receptor homotetramer. This assignment is based on the observation that the ATD-LBD linker and the M3-LBD linker are, respectively, more "distal" and "proximal" from the overall twofold symmetry axis for GluN1a than GluN2B, similar to the orientation of the A-C than of the B-D subunits in the GluA2 AMPA receptor (Fig. 2 and fig. S10).

Although they share a dimer-of-dimers arrangement, the modes of subunit association in each domain differ substantially between NMDA and AMPA receptors. In the ATD, the two GluN1a-GluN2B heterodimers interact with each other at two interfaces involving upper lobes of the two GluN1a subunits (α and β) and lower lobes of the two GluN2B subunits (α and β). In contrast, the GluA2 receptor has only one interface between subunits B and D (Fig. 2A and fig. S11). The ATDs of NMDA receptor and AMPA receptor subunits have low sequence identity, and this is reflected in the large differences in structures (*7*, *8*). Consequently, the ATD layer is more compactly packed in GluN1a-GluN2B than in GluA2. At the LBD, the dimer-of-dimers arrangement is comparable between the GluN1a-GluN2B and GluA2 receptors. The GluN1a-GluN2B heterodimers interact between the lower lobe of GluN1a and the upper lobe of GluN2B at the two equivalent sites (Fig. 2B and fig. S11). In GluA2, the equivalent regions are much more loosely packed, but instead, there is another closely packed region involving subunits A and C (*10*). Whether these distinct modes of interactions at the LBD represent an architectural difference between NMDA and AMPA receptors or different functional states remains an open question. In the previous study, the GluA2 AMPA receptor was crystallized in the presence of an antagonist (ZK200775), whereas the GluN1a-GluN2B NMDA receptor was crystallized in the presence of the allosteric inhibitor, ifenprodil, and agonists, glycine and L-glutamate. Finally, at the TMD, the subunits form pseudo-fourfold symmetrical interactions between the M3 helices at the center of the ion channel and between M4 helices of one subunit and M1 and M3 helices of the adjacent subunit, similar to the GluA2 AMPA receptor (Fig. 2C and fig. S11). Within the pore, the M2 helices are close to the M1 and M3 helices of the same subunit and the M3 helices of the adjacent subunit.

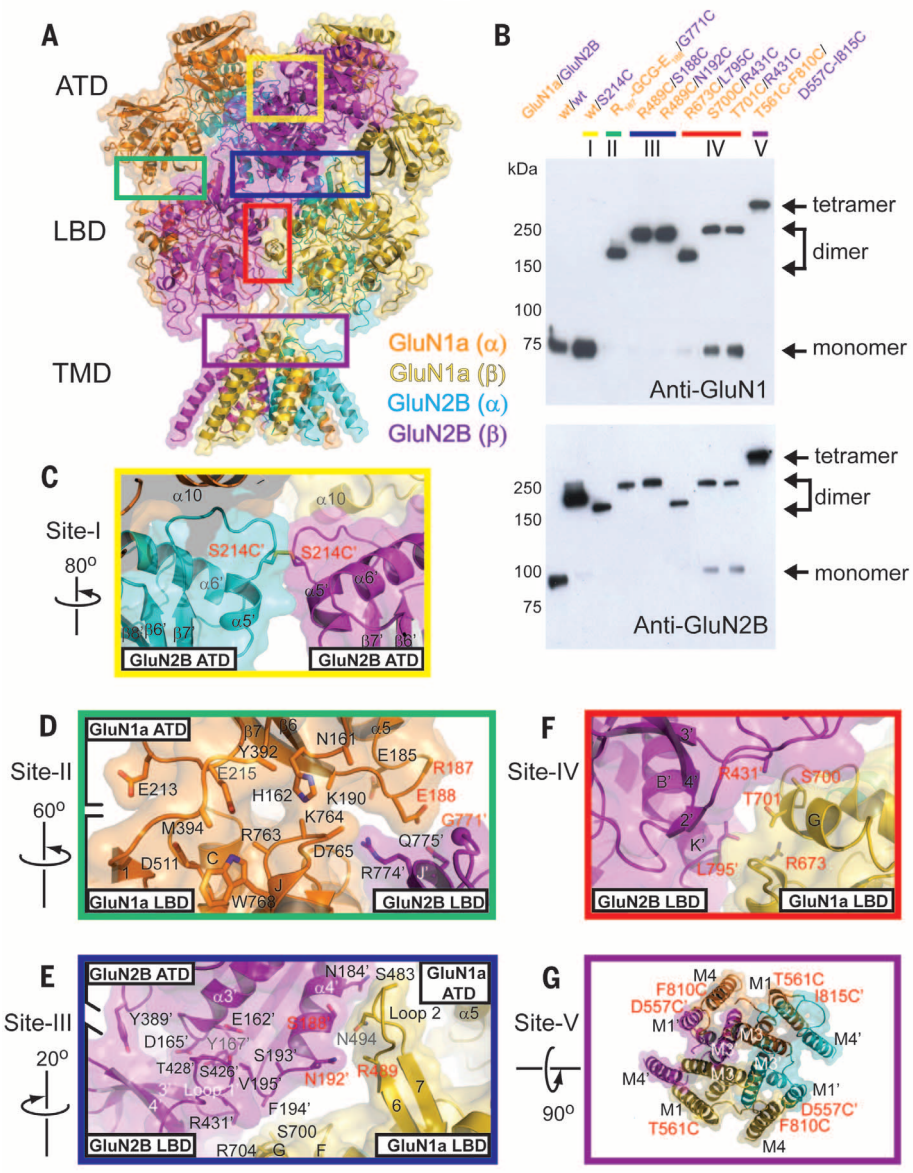


Fig. 3. Inter- and intrasubunit interfaces in GluN1a-GluN2B NMDA receptors (**A**) Ribbon and surface representation of GluN1a-GluN2B NMDA receptor colored as in Fig. 1. Intersubunit interfaces that are probed by disulfide cross-linking experiments are surrounded by colored boxes. (**B**) Western blot analysis of disulfide bond formation by cysteine substitutions at the subunit interfaces probed by anti-GluN1 (top) and anti-GluN2B (bottom) antibodies under nonreducing conditions. Arrows indicate positions of non–cross-linked monomers and cross-linked dimers and tetramers. (**C** to **G**) Close-up views of the inter- and intrasubunit interfaces between GluN2B ATD (α) and GluN2B-ATD (β) (site I, yellow box) (C), between GluN1a ATD and GluN1a LBD, and GluN1a-ATD and GluN2B-LBD (site II, green box) (D), between GluN1a LBD and GluN2B ATD, and GluN2B ATD and GluN2B LBD (site III, blue box) (E), between GluN1a LBD and GluN2B LBD (site IV, red box) (F) and between GluN1a TMD and GluN2B TMD (site V, purple box) (G). Side chains without clear electron densities are modeled as alanine. Residues that are mutated to cysteine are labeled in red.

Intersubunit Interfaces and Function

The crystal structure of the heterotetrameric GluN1a-GluN2B NMDA receptor shows intersubunit interfaces that are distinct from those in the GluA2 AMPA receptor. Thus, we have tested whether the distinct interfaces observed in our crystal structure are present in intact NMDA receptors in the membrane environment. We engineered cysteine residues and tested for spontaneous

disulfide bond formation at the following subunit interfaces: (i) GluN2B (ATD)–GluN2B (ATD); (ii) GluN1a (ATD)–GluN2B (LBD); (iii) GluN1a (LBD)–GluN2B (ATD); (iv) GluN1a (LBD)–GluN2B (LBD); and (v) GluN1a (TMD)–GluN2B (TMD) (Fig. 3). The Western blot experiments on the mutant GluN1a-GluN2B NMDA receptor proteins have shown that all of the single-cysteine mutant pairs in the extracellular region form disulfide cross-links resulting in GluN2B-GluN2B homodimer formation (i) and GluN1a-GluN2B heterodimer formation (ii, iii, and iv), whereas the double-cysteine mutant pair in the TMD forms GluN1a-GluN2B-GluN1a-GluN2B disulfide cross-links resulting in heterotetramer formation (v) in the absence of a reducing agent (Fig. 3B). In the presence of reducing agents or when a subunit with the cysteine mutation is expressed with a subunit with no mutation, bands representing monomers of GluN1a and GluN2B appear (fig. S12). This indicates that the disulfide cross-links are formed by engineered cysteine pairs and validates the physiological relevance of the subunit arrangement observed in our crystal structure.

What are the molecular determinants that favor the 1-2-1-2 arrangement over 1-1-2-2 arrangement? Previous studies have shown that the ATD is important for allosteric modulation and for controlling open probability and deactivation speeds (*4*, *5*) but is not required for formation of functional ion channels (*22*). Furthermore, interactions of helices in the TMD are similar to those in the homotetrameric GluA2 AMPA receptor structure, thus, the structural determinant for the 1-2-1-2 subunit arrangement may reside in the LBDs. In silico construction of GluN1a-GluN2B heterotetramers in the 1-1-2-2 format by superposing the GluN1 LBD structure onto the GluN2B LBD structure and vice versa revealed steric clashes in both the GluN1a-GluN1a and the GluN2B-GluN2B interfaces (fig. S13). The GluN1a-GluN1a interaction is prevented by a collision between loop1 of one GluN1a and helix G of the other, whereas the GluN2B-GluN2B interaction is disfavored by a steric hindrance between helix K′ of one subunit and helices E′ and F′ of the other (fig. S13). Thus, although the TMD is essential for tetramerization, the structural features in the LBD appear to favor the 1-2-1-2 arrangement.

The GluN1a-GluN2B heterotetrameric structure shows that some residues and motifs previously shown to play important roles in function are located at the interface between GluN1-GluN2B heterodimers (fig. S14). One example is loop 1′ of GluN2B located within the LBD. The equivalent motif in GluN2A has been suggested to play a major role in negative cooperativity between the glycine- and L-glutamate–binding sites (*23*). Another example is a point mutation on helix E of the GluN1 LBD lobe (Asp669Asn), which has previously been shown to affect gating properties by altering sensitivity to pH, spermine, and ifenprodil (*24*). Our cross-linking results also showed "trapping"; GluN1a-GluN2B ATD attenuates the ion channel activity. Taken together these results suggest that rearrangement between the two GluN1a-GluN2B dimers may be important for activity. Consistent with this, a recent study on GluA2 AMPA receptor showed that rearrangement of two GluA2 homodimers at the LBD regulates ion channel gating activity (*25*).

Interdomain Interaction Between ATD and LBD and Function

One of the major functional differences between NMDA receptors and non-NMDA receptors is the ATD-mediated regulation of ion channel activity present in the former and absent in the latter. In NMDA receptors, binding of allosteric modulators at the ATD alters agonist potency at the LBD, which indicates tight functional coupling between the ATD and the LBD (*26*). This coupling is structurally well represented by the more extensive ATD-LBD interaction in NMDA receptors (3107 Å^2) than in AMPA receptors (1470 Å^2). The crystal structure shows the two major sites, site II and site III, mediating the tight ATD-LBD association mainly through hydrophilic interactions, even though the exact mode of residue-by-residue contacts cannot be pinpointed because of the limitation in resolution (Fig. 3, D and E). In site II, GluN1a ATD and the GluN1a-GluN2B LBD heterodimer are packed together through interaction between the loop extending from helix α*5* to strand β7 at GluN1a ATD and GluN2B helix J′ at the GluN1a-GluN2B interface at LBD (Fig. 3D). The region around GluN1a helix α*5* is where the 21-residue long loop that contains numbers of basic amino acids would be present in the GluN1b splice variant. This loop, encoded by exon 5, has been shown to accelerate the deactivation time course (*27*) and to influence allosteric modulation by decreasing potency of protons, polyamines, and Zn^{2+} (*28*). In site III, the GluN1a LBD and the GluN1a-GluN2B ATD heterodimer are packed together by GluN1a loop 2 "wedging" into the interface between GluN1a ATD and GluN2B ATD. Furthermore, GluN1a helices F and G, GluN2B loop 1′ and the loop extending from GluN2B helix α4′ stack onto each other to further stabilize the ATD-LBD interaction (Fig. 3E). Helix F in GluN1 has been implicated in gating control; thus, this may be a key locus where ATD may have an impact on gating properties (*29*). Overall, the ATD and the LBD are in a tight arrangement that is suited to transmit structural changes between domains (fig. S15).

Transmembrane Domain and the Extracellular Vestibule

The TMD of the GluN1a-GluN2B NMDA receptor forms a heterotetrameric ion channel with

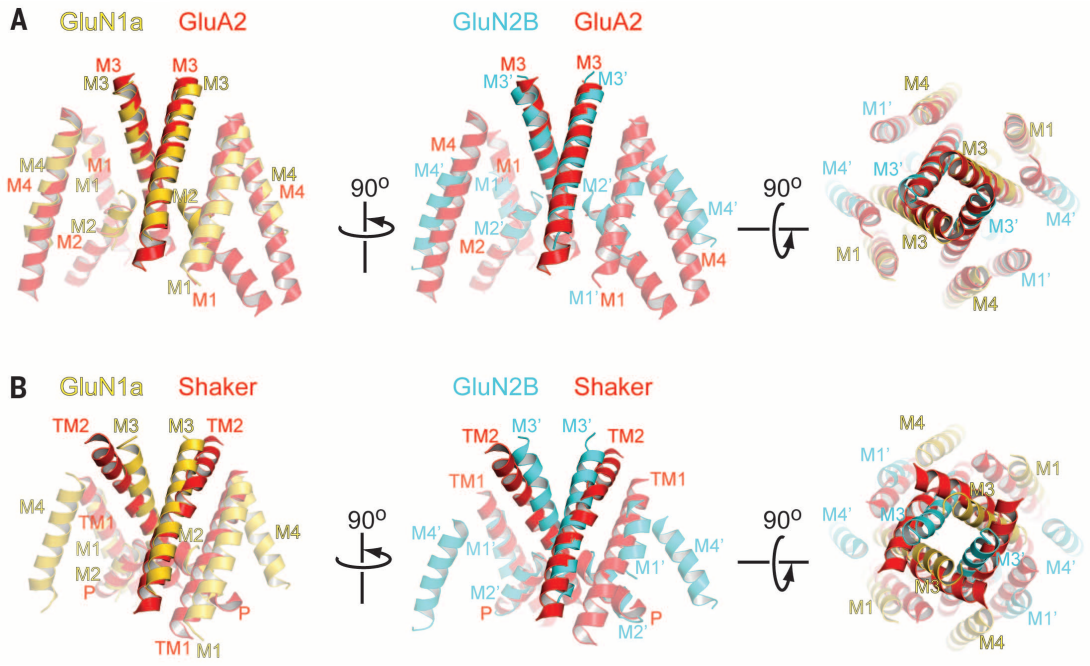


Fig. 4. Structural comparison of NMDA receptor ion channel with GluA2 AMPA receptor and Shaker potassium channels. TMDs of GluN1a subunits (yellow, left) and GluN2B subunits (cyan, middle) are superposed onto the ion channel regions (red) of the closed conformation of GluA2 AMPA receptor (PDB ID: 3KG2) (**A**) and open conformation of Shaker potassium channel (PDB ID: 2R9R) (**B**). The superposed structures are viewed from the side (left and middle) or from the extracellular side (right). Superposition is performed using secondary structure matching (SSM) tool in the program Coot. Loops are excluded from the figure for clarity.

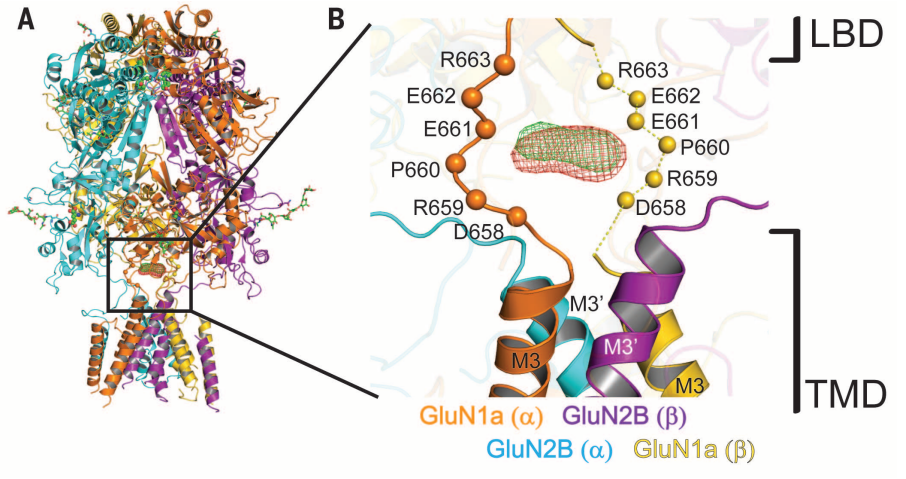


Fig. 5. Putative calcium binding site at the extracellular vestibule. (**A**) Overall structure of GluN1a-GluN2B NMDA receptors with the anomalous Fourier difference maps for holmium (green mesh; from the 7.5 Å data set) and gadolinium (red mesh; from the 7.8 Å data set) countered at 4.5 σ. (**B**) Close-up view of the boxed region in (A). Holmium- and gadolinium-binding sites are located at the extracellular vestibule over the bundle of M3 helices. Cα atoms of the residues on GluN1a DRPEER motif from the GluN1a-$GluN2B_{crystx}$ structure are shown as spheres. Residues for the disordered DRPEER motif (shown as dashed lines) on the GluN1a (β) protomer (yellow) are positioned based on the structural alignment of the GluN1a (α) protomer (orange).

pseudo-fourfold symmetry, similar in overall shape to the homotetrameric ion channel of the GluA2 AMPA receptors (RMSD 2.2 Å) except the tilt angle of the M4 helix in GluN2B (Fig. 4A). The tetrameric crossing of the M3 helices occludes the ion penetration pathway to a similar degree in the presumed allosterically inhibited GluN1a-GluN2B NMDA receptor to the closed GluA2 AMPA receptor (Fig. 4A). This crossing of the M3 helices occurs around the highly conserved SYTANLAAF (*16*) motifs in iGluRs, mutations of which are known to modify gating properties (*30*). The ion channel pore (M1 to M3) of the GluN1a-GluN2B NMDA receptor shows high structural similarity to that of potassium crystallographically sited activation channels (KcsA channels) in a closed conformation (*31*) (RMSD 2.4 Å), despite the low sequence identity (19%) (fig. S16). In contrast, Shaker (*32*) and MthK (*33*) potassium channels in open conformation do not superpose well, mainly because their TM2 helices bend differently from the M3 helices in the GluN1a-GluN2B NMDA receptor (Fig. 4B and fig. S16). On the basis of structural similarities with the potassium channel, we speculate that gating of the GluN1a-GluN2B NMDA receptor may involve rearrangement of M3 helices.

One of the hallmarks of NMDA receptor function is the high permeation of calcium ions, which plays a major role in neuronal plasticity, as well as excitotoxicity. The crystal structure complexed with holmium or gadolinium, lanthanides known to occupy calcium binding sites in many biological macromolecules (*34*, *35*), shows binding between the LBD-TMD linkers from the two GluN1 subunits around the center of the ion channel (Fig. 5). A set of acidic residues in GluN1 [DRPEER motif (*16*)] located in this region is critical for the high calcium flux characteristic of NMDA receptors (*36*). Thus, the lanthanide-binding site along with the previous electrophysiological study further confirms the presence of the calcium pool located right outside of the ion channel. A similar charge-based ion pooling mechanism has been suggested for cation conductance in P2X4 receptors and nicotinic acetylcholine receptors (*37*, *38*). Despite extensive efforts, the regions of the TMD that determine voltage-dependent Mg^{2+} block and Ca^{2+} permeation (*39*) are not resolved in this crystal structure. Structure-based understanding of cation selectivity and voltage-dependent Mg^{2+} block is thus a question that remains to be addressed.

Conclusion

The crystal structure of GluN1a-GluN2B NMDA receptors in the current study reveals the patterns of intersubunit and interdomain interactions, which are different from those observed in AMPA receptors. These differences widely reflect functional differences. The structure will serve as a template for designing experiments that addresses functional questions specific to NMDA receptors. Finally, the defined subunit interfaces should serve as an important blueprint for design of therapeutic compounds.

REFERENCES AND NOTES

1. T. Hayashi, *Keio J. Med.* **3**, 183–192 (1954).
2. M. L. Mayer, G. L. Westbrook, P. B. Guthrie, *Nature* **309**, 261–263 (1984).
3. S. F. Traynelis *et al.*, *Pharmacol. Rev.* **62**, 405–496 (2010).
4. M. Gielen, B. Siegler Retchless, L. Mony, J. W. Johnson, P. Paoletti, *Nature* **459**, 703–707 (2009).
5. H. Yuan, K. B. Hansen, K. M. Vance, K. K. Ogden, S. F. Traynelis, *J. Neurosci.* **29**, 12045–12058 (2009).
6. K. B. Hansen, H. Furukawa, S. F. Traynelis, *Mol. Pharmacol.* **78**, 535–549 (2010).
7. E. Karakas, N. Simorowski, H. Furukawa, *EMBO J.* **28**, 3910–3920 (2009).
8. E. Karakas, N. Simorowski, H. Furukawa, *Nature* **475**, 249–253 (2011).
9. L. Mony, S. Zhu, S. Carvalho, P. Paoletti, *EMBO J.* **30**, 3134–3146 (2011).
10. A. I. Sobolevsky, M. P. Rosconi, E. Gouaux, *Nature* **462**, 745–756 (2009).
11. A. N. Farina *et al.*, *J. Neurosci.* **31**, 3565–3579 (2011).
12. H. Furukawa, S. K. Singh, R. Mancusso, E. Gouaux, *Nature* **438**, 185–192 (2005).
13. K. M. Vance, N. Simorowski, S. F. Traynelis, H. Furukawa, *Nat. Commun.* **2**, 294 (2011).
14. Y. Yao, C. B. Harrison, P. L. Freddolino, K. Schulten, M. L. Mayer, *EMBO J.* **27**, 2158–2170 (2008).
15. A. Jespersen, N. Tajima, G. Fernandez-Cuervo, E. C. Garnier-Amblard, H. Furukawa, *Neuron* **81**, 366–378 (2014).
16. Single-letter abbreviations for the amino acid residues are as follows: A, Ala; C, Cys; D, Asp; E, Glu; F, Phe; G, Gly; H, His; I, Ile; K, Lys; L, Leu; M, Met; N, Asn; P, Pro; Q, Gln; R, Arg; S, Ser; T, Thr; V, Val; W, Trp; and Y, Tyr.
17. G. N. Murshudov *et al.*, *Acta Crystallogr. D Biol. Crystallogr.* **67**, 355–367 (2011).
18. G. F. Schröder, M. Levitt, A. T. Brunger, *Nature* **464**, 1218–1222 (2010).
19. C. L. Salussolia, M. L. Prodromou, P. Borker, L. P. Wollmuth, *J. Neurosci.* **31**, 11295–11304 (2011).
20. M. Riou, D. Stroebel, J. M. Edwardson, P. Paoletti, *PLOS ONE* **7**, e35134 (2012).
21. U. Das, J. Kumar, M. L. Mayer, A. J. Plested, *Proc. Natl. Acad. Sci. U.S.A.* **107**, 8463–8468 (2010).
22. J. Rachline, F. Perin-Dureau, A. Le Goff, J. Neyton, P. Paoletti, *J. Neurosci.* **25**, 308–317 (2005).
23. M. P. Regalado, A. Villarroel, J. Lerma, *Neuron* **32**, 1085–1096 (2001).
24. K. Kashiwagi, J. Fukuchi, J. Chao, K. Igarashi, K. Williams, *Mol. Pharmacol.* **49**, 1131–1141 (1996).
25. A. Y. Lau *et al.*, *Neuron* **79**, 492–503 (2013).
26. F. Zheng *et al.*, *Nat. Neurosci.* **4**, 894–901 (2001).
27. K. M. Vance, K. B. Hansen, S. F. Traynelis, *J. Physiol.* **590**, 3857–3875 (2012).
28. S. F. Traynelis, M. Hartley, S. F. Heinemann, *Science* **268**, 873–876 (1995).
29. A. Inanobe, H. Furukawa, E. Gouaux, *Neuron* **47**, 71–84 (2005).
30. J. Zuo *et al.*, *Nature* **388**, 769–773 (1997).
31. Y. Zhou, J. H. Morais-Cabral, A. Kaufman, R. MacKinnon, *Nature* **414**, 43–48 (2001).
32. S. B. Long, X. Tao, E. B. Campbell, R. MacKinnon, *Nature* **450**, 376–382 (2007).
33. S. Ye, Y. Li, Y. Jiang, *Nat. Struct. Mol. Biol.* **17**, 1019–1023 (2010).
34. W. Li, R. W. Aldrich, *Proc. Natl. Acad. Sci. U.S.A.* **106**, 1075–1080 (2009).
35. R. C. Liddington *et al.*, *Nature* **354**, 278–284 (1991).
36. J. Watanabe, C. Beck, T. Kuner, L. S. Premkumar, L. P. Wollmuth, *J. Neurosci.* **22**, 10209–10216 (2002).
37. K. Imoto *et al.*, *Nature* **335**, 645–648 (1988).
38. T. Kawate, J. C. Michel, W. T. Birdsong, E. Gouaux, *Nature* **460**, 592–598 (2009).
39. B. Siegler Retchless, W. Gao, J. W. Johnson, *Nat. Neurosci.* **15**, 406–413, S1–S2 (2012).

ACKNOWLEDGMENTS

We thank staffs at the 23-ID-B and D beamlines at the Advanced Photon System in the Argonne National Laboratory and the BL41XU beamline at the Spring 8 for their excellent beamline supports. We thank N. Simorowski for her technical support, H. Yuan and S. Traynelis for sharing unpublished data with us and for critical comments on this manuscript, and S. Harrison for making important comments on this work. This work was supported by NIH (MH085926 to H.F.), Mirus Research Award (to H.F.), and a Robertson Research Fund of Cold Spring Harbor Laboratory (to H.F.). Coordinates and structure factors have been deposited in the Protein Data Bank under accession code 4PE5. DNA constructs, recombinant virus, and proteins used in this study are available from H.F. under a material transfer agreement with Cold Spring Harbor Laboratory.

SUPPLEMENTARY MATERIALS

www.sciencemag.org/content/344/6187/992/suppl/DC1
Materials and Methods
Figs. S1 to S16
Table S1
References (*40*–*46*)

7 February 2014; accepted 2 May 2014
10.1126/science.1251915

REPORTS

CHILDHOOD DEVELOPMENT

Labor market returns to an early childhood stimulation intervention in Jamaica

Paul Gertler,[1,2]* James Heckman,[3,4,5] Rodrigo Pinto,[3] Arianna Zanolini,[3] Christel Vermeersch,[6] Susan Walker,[7] Susan M. Chang,[7] Sally Grantham-McGregor[8]

A substantial literature shows that U.S. early childhood interventions have important long-term economic benefits. However, there is little evidence on this question for developing countries. We report substantial effects on the earnings of participants in a randomized intervention conducted in 1986–1987 that gave psychosocial stimulation to growth-stunted Jamaican toddlers. The intervention consisted of weekly visits from community health workers over a 2-year period that taught parenting skills and encouraged mothers and children to interact in ways that develop cognitive and socioemotional skills. The authors reinterviewed 105 out of 129 study participants 20 years later and found that the intervention increased earnings by 25%, enough for them to catch up to the earnings of a nonstunted comparison group identified at baseline (65 out of 84 participants).

Early childhood, when brain plasticity and neurogenesis are very high, is an important period for cognitive and psychosocial skill development (*1*–*3*). Investments and experiences during this period create the foundations for lifetime success (*4*–*13*). A large body of evidence demonstrates substantial positive impacts of early childhood development (ECD) interventions aimed at skill development (*14*, *15*). ECD interventions are estimated to have substantially higher rates of return than most remedial later-life skill investments (*6*, *8*, *13*, *16*).

More than 200 million children under the age of 5 currently living in developing countries are at risk of not reaching their full developmental potential, with most living in extreme poverty (*17*, *18*). These children start disadvantaged, receive lower levels of parental investment, and throughout their lives fall further behind the advantaged (*15*, *19*, *20*).

The evidence of substantial long-term economic benefits from ECD is primarily based on U.S. data (*21*–*30*). There are reasons to suspect that these benefits may be higher in developing countries. Children there typically live in homes where the environment is less stimulating than in developed countries. As a result, they enter ECD programs with lower levels of skills. Programs that boost skills are likely to have greater benefits in developing countries because skills are less abundant there. For example, the returns to investment in schooling are typically higher in developing countries (*31*).

We report estimates of the causal effects on earnings of an intervention that gave 2 years of psychosocial stimulation to growth-stunted toddlers living in poverty in Jamaica (*32*). To our knowledge, this is the first experimental evaluation of the impact of an ECD psychosocial stimulation intervention on long-term economic outcomes in a developing country (*33*).

Unlike many other early childhood interventions with treatment effects that fade out over time (*8*, *13*, *15*), the Jamaican intervention had large impacts on cognitive development 20 years later (*34*). We show that the intervention had large positive effects on earnings, enough for stunted participants to completely catch up with

[1]University of California Berkeley, Berkeley, CA, USA. [2]National Bureau of Economic Research (NBER), Cambridge, MA, USA. [3]University of Chicago, Chicago, IL, USA. [4]American Bar Foundation, Chicago, IL, USA. [5]Institute for Fiscal Studies, University College London, London, UK. [6]The World Bank, Washington, DC, USA. [7]The University of The West Indies, Kingston, Jamaica. [8]University College London, London, UK.
*Corresponding author. E-mail: gertler@haas.berkeley.edu

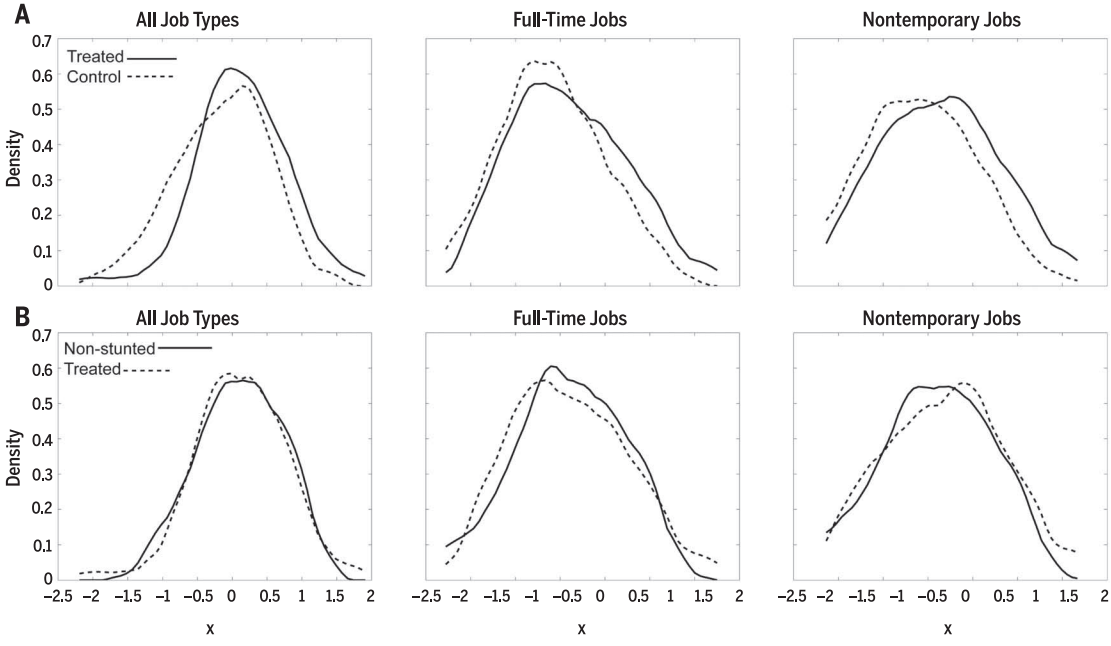


Fig. 1. Impact of stimulation treatment and catch-up on the densities of average earnings at age 22. (**A**) Treated (solid line) and control (dotted line) densities for average earnings. Panel presents the log earnings densities for the treatment (solid line) and control (dotted line) groups using data where earnings of migrant workers who were lost to follow-up were imputed. (**B**) Comparison (dotted line) and treated (solid line) densities for average earnings. Panel presents the log earnings densities for the nonstunted comparison (solid line) and stunted treatment (dotted line) groups, where earnings of migrant workers who were lost to follow-up were imputed. The densities are estimated using Epanechnikov kernels. The treatment densities were estimated with an optimal bandwidth defined as the width that would minimize the mean integrated squared error under the assumption that the data are Gaussian. For purposes of comparability, the same bandwidth was used for the corresponding control group.

a nonstunted comparison group. The intervention compensated for early developmental delays and reduced later-life inequality. The Jamaican intervention had substantially larger effects on earnings than any of the U.S. programs, suggesting that ECD programs may be an effective strategy for improving long-term outcomes of disadvantaged children in developing countries.

The Jamaican Study enrolled 129 growth-stunted children age 9 to 24 months who lived in Kingston, Jamaica, in 1986–1987 (*35*). Section A of the supplementary materials gives a detailed description of the intervention and original study design. The children were stratified by age and sex. Within each stratum, children were randomly assigned to one of four groups: (i) psychosocial stimulation (N = 32); (ii) nutritional supplementation (N = 32); (iii) both psychosocial stimulation and nutritional supplementation (N = 32); and (iv) a control group that received neither intervention (N = 33). The Jamaican Study also surveyed a comparison group of 84 nonstunted children who lived nearby. All participants were given access to free health care.

The stimulation intervention (groups 1 and 3) consisted of 2 years of weekly 1-hour play sessions at home with trained community health aides designed to develop child cognitive, language, and psychosocial skills. The stimulation arms of the Jamaica Study showed significant long-term cognitive benefits through age 22 (*36*, *37*). Moreover, stimulation had positive impacts on psychosocial skills and schooling attainment and reduced participation in violent crimes (*36*).

The nutritional intervention (groups 2 and 3) consisted of giving 1 kg of formula containing 66% of daily-recommended energy (calories), protein, and micronutrients provided weekly for 24 months. The nutrition-only arm, however, had no long-term effect on any measured outcome (*36*, *38*). In addition, there were no statistically significant differences in effects between the stimulation and stimulation-nutrition arms on any long-term outcome, although the arm with both interventions had somewhat stronger outcomes (see supplementary materials, section D). Hence, we combine the two psychosocial stimulation arms into a single "stimulation" treatment group and combine the nutritional supplementation–only group with the pure control group into a single "control" group, understating the benefits of the joint intervention.

We resurveyed both the stunted and nonstunted samples in 2007–2008, some 20 years after the original intervention when the participants were ~22 years old. We found and interviewed 105 out of the original 129 stunted study participants. This sample was balanced. We only observe statistically significant differences in 3 out of 23 variables at baseline (table S.1). In addition, there is no evidence of selective attrition. We also found and interviewed 65 out of the 84 children of the original comparison sample. For that sample there are significant differences in the baseline characteristics of the attrition and nonattrition groups (table S.3).

We estimate the impact of the stimulation intervention on earnings by comparing the earnings of the stunted treatment group to those of the stunted-comparison group. We control for potential bias from baseline imbalances using inverse propensity weighting (IPW) (*39*). We then assess the degree to which the intervention enabled the stunted treatment group to catch up to the nonstunted comparison group by comparing the earnings of the treatment group to those of the comparison group. In the catch-up analysis, we correct for potential attrition bias using IPW weighting. See supplementary methods, section B, for the analysis of baseline balance, attrition, and the details of implementing IPW.

To better understand the external validity of our catch-up analysis, we compare the nonstunted group to the general population using data on individuals 21 to 23 years old living in the greater Kingston area from the 2008 Jamaican Labor Force Survey (JLF) survey. By age 22, the nonstunted group attained levels of skills comparable to those of persons the same age who were living in the Kingston area interviewed in the JLF (table S.4). The two samples are equally likely to still be in school and achieve the same educational level in terms of the highest grade of schooling attained and passing national comprehensive matriculation exams.

Statistical inference is complicated by small sample size and multiple outcomes. We address the problem of small sample size by using exact permutation tests as implemented in (*21*). We correct for the danger of arbitrarily selecting statistically significant treatment effects in the presence of multiple outcomes by performing multiple hypothesis testing based on the stepdown algorithm proposed in (*40*). In addition, we aggregate over outcomes using a nonparametric combining statistic. Section C of the supplementary methods gives details.

The stimulation intervention was designed to improve maternal-child interactions and the quality of parenting. Using the infant-toddler HOME score (*41*, *42*), we examine whether treatment resulted in more maternal investment in stimulation activities at home during the experimental period. The HOME score captures the quality of parental interaction and investment in children by observing the home environment and maternal activities with her child.

The intervention increased the HOME inventory during the intervention period. At baseline, there was no difference in parenting between treatment and control groups (table S.1). At the end of the 2-year intervention, the HOME inventory of the stunted treatment group was 16%, greater than that of the control group (P = 0.01). However, the effect of the intervention on home environment and maternal activities with her child appears to have declined afterward. Using a series of HOME-like questions designed to capture stimulation activities in mid-to-late childhood (*43*), there was no difference between the treatment and control groups at age 7 or later at age 11.

Although most of the direct parental stimulation encouraged by the intervention seems to have occurred during the treatment period, the intervention may have also affected other types of parental investments later in life that, in turn, also contributed to improved earnings. As children exited the intervention period with higher skills, parents may have realized that investments, such as schooling, had higher returns than they might otherwise have thought. Indeed, significant differences in schooling attainment appear at age 17 (*36*). By age 22, the treatment group had 0.6 (P = 0.08) more years of schooling attainment than the control group. The proportion of the treatment group still enrolled in school full-time (0.22) was more than five times larger than in the control group (0.04) ($P \leq 0.01$).

Table 1. Treatment effect on average log earnings at age 22 (statistically significant results in bold). This table reports the estimated impacts of treatment on log monthly earnings for the observed sample with imputations for the earnings of missing migrants (9 observations imputed). The treatment effects are interpreted as the differences in the means of log earnings between the stunted treatment and stunted control groups conditional on baseline values of child age, gender, weight-for-height z-score, maternal employment, and maternal education. Our P-values are for one-sided block permutation tests of the null hypothesis of no treatment effect (single P-value, in parentheses) and multiple hypotheses (stepdown P-value, in brackets) of no treatment. Permutation blocks are based on the conditioning variables used in the treatment effect regressions. The last column uses a combined statistic that summarizes the participant's outcomes. Specifically, we perform a single-hypothesis inference using the average rank across variables as a test statistic. See section C of the supplementary materials for details.

Job type	All job types	Full-time jobs	Nontemporary jobs	Combined (rank mean)
Treatment effect	**0.30**	**0.22**	**0.39**	**0.09**
Single P-value	**(0.01)**	**(0.04)**	**(0.01)**	**(0.04)**
Stepdown P-value	**[0.02]**	**[0.04]**	**[0.02]**	–
Control mean	9.40	9.59	9.67	0.36
Sample size	109	105	82	109

The stimulation treatment may have improved children's skills enough so that families were encouraged to move overseas to take advantage of better education and labor market opportunities. The overall migration rate of the treatment group (0.22) was significantly higher than that of the control group (0.12) (P = 0.09), implying that treatment is associated with migration.

We examine the impact of the stimulation intervention on average monthly earnings, which are calcuated as total earnings through the date of the survey divided by the number of months worked to that date. Earnings are expressed in 2005 dollars using the Jamaican consumer price index (CPI) and are then transformed into logarithms. Migrants' earnings are first deflated to 2005 using the CPI of residence and were then converted to Jamaican dollars using purchasing power parity (PPP) adjusted exchange rates. In section B.3 of the supplementary materials we report the results of all analyses separately for earnings from the first job, last job, and current job. See section E of the supplementary materials for more details on the construction of these variables.

One issue is that in the treatment group, there are more individuals who both work and attend school full-time than in the control group. Working, full-time students are likely to have lower earnings than nonstudents with the same education. Hence, observed average earnings likely understate the long-run earnings of the treatment group more than the control group, implying that we underestimate the long-run effects of treatment on earnings. We address this issue by restricting the sample to earnings in full-time jobs (at least 20 days per month), which excludes those who had part-time jobs while primarily attending school. We additionally examine a sample restricted to nontemporary permanent jobs (8 months a year or more) in order to omit students working in summer jobs that may have been full-time. Of the 105 individuals in the sample, 103 had participated in the labor force, 99 had a full-time job, and 75 had a nontemporary full-time job.

Another issue is the selective attrition of the migrants. We were able to locate and interview 14 out of the 23 migrants. Among those 14 migrants, we found a significantly larger share of the treatment migrants than of the control migrants. Overrepresentation of treatment migrants can be a source of bias as migrant workers earn substantially more than those who stay in Jamaica. We address potential bias by imputing earnings for the nine missing migrants. We replace missing values with predicted log earnings from an ordinary least-squares regression on treatment, gender, and migration status. Imputing the missing observations reweights the data so that the treatment and control groups of migrants are no longer under- or overrepresented in the sample. In a sensitivity analysis, we omit migrants and still find strong and statistically significant effects of the program on earnings (see section D.4 of the supplementary materials).

We begin by examining the impact of the intervention on densities of log earnings at age 22. Figure 1A presents Epanechnikov kernel density estimates of the treatment and control groups estimated using bandwidths that minimize mean integrated squared error for Gaussian data. The panels show that for all comparisons, the densities of log earnings for the treatment group are shifted everywhere to the right of the control group densities. The differences are greater when we restrict the sample to full-time workers and even greater when we restrict the sample further to nontemporary workers.

The estimated impacts on log earnings, reported in Table 1, show that the intervention had a large and statistically significant effect on earnings. Average earnings from full-time jobs are 25% higher for the treatment group than for the control group, where the percent difference is estimated by exp(β) − 1 and β denotes the treatment effect estimate from Table 1. The impact is substantially larger for full-time permanent (nontemporary) jobs.

The results of the catch-up analysis, presented in Table 2, show that the stunted treatment group caught up with the nonstunted comparison group, whereas the control group remained behind. The differences in log earnings between the nonstunted group and the stunted treatment group are not statistically significant and average around zero. The graphs in Fig. 1B generally show little difference between the earnings densities for the two groups. In contrast, the stunted control group remains behind. The nonstunted comparison group consistently earns significantly more than the stunted control group (Table 2).

Section D of the supplementary materials presents the results of a range of specification tests that corroborate the robustness of the estimates presented in Table 1. Specifically, we first examine treatment effects separately for the pure stimulation intervention and for the combined stimulation/supplemental intervention and test whether we can pool the two arms. Second, we test the hypothesis that there is no effect of nutritional supplementation on log earnings and whether we can pool the supplementation and pure control groups. Third, we examine the extent to which the estimates may be affected by censoring that arises because we only observe the earnings of those employed who are in the labor force. Fourth, we examine the extent to which the imputation of the earnings of missing migrants influences the estimates. Finally, we assess the extent to which the IPW correction for baseline imbalance affected the estimates by reestimating the effects of treatment on earnings without the IPW weights.

Table 2. Catch-up—comparison of average earning at age 22 of the nonstunted and stunted treatment and control samples (statistically significant results in bold). The table presents estimates of the difference in the means of log earnings between, respectively, (I) the weighted nonstunted comparison group and the stunted cognitive stimulation group and (II) the weighted nonstunted comparison group and the stunted control group. Our P-values are for one-sided block permutation tests of the null hypothesis of complete catch-up on each outcome (single P-value, in parentheses) and accounting for multiple hypotheses (stepdown P-values, in brackets). Permutation blocks are based on gender only, but do not control for differences in baseline values, because the aim is to test for catch-up despite the initial disadvantage. The last column uses a combined statistic that summarizes the participant's outcomes. Specifically, we perform a a single-hypothesis inference using the average rank across variables as a test statistic. See section C of the supplementary materials for details.

Job type	All job types	Full-time jobs	Nontemporary jobs	Combined (rank mean)
			(I) Nonstunted—treatment	
Treatment effect	−0.06	−0.08	−0.24	−0.01
Single P-value	(0.68)	(0.75)	(0.94)	(0.59)
Stepdown P-value	[0.78]	[0.79]	[0.94]	–
Control mean	9.90	9.97	10.11	0.47
Sample size	120	116	97	120
			(II) Nonstunted—control	
Treatment effect	0.21	0.13	0.10	0.07
Single P-value	**(0.05)**	(0.15)	(0.24)	**(0.09)**
Stepdown P-value	**[0.08]**	[0.18]	[0.24]	–
Control mean	9.63	9.76	9.77	0.44
Sample size	121	119	101	121

This study experimentally evaluates the long-term impact of an early childhood psychosocial stimulation intervention on earnings in a low-income country. Twenty years after the intervention was conducted, we find that the earnings of the stimulation group are 25% higher than those of the control group and caught up to the earnings of a nonstunted comparison group. These findings show that a simple psychosocial stimulation intervention in early childhood for disadvantaged children can have a substantial effect on labor market outcomes and can compensate for developmental delays. The estimated impacts are substantially larger than the impacts reported for the U.S.-based interventions, suggesting that ECD interventions may be an especially effective strategy for improving long-term outcomes of disadvantaged children in developing countries.

REFERENCES AND NOTES

1. P. R. Huttenlocher, *Brain Res.* **163**, 195–205 (1979).
2. P. R. Huttenlocher, *Neural Plasticity: The Effects of Environment on the Development of the Cerebral Cortex* (Harvard Univ. Press, Cambridge, MA, 2002).
3. R. A. Thompson, C. A. Nelson, *Am. Psychol.* **56**, 5–15 (2001).
4. E. I. Knudsen, J. J. Heckman, J. L. Cameron, J. P. Shonkoff, *Proc. Natl. Acad. Sci. U.S.A.* **103**, 10155–10162 (2006).
5. J. J. Heckman, *Science* **312**, 1900–1902 (2006).
6. J. J. Heckman, *Econ. Inq.* **46**, 289–324 (2008).
7. P. Carneiro, J. J. Heckman, in *Inequality in America: What Role for Human Capital Policies?* J. J. Heckman, A. B. Krueger, B. M. Friedman, Eds. (MIT Press, Cambridge, MA, 2003), pp. 77–239.
8. F. Cunha, J. J. Heckman, L. J. Lochner, D. V. Masterov, in *Handbook of the Economics of Education*, E. A. Hanushek, F. Welch, Eds. (North-Holland, Amsterdam, 2006), chap. 12, pp. 697–812.
9. G. J. van den Berg, M. Lindeboom, F. Portrait, *Am. Econ. Rev.* **96**, 290–302 (2006).
10. D. Almond, L. Edlund, H. Li, J. Zhang, Long-term effects of the 1959-1961 China famine: Mainland China and Hong Kong, *Working Paper 13384*, National Bureau of Economic Research (2007).
11. H. Bleakley, *Q. J. Econ.* **122**, 73–117 (2007).
12. S. L. Maccini, D. Yang, *Am. Econ. Rev.* **99**, 1006–1026 (2009).
13. D. Almond, J. Currie, in *Handbook of Labor Economics*, O. Ashenfelter, D. Card, Eds. (Elsevier, North Holland, 2011), vol. 4B, chap. 15, pp. 1315–1486.
14. P. L. Engle *et al.*, *Lancet* **369**, 229–242 (2007).
15. P. L. Engle *et al.*, *Lancet* **378**, 1339–1353 (2011).
16. J. J. Heckman, *Res. Econ.* **54**, 3–56 (2000).
17. S. Grantham-McGregor *et al.*, *Lancet* **369**, 60–70 (2007).
18. S. P. Walker *et al.*, *Lancet* **369**, 145–157 (2007).
19. C. Paxson, N. Schady, *J. Hum. Resour.* **42**, 49 (2007).
20. L. C. Fernald, P. Kariger, M. Hidrobo, P. J. Gertler, *Proc. Natl. Acad. Sci. U.S.A.* **109** (suppl. 2), 17273–17280 (2012).
21. J. Heckman, S. H. Moon, R. Pinto, P. Savelyev, A. Yavitz, *Quant. Econom.* **1**, 1–46 (2010).
22. J. J. Heckman, S. H. Moon, R. Pinto, P. A. Savelyev, A. Yavitz, *J. Public Econ.* **94**, 114–128 (2010).
23. A. J. Reynolds, S.-R. Ou, J. W. Topitzes, *Child Dev.* **75**, 1299–1328 (2004).
24. A. J. Reynolds *et al.*, *Arch. Pediatr. Adolesc. Med.* **161**, 730–739 (2007).
25. A. J. Reynolds, J. A. Temple, S.-R. Ou, I. A. Arteaga, B. A. B. White, *Science* **333**, 360–364 (2011).
26. F. A. Campbell, C. T. Ramey, E. Pungello, J. Sparling, S. Miller-Johnson, *Appl. Dev. Sci.* **6**, 42–57 (2002).
27. F. A. Campbell *et al.*, *Dev. Psychol.* **48**, 1033–1043 (2012).
28. F. Campbell *et al.*, *Science* **343**, 1478–1485 (2014).
29. A. Aughinbaugh, *J. Hum. Resour.* **36**, 641 (2001).
30. E. Garces, D. Thomas, J. Currie, *Am. Econ. Rev.* **92**, 999–1012 (2002).
31. G. Psacharopoulos, H. A. Patrinos, *Educ. Econ.* **12**, 111–134 (2004).
32. S. M. Grantham-McGregor, C. A. Powell, S. P. Walker, J. H. Himes, *Lancet* **338**, 1–5 (1991).
33. There are, however, experimental studies that show that early-life nutritional interventions also have substantial impacts on earnings (*44*).
34. S. P. Walker, S. M. Chang, M. Vera-Hernández, S. Grantham-McGregor, *Pediatrics* **127**, 849–857 (2011).
35. S. P. Walker, C. A. Powell, S. M. Grantham-McGregor, *Eur. J. Clin. Nutr.* **44**, 527–534 (1990).
36. S. P. Walker, S. M. Chang, C. A. Powell, S. M. Grantham-McGregor, *Lancet* **366**, 1804–1807 (2005).
37. S. P. Walker, S. M. Chang, M. Vera-Hernández, S. Grantham-McGregor, *Pediatrics* **127**, 849–857 (2011).
38. S. P. Walker, S. M. Grantham-Mcgregor, C. A. Powell, S. M. Chang, *J. Pediatr.* **137**, 36–41 (2000).
39. J. M. Robins, A. Rotnitzky, L. P. Zhao, *J. Am. Stat. Assoc.* **89**, 846–866 (1994).
40. J. P. Romano, M. Wolf, *J. Am. Stat. Assoc.* **100**, 94–108 (2005).
41. B. M. Caldwell, *Pediatrics* **40**, 46–54 (1967).
42. B. M. Caldwell, R. H. Bradley, *HOME Observation for Measurement of the Environment* (University of Arkansas at Little Rock, Little Rock, AR, 1984).
43. S. M. Grantham-McGregor, S. P. Walker, S. M. Chang, C. A. Powell, *Am. J. Clin. Nutr.* **66**, 247–253 (1997).
44. J. Hoddinott, J. A. Maluccio, J. R. Behrman, R. Flores, R. Martorell, *Lancet* **371**, 411–416 (2008).

ACKNOWLEDGMENTS

We gratefully acknowledge research support from the World Bank Strategic Impact Evaluation Fund; the American Bar Foundation; The Pritzker Children's Initiative; grants R37HD065072 and R01HD54702 from the Eunice Kennedy Shriver National Institute of Child Health and Human Development; the Human Capital and Economic Opportunity Global Working Group—an initiative of the Becker Friedman Institute for Research in Economics funded by the Institute for New Economic Thinking (INET); a European Research Council grant hosted by University College Dublin; DEVHEALTH 269874; and an anonymous funder. We have benefited from comments of participants in seminars at the University of Chicago; University of California, Berkeley; Massachusetts Institute of Technology; the 2011 LACEA Meetings in Santiago, Chile; and the 2013 AEA Meetings. We thank the study participants for their continued cooperation and willingness to participate, and S. Pellington for conducting the interviews. The authors have not received any compensation for the research nor do they have any financial stake in the analyses reported here. Replication data for this article have been deposited at Interuniversity Consortium for Political and Social Research (ICPSR) and can be accessed at http://doi.org/10.3886/E2402V1.

SUPPLEMENTARY MATERIALS

www.sciencemag.org/content/344/6187/998/suppl/DC1
Materials and Methods
Figs. S1 and S2
Tables S1 to S17
References (*45*–*50*)

22 January 2014; accepted 6 May 2014
10.1126/science.1251178

SOLAR CELLS

Coherent ultrafast charge transfer in an organic photovoltaic blend

Sarah Maria Falke,[1,2]* Carlo Andrea Rozzi,[3]* Daniele Brida,[4,5] Margherita Maiuri,[4] Michele Amato,[6] Ephraim Sommer,[1,2] Antonietta De Sio,[1,2] Angel Rubio,[7,8] Giulio Cerullo,[4] Elisa Molinari,[3,9]† Christoph Lienau[1,2]†

Blends of conjugated polymers and fullerene derivatives are prototype systems for organic photovoltaic devices. The primary charge-generation mechanism involves a light-induced ultrafast electron transfer from the light-absorbing and electron-donating polymer to the fullerene electron acceptor. Here, we elucidate the initial quantum dynamics of this process. Experimentally, we observed coherent vibrational motion of the fullerene moiety after impulsive optical excitation of the polymer donor. Comparison with first-principle theoretical simulations evidences coherent electron transfer between donor and acceptor and oscillations of the transferred charge with a 25-femtosecond period matching that of the observed vibrational modes. Our results show that coherent vibronic coupling between electronic and nuclear degrees of freedom is of key importance in triggering charge delocalization and transfer in a noncovalently bound reference system.

The currently accepted model for the basic working principle of a bulk-heterojunction organic solar cell (*1*, *2*), comprising a conjugated polymer donor and an electron acceptor material, relies on four elementary steps: (i) photon absorption, creating a spatially localized, Coulomb-bound electron-hole pair (exciton) in the donor phase; (ii) exciton diffusion to the donor/acceptor interface; (iii) exciton dissociation at the interface leading to the formation of a charge-separated state (*3*, *4*), often called charge-transfer exciton or polaron pair; and (iv) dissociation of the polaron pair into free charges and their transport to the electrodes.

In this work, we focused on the dynamics of the primary light-induced steps, (i) and (iii), which lead to a charge-separated state in organic photovoltaic (OPV) materials and represent the key process in OPV cells. Over the past years, charge photogeneration has been investigated in several technologically relevant materials, such as blends of polyphenylene-vinylene (*5*, *6*), polythiophene (*7*, *8*), or low band gap polymers (*9*, *10*) with fullerene derivatives. In all of these systems, it is now accepted that charge separation is an ultrafast process occurring on a sub-100-fs time scale. So far the experimental studies on charge photogeneration in OPV materials have mainly been described within the framework of an incoherent transfer model (*11*, *12*), giving a rate constant for the transfer process. These rate constants may be enhanced by hot exciton dissociation

(*10*, *13*). Recently, several theoretical studies have simulated the electronic structure (*14*–*16*) and charge transfer in this class of systems (*17*–*19*) by ab initio and/or model approaches and point toward an important role of vibronic quantum coherence for the charge separation (*17*, *18*). In biological (*20*–*22*) and in some prototypical artificial (*23*, *24*) light-harvesting systems, quantum coherence phenomena have recently been observed experimentally, and this has marked a breakthrough in the description of the primary processes of energy and charge transfer in macromolecular complexes. However, still very little is known about the role of quantum coherence at room temperature in the earliest stage of the dynamics in technologically relevant OPV materials. Recent experiments found evidence for an ultrafast long-range charge separation in such systems but could not differentiate between coherent and incoherent charge-transfer models (*25*).

We studied the ultrafast optical response of a reference OPV material system by combining high time-resolution pump-probe spectroscopy and time-dependent density functional theory (TDDFT) simulations. We observed that the ultrafast electron transfer from the polymer triggers coherent vibrational motion of the fullerene and constitutes the primary step of the photoinduced charge-separation process.

We investigated thin films of the conjugated polymer poly-3-hexylthiophene (P3HT), the fullerene derivative [6,6]-phenyl-C61 butyric acid methyl ester (PCBM), and P3HT:PCBM blends with 1:1 mixing ratio in weight, prepared by spin coating from chlorobenzene solutions. Such blended films are a prototypical material for OPV cells (*26*, *27*), and power conversion efficiencies of up to 5% have been reported (*28*). The absorption spectrum of a P3HT:PCBM blend (Fig. 1A, solid line) appears mainly as a linear superposition of those of the two separate components (Fig. 1B, solid lines) (*29*), indicating that no direct charge-transfer transitions occur in the ground state. Weak absorption features below the lowest excitonic resonance (*30*, *31*) may reflect defects or charge-transfer exciton transitions associated to specific local configurations.

In order to gain insight into the primary photoinduced charge-transfer dynamics of the blend, we performed ultrafast spectroscopic studies on such thin films by using a two-color pump-probe spectrometer providing independently tunable pulses (*32*). Because the charge-carrier photogeneration in P3HT:PCBM blends is essentially independent of temperature (*33*), all experiments were performed at room temperature. The overall time resolution of the setup is better than 15 fs. Pump pulses centered at 540 nm resonantly excite the π–π^* absorption band of P3HT (*30*, *34*), whereas broadband probe pulses monitor the transient absorption in the blue-to-green wavelength range.

Figure 2A shows a measurement of the pump-induced change in optical transmission ($\Delta T/T$) for the P3HT:PCBM blend as a function of probe wavelength λ and pump-probe delay τ. A similar measurement for the pristine P3HT film is reported in the supplementary materials. For probe wavelengths between 500 and 525 nm, the signal is in both samples dominated by ground-state bleaching of the optically excited exciton transition in the polymer. In the shorter wavelength range, the dynamics are substantially different. There, the exciton bleaching of the polymer becomes less prominent, and we have, in the blend, access to an additional stimulated emission signal from the fullerene or intermediate states. In this region, the blended sample displayed an additional and fast-decaying component on a 100-fs time scale (supplementary materials), which can be assigned to an ultrafast charge transfer from the polymer to the fullerene. This time scale is in agreement with previous reports on similar blends (*5*) and with the results of detailed pump-probe measurements covering the probe wavelength range between 550 and 1400 nm. These results (supplementary materials) show that a substantial fraction of all photogenerated excitons in the blend undergo rapid charge separation on a 50- to 70-fs time scale.

For both the pristine P3HT and the blend samples, the $\Delta T/T$ map (Fig. 2A and fig. S2) shows a pronounced oscillatory contrast throughout the entire visible range. We further analyzed these $\Delta T/T$ data by taking the Fourier transform of the oscillatory component after subtraction of a slowly varying background. In the 500- to 520-nm wavelength region (Fig. 2, B and C), we observed, for both the polymer and the blend, the characteristic C=C stretching frequency of the polymer (1450 cm^{-1}, corresponding to a vibrational period of 23 fs). For shorter probe wavelengths, the behavior became more complex: In the pristine film we saw almost no contrast, whereas in the blended film we detected a strong oscillatory component at a higher frequency of 1470 cm^{-1}. This frequency corresponds to the pinch mode dominating the Raman spectrum

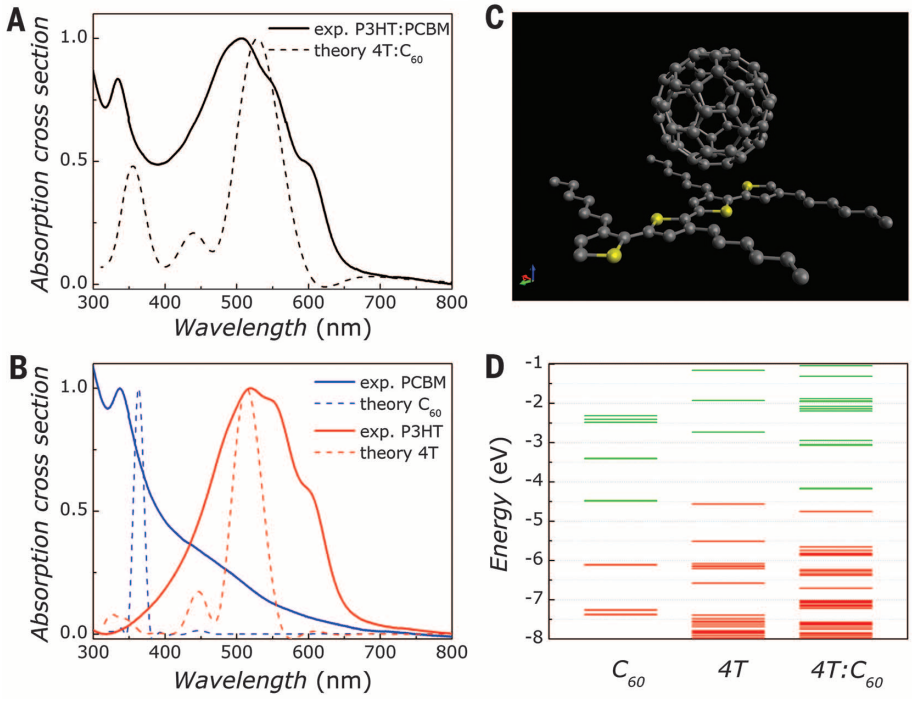


Fig. 1. Linear optical and electronic properties of the materials. (**A**) Normalized thin-film absorption cross section of P3HT:PCBM 1:1 ratio in weight (solid) together with the theoretical 4T:C_{60} absorption spectrum (dashed). No signature of ground-state mixing in the blend is observed. (**B**) Normalized experimental absorption cross sections of PCBM (solid blue) and pristine P3HT (solid red) and the theoretical absorption of C_{60} (dashed blue) and 4T (dashed red). (**C**) Molecular structure of the P3HT:C_{60} blend system. The sulfur atoms belonging to the thiophene rings are depicted in yellow, whereas the carbon atoms are shown in gray. (**D**) Calculated electronic Kohn-Sham levels of (from left to right) C_{60}, 4T, and 4T:C_{60} blend.

[1]Institut für Physik, Carl von Ossietzky Universität, 26129 Oldenburg, Germany. [2]Center of Interface Science, Carl von Ossietzky Universität, 26129 Oldenburg, Germany. [3]Istituto Nanoscienze–Consiglio Nazionale delle Ricerche (CNR), Centro S3, via Campi 213a, 41125 Modena, Italy. [4]Istituto di Fotonica e Nanotecnologie–CNR, Dipartimento di Fisica, Politecnico di Milano, 20133 Milano, Italy. [5]Department of Physics and Center for Applied Photonics, University of Konstanz, 78457 Konstanz, Germany. [6]Institut d'Électronique Fondamentale, UMR8622, CNRS, Universitè Paris-Sud, 91405 Orsay, France. [7]Nano-Bio Spectroscopy Group and European Theoretical Spectroscopy Facility Scientific Development Centre, Departamento Física de Materiales, Universidad del País Vasco (UPV), Centro de Física de Materiales Consejo Superior de Investigaciones Científicas–UPV/Euskal Herriko Unibertsitatea–Materials Physics Center and Donostia International Physics Center, Avenida Tolosa 72, 20018 San Sebastián, Spain. [8]Fritz-Haber-Institut der Max-Planck-Gesellschaft, 14195 Berlin, Germany. [9]Dipartimento di Scienze Fisiche, Informatiche e Matematiche, Università di Modena e Reggio Emilia, via Campi 213a, 41125 Modena, Italy.

*These authors contributed equally to this work. **†Corresponding author. E-mail: elisa.molinari@unimore.it (E.M.); christoph.lienau@uni-oldenburg.de (C.L.)**

of the PCBM film (*35*, *36*). Also in the 470- to 480-nm probe wavelength range, we found vibrational characteristics of the fullerene. There, we saw a weak vibrational mode at 1289 cm^{-1}, corresponding to the $T_{1g}(3)$ mode of PCBM. Control experiments on pristine PCBM films (fig. S3) did not show any evidence of coherence, thus ruling out direct PCBM excitation as a cause for the observed oscillations at 1470 cm^{-1}. These results are difficult to reconcile with an incoherent charge-transfer model, which predicts a gradual and monotonous buildup of charge on the fullerene acceptor on a 100-fs time scale that will not trigger coherent motion on a faster time scale. Also, they cannot be interpreted in terms of an incoherent charge transfer taking place within less than one vibrational period (23 fs) because such a fast transfer is neither seen in the $\Delta T/T$ data in the supplementary materials nor consistent with finding essentially the same linewidths in the absorption spectra of the pristine P3HT film and the blend. Instead, they provide evidence for a coherent charge transfer mediated by strong vibronic couplings between polymer and fullerene.

To analyze the experimental observations, we have performed first-principle calculations (*25*) on the simplest possible model of the experimentally studied thin-film blend, a periodic crystal of charge transfer dimers. PBCM has been substituted with a C_{60} molecule, and the alkyl side chains on the polymer have been removed in order to reduce the numerical complexity, checking that this does not affect the ground-state properties of the system. By using density functional theory (DFT) at the local density approximation (LDA) level, we relaxed the ground state of the system and found an equilibrium distance of 3.2 Å between 4T and C_{60}. The Kohn-Sham electron energy levels of the 4T:C_{60} unit are shown in Fig. 1D together with the electronic structure of the isolated C_{60} and 4T, all aligned to vacuum. The orbital localization shows a highest occupied molecular orbital (HOMO) with 96% localization on the thiophene chain and a lowest unoccupied molecular orbital (LUMO) almost fully localized on the fullerene. The lowest-lying available single-particle thiophene excitation corresponds to a HOMO-to-LUMO transition with 94% localization on the polymer. Steady-state optical absorption spectra (*37*, *38*) of the blend and the isolated components are depicted in Fig. 1, A and B, respectively. The absorption cross sections of both the isolated moieties and of 4T:C_{60} are in good agreement with the experimentally observed ones. They consist of two distinct absorption bands, centered at 528 and 354 nm, that correspond to thiophene and fullerene excitations, respectively. This calculation supports the picture of a system composed of moieties that are weakly interacting in their ground states.

TDDFT simulations of the dynamics of the photoexcited 4T:C_{60} model system were performed by imposing periodic boundary conditions in order to mimic the experimental configuration of a blended thin film. We interrogated the system dynamics by assuming an initial instantaneously excited electronic state corresponding to the removal of an electron from the polymer HOMO and the creation of an electron in the polymer LUMO. We chose as initial condition a Maxwellian distribution of random nuclear velocities to approximate the experimental room-temperature environment. We observed that an electron is transferred to C_{60} with 60% probability within 97 fs, in good agreement with experimental findings (*7*, *8*). Moreover, the charge-transfer probability, taken as the spatially integrated excess charge density on the C_{60}, oscillated in time with a period of about 25 ± 4 fs (Fig. 3A). This period approximately matches the oscillation frequency observed in the experiments. A useful insight into the charge delocalization mechanism is gained by looking at the first few time-dependent Kohn-Sham eigenvalues above the 4T HOMO (Fig. 3C). The continuous purple line represents the 4T LUMO, occupied at time 0 by one electron removed from the 4T HOMO (purple broken line). Its energy undergoes pronounced oscillations in antiphase with the C_{60} LUMO. At each crossing of the two levels, the charge density is free to move through the system (Fig. 3C), causing a transient peak in the current flowing between 4T and C_{60} and back (Fig. 3A). Instead, the current flow is suppressed when 4T and C_{60} LUMOs are energetically detuned, resulting in a periodic variation of the current flow and thus an oscillatory modulation of amount of charge transferred to the C_{60} moiety. In the long term, the charge will be localized on the acceptor both by a nuclear rearrangement and by energy dissipation. This regime, however, is out of the scope of the present calculations. Our simulations thus predict that vibronic coupling is necessary for charge transfer to occur and indicate that this coupling is responsible for dynamically driving 4T and C_{60} LUMOs in resonance, explaining the coherent oscillations of the transferred charge. In fact, the electronic excitation remains fully localized on the polymer when keeping the ions in fixed positions (fig. S4).

The charge separation is further analyzed by examining the time-dependent dipole moment of the system (Fig. 3B). Its z component is oriented along the axis from the polymer to the C_{60} and oscillates in phase with the displaced charge, whereas the y component shows weakly anticorrelated oscillations along the polymer chain. This again points to vibronic coherence and a periodic charge flow between polymer and fullerene. The dynamics of the charge separation process are nicely visualized by displaying the time evolution of the electronic density projected onto the coupled LUMO orbitals of the blend (Fig. 3, D to F, and movie S1). This charge density is created by photoexcitation at time zero and is initially fully localized on the polymer (Fig. 3D). As the time evolves, the charge density delocalizes between polymer and C_{60}, and the degree of fractional charge on both moieties displays anticorrelated temporal oscillations. At the end of the simulation, it is shared between donor and acceptor (Fig. 3F).

In the simulations, we also analyzed the time-dependent ionic displacements (movie S2) and found that the photoexcitation of 4T promotes vibrational motion of the C_{60} with similar oscillation period as is found in the charge transfer probability. This is consistent with the experimental observation of collective vibronic coherence of the fullerene triggered by impulsive photoexcitation of the polymer.

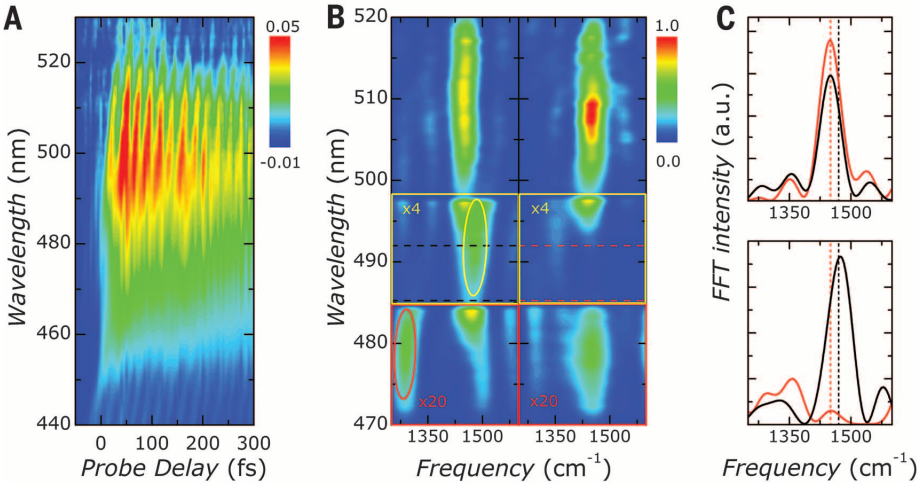


Fig. 2. Charge transfer dynamics of the P3HT:PCBM blend. (**A**) Experimental differential transmission ($\Delta T/T$) map of the P3HT:PCBM blend as a function of probe delay and probe wavelength. The pronounced oscillations in the $\Delta T/T$ signal reflect coherent vibrational wave-packet motion initiated by the short pump pulse. (**B**) Fourier transform spectra of the $\Delta T/T$ dynamics of the blend (left) and pristine P3HT (right). The spectral intensity is amplified by a factor of 4 for λ = 498 to 485 nm and by a factor of 20 for λ = 485 to 470 nm. (**C**) Integrated Fourier transform spectra for λ = 520 to 498 nm (top) and λ = 492 to 485 nm [bottom, dashed lines in (B)] of the blend (black) and pristine P3HT (red). The dashed vertical lines indicate the frequency of the P3HT C=C stretch mode (red) at 1450 cm^{-1} and pentagonal-pinch mode of the fullerene (black) at 1470 cm^{-1}.

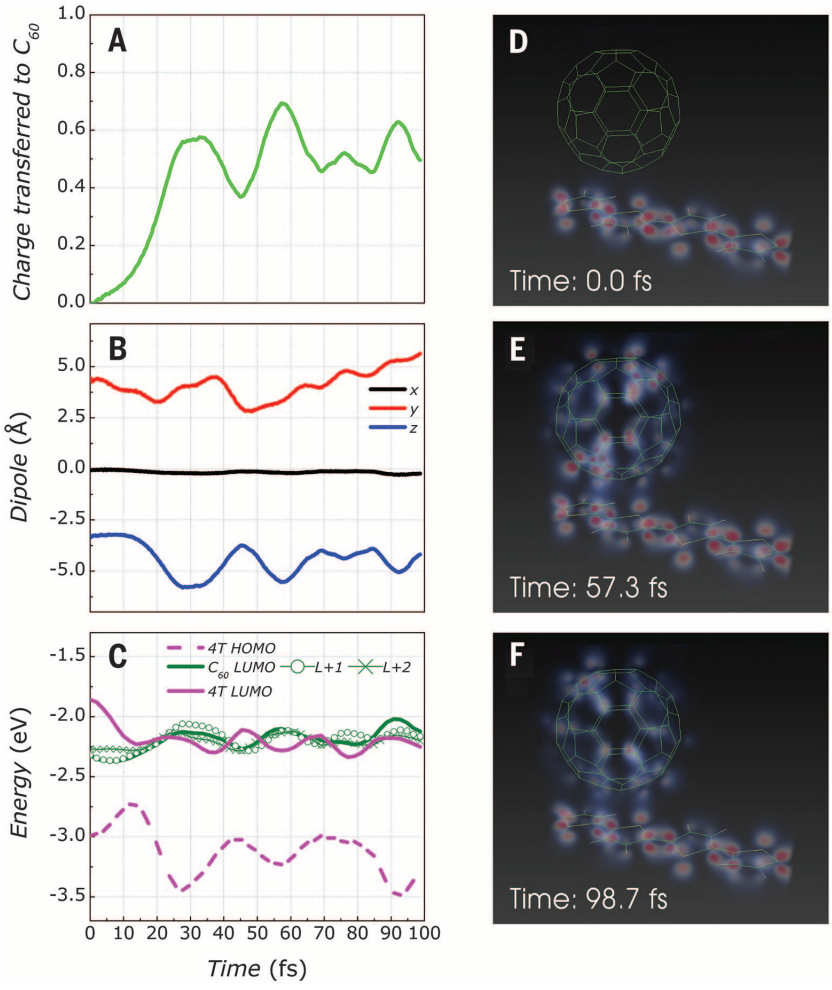


Fig. 3. Simulation of the charge transfer dynamics. (**A**) Charge-transfer dynamics in a crystal of 4T:C60 aggregates after impulsive 4T excitation at time zero. After 97 fs, the charge-transfer probability from 4T to C_{60} is 60%. Strong oscillations of the transfer probability, with a period of about 25 ± 4 fs, are the signature of coherent charge-transfer dynamics. (**B**) Time dynamics of the molecular dipole. The *z* component, oriented along the axis from the 4T to the C_{60}, oscillates in phase with the displaced charge. (**C**) Time-dependent Kohn-Sham eigenvalues. The purple lines refer to the 4T HOMO (broken) and 4T LUMO (solid) levels; the green lines to the lowest unoccupied C_{60} levels, respectively. (**D** to **F**) Snapshots of the simulated time evolution of the charge density in the coupled 4T and C_{60} LUMOs. Initially (D), the charge is completely localized on the 4T chain. As time evolves, it delocalizes between 4T and C_{60} [(E) 57.3 fs]. After 98.7 fs (F), the charge density is shared between 4T and C_{60}.

We recently studied the charge-transfer dynamics in a very different system, a supramolecular carotene-porphyrin-fullerene triad (*24*), a model system for artificial light harvesting. The physical nature of this system, a covalently bound molecular complex in solution, is fundamentally different from the one studied here. Nevertheless, we find similar charge oscillations, with a period of about 30 fs, when studying the charge transfer between porpyhrin and fullerene. We believe that the key to the similarity of those values can be found in Fig. 3C. It shows that the energies of the relevant LUMOs of the polymer and fullerene vary in time with a period corresponding to that of the vibrational mode to which the electronic state is strongly coupled. The probability for charge transfer is large whenever the polymer and fullerene LUMOs are transiently brought into resonance. Hence, the amount of transferred charge (Fig. 3A) oscillates at the (average) period of the vibrational mode(s) most strongly coupled to the electronic system.

In case of the P3HT:PCBM blend, these are the C=C stretch mode of the polymer at 1450 cm^{-1} and the pentagonal pinch mode of PCBM at 1470 cm^{-1}, corresponding to an oscillation period of ~23 fs. This agrees reasonably well with the period of 25 ± 4 fs that we deduce from Fig. 3, A to C. This period is slightly shorter than the 30 fs that we saw in the case of the triad.

We suggest that the similarity of oscillation periods is a direct consequence of strong vibronic coupling. The time evolution of the charge distribution is modulated with a period matching that of the vibrational modes that are most strongly coupled to the charge excitations. Because all carbon-based organic systems have strong vibrations in the 1000 to 1500 cm^{-1} range, it is likely to experimentally find oscillation periods between 20 and 30 fs. Our results suggest that, despite the very different microscopic properties of the triad and the P3HT:PCBM blend, the coherent charge-transfer dynamics are in both cases governed by strong vibronic coupling.

A consistent and general picture of the elementary photoinduced charge-transfer process in the P3HT:PCBM blend emerges from our detailed experimental and theoretical results. Optical excitation locally creates an electron-hole pair on the polymer moiety. The strong vibronic coupling between electronic and nuclear degrees of freedom promotes a delocalization of the optically excited electronic wave packet across the interface. Both the electronic density and the nuclei display correlated oscillations on the same time scales, which are essential for an ultrafast charge transfer from the donor to the acceptor. The observation of coherent electron-nuclear motion in a noncovalently bound complex, averaging over a macroscopic ensemble of P3HT:PCBM moieties with variable environment and interfaces, is strong evidence for the dominant role of quantum coherences in the early stages of the charge transfer dynamics in this class of OPV materials.

REFERENCES AND NOTES

1. G. Yu, J. Gao, J. C. Hummelen, F. Wudl, A. J. Heeger, *Science* **270**, 1789–1791 (1995).
2. C. J. Brabec *et al.*, *Adv. Mater.* **22**, 3839–3856 (2010).
3. I.-W. Hwang, D. Moses, A. J. Heeger, *J. Phys. Chem. C* **112**, 4350–4354 (2008).
4. M. Hallermann, S. Haneder, E. Da Como, *Appl. Phys. Lett.* **93**, 053307–053303 (2008).
5. C. J. Brabec *et al.*, *Chem. Phys. Lett.* **340**, 232–236 (2001).
6. N. S. Sariciftci, L. Smilowitz, A. J. Heeger, F. Wudl, *Science* **258**, 1474–1476 (1992).
7. J. Guo, H. Ohkita, H. Benten, S. Ito, *J. Am. Chem. Soc.* **132**, 6154–6164 (2010).
8. I. A. Howard, R. Mauer, M. Meister, F. Laquai, *J. Am. Chem. Soc.* **132**, 14866–14876 (2010).
9. I. W. Hwang *et al.*, *Adv. Mater.* **19**, 2307–2312 (2007).
10. G. Grancini *et al.*, *Nat. Mater.* **12**, 29–33 (2013).
11. R. A. Marcus, *Angew. Chem. Int. Ed. Engl.* **32**, 1111–1121 (1993).
12. A. A. Bakulin *et al.*, *Science* **335**, 1340–1344 (2012).
13. A. E. Jailaubekov *et al.*, *Nat. Mater.* **12**, 66–73 (2013).
14. L. Pandey, C. Risko, J. E. Norton, J.-L. Brédas, *Macromolecules* **45**, 6405–6414 (2012).
15. Y. Kanai, Z. Wu, J. C. Grossman, *J. Mater. Chem.* **20**, 1053–1061 (2010).
16. J. Ren, S. Meng, E. Kaxiras, *Nano Res.* **5**, 248–257 (2012).
17. H. Tamura, R. Martinazzo, M. Ruckenbauer, I. Burghardt, *J. Chem. Phys.* **137**, A540 (2012).
18. H. Tamura, I. Burghardt, M. Tsukada, *J. Phys. Chem. C* **115**, 10205–10210 (2011).
19. H. Tamura, I. Burghardt, *J. Phys. Chem. C* **117**, 15020–15025 (2013).
20. H. Lee, Y. C. Cheng, G. R. Fleming, *Science* **316**, 1462–1465 (2007).
21. E. Collini *et al.*, *Nature* **463**, 644–647 (2010).
22. G. D. Scholes, G. R. Fleming, A. Olaya-Castro, R. van Grondelle, *Nat. Chem.* **3**, 763–774 (2011).
23. E. Collini, G. D. Scholes, *Science* **323**, 369–373 (2009).
24. C. A. Rozzi *et al.*, *Nat Commun* **4**, 1602 (2013).
25. S. Gélinas *et al.*, *Science* **343**, 512–516 (2014).
26. G. Dennler, M. C. Scharber, C. J. Brabec, *Adv. Mater.* **21**, 1323–1338 (2009).
27. M. T. Dang, L. Hirsch, G. Wantz, *Adv. Mater.* **23**, 3597–3602 (2011).

28. W. Ma, C. Yang, X. Gong, K. Lee, A. J. Heeger, *Adv. Funct. Mater.* **15**, 1617–1622 (2005).
29. S. Cook, R. Katoh, A. Furube, *J. Phys. Chem. C* **113**, 2547–2552 (2009).
30. J. Clark, C. Silva, R. H. Friend, F. C. Spano, *Phys. Rev. Lett.* **98**, 206406 (2007).
31. W. J. D. Beenken *et al.*, *Phys. Chem. Chem. Phys.* **15**, 16494–16502 (2013).
32. C. Manzoni, D. Polli, G. Cerullo, *Rev. Sci. Instrum.* **77**, 023103 (2006).
33. W. J. Grzegorczyk *et al.*, *J. Phys. Chem. C* **114**, 5182–5186 (2010).
34. P. J. Brown *et al.*, *Phys. Rev. B* **67**, 064203 (2003).
35. D. S. Bethune, G. Meijer, W. C. Tang, H. J. Rosen, *Chem. Phys. Lett.* **174**, 219–222 (1990).
36. S. Falke, P. Eravuchira, A. Materny, C. Lienau, *J. Raman Spectrosc.* **42**, 1897–1900 (2011).
37. X. Andrade *et al.*, *J. Chem. Theory Comput.* **5**, 728–742 (2009).
38. A. Castro *et al.*, *Phys. Status Solidi B Basic Res.* **243**, 2465–2488 (2006).

ACKNOWLEDGMENTS

Financial support by the European Union project CRONOS (grant number 280879-2), the Deutsche Forschungsgemeinschaft (SPP1391), the Korea Foundation for International Cooperation of Science and Technology (Global Research Laboratory project, K20815000003), and the Italian Fondo per gli Investimenti della Ricerca di Base (Flashit project) is gratefully acknowledged. C.A.R. and E.M. acknowledge the Partnership for Advanced Computing in Europe (project LAIT) for awarding us access to supercomputing resources at CINECA, Italy, and useful discussions with C. Cocchi and Y. Kanai. S.M.F. is grateful for a Ph.D. fellowship from Stiftung der Metallindustrie im Nord-Westen. C.L. and G.C. acknowledge support from the European Community (Seventh Framework Programme INFRASTRUCTURES-2008-1, Laserlab Europe II contract no. 228334); A.R. acknowledges financial support from the European Research Council (ERC-2010-AdG-267374), Spanish grant (FIS2010-21282-C02-01), Grupos Consolidados (IT578-13), Ikerbasque. G.C. acknowledges financial support by the European Research Council (ERC-2011-AdG no. 291198). C.L., S.M.F., G.C., C.A.R., and E.M. initiated this work. S.M.F. prepared the samples. S.M.F., D.B., M.M., E.S., and A.D.S. performed the ultrafast spectroscopy experiments. C.A.R. and M.A. performed DFT and TDDFT simulations. S.M.F., A.D.S., D.B., G.C., and C.L. analyzed and discussed the experimental data. C.A.R., M.A., E.M., and A.R. analyzed and discussed the theoretical data. C.A.R., E.M., G.C., A.D.S., and C.L. designed the paper. All authors discussed the implications and contributed to the writing of the paper. The authors declare no competing financial interests.

SUPPLEMENTARY MATERIALS

www.sciencemag.org/content/344/6187/1001/suppl/DC1
Materials and Methods
Supplementary Text
Figs. S1 to S10
References (*39*–*48*)
Movies S1 and S2

16 December 2013; accepted 7 May 2014
10.1126/science.1249771

WATER SPLITTING

Amorphous TiO_2 coatings stabilize Si, GaAs, and GaP photoanodes for efficient water oxidation

Shu Hu,[1,2] Matthew R. Shaner,[1,2] Joseph A. Beardslee,[1] Michael Lichterman,[1,2] Bruce S. Brunschwig,[3] Nathan S. Lewis[1,2,3,4]*

Although semiconductors such as silicon (Si), gallium arsenide (GaAs), and gallium phosphide (GaP) have band gaps that make them efficient photoanodes for solar fuel production, these materials are unstable in aqueous media. We show that TiO_2 coatings (4 to 143 nanometers thick) grown by atomic layer deposition prevent corrosion, have electronic defects that promote hole conduction, and are sufficiently transparent to reach the light-limited performance of protected semiconductors. In conjunction with a thin layer or islands of Ni oxide electrocatalysts, Si photoanodes exhibited continuous oxidation of 1.0 molar aqueous KOH to O_2 for more than 100 hours at photocurrent densities of >30 milliamperes per square centimeter and ~100% Faradaic efficiency. TiO_2-coated GaAs and GaP photoelectrodes exhibited photovoltages of 0.81 and 0.59 V and light-limiting photocurrent densities of 14.3 and 3.4 milliamperes per square centimeter, respectively, for water oxidation.

The oxidation of water to O_2 is a key process in the direct photoelectrochemical (PEC) production of fuels from sunlight (*1*, *2*). A fuel-forming reductive half-reaction involving the reduction of CO_2 to lower hydrocarbons or the reduction of H_2O to H_2 requires an oxidative half-reaction, such as the oxidation of water to O_2. Metal oxide photoanodes can oxidize water to O_2 in alkaline or acidic media, but thus far have been inefficient because their band gaps are too large and because the potential of their valence band edge is much more positive than the formal potential for water oxidation, $E^{o'}(O_2/H_2O)$ (*3*). Although many semiconductors, including silicon (Si), gallium arsenide (GaAs), and gallium phosphide (GaP), have valence-band edges at more negative potentials than metal oxides and also typically have optimal band gaps for efficient solar-driven water splitting, these semiconductors are unstable when operated under photoanodic conditions in aqueous electrolytes. Specifically, in competition with oxidizing water to O_2, these materials either anodically photocorrode or photopassivate (*3*, *4*). Furthermore, passive and intrinsically safe solar-driven water-splitting systems can only be constructed (*5*) in either alkaline or acidic media, and the development of general strategies to stabilize existing photoelectrode materials under water-oxidation conditions is an important goal.

Various coating strategies have been explored to stabilize semiconductors with optimal band gaps (1.1 to 1.7 eV) for direct water splitting (*6*). Deposition of thin films of Pd (*7*), Pt (*8*), Ni (*9*), or metal-doped SiO_x (*10*) onto n-type Si or n-GaAs photoanodes yields improved stability under water-oxidation conditions, primarily near neutral pH, as well as in strongly alkaline (*9*) or acidic (*10*) media for up to 12 hours. However, these stabilized photoanodes generally exhibit low photovoltages; additionally, the protective metal coating is either too thick to be highly optically transmissive or too thin to afford extended stability during water oxidation, particularly in alkaline or acidic media. Transparent conductive oxide (TCO) coatings on Si and GaAs are not stable in strongly alkaline or acidic media, and also produce low voltages because of defective semiconductor/TCO interfaces. (*11*, *12*) Coatings of Ni islands (*9*), as well as MnO_x (*13*) and NiO_x (*14*) films on Si, have been used to catalyze the oxidation of water and thus provide some degree of stability enhancement. However, such coatings do not enable prolonged operation in alkaline media and/or yield very low photovoltages because of a large density of interface states at the Si/Ni interface.

Conformal layers of 2-nm thin TiO_2 formed by atomic layer deposition (ALD) have been used to stabilize Si, and in conjunction with an IrO_x catalyst, to effect water oxidation (*15*). Deposition of such electrically insulating films at larger thickness, to reliably prevent pinholes and thus suppress active corrosion over macroscopic areas, creates a tunneling barrier for photogenerated holes. As this barrier becomes thicker, it no longer conducts holes via a tunneling mechanism and also introduces a large series resistance to a PEC device, degrading its efficiency to low values. Specifically, as the TiO_2 thickness was increased, the overpotential for the oxygen-evolution reaction (OER) increased linearly at a rate of ~21 mV nm^{-1} (*16*), resulting in an additional voltage loss of ~200 mV for a 12-nm thick TiO_2 overlayer, even at a current density of 1 mA cm^{-2}.

We describe a general approach to significantly improve the stability of Si, GaAs, and GaP photoanodes against both photocorrosion and photopassivation for water oxidation in alkaline media [all results reported below are

[1]Division of Chemistry and Chemical Engineering, California Institute of Technology, Pasadena, CA 91125, USA. [2]Joint Center for Artificial Photosynthesis, California Institute of Technology, Pasadena, CA 91125, USA. [3]Beckman Institute and Molecular Materials Research Center, California Institute of Technology, Pasadena, CA 91125, USA. [4]Kavli Nanoscience Institute, California Institute of Technology, Pasadena, CA 91125, USA.
*Corresponding author. E-mail: nslewis@caltech.edu

for 1.0 M aqueous KOH (pH 13.7) unless noted otherwise]. Instead of promoting corrosion of the underlying anode, the photogenerated holes are conducted away from the semiconductor through hundred-nanometer-thick, "electronically leaky" TiO_2 films to Ni islands on the surface of the film, where the holes are used by Ni oxide to oxidize water to O_2 (Fig. 1A). The Ni islands or thin Ni film/TiO_2 coating transmits most of the incident light and preserves high short-circuit photocurrent densities expected from the underlying semiconductor under simulated sunlight. The conduction mechanism through the protective coating is different from that obtained from a tunneling barrier, and the photoanodes additionally exhibited much larger photovoltages than those obtained from the direct deposition of metal or TCO films onto Si or GaAs photoanodes (*6*, *7*, *10*, *11*).

Thick overlayers of TiO_2 (4 to 143 nm) were deposited on Si, GaAs, and GaP electrodes by ALD, to provide a range of coating thicknesses that allowed for minimization of the pinhole density while providing conformality and acceptable barrier layer properties. Thermal annealing produced stoichiometric insulating crystalline TiO_2 films that created an interfacial tunneling barrier for photogenerated charge carriers. Hence, instead we used unannealed TiO_2, which is electronically defective and possibly nonstoichiometric, to allow for the passage of very high (>1 A cm^{-2}) current densities as a "leaky" dielectric (*17*). The electronic defects in these unannealed ALD-grown TiO_2 films presumably arise from structural disorder (amorphous phase) and/or chemical impurities (such as carbon or nitrogen) from the precursors used in the ALD process [as shown by secondary-ion mass spectroscopy, fig. S1 (*18*)]. Hall measurements indicated that the concentration of electrons in the as-grown ALD-TiO_2 was 4×10^{16} cm^{-3}. We then deposited a 100-nm-thick Ni film or 100-nm-thick Ni islands (square arrays of 3-μm-diameter circles on a 7-μm pitch) onto the TiO_2 overlayer by sputtering or electron-beam evaporation.

The electrochemical current density (J) versus potential (E) behavior of degenerately p-type doped p^+-Si and p^+-GaAs electrodes covered with 4 to 143 nm of TiO_2 and a 100-nm-thick Ni film were measured in the dark to determine the overpotential associated with these films. The catalytic activity of Ni oxide improves over time in alkaline electrolytes, and hence the depicted data are from the third voltammetric cycle of the electrode. The overpotential required to drive the OER at a current density of 10 mA cm^{-2} was 0.34 to 0.37 V for a degenerately doped p^+-Si/TiO_2/Ni-film electrode and was 0.37 V for a p^+-GaAs/TiO_2/Ni-film electrode [fig. S2 (*18*)]. At a current density of 20 mA cm^{-2}, the voltage loss caused by the TiO_2 coatings on a p^+-Si/TiO_2/Ni-film electrode was thus <50 mV as compared to that of a continuous 100–nm-thick Ni film with no intervening TiO_2 layer. The measured overpotentials are in accord with the reported behavior of Ni oxide for OER in alkaline media. (*19*–*21*) An oxygen probe indicated that O_2 (gaseous) was produced with 99 ± 1% Faradaic efficiency in these systems.

The PEC behavior of unannealed TiO_2 coatings on photoactive n-Si and n-GaP, as well as the behavior of unannealed TiO_2 on buried-junction n-p^+-Si photoelectrodes and on buried-junction n-p^+-GaAs electrodes, is shown in Fig. 1, B to E. The electrocatalyst overlayers were 100-nm-thick patterned Ni islands on Si and were 2-nm Ni films on GaAs and GaP. A p^+ emitter layer was additionally formed on the n-Si to demonstrate

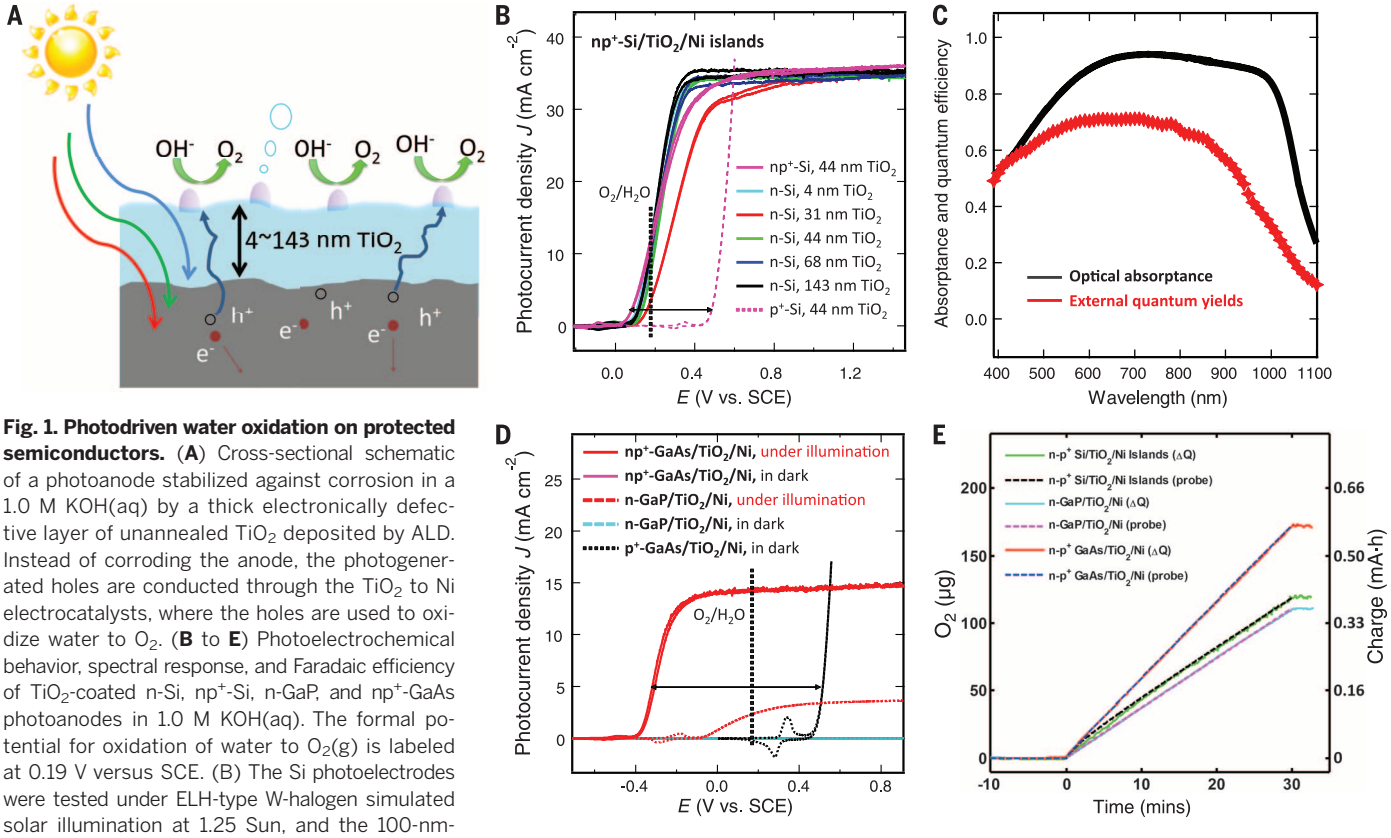


Fig. 1. Photodriven water oxidation on protected semiconductors. (**A**) Cross-sectional schematic of a photoanode stabilized against corrosion in a 1.0 M KOH(aq) by a thick electronically defective layer of unannealed TiO_2 deposited by ALD. Instead of corroding the anode, the photogenerated holes are conducted through the TiO_2 to Ni electrocatalysts, where the holes are used to oxidize water to O_2. (**B** to **E**) Photoelectrochemical behavior, spectral response, and Faradaic efficiency of TiO_2-coated n-Si, np^+-Si, n-GaP, and np^+-GaAs photoanodes in 1.0 M KOH(aq). The formal potential for oxidation of water to O_2(g) is labeled at 0.19 V versus SCE. (B) The Si photoelectrodes were tested under ELH-type W-halogen simulated solar illumination at 1.25 Sun, and the 100-nm-thick Ni-island electrocatalysts were patterned in square arrays of 3-μm-diameter circles on a 7-μm pitch. (**C**) Overlay of the normal-incidence optical absorptance and external quantum yields for n-Si photoelectrodes coated with 68 nm of TiO_2 and patterned Ni islands. The electrode potential was held at 0.35 V versus SCE. (**D**) The 2-nm Ni /118-nm TiO_2–coated np^+-GaAs and n-GaP photoelectrodes were tested under simulated AM 1.5 illumination at 1 Sun and in the dark. The dark behavior of typical p^+-Si/TiO_2/Ni and p^+-GaAs/TiO_2/Ni electrodes is chosen from fig. S2 (*18*) and included in (B) and (D), respectively, to show the shift in potential of the photoelectrodes. (**E**) Overlay of the cumulative O_2(g) detected and charge passed from 0 to 30 min for Ni islands/44-nm TiO_2-coated np^+-Si and np^+-GaAs photoelectrodes, and 2-nm Ni/118-nm TiO_2-coated n-GaP photoelectrodes. The electrodes were held at 0.05, −0.32. and 0.18 V versus SCE, respectively. The axes were labeled assuming a 100% Faradaic efficiency when the data for charge passed and O_2 detected overlap.

the versatility of the protection strategy, because this buried junction was expected to produce a characteristic open-circuit voltage, V_{oc}, of 0.50 to 0.55 V at illumination intensities sufficient to produce short-circuit photocurrent densities of 33.6 mA cm^{-2}, in accord with expectations based on the diode-limited performance of Si n-p^+ junctions at the doping densities investigated.

Under 1.25-Sun of ELH-type W-halogen simulated solar illumination, the light-limited photocurrent density of the n-Si/TiO_2/Ni-island and n-p^+-Si/TiO_2/Ni-island electrodes was 34.7 ± 1.7 mA cm^{-2} for a TiO_2 thickness of 4 to 143 nm (Fig. 2A), corresponding to a photocurrent density of 27.7 ± 1.4 mA cm^{-2} at 1 Sun. This current density is in accord with expectations (27.0 mA cm^{-2}) based on an integration of the measured spectral response of the photoanodes (Fig. 2B) with the air mass (AM) 1.5 1-Sun solar spectrum. The n-p^+-Si/TiO_2/Ni-island and n-p^+-GaAs/TiO_2/Ni-film photoanodes exhibited photovoltages of 0.52 ± 0.03 V and 0.81 ± 0.02 V relative to the formal potential for water oxidation, $E^{o\prime}(O_2/H_2O)$ of 0.19 V versus a saturated calomel electrode (SCE), respectively. Under the respective illumination conditions, the Si/TiO_2/Ni island photoelectrode exhibited a photocurrent density of 6.6 mA cm^{-2} at a potential of 0.13 V versus SCE, and the GaAs/TiO_2/Ni film photoelectrode exhibited a photocurrent density of 11.9 mA cm^{-2} at a potential of −0.22 V versus SCE. The n-GaP/TiO_2/Ni film photoanodes showed a 0.59 ± 0.02 V photovoltage versus $E^{o\prime}(O_2/H_2O)$ under simulated AM 1.5 1-Sun illumination, with a photocurrent density of 1.4 mA cm^{-2} at a potential of 0.06 V versus SCE. The light-limited photocurrent densities for the TiO_2-coated GaAs and GaP photoelectrodes were 14.3 and 3.4 mA cm^{-2} at 1 Sun, respectively. The catalytic currents for Si, GaAs, and GaP photoanodes became significant on this current scale at ~0.3 V more positive than the measured open-circuit potentials of the respective photoelectrodes under illumination, due to the overpotentials associated with electrocatalysis of the OER under these conditions. The O_2(g) detected by an O_2 probe (Fig. 1E) was plotted assuming that four holes generated one molecule of O_2(g) at 100% Faradaic efficiency; i.e., 0.33 mA hour of charge passed corresponded to 100 μg of generated O_2. All of these photoelectrodes thus showed 99 ± 1% Faradaic efficiency for O_2 production, as determined by the calibrated O_2 probe.

Figure 2 shows the photocurrent density as a function of time for an n-p^+-Si/TiO_2/Ni-island electrode under light-limited conditions (1.25 Sun) at 0.93 V versus SCE. The light intensity was monitored by a photodiode, and fluctuations of the photocurrent were caused by the formation of O_2 bubbles on the electrode as well as by variations in the illumination intensity from the lamp. The photocurrent for the unannealed, electronically defective TiO_2-coated Si photoelectrode with patterned Ni islands decreased by ~10% after 100 hours of continuous operation, and the fill factor (*ff*) decreased only slightly [<5%; fig. S5 (*18*)]. The analogous n-p^+-GaAs/TiO_2/Ni-film and n-GaP/TiO_2/Ni-film photoanodes also exhibited stable water-oxidation photocurrents for >25 hours of continuous operation [fig. S6 (*18*)]. The photocurrent and *ff* decreased by ~8% and <5% after 5 hours, respectively.

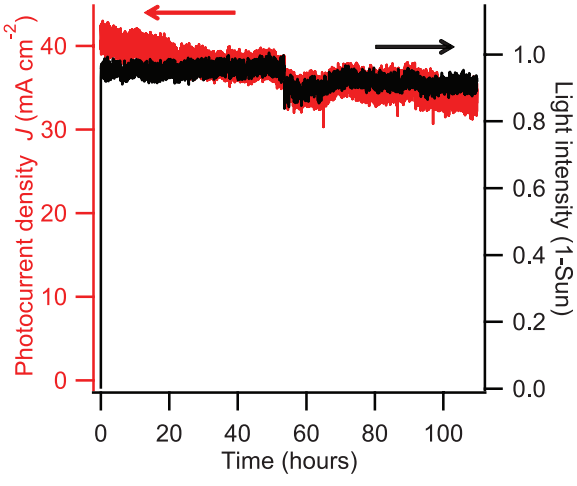


Fig. 2. Chronoamperometry of an n-p^+-Si photoanode coated with 44 nm of TiO_2 and Ni islands for over 100 hours in 1.0 M KOH(aq). The photocurrent density versus time (red curve) was overlaid with the illumination intensity versus time (black curve). The electrode potential was held at 0.93 V versus SCE. The ENH-type tungsten-halogen light bulb burned out at the 54th hour and was then replaced with another ENH bulb, and the experiment was continued as indicated. The illumination intensity was 1.25 Sun.

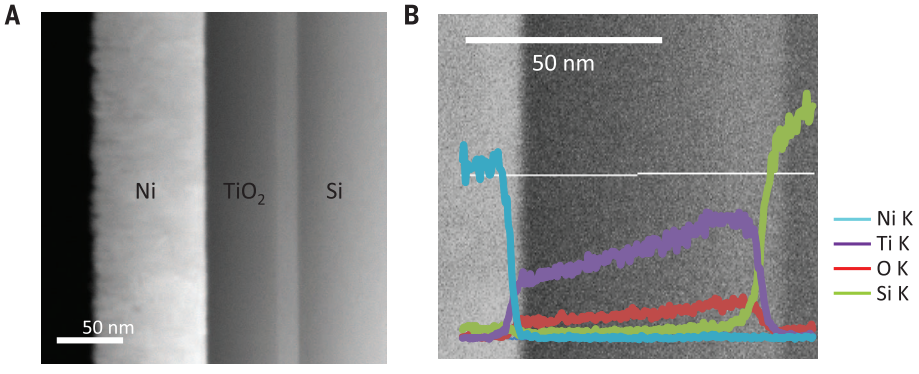


Fig. 3. Structural and chemical characterization of the Si/TiO_2/Ni interface. Both Ni and TiO_2 films in this study were continuous, with thicknesses of 100 nm and 68 nm, respectively. (**A**) Elemental contrast image of the Si/TiO_2/Ni interface by scanning TEM. (**B**) EDS line profiles of Ni, Ti, O, and Si across the TiO_2 interface.

The Si/TiO_2/Ni interface was characterized in cross-section using element-contrast scanning transmission electron microscopy (Fig. 3A) as well as energy-dispersive x-ray spectroscopy (EDS) with <1 nm spatial resolution (Fig. 3B). The EDS line profiles of Ni, Ti, and O across the same TiO_2/Ni interface showed a gradual decrease of the Ni signal as the Ti signal increased when the sampled area was scanned from the bulk Ni film into the TiO_2 film. Hence, detectable intermixing of Ni and TiO_2 occurred only within a region ~5 nm in depth. The major diffraction-ring pattern observed in a selected-area diffraction pattern acquired at the Ni/TiO_2 interface indicated the presence of a polycrystalline phase of Ni, whereas the diffused ring that surrounded the transmitted beam can be attributed to the amorphous structure of the TiO_2 [fig. S7 (*18*)].

Secondary-ion mass spectrometry (SIMS) on TiO_2 films with and without Ni deposition [fig. S1 (*18*)] confirmed the EDS results. The SIMS data also indicated that the deposited Ni did not penetrate through the full 143-nm depth of TiO_2. Specifically, no Ni filaments extending through the film were detected either from the SIMS data on a 125 × 125 $μm^2$ area of the TiO_2 sample or by the TEM characterization within ~10 μm width of the thin region.

Figure 4 shows the behavior of Si/TiO_2/Ni film or Ni-island electrodes in contact with an aqueous solution of the one-electron, outer-sphere, reversible, $Fe(CN)_6^{3-/4-}$ (50 mM/ 350 mM) redox couple. Mass transport–limited anodic current densities of 120 mA cm^{-2} were observed for p^+-Si/TiO_2/Ni-film electrodes in the dark (Fig. 4A), and light-limited anodic current densities of 35 mA cm^{-2} were observed for n-Si/TiO_2/Ni-island electrodes under illumination (Fig. 4B). These results indicate that holes were readily conducted through the TiO_2 overlayer to the $Fe(CN)_6^{3-/4-}$ redox couple in the presence of Ni films or Ni islands on the TiO_2 surface. For comparison, Fig. 4A displays the behavior of a continuous Ni film electrode tested under the same conditions (orange curve). The p^+-Si/TiO_2/Ni-film and the Ni film electrodes showed mutually similar resistances near the rest potential of 0.19 V versus SCE. The upper and lower limits of each data set in Fig. 4A are indicative of the limiting anodic and cathodic current densities, respectfully, and result from diffusion and convection of redox species in an

agitated solution. The same behavior was also observed in the dark for p^+-GaAs/68-nm TiO_2/Ni electrodes [fig. S8 (*18*)].

Under simulated 1.25-Sun illumination, an n-Si/TiO_2/Ni-island electrode in contact with the $Fe(CN)_6^{3-/4-}$ redox couple exhibited V_{oc} = 0.41 ± 0.03 V [versus the $Fe(CN)_6^{3-/4-}$ Nernstian cell potential] and light-limited photocurrent densities of 34.6 ± 0.6 mA cm^{-2} (Fig. 4B). A *ff* of 0.49 ± 0.08 was calculated at the maximum power-conversion point, with the V_{oc} defined as the potential difference between the n-Si/TiO_2/Ni-island photoanode under illumination and the Nernstian potential of the $Fe(CN)_6^{3-/4-}$ solution. The light-limited photocurrent densities in contact with $Fe(CN)_6^{3-/4-}$(aq) were within ± 2 mA cm^{-2} of those observed for the same electrodes during the OER in contact with 1.0 M KOH(aq).

The data indicate that the unannealed ALD-TiO_2 films prepared and exploited in our work are "leaky" (electronically defective) and thus highly conductive, with the exception of a thin insulating barrier layer at the surface of the as-grown film. In this model, intermixing of the deposited Ni provides electrical contact through the insulating surface layer. This combination allowed the thick ALD-TiO_2 films to act as a highly effective corrosion barrier while facilitating interfacial charge transport with minimal resistive loss. Consistently, without a Ni film or Ni islands, rectifying *J-E* behavior and low anodic current densities were observed for p^+-Si/TiO_2 electrodes in the dark and for n-Si/TiO_2 under illumination. This hypothesis is also consistent with the behavior observed in contact with $Fe(CN)_6^{3-/4-}$(aq) [fig. S9 (*18*)] and 1.0 M KOH(aq) [fig. S10 (*18*)]. When the ALD-TiO_2 surface was sputtered to remove the top layer and left with trace metals on the surface [fig. S11 (*18*)], the TiO_2 film exhibited anodic current densities of >120 mA cm^{-2} in contact with $Fe(CN)_6^{3-/4-}$(aq). Furthermore, when a Hg drop was used to contact p^+-Si/unannealed TiO_2 samples, anodic current densities of <0.2 μA cm^{-2} were measured at a 0.02 V bias voltage, whereas the Hg-drop–contacted samples passed >10^4 larger anodic current densities at this bias when the top layer of the ALD-TiO_2 films was either intermixed with Ni or was removed physically [fig. S12 (*18*)]. Ir deposits also enabled anodic conduction through the unannealed TiO_2 films, but the observation of anodic current densities of 50 to 120 mA cm^{-2} required additional voltage losses of ~0.40 V when Ir was used instead of Ni.

The observed energy-band alignment for a p^+-Si substrate with an ALD-grown unannealed TiO_2 film indicated a large valence-band offset of 2.22 ± 0.08 eV [fig. S13 (*18*)]. The potential distribution under operation is expected to be a complicated function of the energetics and charge-transfer kinetics at the various interfaces in these multicomponent photoelectrode systems. Spectroscopic ellipsometry data indicated that the optical band gap for the TiO_2 film was 3.34 ± 0.01 eV [fig. S14 (*18*)]. Unlike photocathodes, where electrons can be expected to inject into the conduction band of TiO_2 (*22*), stoichiometric nondefective TiO_2 films should present a tunneling barrier for holes in the valence band. Hence, TiO_2 films with thicknesses of 4 to 143 nm should attenuate anodic currents to levels at or below 100 μA cm^{-2}, in accord with prior observations (*23*, *24*). A Mott-Schottky analysis indicated that the flat-band potential of TiO_2 in contact with $Fe(CN)_6^{3-/4-}$(aq) was –1.4 V versus SCE [fig. S15 (*18*)]. However, x-ray photoemission spectra revealed a 2-eV-wide distribution of filled defect states spanning from the conduction band to the mid-gap region (Fig. 4C), suggesting that holes could be transported through TiO_2 preferentially via the defect states instead of by the valence band. These defect states are not present, presumably due to oxidation by air or water, at the TiO_2 surface after the ALD process. This hypothesis is consistent with the observation that invasive contacts, established by Ni intermixing or physical removal of the most exposed layer of the TiO_2 film, enabled conduction pathways via these defect states, whereas nonpenetrating contacts such as the Hg drop or an aqueous redox solution did not effectively access these defect states and thus exhibited minimal conduction through the entire unannealed TiO_2 thick overlayer.

Consistently, relatively large cathodic current densities, >15 mA cm^{-2}, were observed for TiO_2-coated Si and GaAs, even without a thin metallic film deposited on the TiO_2 surface (Fig. 4 and fig. S10). The 0.0 ± 0.1 eV conduction band offset for Si and TiO_2 suggests a band-transport mechanism for electron conduction. Three- to 100-nm-thick TiO_2 coatings have been shown to protect photocathodes of p-InP (*25*), p-Cu_2O/n-ZnO (*26*), and p-Si (*27*) by allowing electrons to transport via the conduction band of TiO_2 and are normally designed to block hole transport (*28*).

The key to enabling the conduction of holes across the thick TiO_2 protective coating is the use of unannealed ALD-TiO_2. Unannealed ALD TiO_2 combines optical transparency and high electrical conductivity to both electrons and holes, while allowing the incorporation of metal catalyst overlayers and providing chemical stability in a variety of aqueous media, specifically including alkaline anodic operational conditions. Because defect states (0 to 2 eV versus the conduction-band edge) exist in the ALD-TiO_2 film (Fig. 4C), the observed hole conduction exhibited negligible voltage loss and was independent of film thickness over the range of 4 to 143 nm. When the TiO_2 film was annealed, the observed anodic current densities decreased to 2 mA cm^{-2} at 0.50 V overpotential versus $Fe(CN)_6^{3-/4-}$(aq), even when a Ni overlayer was deposited on top of 4 nm of ALD-TiO_2 [fig. S16 (*18*)].

For the n-p^+-Si/TiO_2/Ni-island photoanode, the photovoltage from the Si mainly offset the overpotential for water oxidation for this

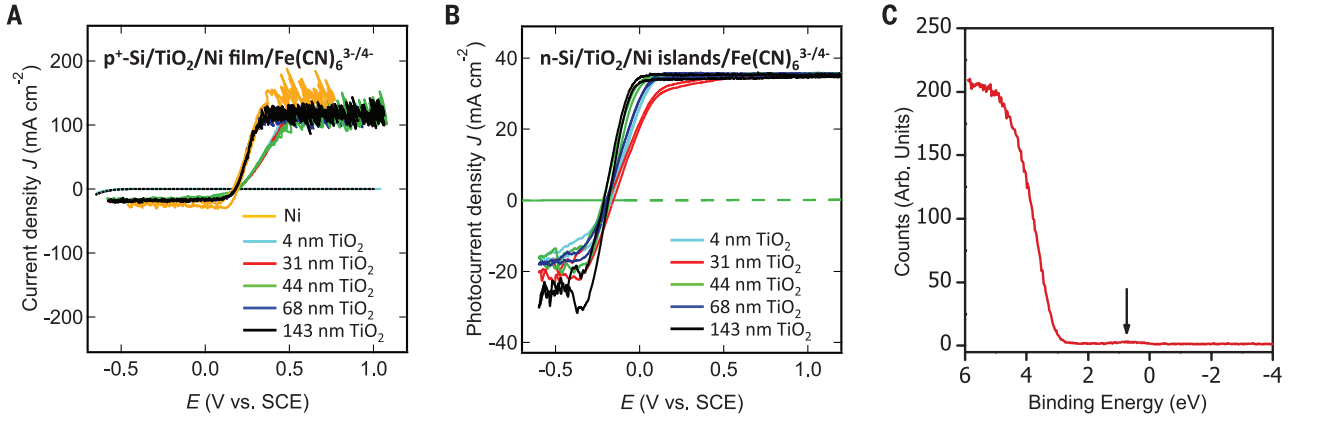


Fig. 4. Defect-state–mediated hole-conduction mechanism. (**A**) Electrochemical behavior of p^+-Si/TiO_2/Ni-film electrodes in contact with 50 mM $Fe(CN)_6^{3-}$ and 350 mM $Fe(CN)_6^{4-}$(aq) in the dark. The dashed curves indicate the behavior without Ni; i.e., p^+-Si/3-nm and 143-nm TiO_2 [all thicknesses are shown in fig. S10 (*18*)]. (**B**) PEC behavior of n-Si/TiO_2/Ni island photoelectrodes in the same electrolyte under simulated ELH-type 1.25-Sun illumination. The dashed curve indicates the behavior of n-Si/44-nm TiO_2 photoelectrodes without Ni. The Nernstian potential of the $Fe(CN)_6^{3-/4-}$ solution was 0.19 V versus SCE. Ni films were deposited for TiO_2-coated p^+-Si, whereas Ni islands (square arrays of 3-μm-diameter circles in 7-μm pitch) were deposited on TiO_2-coated n-Si. (**C**) X-ray photoemission valence spectrum of the 44-nm ALD-TiO_2 on Si without removing the top layer of the nonconducting TiO_2, indicating the filled defect states in the TiO_2 band gap.

state-of-the-art electrolyte/electrocatalyst combination (*29*). The *J-E* data for this photoanode thus extended only slightly into the power-producing region; i.e., anodic photocurrents of ~10 mA cm^{-2} were observed at negative electrode potentials relative to $E^{o'}(O_2/H_2O)$. Nevertheless, to provide perspective on the shift in potential provided by the photoelectrode, obtaining the observed *J-E* performance of the n-p^+-Si/44-nm TiO_2/Ni island photoanode with a Si photovoltaic (PV) cell electrically in series with an electrocatalytic anode that exhibited identical *J-E* behavior to that of the p^+-Si/44-nm TiO_2/Ni film electrode in the dark (*30*) would require the use of a 9.4% efficient Si PV cell with a V_{oc} of 0.43 V, a J_{sc} (short-circuit photocurrent density) of 27.7 mA cm^{-2}, and a *ff* of 0.79. In fact, the required 9.4% PV energy-conversion efficiency is an underestimation of the light-induced performance of the photoelectrode, because the light-blocking electrocatalytic Ni islands covered 14.4% of the electrode surface, and thus an ~11.0% efficient PV cell connected in series with the electrocatalyst/electrolyte combination would be required to produce the PEC *J-E* data observed from the photochemically active area of the integrated n-p^+-Si/TiO_2/Ni-island photoelectrode asssembly described here. An analogous calculation indicated that a 12.7% GaAs PV cell would be required to produce the *J-E* behavior observed for the integrated n-p^+-GaAs/TiO_2/Ni film photoelectode assembly described here.

The photovoltage produced by the n-Si/TiO_2 interfaces was ~0.4 V, which is lower than that of an np^+-Si diode or than the theoretical bulk recombination limit. The photovoltage might be improved by exercising further control over the interface; for example, by initiating ALD with a seed layer of C-Si bonds. Methyl termination passivates the Si surface electronically and introduces interfacial dipoles that can generate high photovoltages (*31*). In addition, the ability to engineer the energy levels and the distribution of defect states in chemically stable coatings such as TiO_2 offers the opportunity to stabilize a host of narrow band-gap semiconductors for use in oxidative photochemistry. We have explored the use of thick pinhole-free ALD-TiO_2 films to protect Si, as well as GaAs and GaP, from photocorrosion. This method suggests a logical extension to other materials such as II-VIs (e.g., CdSe), III-nitrides (e.g., InGaN), and chalcolpyrites (e.g., $CuInGaSe_2$), which opens the possibility for the use of earth-abundant semiconductors other than stable metal oxides for efficient solar fuel production.

REFERENCES AND NOTES

1. N. Lewis, *Electrochem. Soc. Interface* **22**, 43–49 (2013).
2. B. A. Pinaud *et al.*, *Energy Environ. Sci.* **6**, 1983–2002 (2013).
3. M. G. Walter *et al.*, *Chem. Rev.* **110**, 6446–6473 (2010).
4. M. Pourbaix, *Atlas of Electrochemical Equilibria in Aqueous Solutions* (National Association of Corrosion Engineers, Houston, TX, ed. 2, 1974).
5. J. R. McKone, N. S. Lewis, H. B. Gray, *Chem. Mater.* **26**, 407–414 (2014).
6. S. Hu, C. Xiang, S. Haussener, A. D. Berger, N. S. Lewis, *Energy Environ. Sci.* **6**, 2984–2993 (2013).
7. Y. Nakato, T. Ohnishi, H. Tsubomura, *Chem. Lett.* **3**, 883–886 (1975).
8. R. C. Kainthla, *J. Electrochem. Soc.* **134**, 841–845 (1987).
9. M. J. Kenney *et al.*, *Science* **342**, 836–840 (2013).
10. F. R. F. Fan, R. G. Keil, A. J. Bard, *J. Am. Chem. Soc.* **105**, 220–224 (1983).
11. F. Decker, M. Fracastoro-Decker, W. Badawy, K. Doblhofer, H. Gerischer, *J. Electrochem. Soc.* **130**, 2173–2179 (1983).
12. F. Fan, B. Wheeler, A. Bard, R. Noufi, *J. Electrochem. Soc.* **128**, 2042–2045 (1981).
13. N. C. Strandwitz *et al.*, *J. Phys. Chem. C* **117**, 4931–4936 (2013).
14. K. Sun *et al.*, *Energy Environ. Sci.* **5**, 7872–7877 (2012).
15. Y. W. Chen *et al.*, *Nat. Mater.* **10**, 539–544 (2011).
16. A. G. Scheuermann, J. D. Prange, M. Gunji, C. E. D. Chidsey, P. C. McIntyre, *Energy Environ. Sci.* **6**, 2487–2496 (2013).
17. S. Dueñas *et al.*, *Semicond. Sci. Technol.* **20**, 1044–1051 (2005).
18. Materials and methods are available as supplementary materials on *Science* Online.
19. Y. Matsumoto, E. Sato, *Mater. Chem. Phys.* **14**, 397–426 (1986).
20. D. A. Corrigan, *J. Electrochem. Soc.* **136**, 723–728 (1989).
21. B. S. Yeo, A. T. Bell, *J. Phys. Chem. C* **116**, 8394–8400 (2012).
22. H. N. Ghosh, J. B. Asbury, Y. Weng, T. Lian, *J. Phys. Chem. B* **102**, 10208–10215 (1998).
23. S. A. Campbell *et al.*, *IBM J. Res. Develop.* **43**, 383–392 (1999).
24. B. Kalanyan, G. Parsons, *ECS Trans.* **41**, 285–292 (2011).
25. M. H. Lee *et al.*, *Angew. Chem. Int. Ed. Engl.* **51**, 10760–10764 (2012).
26. A. Paracchino, V. Laporte, K. Sivula, M. Grätzel, E. Thimsen, *Nat. Mater.* **10**, 456–461 (2011).
27. B. Seger *et al.*, *J. Am. Chem. Soc.* **135**, 1057–1064 (2013).
28. S. Avasthi *et al.*, *Appl. Phys. Lett.* **102**, 203901 (2013).
29. C. C. L. McCrory, S. Jung, J. C. Peters, T. F. Jaramillo, *J. Am. Chem. Soc.* **135**, 16977–16987 (2013).
30. M. R. Shaner, K. T. Fountaine, H.-J. Lewerenz, *Appl. Phys. Lett.* **103**, 143905 (2013).
31. R. L. Grimm *et al.*, *J. Phys. Chem. C* **116**, 23569–23576 (2012).

ACKNOWLEDGMENTS

This work is supported through the Office of Science of the U.S. Department of Energy (DOE) under award no. DE-SC0004993 to the Joint Center for Artificial Photosynthesis, a DOE Energy Innovation Hub. M.S. acknowledges the Resnick Sustainability Institute for a graduate fellowship, and B.S.B. acknowledges the Beckman Institute at the California Institute of Technology for support. XPS was performed at the Molecular Materials Research Center in the Beckman Institute at the California Institute of Technology. TEM imaging and spectroscopy were performed at the Center for Electron Microscopy and Microanalysis, University of Southern California. We thank H.- J. Lewerenz, C. Koval, and F. Houle for fruitful discussions; Y. Guan for secondary-ion mass spectrometry measurements; S. R. Nutt for use of the microscopy and microanalysis facility; P. D. Dapkus for the use of the metal-organic chemical vapor deposition facility; S. Ardo for help in boron-diffusion doping; and K. Papadantonakis for assistance with editing this manuscript. The authors' institution (California Institute of Technology) has filed a provisional U.S. patent application directly relating to the work described in the paper (patent application no. 61/889,430, filed on 10 October 2013).

SUPPLEMENTARY MATERIALS

www.sciencemag.org/content/344/6187/1005/suppl/DC1
Materials and Methods
Supplementary Text
Figs. S1 to S17
References (*32*, *33*)

28 January 2014; accepted 1 May 2014
10.1126/science.1251428

WATER STRUCTURE

Vibrational spectral signature of the proton defect in the three-dimensional $H^+(H_2O)_{21}$ cluster

Joseph A. Fournier, Christopher J. Johnson, Conrad T. Wolke, Gary H. Weddle, Arron B. Wolk, Mark A. Johnson*

The way in which a three-dimensional network of water molecules accommodates an excess proton is hard to discern from the broad vibrational spectra of dilute acids. The sharper bands displayed by cold gas-phase clusters, $H^+(H_2O)_n$, are therefore useful because they encode the network-dependent speciation of the proton defect and yet are small enough to be accurately treated with electronic structure theory. We identified the previously elusive spectral signature of the proton defect in the three-dimensional cage structure adopted by the particularly stable $H^+(H_2O)_{21}$ cluster. Cryogenically cooling the ion and tagging it with loosely bound deuterium (D_2) enabled detection of its vibrational spectrum over the 600 to 4000 cm^{-1} range. The excess charge is consistent with a tricoordinated H_3O^+ moiety embedded on the surface of a clathrate-like cage.

The nature of proton speciation in water remains an elusive aspect of aqueous chemistry because of the remarkably diffuse vibrational features traceable to the excess proton in dilute acid solutions (*1*–*3*). The spectroscopic properties of small protonated water clusters, $H^+(H_2O)_n$, frozen into well-defined structures, have therefore attracted a great deal of interest over the past decade, as they reveal how the spectral signatures associated

Sterling Chemistry Laboratory, Yale University, New Haven, CT 06520, USA.
***Corresponding author. E-mail: mark.johnson@yale.edu**

with the proton defect depend on the local hydration environment (*4*–*20*). At the smallest sizes ($n \leq 10$), the proton-induced features change markedly with the first 10 or so water molecules, often falling between the bands associated with the two limiting H_2O-H^+-OH_2 "Zundel" and H_3O^+ $(H_2O)_3$ "Eigen" accommodation motifs near 1000 and 2660 cm^{-1}, respectively (*10*). These smaller clusters are thought to occur with sheet-like structures, whereas new features that emerge in the range $n = 10$ to 20 signal the formation of three-dimensional network cage morphologies (*11*). A long-standing puzzle regarding the nature of this intermediate size regime is the origin of a very strong intensity anomaly or "magic number" at $H^+(H_2O)_{21}$, first reported by Searcy and Fenn (*21*) in 1974 and subsequently studied with theory (*22*–*27*), flow tube thermodynamics (*28*, *29*), and vibrational spectroscopy (*8*, *9*, *11*, *13*–*15*). Here, we used recently developed cryogenic ion spectroscopic techniques to study the spectrum of this cluster, with the goal of finally identifying the spectral signature of the excess proton and thus clarifying the nature of charge accommodation in the three-dimensional network regime.

There is a consensus in the theoretical literature that the $n = 21$ cluster adopts a configuration in which an embedded H_3O^+ (hydronium) ion resides on the outside of a puckered cage structure (*22*–*24*, *27*) with one interior neutral water molecule, as depicted in the inset at the upper left of Fig. 1. In this arrangement, the hydronium motif is solvated by three water molecules in single H-bond acceptor configurations, with their OH groups integrated into the surface network formed by essentially neutral water molecules. The first reports (*9*, *11*) of size-selected vibrational spectra of clusters in the range $n = 10$ to 30 focused on the OH stretching bands of the neutral water network that can be accessed with readily available laser sources. The structural implications of the band patterns were drawn through theoretical analysis of the sharp, high-energy bands associated with the exterior, nonbonded OH groups. Indeed, the multiplet of closely spaced OH stretching transitions near 3700 cm^{-1} was observed to collapse into a single feature at $n = 21$ (reproduced in Fig. 1B), consistent with the prediction for the surface-bound H_3O^+ arrangement. Unfortunately, however, the critical strong bands predicted (Fig. 1A) for the symmetric and asymmetric OH stretches of the embedded H_3O^+ near 2600 cm^{-1} were not at all evident in the observed spectra. Scenarios rationalizing their absence include experimental limitations involving insufficient cooling of the free clusters used in those studies (*9*, *11*, *22*), an unexpected role of local structures more akin to the $H_5O_2^+$ motif, and strong anharmonic shifts in the H_3O^+ bands, which would place the key bands below the region surveyed in the experimental studies. More recently, the experimental $H^+(H_2O)_{21}$ spectrum was revisited using predissociation of weakly bound H_2 molecules [so-called messenger tagging (*5*, *30*)] by Fujii and co-workers, who formed the complexes with a supersonic jet ion source (*14*, *15*). Because of the very low binding energy of neutral molecular hydrogen (<500 cm^{-1}), these clusters are sure to be much colder than the bare ions used earlier. Their reported spectrum is reproduced in Fig. 1C, and although this approach revealed substantially enhanced absorption down to 3000 cm^{-1} or so, it again did not reveal any activity in the region predicted for the putative H_3O^+ charge carrier at the harmonic level.

Torrent-Sucarrat and Anglada (*31*) then evaluated the role of anharmonicity by means of the second-order vibrational perturbation theoretical (VPT2) approach (*32*), and concluded that the strongest asymmetric OH stretching band of the embedded H_3O^+ could plausibly occur 500 cm^{-1} or more below the harmonic value [$\nu^a_{H_3O^+}$, Fig. 1E near 2000 cm^{-1}, obtained at the B3LYP/6-31+G (d) level of theory]. Unfortunately, their predicted value falls in a region of the spectrum that is difficult to access with either free electron lasers or the more readily available tabletop parametric converters. In our experiments, we used a new instrument that allows for temperature control of ions in a cryogenic ion trap (*33*–*37*) to extend the predissociation spectrum of the D_2-tagged $H^+(H_2O)_{21}$ cluster down to 600 cm^{-1}.

The electrospray ionization–generated $H^+(H_2O)_n$ clusters were accumulated in a quadrupole ion trap held at 6 K, where they were cooled sufficiently by a pulse of buffer gas (10% D_2 in He) to allow the condensation of a few weakly

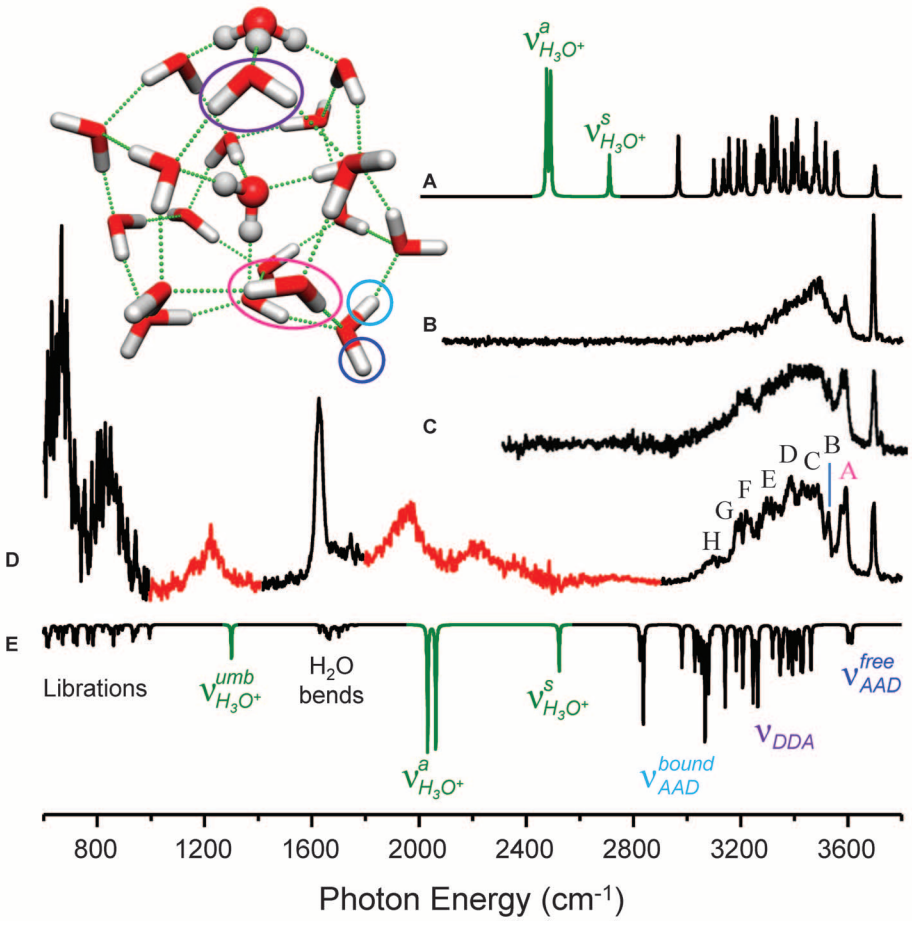


Fig. 1. Comparison of previously calculated and observed vibrational spectra of the $H^+(H_2O)_{21}$ cluster with that reported here. The calculated spectra correspond to (**A**) the earlier (*9*) (B3LYP/aug-cc-pVDZ, scaled by 0.962) harmonic and (**E**) more recent (*31*) VPT2 anharmonic predictions [unscaled B3LYP/6-31+G (d)] for the bare cluster structure identified earlier (*9*) and shown in the inset (see rotatable structure in supplementary materials). The experimental spectra were obtained by vibrational predissociation of (**B**) bare and (**C** and **D**) H_2/D_2-tagged clusters. The present measurement (D) extends the range covered in the earlier report (C) and uses slow buffer gas cooling to process the ion ensemble. Assignments of the symmetric and asymmetric OH stretches (ν^s and ν^a) and the umbrella bending mode (ν^{umb}) of the surface-bound H_3O^+ ion are indicated in green; key features associated with neutral water molecules are denoted according to their local H-bonding environments (D = donor, A = acceptor). Bands identified with letters A through H denote emergent features associated with the neutral water network.

bound D_2 adducts. Figure 1D presents the vibrational predissociation spectrum of the D_2-tagged n = 21 ion obtained in this study. The much wider spectral range accessible in this work yields a clear picture of both the intramolecular and intermolecular motions of the neutral water network. These include the expected intramolecular HOH bending vibrations of the neutral water network near 1600 cm^{-1} and the associated librational modes from 600 to 900 cm^{-1}, as highlighted by the comparison of the spectrum of pure water in Fig. 2A (solid line) with that of the n = 21 cluster in Fig. 2B. The new spectrum clearly reveals modulations in the broad envelope from 3000 to 3500 cm^{-1}, with particular peaks denoted by letters A through H. It is immediately clear that neither the harmonic (*9*) nor the anharmonic (*31*) calculations (Fig. 1, A and E, respectively) for the structure advanced in (*9*) predict a strong, relatively isolated peak (A) at 3580 cm^{-1} before the congested region extending down to 3000 cm^{-1}. Recent higher-level harmonic calculations by Xantheas (*27*), on the other hand, were reported only in the OH stretching region, but three of the surface-bound H_3O^+ structures did display a more distinct peak near the A transition. In that calculation, absorption in this region is due to the OH stretches of DDA-type water molecules (an example position is circled in pink in Fig. 1) attached to three AAD water molecules (where A and D denote acceptor and donor), as was suggested in our original report (*9*). We gain some qualitative insight from the trends in the harmonic frequencies associated with H-bonded OH groups for the structure in Fig. 1, where the features around 3400 cm^{-1} are traced to water molecules in other DDA H-bonding sites while those in AAD sites fall to lower energy as indicated (see inset in Fig. 1 for local motif). As mentioned above, a single isolated band is observed at 3700 cm^{-1} that arises from nonbonded OH groups of water molecules in the AAD network sites.

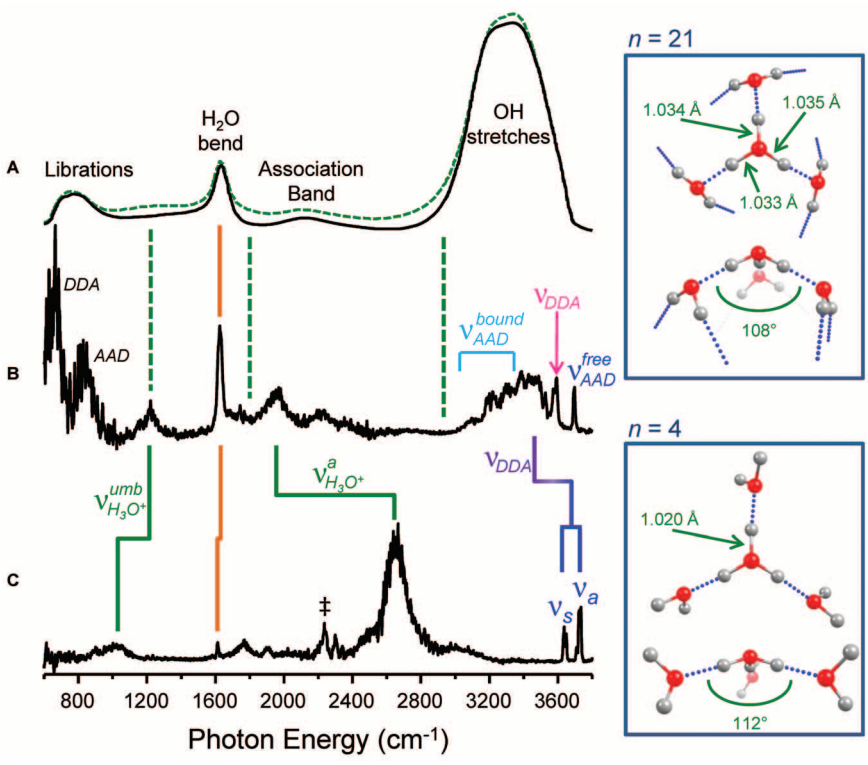


Fig. 2. Comparison of the vibrational predissociation spectra of the D_2-tagged $H_9O_4^+$ Eigen cluster and the n = 21 cluster. (**A**) Spectra (*1*) of bulk water (solid black line) and that attributed to the excess proton in 1.0 M HCl (dashed green line). (**B**) n = 21 cluster spectrum. (**C**) Eigen cluster spectrum. Calculated [B3LYP/6-31+G (d)] structural parameters for both the isolated minimum-energy Eigen (lower right inset) and the embedded Eigen motif within the n = 21 structure (upper right inset) are indicated to illustrate the nature of the distortion induced by the cage. Although the H_3O^+ O-H bond lengths are elongated by ~0.014 Å in the larger cluster, the local environment is calculated to remain essentially three-fold symmetric, with a range of only 0.002 Å in the three O-H bond lengths. There is also a 4° reduction in pyramidal angle. See Fig. 1 caption for band notation. Features unique to the Eigen ion (C) are the symmetric and asymmetric OH stretching vibrations (ν_s and ν_a) of exterior water molecules; ‡ denotes a combination band derived from the intramolecular H_3O^+ bend with frustrated rotation along its symmetry axis. The evolution of the neutral water stretches (blue/purple) and bends (orange) and those of the embedded hydronium ion (green) are indicated by the colored vertical lines.

In the critical lower-energy region from 1000 to 2500 cm^{-1}, the only feature with a clear assignment is the sharp band arising from the bending fundamental of the neutral water molecules around 1600 cm^{-1}, which suggests that the bend is much less responsive to differences in the H-bonding configurations of the various sites. Absorptions that are not anticipated for neutral water at the harmonic level are indicated in red in Fig. 1D and appear above and below the neutral water bend. Three maxima occur in the higher-energy feature at 2000 cm^{-1}, 2200 cm^{-1}, and 2700 cm^{-1}, respectively, with continuous absorption occurring over the 1700 to 2900 cm^{-1} range. The absence of these low-energy absorptions in the previous study of the H_2-tagged ions was rationalized by invoking a distribution of isomers or even the dynamical nature of the clusters in the H_2-tagged regime (*14*). This interpretation was supported by simulations at elevated temperatures, which failed to predict a clear vibrational signature of the excess proton because of the thermal fluctuations (*22*). It is therefore likely that the cryogenic processing of the ions used here, where the warm ions are slowly cooled over tens of milliseconds (rather than microseconds in free jets), yields a cluster distribution close to the vibrational zero-point level. The highest-energy free OH feature in the jet spectrum has a small shoulder on the high-energy side (Fig. 1C), which is absent in the spectrum from the ion cooled in the trap (Fig. 1D). The latter spectrum also displays much better definition of the features in the OH stretching region, consistent with either better cooling or less congestion from locally stable isomers.

We consider the assignment of the features associated with the proton defect in the context of the anharmonic prediction by Torrent-Sucarrat and Anglada (*31*). The bands at 2000 and 1200 cm^{-1} are in remarkable agreement with these recent predictions (Fig. 1E) for the asymmetric OH stretching and umbrella bending modes of the surface-embedded H_3O^+, respectively, whereas the weaker band at 2700 cm^{-1} falls 100 cm^{-1} above the predicted anharmonic value for the symmetric OH stretch. The agreement, while compelling, should not yet be regarded as definitive proof of the structure, as some regions are predicted to be too weak (like the bend relative to the H_3O^+ asymmetric stretch) and the stability of the strong band calculated around 2850 cm^{-1} was shown not to be robust by Xantheas (*27*). Although the most extensive structural searches to date (*22*, *27*) strongly favor a surface-embedded H_3O^+, these inconsistencies, along with improved analysis of the specific motions underlying the intensity modulation pattern throughout the OH stretching region, illustrate the need to engage a new survey of the structural landscape. In particular, it seems likely that more advanced quantum treatments of the anharmonic vibrational level structure will be required to yield an accurate prediction of the experimental spectral pattern.

With the compelling interpretation of the new n = 21 spectrum in the context of the calculated properties of the long-sought embedded hydronium ion, it is useful to compare this band pattern with the D_2-predissociation spectrum of the n = 4, $H_3O^+(H_2O)_3$ "Eigen" ion over the range 600 to 3800 cm^{-1}, recorded with the trap instrument and displayed in Fig. 2C. The high-energy region was first reported by Okumura (*30*), who analyzed it in the context of the structure depicted in the inset to the right of Fig. 2C. The three water molecules form the primary solvation shell of H_3O^+ with acceptor H-bonding motifs. These account for the simple doublet highest in energy in the context of their symmetric and asymmetric OH stretching modes, as well as the sharp band at 1600 cm^{-1} from their intramolecular bends. A small doubling is induced by D_2 attachment to one of the nominally free OH groups of one of these water molecules. The dominant band near 2660 cm^{-1} arises from the OH asymmetric stretching motions of the H_3O^+ ion.

The assignments of the remaining bands have proven to be somewhat controversial (*38*). We previously traced the doublet at 2200 cm^{-1} (labeled ‡ in Fig. 2C) to the combination band involving the H_3O^+ bend together with frustrated rotation of the hydronium in the solvent cage (*39*). This is closely related to the weak feature in this region of the water spectrum, the so-called "association band," that is assigned to a combination band of the HOH bend with the frustrated rotation of water molecules trapped with strong H-bonds to neighbors. The band at 2200 cm^{-1} in the n = 21 spectrum falls in the same region and could thus be attributed to a similar combination band of H_3O^+ in the larger cage. Anharmonic calculations point to the 1000 cm^{-1} feature as the H_3O^+ umbrella mode; the 1750 cm^{-1} and 1900 cm^{-1} transitions are less obvious. The 1750 cm^{-1} feature lies 50 cm^{-1} above the harmonic prediction for the embedded H_3O^+ bend, for example, raising the possibility that these absorptions, like the ‡ doublet, arise from anharmonic coupling of lower-frequency fundamentals. Strong candidates include overtones of the out-of-plane rotations of H_3O^+ as well as their combination with the umbrella fundamental. Such transitions have proven to be commonplace in systems with strong ionic H-bonds, often arising from electrical anharmonicity or non-Condon effects in the transition dipole operator (*39*). Clarification of these assignments, like the situation in n = 21, would clearly benefit from theoretical treatments that take both electrical and mechanical anharmonicities into account. With the currently available information, however, comparison of the observed spectra with the calculated anharmonic predictions indicates that the OH stretches of the H_3O^+ ion shift toward the red by about 500 cm^{-1} in going from n = 4 to n = 21, while the umbrella mode shifts toward the blue by about 200 cm^{-1}.

The relationship between the locations of the proton-induced absorptions and the degree of excess charge delocalization throughout the network has been addressed theoretically in the analysis of the bulk spectra of dilute acids. Figure 2 compares the n = 21 spectrum with that extracted for the excess proton in 1.0 M HCl (Fig. 2A, dashed green line) as well as that of neutral water (Fig. 2A, solid black line) (*1*). This concentration has a ratio of H^+/H_2O similar to that of the n = 21 cluster (0.02 and 0.04, respectively). The observed absorption enhancements in acidic solution near 1200 cm^{-1} and from 1800 to 3000 cm^{-1} are similar in magnitude and position to the proton defect bands of the n = 21 cluster highlighted in red in Fig. 1D. Voth and co-workers (*2*) attributed the broad 1800 to 3000 cm^{-1} absorption enhancement to the presence of a distorted $H_9O_4^+$ Eigen motif in which one of the hydronium protons binds more strongly to nearby H_2O to create a transient strong H-bonded pair. Inspection of the calculated structures in Fig. 2 indicates that upon incorporation into the cage network in n = 21, the O-H bond lengths of the hydronium increase from 1.020 Å in $H_9O_4^+$ to about 1.034 Å in n = 21, but the calculated environment of the H_3O^+ in n = 21 is actually quite symmetrical, with a variation of only 0.01 Å in the O-O bond lengths. The minimal extent of symmetry breaking is manifested in the calculated n = 21 spectrum by the splitting of the two asymmetric stretches (Fig. 1E). The Eigen motif within the n = 21 structure also involves contraction of the hydronium HOH bond angles from 112° to 108°, making the structure a more pyramidal arrangement. This deformation could therefore be one of the factors contributing to the location of the bands associated with the excess proton, in addition to symmetry breaking and anharmonic coupling to soft modes that govern molecular displacements in the cage scaffold.

The origin of the breadths associated with both the OH stretch and umbrella features is not evident at this time, and it will be of great interest to follow the temperature and size evolution of these bands. It is hoped that this new information will stimulate further theoretical investigations with more sophisticated structure search algorithms to refine the accepted structure as well as canvas the potential energy landscape for possible alternative morphologies. In particular, reproducing the increasingly well-defined fine structure on the various bands with realistic quantum treatment of the vibrational degree of freedom will provide a stringent benchmark for models of both water and proton migration in three-dimensional hydrogen-bonded networks.

REFERENCES AND NOTES

1. J. Kim, U. W. Schmitt, J. A. Gruetzmacher, G. A. Voth, N. E. Scherer, *J. Chem. Phys.* **116**, 737 (2002).
2. J. Q. Xu, Y. Zhang, G. A. Voth, *J. Phys. Chem. Lett.* **2**, 81–86 (2011).
3. C. Knight, G. A. Voth, *Acc. Chem. Res.* **45**, 101–109 (2012).
4. L. I. Yeh, M. Okumura, J. D. Myers, J. M. Price, Y. T. Lee, *J. Chem. Phys.* **91**, 7319 (1989).
5. M. Okumura, L. I. Yeh, J. D. Myers, Y. T. Lee, *J. Phys. Chem.* **94**, 3416–3427 (1990).
6. J.-C. Jiang *et al.*, *J. Am. Chem. Soc.* **122**, 1398–1410 (2000).
7. C.-K. Lin *et al.*, *Phys. Chem. Chem. Phys.* **7**, 938–944 (2005).
8. C. C. Wu *et al.*, *J. Chem. Phys.* **122**, 074315 (2005).
9. J.-W. Shin *et al.*, *Science* **304**, 1137–1140 (2004).
10. J. M. Headrick *et al.*, *Science* **308**, 1765–1769 (2005).
11. M. Miyazaki, A. Fujii, T. Ebata, N. Mikami, *Science* **304**, 1134–1137 (2004).
12. K. Mizuse, A. Fujii, N. Mikami, *J. Chem. Phys.* **126**, 231101 (2007).
13. K. Mizuse, N. Mikami, A. Fujii, *Angew. Chem. Int. Ed.* **49**, 10119–10122 (2010).
14. K. Mizuse, A. Fujii, *J. Phys. Chem. Lett.* **2**, 2130–2134 (2011).
15. K. Mizuse, A. Fujii, *Chem. Phys.* **419**, 2–7 (2013).
16. G. E. Douberly, A. M. Ricks, M. A. Duncan, *J. Phys. Chem. A* **113**, 8449–8453 (2009).
17. G. E. Douberly, R. S. Walters, J. Cui, K. D. Jordan, M. A. Duncan, *J. Phys. Chem. A* **114**, 4570–4579 (2010).
18. T. C. Cheng, B. Bandyopadhyay, J. D. Mosley, M. A. Duncan, *J. Am. Chem. Soc.* **134**, 13046–13055 (2012).
19. K. R. Asmis *et al.*, *Science* **299**, 1375–1377 (2003).
20. N. Heine *et al.*, *J. Am. Chem. Soc.* **135**, 8266–8273 (2013).
21. J. Q. Searcy, J. B. Fenn, *J. Chem. Phys.* **61**, 5282 (1974).
22. S. S. Iyengar *et al.*, *J. Chem. Phys.* **123**, 084309 (2005).
23. A. Khan, *Chem. Phys. Lett.* **319**, 440–450 (2000).
24. M. P. Hodges, D. J. Wales, *Chem. Phys. Lett.* **324**, 279–288 (2000).
25. K. E. Laasonen, M. L. Klein, *J. Phys. Chem. A* **101**, 98–102 (1997).
26. R. Kelterbaum, E. Kochanski, *J. Mol. Struct. THEOCHEM* **371**, 205–218 (1996).
27. S. S. Xantheas, *Can. J. Chem. Eng.* **90**, 843–851 (2012).
28. S. Wei, Z. Shi, A. W. Castleman Jr., *J. Chem. Phys.* **94**, 3268 (1991).
29. Z. Shi, J. V. Ford, S. Wei, A. W. Castleman Jr., *J. Chem. Phys.* **99**, 8009 (1993).
30. M. Okumura, L. I. Yeh, J. D. Myers, Y. T. Lee, *J. Chem. Phys.* **85**, 2328 (1986).
31. M. Torrent-Sucarrat, J. M. Anglada, *J. Chem. Theory Comput.* **7**, 467–472 (2011).
32. V. Barone, *J. Chem. Phys.* **122**, 14108 (2005).
33. M. Z. Kamrath, R. A. Relph, T. L. Guasco, C. M. Leavitt, M. A. Johnson, *Int. J. Mass Spectrom.* **300**, 91–98 (2011).
34. E. Garand *et al.*, *Science* **335**, 694–698 (2012).
35. A. B. Wolk, C. M. Leavitt, E. Garand, M. A. Johnson, *Acc. Chem. Res.* **47**, 202–210 (2014).
36. X. B. Wang, X. P. Xing, L. S. Wang, *J. Phys. Chem. A* **112**, 13271–13274 (2008).
37. N. S. Nagornova, T. R. Rizzo, O. V. Boyarkin, *Science* **336**, 320–323 (2012).
38. W. Kulig, N. Agmon, *J. Phys. Chem. B* **118**, 278–286 (2014).
39. A. B. McCoy, T. L. Guasco, C. M. Leavitt, S. G. Olesen, M. A. Johnson, *Phys. Chem. Chem. Phys.* **14**, 7205–7214 (2012).

ACKNOWLEDGMENTS

M.A.J. thanks the U.S. Department of Energy for support under grant DE-FG02-06ER15800. Development of the cryogenic ion spectrometer was supported by the Air Force Office of Scientific Research under grant FA9550-13-1-0007. J.A.F. thanks the U.S. Department of Defense for support through a National Defense Science and Engineering Graduate Fellowship. This work was supported in part by the facilities and staff of the Yale University Faculty of Arts and Sciences High Performance Computing Center, and by NSF grant CNS 08-21132, which partially funded acquisition of the facilities.

SUPPLEMENTARY MATERIALS

www.sciencemag.org/content/344/6187/1009/suppl/DC1
Materials and Methods
Rotatable n = 21 structure
References (*40*–*42*)

24 March 2014; accepted 2 May 2014
10.1126/science.1253788

IMAGING TECHNIQUES

X-ray birefringence imaging

Benjamin A. Palmer,[1]* Gregory R. Edwards-Gau,[1] Benson M. Kariuki,[1] Kenneth D. M. Harris,[1]† Igor P. Dolbnya,[2] Stephen P. Collins[2]

The polarizing optical microscope has been used since the 19th century to study the structural anisotropy of materials, based on the phenomenon of optical birefringence. In contrast, the phenomenon of x-ray birefringence has been demonstrated only recently and has been shown to be a sensitive probe of the orientational properties of individual molecules and/or bonds in anisotropic solids. Here, we report a technique—x-ray birefringence imaging (XBI)—that enables spatially resolved mapping of x-ray birefringence of materials, representing the x-ray analog of the polarizing optical microscope. Our results demonstrate the utility and potential of XBI as a sensitive technique for imaging the local orientational properties of anisotropic materials, including characterization of changes in molecular orientational ordering associated with solid-state phase transitions and identification of the size, spatial distribution, and temperature dependence of domain structures.

Since its invention in the 19th century, the polarizing optical microscope has found ubiquitous applications in mineralogy (*1*), crystallography (*2*, *3*), materials science (*4*, *5*), and biology (*6*, *7*) to investigate the structural properties of birefringent materials. From liquid crystals (*8*) to collagen fibers in tendons (*9*) and cartilage (*10*), and from amyloid plaques (*11*) to butterfly wings (*12*) and spider silk (*13*), the polarizing optical microscope has been used to establish the relationship between the structural anisotropy of materials and their function. In the phenomenon of birefringence, the refractive index of an anisotropic material depends on the orientation of the material with respect to the direction of linearly polarized incident radiation. When such a material is viewed in a polarizing optical microscope in crossed-polarizer configuration, the intensity of light transmitted through the polarization analyzer depends on the orientation of the optic axis or axes of the material relative to the direction of polarization of the incident light. By measuring the intensity of transmitted light as a function of the orientation of the material, information on the orientation of the optic axis or axes can be established. Furthermore, if the material comprises orientationally distinct domains, the spatial distribution and orientational relationships between the domains may be revealed.

[1]School of Chemistry, Cardiff University, Park Place, Cardiff CF10 3AT, Wales. [2]Diamond Light Source, Harwell Science and Innovation Campus, Didcot, Oxfordshire OX11 0DE, England.
*Present address: Department of Structural Biology, Weizmann Institute of Science, Rehovot, 7610001, Israel. †Corresponding author. E-mail: harriskdm@cardiff.ac.uk

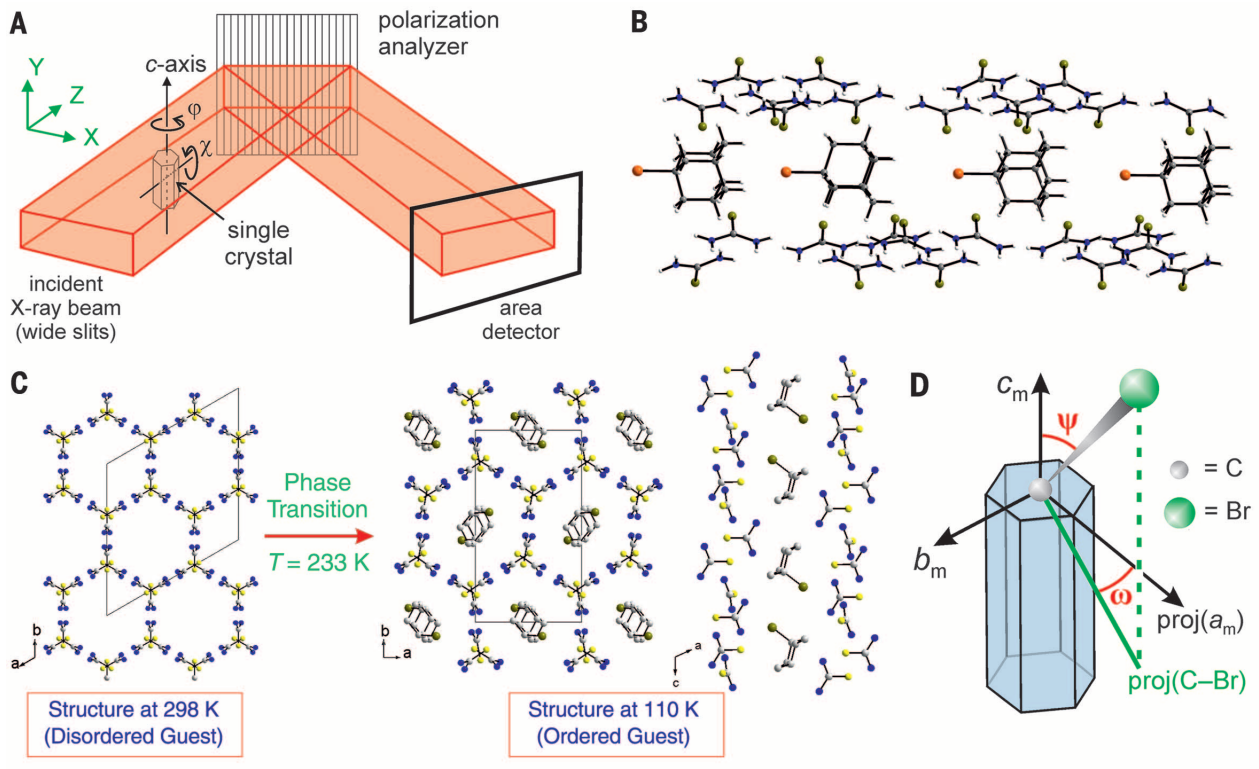


Fig. 1. Experimental setup and structures of materials. (**A**) Experimental setup for XBI. The incident x-ray beam propagates along the *z* axis and is linearly polarized along the *x* axis. The tunnel axis (*c* axis; long-needle axis of crystal morphology) of the crystal was maintained in the plane (*x*-*y* plane) perpendicular to the incident x-ray propagation direction (*z* axis). The crystal orientation was altered by variation of angles χ and φ, where χ refers to rotation of the *c* axis of the crystal around the laboratory *z* axis and φ refers to rotation of the crystal around its *c* axis. (**B**) Structure of 1-BA/thiourea viewed perpendicular to the thiourea host tunnel (horizontal); the C–Br bonds of all 1-BA guest molecules are parallel to the tunnel axis (*c* axis), which is also parallel to the long-needle axis of the crystal morphology. (**C**) Structural changes associated with the phase transition in BrCH/thiourea (with H atoms omitted for clarity). (Left) Rhombohedral high-temperature phase viewed along the thiourea host tunnels (the isotropically disordered BrCH guests are not shown). (Middle and Right) Monoclinic low-temperature phase (110 K) viewed along the host tunnels (middle) and perpendicular to the tunnel (right); the C–Br bonds of all BrCH guests form an angle ψ ≈ 52.5° with respect to the tunnel axis (vertical at right). (**D**) Definition of angles ψ and ω specifying the orientation of the C–Br bond relative to the unit cell axes of the thiourea host structure in the low-temperature phase (shown superimposed on a schematic of the crystal morphology).

Although x-ray and optical birefringence share several common characteristics, optical birefringence relates to the anisotropy of the material as a whole (for example, for a crystalline material it depends on the overall symmetry of the crystal structure), whereas x-ray birefringence (XB), when studied at an x-ray energy close to the absorption edge of a specific type of atom in the material, depends on the local anisotropy in the vicinity of the selected type of atom. Thus, XB depends on the orientational properties of the bonding environment of the x-ray–absorbing atom. As a consequence, the "optic axis" in the case of XB is not necessarily related to a crystallographic "optic axis," and measurement of XB has the potential to yield structural information on the local orientational properties of individual molecules and/or bonds (*14*).

Previous studies of XB (*15*–*18*) used a narrowly focused x-ray beam and did not provide spatially resolved mapping of the material. We propose an experimental setup (Fig. 1A) that allows XB measurements to be carried out in a spatially resolved imaging mode, using a large-area linearly polarized x-ray beam [with dimensions 0.8 mm (vertical) by 4.0 mm (horizontal)] incident on the sample (*19*). The intensity of the wide x-ray beam emerging from the polarization analyzer is recorded by using an area detector, mapping the XB of the material in a spatially resolved manner, with resolution of the order of 10 μm (*20*). In the present work, the exposure time to record each XB image was 1 s.

To demonstrate the XB imaging (XBI) technique, we focused on materials containing brominated organic molecules, using incident linearly polarized x-rays from a synchrotron source [beamline B16 at the Diamond Light Source (*21*)], with energy corresponding to the Br K-edge. In this case (*15*, *16*, *22*–*24*), XB depends on the orientation of C–Br bonds relative to the incident polarized x-ray beam. To demonstrate the sensitivity and utility of XBI for spatially resolved mapping, our first experiment focused on a model material in which all C–Br bonds are parallel to each other—specifically, the thiourea inclusion compound containing 1-bromoadamantane (1-BA) guest molecules (Fig. 1B) (*25*). The orientation of the crystal relative to the linearly polarized incident x-ray beam is specified by the crystal orientation angles χ and φ defined in Fig. 1A.

XB images for a single crystal of 1-BA/thiourea as a function of χ (with φ fixed) are provided in Fig. 2 and movie S1. Each image shows a spatially resolved map of the transmitted x-ray intensity (brightness scales proportionally with intensity) for a specific orientation of the crystal. In Fig. 2, the intensity varies markedly as a function of χ, with maximum brightness at $\chi \approx 45°$ and minimum brightness at $\chi \approx 90°$ (*26*). Maximum intensity arises when the orientation of the C–Br bonds is at ~45° with respect to the direction of linear polarization of the incident x-ray beam. For each crystal orientation, the transmitted intensity is uniform across the entire crystal, indicating that the crystal comprises a single orientational domain. The observed dependence of intensity on χ is directly analogous to the behavior of a uniaxial crystal in the polarizing optical microscope. XB images recorded for 1-BA/thiourea as a function of φ (with χ fixed at 40°, close to the maximum transmitted intensity in Fig. 2) are provided in fig. S1 and movie S2. Because the orientational properties of the C–Br bonds are not altered by rotation around the bond axis, no appreciable change in transmitted intensity is observed as a function of φ.

To assess the potential to exploit XBI to probe changes in molecular orientational distributions as a function of temperature, XBI experiments were carried out on a single crystal of the thiourea inclusion compound containing bromocyclohexane (BrCH) guest molecules (Fig. 1, C and D). This material is known (*27*) to undergo a phase transition at 233 K from a high-temperature phase in which the orientational distribution of the BrCH guest molecules is essentially isotropic (as a result of rapid molecular motion) to a low-temperature phase in which the BrCH molecules become orientationally ordered (specifically, with the C–Br bonds of all BrCH molecules oriented at $\psi \approx 52.5°$ and $\omega \approx 3.5°$ with respect to the thiourea host structure, as defined in Fig. 1D).

XB images recorded for BrCH/thiourea at 298 K (Fig. 3A and movies S3 and S4) demonstrate that for the high-temperature phase, there is no variation in transmitted x-ray intensity as a function of crystal orientation, which is fully consistent with the isotropic orientational distribution of the C–Br bonds of the BrCH guest molecules in this phase. In contrast, under the same conditions in the polarizing optical microscope in crossed-polarizer configuration (Fig. 3B) a single crystal of BrCH/thiourea exhibits the classical behavior of a uniaxial crystal, with minimum transmitted intensity when the optic axis is parallel to the polarizer or analyzer and with maximum transmitted intensity when the optic axis is at 45° to these directions (for BrCH/

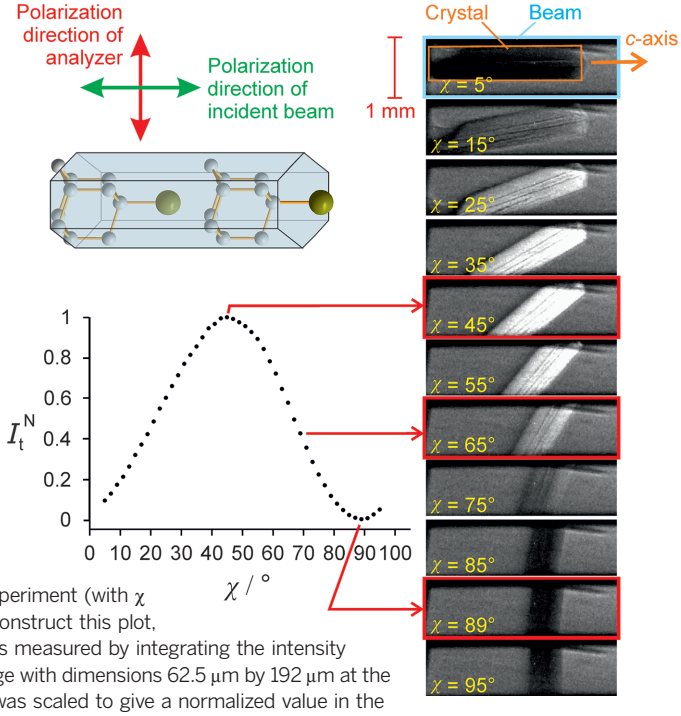


Fig. 2. XB images for a model material with uni-directional alignment of C–Br bonds. XBI data recorded at 280 K for a single crystal of 1-BA/thiourea as a function of χ (with φ fixed). The images represent spatially resolved maps of transmitted x-ray intensity across the crystal. Relative brightness in the images scales with x-ray intensity. The variation of normalized transmitted intensity (I_t^N) as a function of χ is shown in the plot at left, using data from all images recorded in the experiment (with χ varied in steps of 2°). To construct this plot, transmitted intensity I_t was measured by integrating the intensity across a region of the image with dimensions 62.5 μm by 192 μm at the center of the crystal and was scaled to give a normalized value in the range $0 \le I_t^N \le 1$.

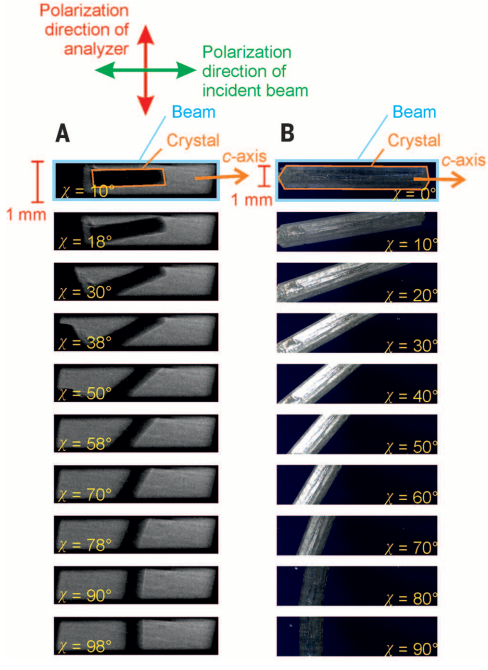


Fig. 3. Comparison of XBI and polarizing optical microscopy. (**A**) XB images and (**B**) polarizing optical microscope images recorded as a function of χ for single crystals of BrCH/thiourea in the high-temperature phase [(A) 298 K and (B) 293 K].

thiourea, the optic axis is the *c* axis of the rhombohedral thiourea host structure, parallel to the long-needle axis of the crystal morphology in Fig. 3B). These results demonstrate the difference between optical and x-ray birefringence: The former depends on the overall crystal symmetry, whereas the latter depends on the local orientational properties in the vicinity of the x-ray–absorbing atom within the material (in the present case, the orientational distribution of the C–Br bonds).

In the low-temperature phase of BrCH/thiourea, the XB behavior changes dramatically. At 20 K, for the crystal orientation (*28*) {χ = 10°, φ = 0°} (Fig. 4, top left, and fig. S2) it is evident that the crystal comprises orientationally distinct domains. Thus, a large parallelogram-shaped domain (with dimensions of a few hundred micrometers) dominates the central region of the crystal (bright region in the image), with two smaller domains (dark regions) at each end of the crystal. The domain boundaries between the major domain and the two minor domains are parallel to each other and intersect the *c* axis at an angle of ~136°, allowing the domain boundary to be assigned as the crystallographic (10 $\bar{1}$) plane. For crystal orientation {χ = 10°, φ = 180°}, the XB image (Fig. 4, top right, and movie S5) is essentially an "inverted" form of the image for {χ = 10°, φ = 0°}, as expected given that these crystal orientations correspond to the incident x-ray beam passing in opposite directions through the crystal.

XB images recorded as a function of χ (with φ fixed at 0°) for BrCH/thiourea in the low-temperature phase (at 20 K) are provided in Fig. 4, left, and movie S6. For φ = 0°, the C–Br bonds in the major domain are very nearly perpendicular to the direction of propagation of the incident x-ray beam (*29*). The transmitted intensity for the major domain varies markedly with χ, with maxima and minima in intensity separated by $\Delta\chi \approx 45°$. As shown in Fig. 4 and given that the C–Br bonds are known (*27*) to form an angle $\psi \approx 52.5°$ with respect to the tunnel (*c* axis) of the thiourea host structure in the low-temperature phase, the observed intensity maximum (at $\chi \approx 82°$) corresponds to the C–Br bonds forming an angle of ~45° with respect to the direction of polarization of the incident x-ray beam (horizontal). Correspondingly, minimum transmitted intensity (observed at $\chi \approx 38°$ in Fig. 4) occurs when the C–Br bonds form an angle of ~90° with respect to the direction of polarization of the incident x-ray beam. Thus, the χ-dependence of the XB images shown (for φ = 0°) in Fig. 4 is analogous to the behavior of a uniaxial crystal in the polarizing optical microscope, with the direction of the C–Br bonds representing the "optic axis" in the case of the XBI data. XB images (fig. S3 and movie S7) recorded as a function of temperature indicate that there is no change in the size and spatial distribution of the domains with variation of temperature in the low-temperature phase (*30*).

As demonstrated above, XBI enables spatially resolved mapping of the orientational properties of specific types of molecule and/or bond in materials, offering particular opportunities in cases for which the application of x-ray diffraction techniques may not be feasible (such as partially ordered materials, multiply twinned crystals, or other materials with complex domain structures). Although demonstrated here for the study of single-crystal samples, there is no requirement for crystallinity because XB is sensitive specifically to local molecular orientations; thus, XBI may be applied to any material (including liquids or amorphous solids) with an anisotropic distribution of molecular orientations. The results reported for BrCH/thiourea in the low-temperature phase highlight the potential to exploit XBI for spatially resolved analysis of orientationally distinct domains. Knowledge of domain structures (in particular, aspects such as domain sizes, the orientational relationships between domains, and the nature of domain boundaries) can be critical for controlling the performance of electronic, optical, and magnetic devices (*31*, *32*) and the mechanical properties of biomaterials (*33*).

Because XBI is a full-field imaging technique (*34*), with the entire image recorded simultaneously, the measurement of XB images is fast (exposure time of 1 s for each image shown here), leading to the potential to study dynamic processes (such as the propagation of domain boundaries during phase transitions). The time to record a single image in XBI could be reduced to ~1 ms for a storage ring undulator source (rather than the bending-magnet source used here) and by using a faster x-ray detector than that used in the present study, and could even be reduced to less than 100 fs by using a single pulse from an x-ray free-electron laser, creating a new opportunity for imaging ultra-fast molecular dynamics.

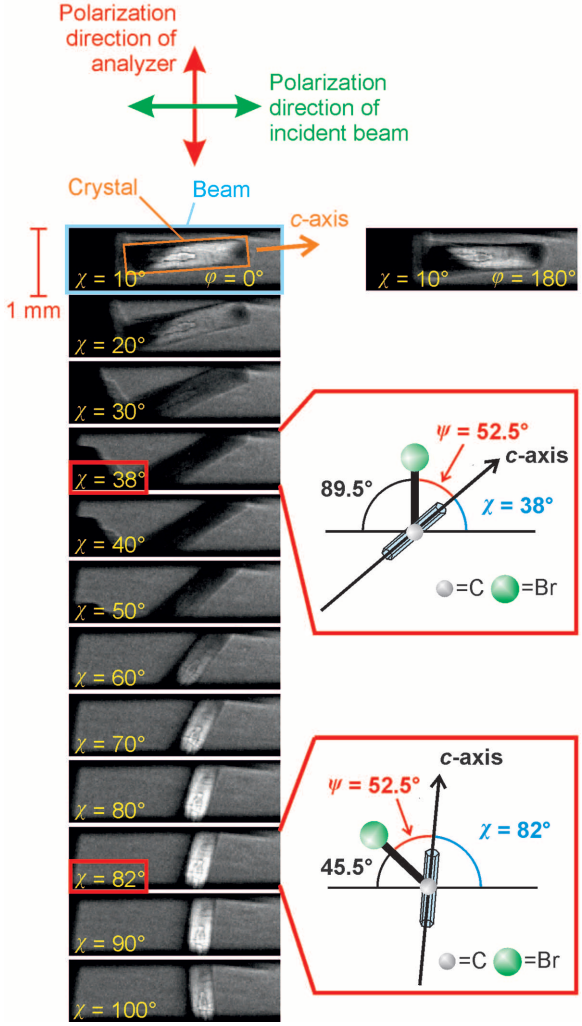


Fig. 4. XB images for the orientationally ordered phase of BrCH/thiourea. XBI data recorded at 20 K for a single crystal of BrCH/thiourea as a function of χ (with φ fixed at 0°). Maximum brightness (for the large central domain) arises when the C–Br bonds form an angle of ~45° with respect to the linearly polarized incident beam (achieved at $\chi \approx 82°$) and minimum brightness arises when the C–Br bonds form an angle of ~90° with respect to the linearly polarized incident beam (achieved at $\chi \approx 38°$).

REFERENCES AND NOTES

1. A. El Goresy, M. Chen, L. Dubrovinsky, P. Gillet, G. Graup, *Science* **293**, 1467–1470 (2001).
2. N. H. Hartshorne, A. Stuart, *Practical Optical Crystallography* (Edward Arnold, London, 1969).
3. W. Kaminsky, K. Claborn, B. Kahr, *Chem. Soc. Rev.* **33**, 514–525 (2004).
4. L. Schmidt-Mende *et al.*, *Science* **293**, 1119–1122 (2001).
5. H. Yang, N. Coombs, G. A. Ozin, *Nature* **386**, 692–695 (1997).
6. H. E. Warriner, S. H. J. Idziak, N. L. Slack, P. Davidson, C. R. Safinya, *Science* **271**, 969–973 (1996).
7. S. E. Malawista, H. Sato, K. G. Bensch, *Science* **160**, 770–772 (1968).
8. I. K. Iverson, S. W. Tam-Chang, *J. Am. Chem. Soc.* **121**, 5801–5802 (1999).

9. K. M. Kahn, J. L. Cook, F. Bonar, P. Harcourt, M. Astrom, *Sports Med.* **27**, 393–408 (1999).
10. L. C. Hughes, C. W. Archer, I. ap Gwynn, *Eur. Cell. Mater.* **9**, 68–84 (2005).
11. L. W. Jin *et al*., *Proc. Natl. Acad. Sci. U.S.A.* **100**, 15294–15298 (2003).
12. Y. Chen *et al*., *Appl. Phys. Lett.* **94**, 053901 (2009).
13. K. Kerkam, C. Viney, D. Kaplan, S. Lombardi, *Nature* **349**, 596–598 (1991).
14. For molecular solids, XB depends on the orientational properties of the molecule containing the x-ray–absorbing atom, and in particular depends on the bonding environment of this atom in the molecule. Here, we focus on XB studies at the Br K edge for materials containing brominated organic molecules. In this case, XB behavior can be rationalized simply on the basis of the orientational properties of the C–Br bonds (*15*, *16*).
15. B. A. Palmer, A. Morte-Ródenas, B. M. Kariuki, K. D. M. Harris, S. P. Collins, *J. Phys. Chem. Lett* **2**, 2346–2351 (2011).
16. B. A. Palmer *et al*., *J. Phys. Chem. Lett* **3**, 3216–3222 (2012).
17. B. A. Collins *et al*., *Nat. Mater.* **11**, 536–543 (2012).
18. Y. Joly, S. P. Collins, S. Grenier, H. C. N. Tolentino, M. De Santis, *Phys. Rev. B* **86**, 220101 (2012).
19. Materials and methods are available as supplementary materials on *Science* Online.
20. The spatial resolution of the XB images in the vertical direction (~13 μm) is limited by the resolution of the charge-coupled device–based detector, and the spatial resolution in the horizontal direction (~28 μm) is limited by the penetration of the beam into the polarization analyzer [Si(555) reflection]. The latter could be reduced to less than 1 μm by using high-quality crystals of heavier elements.
21. K. J. S. Sawhney *et al*., *AIP Conf. Proc.* **1234**, 387–390 (2010).
22. S. P. Collins *et al*., *J. Phys. Conf. Ser.* **425**, 132015 (2013).
23. C. Brouder, *J. Phys. Condens. Matter* **2**, 701–738 (1990).
24. S. P. Collins *et al*., *J. Phys. Condens. Matter* **14**, 123–134 (2002).
25. M.-H. Chao, B. M. Kariuki, K. D. M. Harris, S. P. Collins, D. Laundy, *Angew. Chem. Int. Ed.* **42**, 2982–2985 (2003).
26. For $\chi = 0°$, the crystal *c* axis is horizontal (*x*-*z* plane), parallel to the linearly polarized incident x-ray beam.
27. B. A. Palmer, B. M. Kariuki, A. Morte-Ródenas, K. D. M. Harris, *Cryst. Growth Des.* **12**, 577–582 (2012).
28. For BrCH/thiourea, the *c* axis is the tunnel axis of the thiourea host structure in both the high- and low-temperature phases. With respect to the hexagonal unit cell (a_h, b_h, c_h) of the high-temperature phase, the crystal orientation {$\chi = 0°$, $\varphi = 0°$} has the c_h axis parallel to the laboratory *x* axis and a {100} plane perpendicular to the *z* axis. With respect to the monoclinic unit cell (a_m, b_m, c_m) of the low-temperature phase, in the crystal orientation {$\chi = 0°$, $\varphi = 0°$} the c_m axis is parallel to the laboratory *x* axis, the b_m axis is parallel to the *z* axis, and the projection of the a_m axis on the plane perpendicular to the c_m axis [denoted proj(a_m)] is perpendicular to the *x*-*z* plane.
29. For $\varphi = 0°$, the b_m axis of the crystal in the low-temperature phase is parallel to the laboratory *z* axis. Hence, because the angle ω (defined in Fig. 1D) is known (*27*) to be only ~3.5°, the C–Br bonds in the major domain are very nearly perpendicular to the direction of propagation of the incident x-ray beam.
30. The changes of transmitted x-ray intensity as a function of temperature in this material have been rationalized previously (*16*) from XB studies using a focused x-ray beam.
31. H. Sirringhaus *et al*., *Appl. Phys. Lett.* **77**, 406–408 (2000).
32. H. Sirringhaus *et al*., *Nature* **401**, 685–688 (1999).
33. J. Stasiak, A. Zaffora, M. L. Constantino, A. Pandolfi, G. D. Moggridge, *Func. Mater. Lett.* **3**, 249–252 (2010).
34. In contrast, other techniques (*35*–*39*) for imaging materials that use incident x-ray radiation (such as scanning x-ray microscopy and x-ray topography) generally involve scanning a focused x-ray beam across the material (leading to the construction of a spatially resolved image through the analysis of the interaction of the beam with the material at each position of the beam). The time required to record a single image in XBI is clearly much faster than would be the case with a scanning probe. One consequence is that the overall radiation dose received by the sample should be lower in the case of XBI, suggesting that XBI may be advantageous in studying materials that are susceptible to radiation damage.
35. H. Ade, B. Hsiao, *Science* **262**, 1427–1429 (1993).
36. D. Sayre, H. N. Chapman, *Acta Crystallogr. A* **51**, 237–252 (1995).
37. D. K. Bowen, B. K. Tanner, *High Resolution X-ray Diffractometry and Topography* (Taylor & Francis, London, UK, 1998).
38. M. Howells, C. Jacobsen, T. Warwick, A. Van den Bos, in *Science of Microscopy*, P. W. Hawkes, J. C. H. Spence, Eds. (Springer, New York, 2007), pp. 835–926.
39. P. Thibault *et al*., *Science* **321**, 379–382 (2008).

ACKNOWLEDGMENTS

We are grateful to Diamond Light Source for the award of beam-time for experiments on beamline B16. We thank the Engineering and Physical Sciences Research Council (studentships to B.A.P. and G.R.E.-G.) and Cardiff University for financial support.

SUPPLEMENTARY MATERIALS

www.sciencemag.org/content/344/6187/1013/suppl/DC1
Materials and Methods
Figs. S1 to S3
Movies S1 to S7

18 March 2014; accepted 29 April 2014
10.1126/science.1253537

MARINE BIOGEOGRAPHY

Quaternary coral reef refugia preserved fish diversity

Loïc Pellissier,[1,2] Fabien Leprieur,[3] Valeriano Parravicini,[4,5] Peter F. Cowman,[6] Michel Kulbicki,[4] Glenn Litsios,[7,8] Steffen M. Olsen,[9] Mary S. Wisz,[2,10] David R. Bellwood,[11] David Mouillot[3,11]*

The most prominent pattern in global marine biogeography is the biodiversity peak in the Indo-Australian Archipelago. Yet the processes that underpin this pattern are still actively debated. By reconstructing global marine paleoenvironments over the past 3 million years on the basis of sediment cores, we assessed the extent to which Quaternary climate fluctuations can explain global variation in current reef fish richness. Comparing global historical coral reef habitat availability with the present-day distribution of 6316 reef fish species, we find that distance from stable coral reef habitats during historical periods of habitat loss explains 62% of the variation in fish richness, outweighing present-day environmental factors. Our results highlight the importance of habitat persistence during periods of climate change for preserving marine biodiversity.

Tropical marine biodiversity shows a unique longitudinal pattern with a peak of species richness in the Indo-Australian Archipelago (IAA) (*1*, *2*). With their biological and structural complexity, coral reefs support the world's greatest diversity of marine fishes (*3*–*5*). Reef-building corals track well-defined conditions of sea surface temperature and light (*6*) and are thus particularly sensitive to changes in climate and sea level. On short temporal and small spatial scales, coral assemblages exhibit highly dynamic fluctuations in species composition and abundance, with species-specific responses to disturbances (*7*, *8*). At longer time scales, fossil records show that coral reefs may have experienced dramatic contractions in response to environmental shifts. The most striking example is the last interglacial period, ~125,000 years ago, when a rise in sea surface temperature caused an equatorial retraction of coral reefs with a rapid loss of marine biodiversity (*9*). Colder temperatures and sea level drops have also been responsible for massive coral habitat loss in the past, with many coral reefs arising after the last glacial maximum (*10*). Given the dependency of most reef fishes on coral reef habitat (*11*, *12*), historical climatic oscillations are likely to have affected fish persistence and thus current biodiversity patterns.

The Quaternary period (2.6 million years ago to present) is characterized by at least 30 glacial-interglacial cycles of repeated global cooling and warming with consequences for reef habitat

[1]University of Fribourg, Department of Biology, Chemin du Musée 10, CH-1700 Fribourg, Switzerland. [2]Department of Bioscience, Aarhus University, 8000 C Aarhus, Denmark. [3]Laboratoire Ecologie des Systèmes Marins Côtiers UMR 5119, CNRS, Institut de Recherche pour le Développement (IRD), Institut Français de Recherche pour l'Exploitation de la Mer, UM2, UM1, cc 093, Place E. Bataillon, FR-34095 Montpellier Cedex 5, France. [4]IRD, UR 227 CoReUs, LABEX (Laboratoire d'Excellence) Corail, Laboratoire Arago, Boîte Postale 44, FR-66651 Banyuls/mer, France. [5]CESAB (Centre de Synthèse et d'Analyse sur la Biodiversité)–FRB (Fondation pour la Recherche sur la Biodiversité), Immeuble Henri Poincaré, Domaine du Petit Arbois, FR-13857 Aix-en-Provence cedex 3, France. [6]Centre for Macroevolution and Macroecology, Research School of Biology, Australian National University, Canberra, ACT 0200, Australia. [7]Department of Ecology and Evolution, Biophore Building, University of Lausanne, 1015 Lausanne, Switzerland. [8]Swiss Institute of Bioinformatics, Quartier Sorge, 1015 Lausanne, Switzerland. [9]Center for Ocean and Ice, Danish Meteorological Institute, Lyngbyvej 100, 2100 Copenhagen, Denmark. [10]Department of Ecology and Environment, DHI Water and Environment, 2970 Hørsholm, Denmark. [11]Australian Research Council Centre of Excellence for Coral Reef Studies, and School of Marine and Tropical Biology, James Cook University, Townsville, QLD 4811, Australia.
***Corresponding author. E-mail: david.mouillot@univ-montp2.fr**

availability. Stable coral reef habitats over geological time may have promoted fish biodiversity by acting as (i) refugia, which preserved species from extinction because of habitat loss (*4*, *13*); (ii) sources for the recolonization of unstable areas during more favorable periods (*14*, *15*); and (iii) evolutionary cradles with high speciation rates (*16*). Given these combined benefits, Quaternary coral reef refugia should have left their imprint on current richness patterns of coral reef fishes worldwide. To explore the influence of environmental history on global fish diversity patterns on tropical reefs, we identified the putative locations of refugia, defined as habitat suitable for corals during cold periods, by reconstructing coral reef paleodistributions during the Quaternary. By building on sea surface temperature and sea level paleoconditions inferred from sediment cores (*17*, *18*) to bind the coral reef environmental envelope (figs. S1 and S2), we mapped the paleodistribution of this habitat for the past three million years with a temporal resolution of 1000 years (Fig. 1A) by using an accurate model [95% of correct classification (fig. S3)]. For each current reef, isolation from refugia was computed as the sea distance to historical coral reef habitats across the glaciation cycles (Fig. 1B). We also mapped, at 5°-by-5° resolution, the global distribution of fish species richness by using the geographic range of 6316 tropical reef fishes (Fig. 1C). We then predicted fish richness patterns from historical (past coral reef area and isolation from refugia) and contemporary (mean sea surface temperature, coral reef area, and isolation) factors by using a set of bivariate and multivariate linear regression models including quadratic terms to account for nonlinear relationships.

We found that isolation from Quaternary refugia was the primary driver of reef fish richness (Fig. 2A) and that its effect was far greater than all other factors, including past and current coral reef area, isolation, and sea surface temperature (table S1). Areas closer to Quaternary refugia display higher fish richness (R^2 = 0.62; P < 0.0001) (Figs. 1 and 2A), emphasizing the crucial role of stable coral reef habitat during the Quaternary. When considering contemporary factors, neither the sea surface temperature (R^2 = 0.25; P < 0.0001) nor the level of isolation of coral reef habitats (R^2 = 0.30; P < 0.0001) or even the coral reef area (R^2 = 0.33; P < 0.0001) provided near or exceeding explanatory power to isolation from Quaternary refugia (table S1). These observations are supported by two complementary analyses. First, isolation from Quaternary refugia received the highest support over all subset models mixing historical and contemporary factors (table S2). Second, when partitioning the explained variance of fish richness (R^2 = 0.73) among historical and contemporary factors included in the model, isolation from Quaternary refugia showed the strongest independent effect, with a higher proportion of explained variance (24.4%) than current coral reef area, coral reef isolation, and sea surface temperature combined (15.5%). Furthermore, the explanatory power of historical extent of coral reef habitat on fish richness peaked during time periods when sea temperature was the lowest, causing the strongest coral reef habitat contractions (R^2 = 0.45, P < 0.0001) (figs. S4 and S5). Similar results are obtained when excluding the tropical Eastern Pacific and Atlantic basins that display the highest levels of isolation from refugia and the lowest extents of coral reef habitat during the cold periods compared with those located in the Indo-Pacific, suggesting that our findings are not biased by a basin effect (table S3 and figs. S6 and S7). Taken together, our results highlight how areas that retained suitable coral reef habitat over geological time served as refugia, buffering species from extinction by minimizing stochastic processes leading to population decline (*19*, *20*).

The impact of past habitat availability on current fish richness patterns should also depend on recolonization ability, mainly through larval dispersal that varies across families (*21*). Among the three families investigated (Pomacentridae, damselfishes; Labridae, wrasses; Chaetodontidae, butterflyfishes), damselfishes should show the strongest response to isolation from refugia, given their low swimming ability during the late pelagic stage and shorter pelagic larval duration, compared with wrasses and butterflyfishes (*21*). We estimated segment breakpoints in the regression models linking fish richness to the isolation from Quaternary refugia to test for a family-specific response (Fig. 2, B to D). Isolation from refugia was closely related to fish richness for the three families, suggesting common drivers (Fig. 2 and table S4), but their breaking points differed (fig. S8). As expected from their ecological characteristics and larval dispersal capacity (*21*), the damselfishes show a break point in fish richness at a lower level of isolation from refugia (46.1 km) compared with butterflyfishes (396.7 km) and wrasses (291.3 km). Lending additional support to this pattern, the effect of past extent of coral reef habitat is a better predictor of richness for damselfishes than for the two other families (table S4). Indeed, damselfishes richness is especially concentrated in the Indo-Pacific, which maintained extensive refugia during the Quaternary.

Historical barriers, such as those created by sea level drops during the Quaternary, may have played important roles in the isolation of populations by cutting off local sea basins (*22*, *23*). Paleohabitat models suggest that not only were

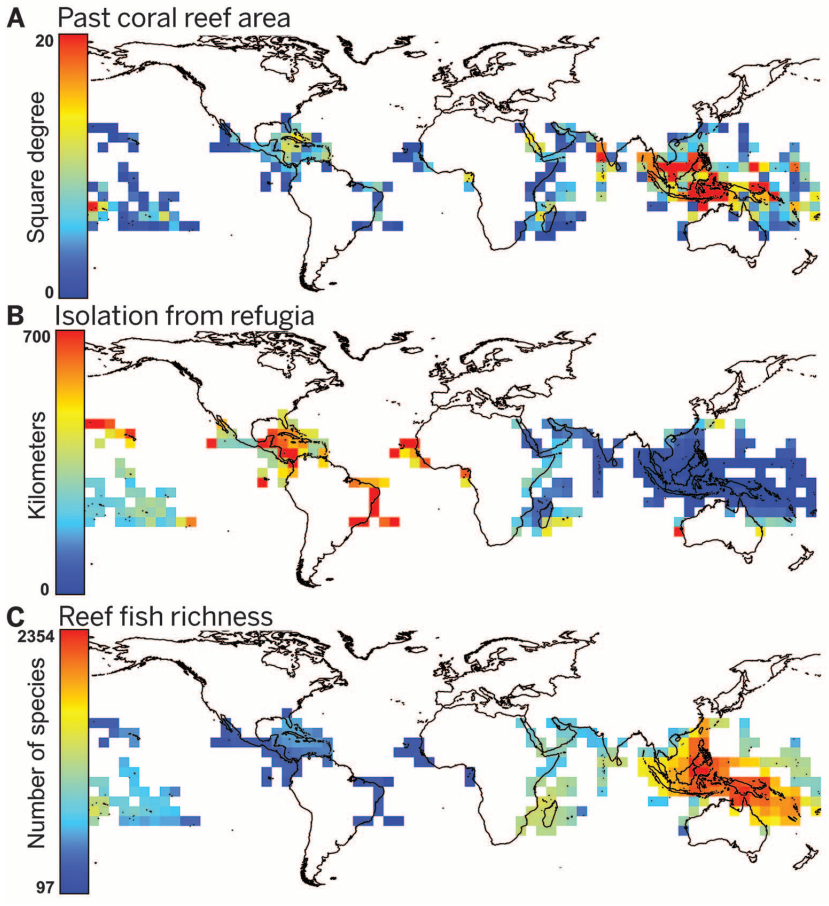


Fig. 1. Location of coral reefs, past isolation, and current fish richness. Maps of (**A**) the coral reef area per 5°-by-5° cell averaged for the periods of marked coral reef contraction, as characterized by lower sea surface temperature and sea level (square degree); (**B**) standardized isolation from stable coral reef areas across the Quaternary (kilometers); and (**C**) current global richness of reef fishes (number of species).

the Atlantic and Indo-Pacific oceans isolated from each other but that coral reefs within the Indo-Pacific were isolated in refugia such as the Red Sea, Madagascar, and Maldives, along with multiple small refugia within the IAA (Fig. 3). In particular, we found an increased spatial fragmentation of coral reef habitat over time from the onset of glaciations in the Indo-Pacific ocean (landscape division index, $R^2 = 0.15$, $P < 0.0001$) (Fig. 3). Fragmentation was highest during the periods with the coldest temperatures ($R^2 = 0.51$, $P < 0.0001$) (fig. S9). Our dated phylogenies indicate that a large proportion of fishes within the target families arose in the past 3 million years (percentage of species with an age of divergence from the most closely related sister species <3 Ma for wrasses is 19%; damselfishes, 31%; butterflyfishes, 65%) (Fig. 3). The number of recently diverged species (<3 Ma) was highest in proximity to refugia where these species could have arisen (wrasses, $R^2 = 0.61$ and $P < 0.0001$; butterflyfishes, $R^2 = 0.65$ and $P < 0.0001$; damselfishes, $R^2 = 0.57$ and $P < 0.0001$). Our results provide evidence for the role of disconnected but stable habitat area in promoting species diversification during the Quaternary, especially in the Indo-Pacific (*24*).

High extinction and low speciation rates in areas outside putative refugia can reduce species richness and should also affect the age of lineages represented in species assemblages (*25*). Refugia are expected to preserve species from extinction and should harbor the oldest species. In contrast, unstable areas are likely to harbor younger colonists, resulting in a narrower range of ages because they lack older species. Consistent with this hypothesis, the difference between the 95th and 5th percentiles of species age distribution is larger in refugia for all three families (wrasses, $R^2 = 0.22$, $P < 0.0001$; butterflyfishes, $R^2 = 0.32$, $P < 0.0001$; and damselfishes, $R^2 = 0.53$, $P < 0.0001$) (Fig. 4) without any bias related to variation in species richness (fig. S10). The effect of isolation from refugia is weaker for the wrasses than for the other two families (Fig. 4). The oldest wrasses occur both in the Indo-Pacific and in the Atlantic, the latter resulting from Atlantic colonization from the west Tethys Sea

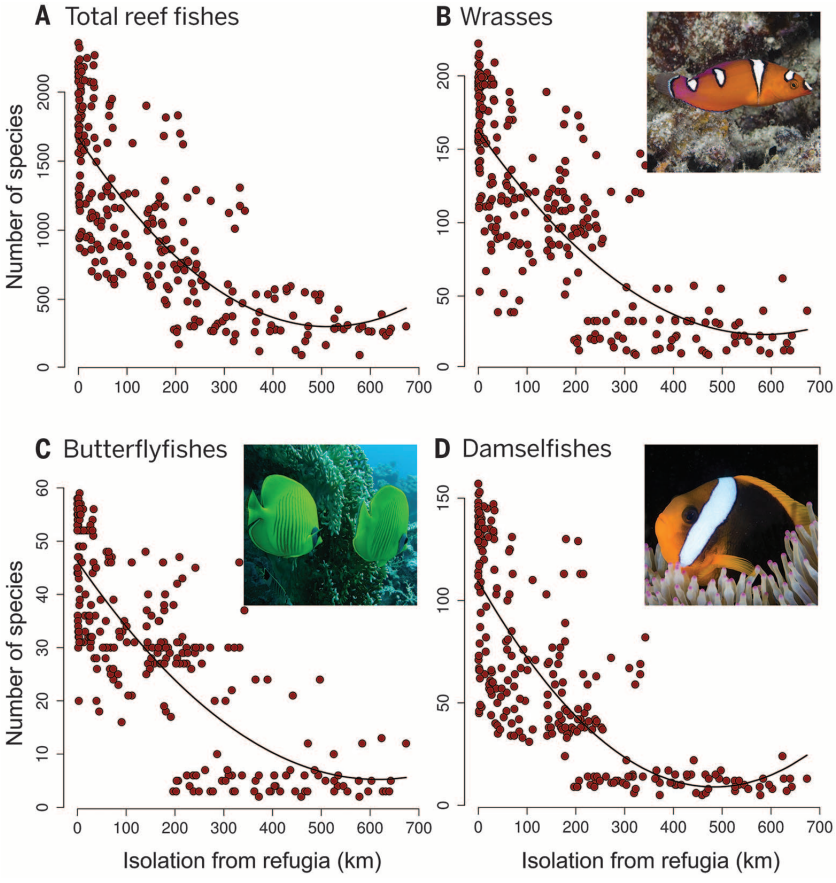
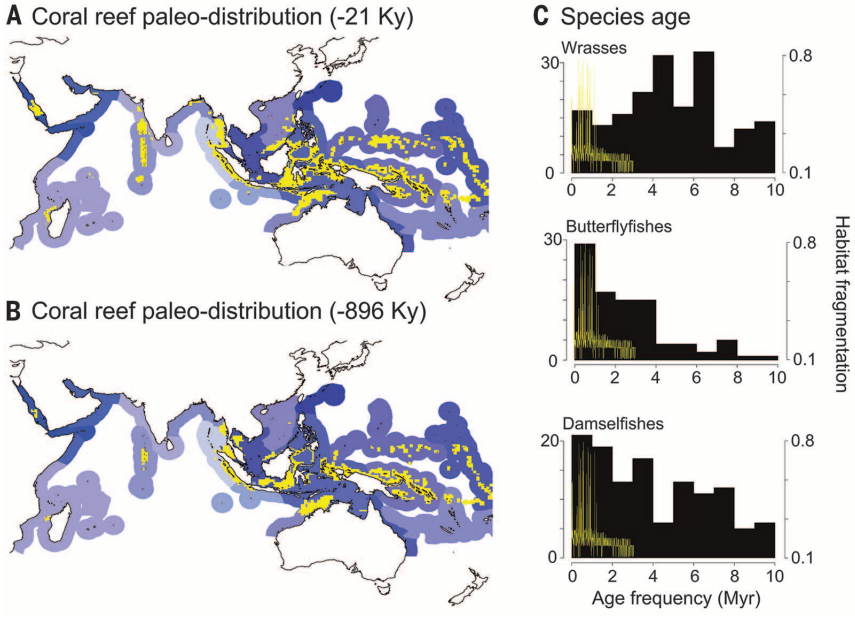


Fig. 2. Relationship between the standardized isolation from stable coral reef areas across the Quaternary and total richness of reef fishes. Shown is the total reef fish richness (**A**) as well as richness of three families: wrasses (**B**), butterflyfishes (**C**), and damselfishes (**D**). [Photo credits: J. P. Krajewski (B) and (D) and S. Gingins (C)]

Fig. 3. Reef paleodistribution and species age. Projected coral reef habitat for two time periods (yellow) based on historical sea surface temperature and sea level at −21 thousand years (Ky) (**A**) and −896 Ky (**B**). Expert-delimited ecoregions based on faunal dissimilarity are shown in shades of blue. The coral reef area for each time step was used to compute the change in habitat fragmentation through time, which is represented as the yellow line in (**C**). Also shown in black is the histogram of species age for wrasses, butterflyfishes, and damselfishes.



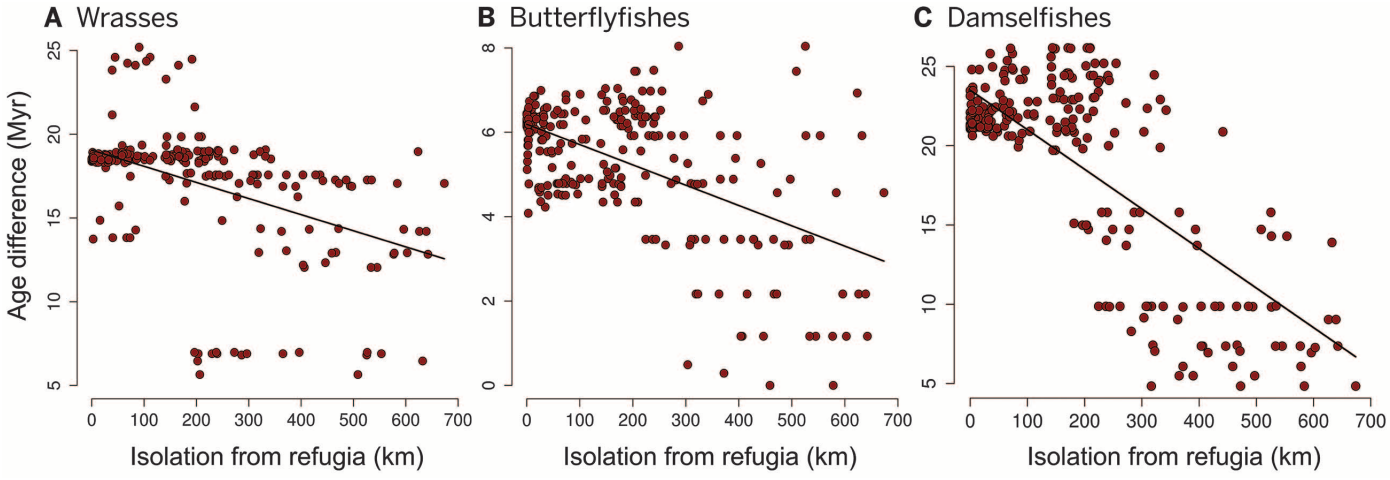


Fig. 4. Isolation distance and species age. (**A** to **C**) Relationship between the standardized isolation from stable coral reef areas across the Quaternary (kilometers) and the difference between the 95th and 5th percentile of species age in assemblages in each cell. Cells closer to refugia during the Quaternary have a larger age range because they contain both older and younger species.

(*3*, *4*). Because Atlantic lineages are less associated with coral reef habitats (*3*, *4*), instability during the Quaternary likely had a lower impact on the persistence of wrasses. In support of this result, the wrasses have exhibited relatively few new species in the past 3 million years (Fig. 3), suggesting a less intense effect of habitat fragmentation during the Quaternary.

Our results highlight the central role of coral reef refugia during Quaternary climatic fluctuations and how isolation from refugia has modulated fish richness patterns. The distance from the Indo-Pacific center was found to be a major determinant of fish richness (*26*). The Indo-Pacific maintained extensive coral reef refugia during cold periods with low sea level stands (Fig. 1A), in areas including the IAA, Maldives, Madagascar, and Red Sea (Fig. 3). These areas thus appear to have acted as centers of survival, as previously suggested (*27*, *28*). By contrast, in the Atlantic, only very limited areas were suitable for coral reefs during cold periods (Fig. 1A), implying a degradation of Caribbean coral reefs after the onset of glaciation. This may explain the relatively weak association of Caribbean fishes with coral reef habitats (*29*) and the high extinction rates around 2 to 1 Ma observed in near-shore environments (*30*). Paralleling results for subtropical rainforest (*31*), we demonstrate that historical habitat availability in coral reefs is as important as current habitat extent in explaining observed distributions of fish species richness. Our results suggest that the possible "cradle" effect of coral reefs may have arisen from increased fragmentation during episodic cold events, especially in the IAA (Fig. 3). Quaternary climatic fluctuations have left their mark on contemporary patterns of reef fish biodiversity through historical shifts in habitat availability and isolation.

Examining how coral reefs have changed in the past may give new insight into understanding how reef species might respond to global change (*32*). Our results suggest that current reef fish biodiversity can be primarily explained by past habitat availability. This finding has important implications for conservation of coral reefs worldwide under ongoing climate change. Most notably, the warm refugia that protected species in the past may in turn be the first to be threatened by future warming (*33*). Ideally, management strategies should focus on the protection of coral reefs over large areas that maintain corridors of suitable habitat that allow the resilience of fish biodiversity through connectivity from historical refugia. Our results emphasize the strong relationship between reef fish biodiversity, past habitat shifts, the role of habitat conservation under climate change, and, more generally, the role of historical habitat shift in shaping the diversity of life we observe today.

REFERENCES AND NOTES

1. D. R. Bellwood, T. P. Hughes, *Science* **292**, 1532–1535 (2001).
2. W. Renema *et al.*, *Science* **321**, 654–657 (2008).
3. S. A. Price, R. Holzman, T. J. Near, P. C. Wainwright, *Ecol. Lett.* **14**, 462–469 (2011).
4. P. F. Cowman, D. R. Bellwood, *J. Biogeogr.* **40**, 209–224 (2013).
5. V. Parravicini *et al.*, *Ecography* **36**, 1254–1262 (2013).
6. J. A. Kleypas *et al.*, *Am. Zool.* **39**, 146 (1999).
7. J. H. Connell, T. P. Hughes, C. C. Wallace, *Ecol. Monogr.* **67**, 461–488 (1997).
8. T. P. Hughes *et al.*, *Curr. Biol.* **22**, 736–741 (2012).
9. W. Kiessling, C. Simpson, B. Beck, H. Mewis, J. M. Pandolfi, *Proc. Natl. Acad. Sci. U.S.A.* **109**, 21378–21383 (2012).
10. J. E. N. Veron, M. Stafford-Smith, *Corals of the World* (Australian Institute of Marine Science, Townsville, Australia, 2000).
11. M. J. Paddack *et al.*, *Curr. Biol.* **19**, 590–595 (2009).
12. M. C. Bonin, G. R. Almany, G. P. Jones, *Ecology* **92**, 1503–1512 (2011).
13. G. Paulay, *Paleobiology* **16**, 415–434 (1990).
14. A. C. Carnaval, M. J. Hickerson, C. F. Haddad, M. T. Rodrigues, C. Moritz, *Science* **323**, 785–789 (2009).
15. B. Sandel *et al.*, *Science* **334**, 660–664 (2011).
16. D. D. McKenna, B. D. Farrell, *Proc. Natl. Acad. Sci. U.S.A.* **103**, 10947–10951 (2006).
17. K. G. Miller *et al.*, *Science* **310**, 1293–1298 (2005).
18. T. D. Herbert, L. C. Peterson, K. T. Lawrence, Z. Liu, *Science* **328**, 1530–1534 (2010).
19. M. L. Rosenzweig, *Species Diversity in Space and Time* (Cambridge Univ. Press, Cambridge, 1995).
20. S. L. Chown, K. J. Gaston, *Trends Ecol. Evol.* **15**, 311–315 (2000).
21. O. J. Luiz *et al.*, *Proc. Natl. Acad. Sci. U.S.A.* **110**, 16498–16502 (2013).
22. J. W. McManus, "Marine speciation, tectonics, and sea-level changes in Southeast Asia," in *Proceedings of the Fifth International Coral Reef Congress*, C. Gabrie, B. Salvat, Eds. (International Coral Reef Symposium, Penang, Malaysia, 1985), vol. **4**, pp. 133–138.
23. D. C. Potts, in *Proceedings of the Fifth International Coral Reef Congress*, C. Gabrie, B. Salvat, Eds. (International Coral Reef Symposium, Penang, Malaysia, 1985), vol. 4, pp. 127–132.
24. A. J. Kohn, in *Proceedings of the Fifth International Coral Reef Congress*, C. Gabrie, B. Salvat, Eds. (International Coral Reef Symposium, Penang, Malaysia, 1995), vol. 4, pp. 139–144.
25. J. Fjeldså, J. C. Lovett, *Biodivers. Conserv.* **6**, 325–346 (1997).
26. C. Mora, P. M. Chittaro, P. F. Sale, J. P. Kritzer, S. A. Ludsin, *Nature* **421**, 933–936 (2003).
27. P. H. Barber, D. R. Bellwood, *Mol. Phylogenetics Evol.* **35**, 235–253 (2005).
28. D. R. Bellwood, C. P. Meyer, *J. Biogeogr.* **36**, 569–576 (2009).
29. D. R. Bellwood, P. C. Wainwright, in *Coral Reef Fishes: Dynamics and Diversity in a Complex Ecosystem*, P. F. Sale, Ed. (Academic Press, San Diego, CA, 2002).
30. A. O'Dea *et al.*, *Proc. Natl. Acad. Sci. U.S.A.* **104**, 5501–5506 (2007).
31. C. H. Graham, C. Moritz, S. E. Williams, *Proc. Natl. Acad. Sci. U.S.A.* **103**, 632–636 (2006).
32. J. M. Pandolfi, S. R. Connolly, D. J. Marshall, A. L. Cohen, *Science* **333**, 418–422 (2011).
33. C. Mora *et al.*, *PLOS Biol.* **11**, e1001682 (2013).

ACKNOWLEDGMENTS

This study was supported by grants from the Danish Council for Independent Research no. 12-126430 to L.P., Marie Curie IOF-GA-2009-236316 to D.M., FRB CESAB–General Approach to Species-Abundance Relationships in a context of global change, reef fish species as a model, and the Australian Research Council. We thank three anonymous reviewers for valuable comments on the manuscript. We thank J. P. Krajewski and S. Gingins for the fish images. Data are available in the supplementary materials.

SUPPLEMENTARY MATERIALS

www.sciencemag.org/content/344/6187/1016/suppl/DC1
Materials and Methods
Figs. S1 to S14
Tables S1 to S4
References (*34*–*80*)
Database S1

17 December 2013; accepted 24 April 2014
10.1156/science.1249853

NEURAL DEVELOPMENT

Retrograde semaphorin signaling regulates synapse elimination in the developing mouse brain

Naofumi Uesaka,[1] Motokazu Uchigashima,[2] Takayasu Mikuni,[1] Takanobu Nakazawa,[1] Harumi Nakao,[3] Hirokazu Hirai,[4] Atsu Aiba,[3] Masahiko Watanabe,[2] Masanobu Kano[1]*

Neural circuits are shaped by elimination of early-formed redundant synapses during postnatal development. Retrograde signaling from postsynaptic cells regulates synapse elimination. In this work, we identified semaphorins, a family of versatile cell recognition molecules, as retrograde signals for elimination of redundant climbing fiber to Purkinje cell synapses in developing mouse cerebellum. Knockdown of Sema3A, a secreted semaphorin, in Purkinje cells or its receptor in climbing fibers accelerated synapse elimination during postnatal day 8 (P8) to P18. Conversely, knockdown of Sema7A, a membrane-anchored semaphorin, in Purkinje cells or either of its two receptors in climbing fibers impaired synapse elimination after P15. The effect of Sema7A involves signaling by metabotropic glutamate receptor 1, a canonical pathway for climbing fiber synapse elimination. These findings define how semaphorins retrogradely regulate multiple processes of synapse elimination.

Neurons form exuberant synapses with target cells early in development. Then necessary synapses are selectively strengthened, whereas unnecessary connections are weakened and eventually eliminated during postnatal development. This process, known as synapse elimination, is crucial for shaping immature neural circuits into functionally mature versions (*1*–*3*) and requires unidentified retrograde signaling from postsynaptic cells. In our work, we searched for retrograde signaling molecules involved in the regression of redundant synapses from climbing fibers onto Purkinje cells during postnatal development of the mouse cerebellum (*2*, *4*–*6*).

First, we profiled genes expressed in postsynaptic Purkinje cells during the period of climbing fiber synapse elimination (figs. S1 and S2) (see supplementary materials and methods). We picked up genes of secreted or membrane-associated molecules as possible candidates that mediate retrograde signaling. We then performed loss-of-function analyses by lentivirus-mediated RNA interference knockdown in Purkinje cells in cocultures of the cerebellum and the inferior olive, the origin of climbing fibers (*7*, *8*). We found that knockdown of Sema3A, a secreted class of semaphorin, caused a significant reduction in the number of climbing fibers innervating each Purkinje cell (Fig. 1, A and C, and fig. S3). Furthermore, the amplitude of excitatory postsynaptic currents induced by climbing fiber stimulation (CF-EPSCs) became significantly smaller after Sema3A knockdown (Fig. 1E). In contrast, knockdown of Sema7A, a membrane-bound class of semaphorin, caused a significant increase in the number of climbing fibers innervating each Purkinje cell without changing CF-EPSC amplitude (Fig. 1, B, D, and F, and fig. S3).

We next evaluated the roles of Sema3A and Sema7A in climbing fiber synapse elimination in vivo. We verified that *Sema3A* and *Sema7A* were strongly expressed in Purkinje cells during synapse elimination (fig. S4 and table S1). We injected lentiviruses expressing a microRNA (miRNA) against Sema3A or Sema7A into the cerebellar vermis of neonatal mice. We then examined climbing fiber innervation in acute cerebellar slices prepared from mice at various ages. We found that Sema3A knockdown caused a significant reduction in the number of climbing fibers (Fig. 2, A and C). This effect was seen from postnatal day 8 (P8) to P18 but not during P6 and P7 or P21 to P30 (fig. S5), indicating that Sema3A knockdown accelerated synapse elimination without affecting axon guidance or initial synapse formation. Furthermore, the amplitude of CF-EPSCs was significantly smaller in Sema3A knockdown Purkinje cells (table S2). There was no change in basic electrophysiological parameters of CF-EPSCs, including paired-pulse ratio (table S2), which suggests that the change is mostly of postsynaptic origin. The effect of Sema3A knockdown was rescued by co-injection of lentiviruses for the expression of a miRNA-resistant Sema3A (Sema3A-rescue) (Fig. 2, A and C). Moreover, the number of climbing fiber terminals around the somata of Sema3A knockdown Purkinje cells was smaller than that of control Purkinje cells (Fig. 2, E and G, and fig. S6). Our morphological analysis, however, was not sensitive enough to capture the intermediate state of climbing fiber terminals undergoing elimination. Taken together, these results indicate that Sema3A maintains or strengthens somatic climbing fiber synapses and opposes their elimination from P8 to P18, which covers both the early and the late phases of climbing fiber elimination (*2*, *9*–*13*). In the present experimental condition, only a subset of Purkinje cells express Sema3A

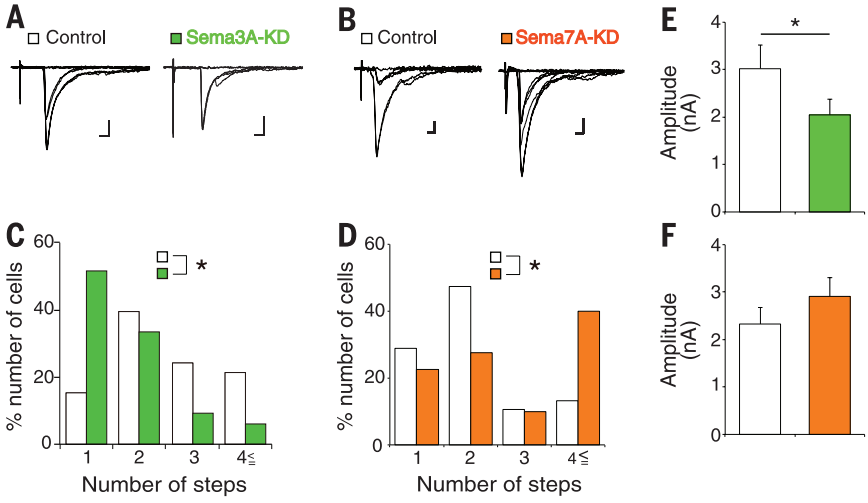


Fig. 1. Effects of Sema3A or Sema7A knockdown in Purkinje cells on climbing fiber synapse elimination in olivo-cerebellar cocultures. (**A** and **B**) Sample CF-EPSCs from control and Sema3A knockdown (Sema3A-KD) (A) or Sema7A knockdown (Sema7A-KD) (B) Purkinje cells at 16 days in vitro (DIV). Scale bars, 0.5 nA (vertical) and 5 ms (horizontal). (**C** and **D**) Frequency distributions of the number of climbing fibers innervating each Purkinje cell during 15 to 18 DIV for (C) control (white columns, n = 32 cells) and Sema3A-KD (green columns, n = 38) and for (D) control (n = 38) and Sema7A-KD (orange columns, n = 40). *P < 0.05 (Mann-Whitney U test). (**E** and **F**) Average amplitudes of CF-EPSCs for (E) control (n = 32) and Sema3A-KD (n = 38) and for (F) control (n = 38) and Sema7A-KD (n = 40). *P < 0.05 (Mann-Whitney U test). Error bars indicate SEM.

[1]Department of Neurophysiology, Graduate School of Medicine, The University of Tokyo, Tokyo 113-0033, Japan. [2]Department of Anatomy, Hokkaido University Graduate School of Medicine, Sapporo 060-8638, Japan. [3]Laboratory of Animal Resources, Center for Disease Biology and Integrated Medicine, Graduate School of Medicine, The University of Tokyo, Tokyo 113-0033, Japan. [4]Department of Neurophysiology, Gunma University Graduate School of Medicine, Maebashi, Gunma 371-8511, Japan.
*Corresponding author. E-mail: mkano-tky@m.u-tokyo.ac.jp

knockdown constructs, and they are surrounded by normal Purkinje cells that secrete Sema3A. Therefore, the diffusion of Sema3A is considered to be limited and does not affect climbing fibers that form synapses on neighboring Purkinje cells.

In contrast to Sema3A, Sema7A knockdown caused a significant increase in the number of climbing fibers (Fig. 2, B and D). This effect was not seen before P14, became obvious during P15 to P18, and persisted into adulthood (fig. S7 and table S3). There was no change in basic electrophysiological parameters of CF-EPSCs (table S3). The number of climbing fiber terminals around the somata of Sema7A knockdown Purkinje cells was larger during P21 to P30 than that of control Purkinje cells (Fig. 2, F and H, and fig. S6), yet the intermediate state of climbing fiber terminals undergoing elimination was not found. These results indicate that Sema7A knockdown specifically impairs elimination of somatic climbing fiber synapses after P15. Our results thus suggest that Sema7A facilitates the late phase of climbing fiber elimination (*2*, *5*, *11*, *13*).

We next tested whether the Sema7A signaling for climbing fiber synapse elimination is downstream of metabotropic glutamate receptor

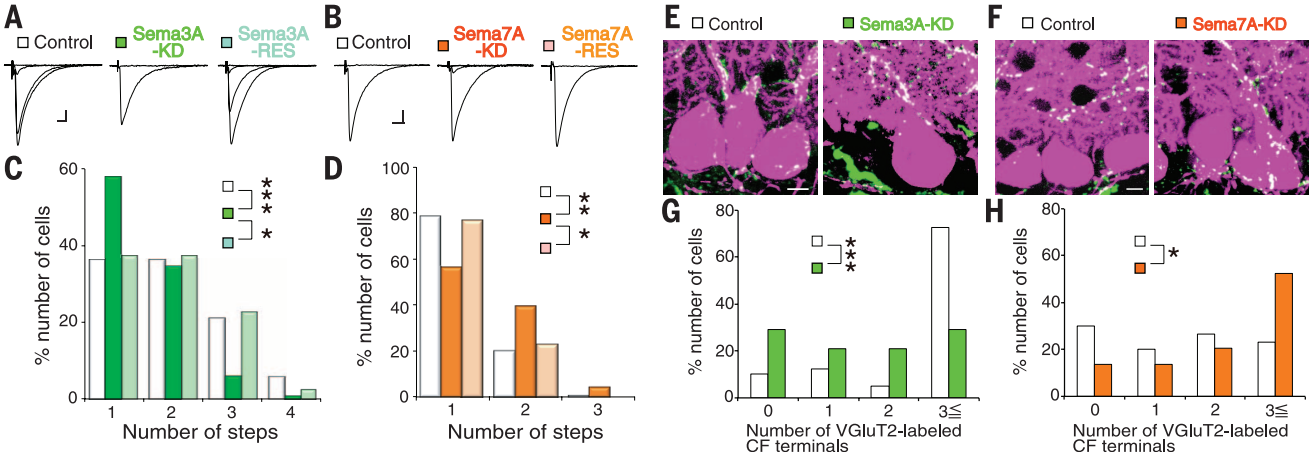


Fig. 2. Postsynaptic Sema3A and Sema7A have opposite effects on climbing fiber synapse elimination in vivo. (**A** to **D**) Sample CF-EPSCs [scale bars, 0.5 nA (vertical) and 5 ms (horizontal)] and frequency distributions of the number of climbing fibers innervating each Purkinje cell (C and D) for control (white columns, $n = 70$), Sema3A-KD (dark green columns, $n = 79$), and Sema3A-rescue (Sema3A-RES, light green columns, $n = 35$) during P12 to P15 (A and C), and for control ($n = 93$), Sema7A-KD (orange columns, n = 84), and Sema7A-rescue (Sema7A-RES, light orange columns, $n = 43$) during P21 to P30 (B and D). $^*P < 0.05$, $^{**}P < 0.005$, $^{***}P < 0.001$ (Mann-Whitney U test). (**E** and **F**) Confocal microscopic images showing immunoreactivities for calbindin, a Purkinje cell marker (magenta), and vesicular glutamate transporter type 2 (VGluT2), a marker of climbing fiber terminals (green), in the same slice from a P14 mouse cerebellum for Sema3A-KD (E) and from a P21 mouse cerebellum for Sema7A-KD (F). Scale bars, 10 μm. (**G** and **H**) Frequency distributions of the number of perisomatic climbing fiber terminals on Purkinje cells for (G) control (white columns, $n = 40$) and Sema3A-KD (green columns, $n = 38$) during P14 and P15 and for (H) control ($n = 30$) and Sema7A-KD (orange columns, $n = 44$) during P21 and P22. $^*P < 0.05$, $^{***}P < 0.001$ (Mann-Whitney U test).

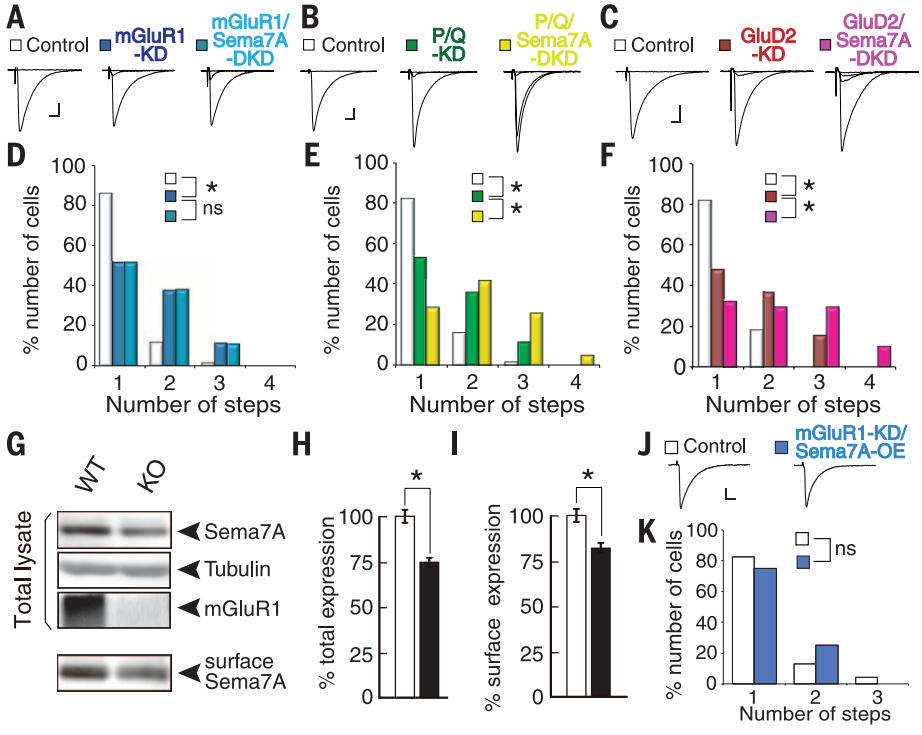


Fig. 3. Sema7A mediates synapse elimination downstream of mGluR1. (**A** to **F**) Sample CF-EPSCs [scale bars, 1 nA (vertical) and 5 ms (horizontal)] and frequency distributions of the number of climbing fibers innervating each Purkinje cell (D to F) during P21 to P30 for control (white columns, $n = 49$), mGluR1 knockdown (mGluR1-KD, darker blue columns, $n = 43$), and mGluR1/Sema7A double knockdown (mGluR1/Sema7A-DKD, lighter blue columns, $n = 45$) (A and D); for control ($n = 43$), P/Q-VGCC knockdown (P/Q-KD, green columns, $n = 42$), and P/Q/Sema7A double knockdown (P/Q/Sema7A-DKD, yellow columns, $n = 39$) (B and E); and for control ($n = 43$), GluD2 knockdown (GluD2-KD, red columns, $n = 42$), and GluD2/Sema7A double knockdown (GluD2/Sema7A-DKD, magenta columns, $n = 39$) (C and F). $^*P < 0.05$; ns indicates no significant difference (Mann-Whitney U test). (**G** to **I**) Total and surface expression of Sema7A in *mGluR1* knockout (KO) and wild-type (WT) mice were analyzed by Western blotting ($n = 4$ mice each). $^*P < 0.05$ (Student's *t* test). Error bars indicate SEM. (**J** and **K**) Sample CF-EPSCs [scale bars, 1 nA (vertical) and 5 ms (horizontal)] and frequency distributions of the number of climbing fibers innervating each Purkinje cell (K) for control ($n = 23$) and combined Sema7A overexpression with mGluR1 knockdown (mGluR1-KD/Sema7A-OE, blue columns, $n = 28$).

1 (mGluR1), P/Q-type voltage-gated calcium channel (P/Q-VGCC), or glutamate receptor δ2 (GluD2), which act in Purkinje cells and are crucial for different aspects of climbing fiber synapse elimination (*5*, *14*, *15*). We found that the effect of double knockdown of Sema7A and mGluR1 was the same as that of single knockdown of mGluR1 (Fig. 3, A and D, and fig. S8), whereas double knockdown of Sema7A and either P/Q-VGCC or GluD2 had additive effects (Fig. 3, B, C, E, and F, and fig. S8). Moreover, Sema7A expression was reduced in *mGluR1* knockout mice (Fig. 3, G to I). Overexpression of Sema7A into mGluR1 knockdown Purkinje cells rescued the effect of mGluR1 knockdown (Fig. 3, J and K). These results suggest that Sema7A mediates synapse elimination downstream of mGluR1 signaling.

We examined the effects of Sema3A or Sema7A knockdown on other types of synapses onto Purkinje cells. Knockdown of Sema3A but not Sema7A enhanced excitatory transmission from parallel fibers to Purkinje cells (fig. S9, A and B). Neither Sema3A nor Sema7A knockdown affected inhibitory synaptic transmission to Purkinje cells (fig. S9, C to H).

Sema3A and Sema7A act on Plexin A2 (PlxnA2) and/or A4 (PlxnA4) and Plexin C1 (PlxnC1)/Integlin B1 (ItgB1), respectively (*16*). We found that mRNAs of receptors for Sema3A or Sema7A were expressed in inferior olivary neurons (fig. S10). We knocked down respective molecules in subsets of climbing fibers (figs. S11 and S12). Purkinje cells surrounded by climbing fibers with PlxnA4 knockdown were innervated by a significantly smaller number of climbing fibers when compared with control Purkinje cells sampled from where PlxnA4 knockdown climbing fibers were absent in the same slices (Fig. 4, A and B). Furthermore, the amplitude of CF-EPSCs was significantly smaller in PlxnA4 knockdown regions (table S2). Scrambled PlxnA4 miRNA did not alter climbing fiber innervation (PlxnA4-SCR) (Fig. 4, A and B), and the effect of PlxnA4 knockdown was rescued by coexpression of a miRNA-resistant PlxnA4 (PlxnA4-rescue) (fig. S13). Double knockdown of Sema3A in Purkinje cells and PlxnA4 in climbing fibers had the same effect as single knockdown of Sema3A (Fig. 4, G and H). The number of climbing fiber terminals around Purkinje cell somata for PlxnA4 knockdown was smaller than that for PlxnA4-SCR during P12 to P15 (fig. S14). Moreover, PlxnA4 knockdown enhanced parallel fiber to Purkinje cell transmission (fig S13). In contrast, PlxnA2 knockdown had no effect on climbing fiber innervation (fig. S15). These results indicate that Sema3A from postsynaptic Purkinje cells strengthens climbing fiber synapses and/or opposes synapse elimination through PlxnA4 in climbing fibers.

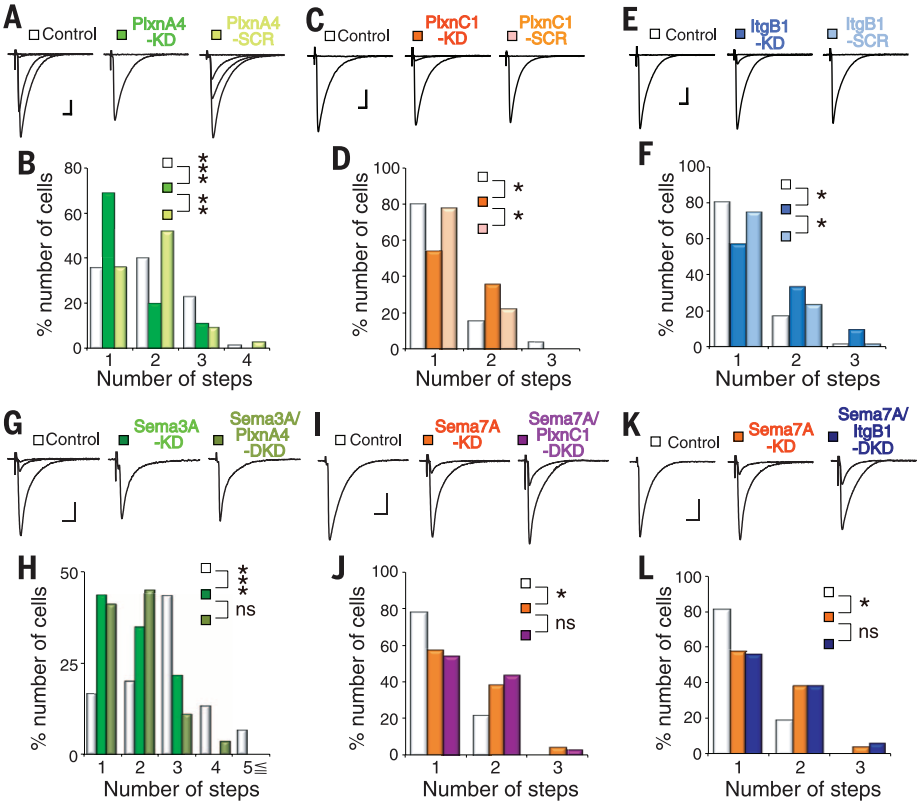


Fig. 4. Sema3A and Sema7A regulate synapse elimination through their receptors on climbing fibers. (**A** to **F**) Sample CF-EPSCs [scale bars, 1 nA (vertical) and 5 ms (horizontal)] and frequency distributions of the number of climbing fibers innervating each Purkinje cell (B, D, and F) for control (white columns, n = 48), PlxnA4 knockdown (PlxnA4-KD) in climbing fibers (darker green columns, n = 35), and PlxnA4-SCR in climbing fibers (lighter green columns, n = 38) during P12 to P15 (A and B); for control (n = 44), PlxnC1 knockdown (PlxnC1-KD) in climbing fibers (orange columns, n = 45), and PlxnC1-SCR in climbing fibers (light orange columns, n = 40) during P21 to P30 (C and D); and for control (n = 40), ItgB1 knockdown (ItgB1-KD) in climbing fibers (darker blue columns, n = 39), and ItgB1-SCR in climbing fibers (lighter blue columns, n = 42) during P21 to P30 (E and F). (**G** to **L**) Sample CF-EPSCs [scale bars, 1 nA (vertical) and 5 ms (horizontal)] and frequency distributions of the number of climbing fibers innervating each Purkinje cell (H, J, and L) for control (n = 30), Sema3A-KD (dark green columns, n = 21), and Sema3A/PlxnA4 double knockdown (Sema3A/PlxnA4-DKD, olive green columns, n = 23) during P9 to P12 (G and H); for control (n = 36), Sema7A-KD (orange columns, n = 21), and PlxnC1/Sema7A double knockdown (PlxnC1/Sema7A-DKD, purple columns, n = 30) during P21-P30 (I and J); and for control (n = 31), Sema7A-KD (orange columns, n = 21), and ItgB1/Sema7A double knockdown (ItgB1/Sema7A-DKD, blue columns, n = 29) during P21 to P30 (K and L). *P < 0.05, **P < 0.01, ***P < 0.001; ns indicates no significant difference (Mann-Whitney U test).

In contrast to PlxnA4, knockdown of PlxnC1 in climbing fibers caused a significant increase in the number of climbing fibers innervating each Purkinje cell (Fig. 4, C and D, and table S3). Knockdown of ItgB1 also impaired climbing fiber synapse elimination (Fig. 4, E and F, and table S3). Scrambled PlxnC1 miRNA or ItgB1 miRNA did not alter climbing fiber innervation (PlxnC1-SCR, ItgB1-SCR) (Fig. 4, C to F). The effects of PlxnC1 or ItgB1 knockdown were rescued by coexpression of miRNA-resistant PlxnC1 or ItgB1 (fig. S16). Moreover, the number of climbing fiber terminals around Purkinje cell somata for PlxnC1 or ItgB1 knockdown was larger than that for PlxnC1-SCR or ItgB1-SCR, respectively, during P21 to P30 (fig. S17). Double knockdown of Sema7A in Purkinje cells and either PlxnC1 or ItgB1 in climbing fibers had the same effects as single knockdown of Sema7A (Fig. 4, I to L). The effect of double knockdown of PlxnC1 and ItgB1 was the same as that of single knockdown of either molecule (fig. S18), suggesting that PlxnC1 and ItgB1 share the same signaling pathway. We further examined whether cofilin and focal adhesion kinase (FAK) function as signals downstream of PlxnC1 and ItgB1, respectively (*17*, *18*). Expression of constitutive-active cofilin (cofilin-CA) and knockdown of FAK caused a significant increase in the number of climbing fibers (figs. S19 and S20). Moreover, simultaneous knockdown of PlxnC1 with overexpression of cofilin-CA and double knockdown of ItgB1 and FAK had the same effects as cofilin-CA overexpression alone and single knockdown of FAK, respectively (fig. S21). We thus conclude that Sema7A facilitates elimination of climbing fiber synapses from Purkinje cell somata through acting on PlxnC1 and ItgB1 in climbing fibers and regulating cofilin and FAK signaling.

Whereas the importance of semaphorins as axon guidance molecules has been well established (*16*), their roles in activity-dependent refinement of neural circuits have been unclear.

Here, we have disclosed that Sema3A and Sema7A function as retrograde signaling molecules that regulate developmental synapse elimination in the cerebellum. Our results suggest that Sema3A and Sema7A have opposite effects and are involved in different stages of synapse elimination (fig. S22). Because semaphorins and their receptors are expressed widely in the brain, it is highly likely that semaphorins play important roles in developmental synapse elimination in various brain areas.

REFERENCES AND NOTES

1. M. Kano, K. Hashimoto, *Curr. Opin. Neurobiol.* **19**, 154–161 (2009).
2. M. Watanabe, M. Kano, *Eur. J. Neurosci.* **34**, 1697–1710 (2011).
3. J. W. Lichtman, H. Colman, *Neuron* **25**, 269–278 (2000).
4. M. Kano *et al.*, *Cell* **83**, 1223–1231 (1995).
5. M. Kano *et al.*, *Neuron* **18**, 71–79 (1997).
6. F. Crepel, *Trends Neurosci.* **5**, 266–269 (1982).
7. N. Uesaka *et al.*, *J. Neurosci.* **32**, 11657–11670 (2012).
8. T. Mikuni *et al.*, *Neuron* **78**, 1024–1035 (2013).
9. K. Hashimoto *et al.*, *Proc. Natl. Acad. Sci. U.S.A.* **108**, 9987–9992 (2011).
10. K. Hashimoto, R. Ichikawa, K. Kitamura, M. Watanabe, M. Kano, *Neuron* **63**, 106–118 (2009).
11. F. Crepel, N. Delhaye-Bouchaud, J. L. Dupont, *Brain Res. Dev. Brain Res.* **1**, 59–71 (1981).
12. K. Hashimoto, M. Kano, *Neuron* **38**, 785–796 (2003).
13. S. Kakizawa, M. Yamasaki, M. Watanabe, M. Kano, *J. Neurosci.* **20**, 4954–4961 (2000).
14. K. Hashimoto *et al.*, *J. Neurosci.* **21**, 9701–9712 (2001).
15. T. Miyazaki, K. Hashimoto, H. S. Shin, M. Kano, M. Watanabe, *J. Neurosci.* **24**, 1734–1743 (2004).
16. R. J. Pasterkamp, *Nat. Rev. Neurosci.* **13**, 605–618 (2012).
17. R. J. Pasterkamp, J. J. Peschon, M. K. Spriggs, A. L. Kolodkin, *Nature* **424**, 398–405 (2003).
18. G. A. Scott, L. A. McClelland, A. F. Fricke, A. Fender, *J. Invest. Dermatol.* **129**, 954–963 (2009).
19. H. Hirai, T. Torashima, Japanese Patent 4975733 (2012).

ACKNOWLEDGMENTS

We thank A. Nienhuis for the gifts of the lentiviral backbone vector and the packaging plasmid. A Purkinje cell–tropic viral vector has been patented (*19*). We also thank K. Kitamura, K. Hashimoto, Y. Sugaya, and M. Mahoney for helpful discussions and K. Matsuyama, M. Sekiguchi, M. Watanabe, S. Tanaka, and A. Koseki for technical assistance. This work was supported by Grants-in-Aid for Scientific Research (21220006 and 25000015 to M.K., 19100005 and 24220007 to M.W., and 23650160 to N.U.), the Funding Program for Next Generation World-Leading Researchers (LS021) to H.H., the Strategic Research Program for Brain Sciences (Development of Biomarker Candidates for Social Behavior), Comprehensive Brain Science Network, and the Global Center of Excellence Program (Integrative Life Science Based on the Study of Biosignaling Mechanisms) from the Ministry of Education, Culture, Sports, Science and Technology of Japan. H.H. and T. Torashima are inventors on a Japanese and a U.S. patent application for a Purkinje cell–tropic viral vector (the modified L7 promoter sequences that enable robust transgene expression specifically in cerebellar Purkinje cells, PCT/JP2007/055017 filed on 7 March 2007 and US20100146649), which is owned by Japan Science and Technology Agency (*19*). Materials described here are available from H.H. and A. Nienhuis, subject to a material transfer agreement (MTA) with Gunma University for the modified L7 promoter and an MTA with St. Jude Children's Research Hospital and the George Washington University for the pCL20c MSCV-GFP. Additional data can be found in the supplementary materials.

SUPPLEMENTARY MATERIALS

www.sciencemag.org/content/344/6187/1020/suppl/DC1
Materials and Methods
Figs. S1 to S22
Tables S1 to S3
References (*20*–*26*)

21 February 2014; accepted 6 May 2014
Published online 15 May 2014;
10.1126/science.1252514

SYNAPSES

Composition of isolated synaptic boutons reveals the amounts of vesicle trafficking proteins

Benjamin G. Wilhelm,[1,2] Sunit Mandad,[3]* Sven Truckenbrodt,[1,5]* Katharina Kröhnert,[1] Christina Schäfer,[1] Burkhard Rammner,[1] Seong Joo Koo,[6] Gala A. Claßen,[6] Michael Krauss,[6] Volker Haucke,[6] Henning Urlaub,[3,4] Silvio O. Rizzoli[1]†

Synaptic vesicle recycling has long served as a model for the general mechanisms of cellular trafficking. We used an integrative approach, combining quantitative immunoblotting and mass spectrometry to determine protein numbers; electron microscopy to measure organelle numbers, sizes, and positions; and super-resolution fluorescence microscopy to localize the proteins. Using these data, we generated a three-dimensional model of an "average" synapse, displaying 300,000 proteins in atomic detail. The copy numbers of proteins involved in the same step of synaptic vesicle recycling correlated closely. In contrast, copy numbers varied over more than three orders of magnitude between steps, from about 150 copies for the endosomal fusion proteins to more than 20,000 for the exocytotic ones.

The quantitative organization of cellular pathways is not well understood. One well-researched membrane trafficking pathway, synaptic vesicle recycling, occupies its own compartment, the synaptic bouton, and can therefore be studied in isolation. It is a relatively simple pathway, comprising only a few steps (*1*–*3*). First, neurotransmitter-filled synaptic vesicles dock to the release site (active zone), are primed for release, and then fuse with the plasma membrane (exocytosis). The vesicle molecules are later sorted and retrieved from the plasma membrane (endocytosis). An additional sorting step in an early endosome (*3*–*5*) may take place before the vesicle refills with neurotransmitter.

To quantify the organization of synaptic vesicle recycling, we first purified synaptic boutons (synaptosomes) from the cellular layers of the cortex and cerebellum of adult rats, using a modified version (*6*) of a classical brain fractionation protocol (*7*) (Fig. 1A). The different cellular components were separated by Ficoll density gradients, resulting in a heterogeneous sample, which we first analyzed by electron microscopy. About 58.5% of all organelles were resealed, vesicle-loaded synaptosomes (fig. S1). Most of the remaining organelles, such as mitochondria (~20%) and myelin (8%) (fig. S1), contained few proteins relevant to synaptic vesicle recycling and thus did not bias synaptic protein quantification. The electron microscopy analysis of the synaptosomes also provided their spatial parameters (size, surface, and volume), which are critical in understanding protein concentrations (Fig. 1, B and C).

Before proceeding to investigate the synaptic protein copy numbers, we tested whether the synaptosomes lost a significant proportion of their proteins during the purification procedure. We compared the amounts of 27 soluble proteins and 2 transmembrane proteins in synaptosomes and in undisturbed synapses from brain slices, using fluorescence microscopy (fig. S2, A and B). The large majority of the proteins exhibited no significant changes after synaptosome purification (fig. S2C).

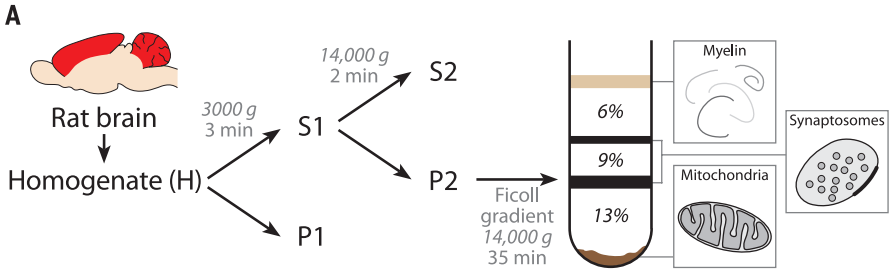
Having verified that the purification procedure maintains the protein composition of the synaptic bouton, we used quantitative immunoblotting to determine the amount of protein of interest per microgram of synaptosomes for 62 synaptic proteins (Fig. 1, D and E). To transform this value into copy numbers per synaptosome, we determined the number of particles in the synaptosome preparation by fluorescence microscopy (~17 million) (fig. S3) and the fraction represented by synaptosomes by electron microscopy (fig. S1, A and B) and by immunostaining for synaptic markers (fig. S1B). Both measurements indicate that ~58% of all particles are synaptosomes, ~9.95 million synaptosomes per microgram.

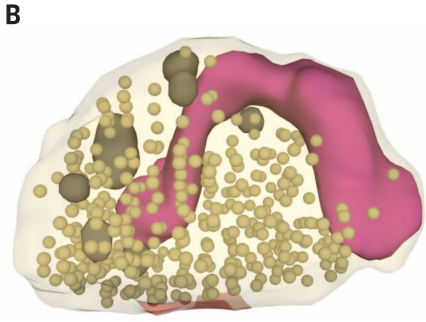
The results we obtained for all proteins tested are included in table S1. Despite the heterogeneous preparation we started with, our results are very close to synaptic vesicles purified to more than 95% (*8*), taking into account the

[1]Department of Neuro- and Sensory Physiology, University of Göttingen Medical Center, European Neuroscience Institute, Cluster of Excellence Nanoscale Microscopy and Molecular Physiology of the Brain, Göttingen, Germany. [2]International Max Planck Research School Neurosciences, 37077 Göttingen, Germany. [3]Bioanalytical Mass Spectrometry Group, Max-Planck-Institute for Biophysical Chemistry, 37077 Göttingen, Germany. [4]Bioanalytics, Department of Clinical Chemistry, University Medical Center Göttingen, 37075 Göttingen, Germany. [5]International Max Planck Research School Molecular Biology, 37077 Göttingen, Germany. [6]Leibniz Institut für Molekulare Pharmakologie, Department of Molecular Pharmacology and Cell Biology, Robert-Rössle-Strasse 10, 13125 Berlin, Germany.
*These authors contributed equally to this work. **†Corresponding author. E-mail: srizzol@gwdg.de**

known fractions of these proteins on the synaptic plasma membrane (*9*, *10*) (Fig. 1F). We only detected a sizeable difference for synaptic vesicle 2 (SV2) [12 copies per synaptic vesicle in our study, versus 1.7 for (*8*)]. A more recent study, using an antibody-based approach that is likely to underestimate the copy numbers of abundant synaptic vesicle proteins, found about five SV2 molecules per vesicle (*11*).

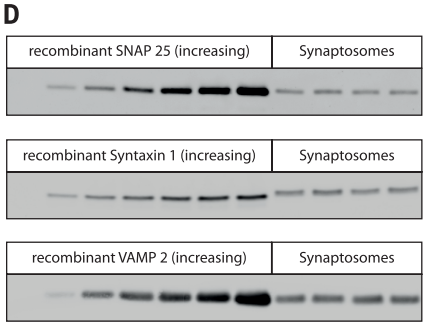
The immunoblot analysis also provided the total mass of each protein per microgram of synaptosome preparation, which could be translated to percentage of the total protein in the preparation. Our quantification of synaptic proteins addressed ~23% of the total protein in the preparation. Because the synaptosomes make ~58% of the preparation, our quantification thus addressed ~40.5% of the total protein in synaptosomes (without presynaptic mitochondria). To test and extend these values, we turned to quantitative mass spectrometry, using a label-free approach, intensity-based absolute quantification (iBAQ) (*12*). iBAQ estimates the abundance of particular proteins by summing the intensities of all peptides derived from them and then normalizing to the total possible number of peptides. We compared the peptides derived from recombinant synaptic proteins (same as those used for quantitative immunoblotting) from human Universal Protein Standards (UPS2) and finally from synaptosomes, using a hybrid mass spectrometer. iBAQ values were then calculated using MaxQuant (*13*) and the Andromeda search engine (*14*), and the amounts of proteins present in synaptosomes were determined by linear regression. The estimates obtained by iBAQ correlated well with the immunoblotting results (fig. S4). The iBAQ approach generated abundance estimates for ~1100 additional proteins in the preparation (see table S2 for a number of well-known proteins relevant to synaptic activity; see table S3 for all other proteins). All quantified proteins (iBAQ and immunoblot analysis) added up to ~88.4% of the protein weight of the entire synaptosome preparation (obtained

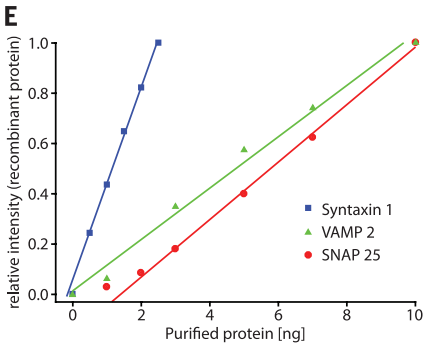




C

Physical characteristics of the average synaptosome	
Volume	0.37 ± 0.04 μm³
Surface	2.31 ± 0.14 μm²
Number of vesicles	383.7 ± 37.9
Volume of vesicles	0.015 ± 0.001 μm³
Inter-vesicle distance	59.15 ± 0.37 nm
Surface of active zone	0.070 ± 0.014 μm²
Volume of mitochondria	0.12 ± 0.02 μm³





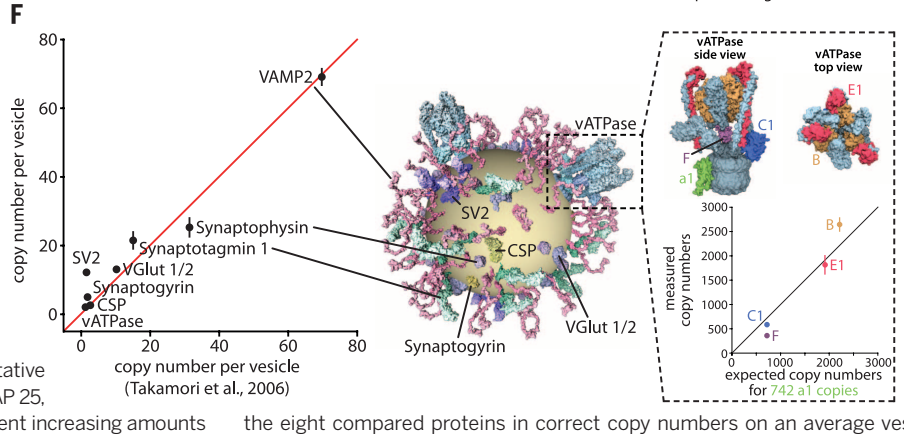


Fig. 1. Physical characteristics of the average synaptosome. (**A**) Schema illustrating the purification of synaptosomes. See the supplementary materials for details. (**B**) Serial electron micrographs of purified synaptosomes were used to reconstruct entire synapses. The plasma membrane is depicted in light beige, the active zone in red, synaptic vesicles in dark beige, larger organelles in dark gray, and mitochondria in purple. This synaptosome resembles the average physical parameters (C) and was used to model the average presynaptic terminal (Fig. 3). (**C**) Table listing the average physical parameters of synaptosomes. The values represent mean ± SEM of 65 reconstructions from four independent synaptosome preparations. (**D**) Quantitative immunoblots of the three synaptic SNARE proteins (SNAP 25, syntaxin 1, and VAMP 2). The lanes on the left represent increasing amounts of the purified protein of interest, forming a standard curve (protein amount versus band intensity). The different synaptosome samples are depicted in the four lanes on the right. (**E**) Standard curves of the three SNARE proteins obtained from the immunoblots depicted in (D). Linear regression was used to determine the absolute amount of the protein of interest in the synaptosomes. (**F**) (Left) The copy numbers for eight major synaptic vesicle proteins, normalized to the number of synaptic vesicles per synaptosome, are compared with the numbers obtained in a previous quantification of synaptic vesicles (*8*). The red line represents identity. (Middle) The model shows the eight compared proteins in correct copy numbers on an average vesicle. (Right) Correlation between the copy numbers of different vATPase subunits (highlighted in different colors in the vATPase model, above the graph). The immunoblot quantification of the a1 subunit (green; only the transmembrane part is shown) suggests the presence of 742 vATPase complexes per bouton. The copy numbers of the B, C, E, and F subunits (derived from iBAQ mass spectrometry) are plotted against their expected stoichiometries for 742 complexes. The stoichiometry of the different vATPase subunits was obtained from (*34*). The black line represents identity. All data represent means ± SEM from four independent preparations.

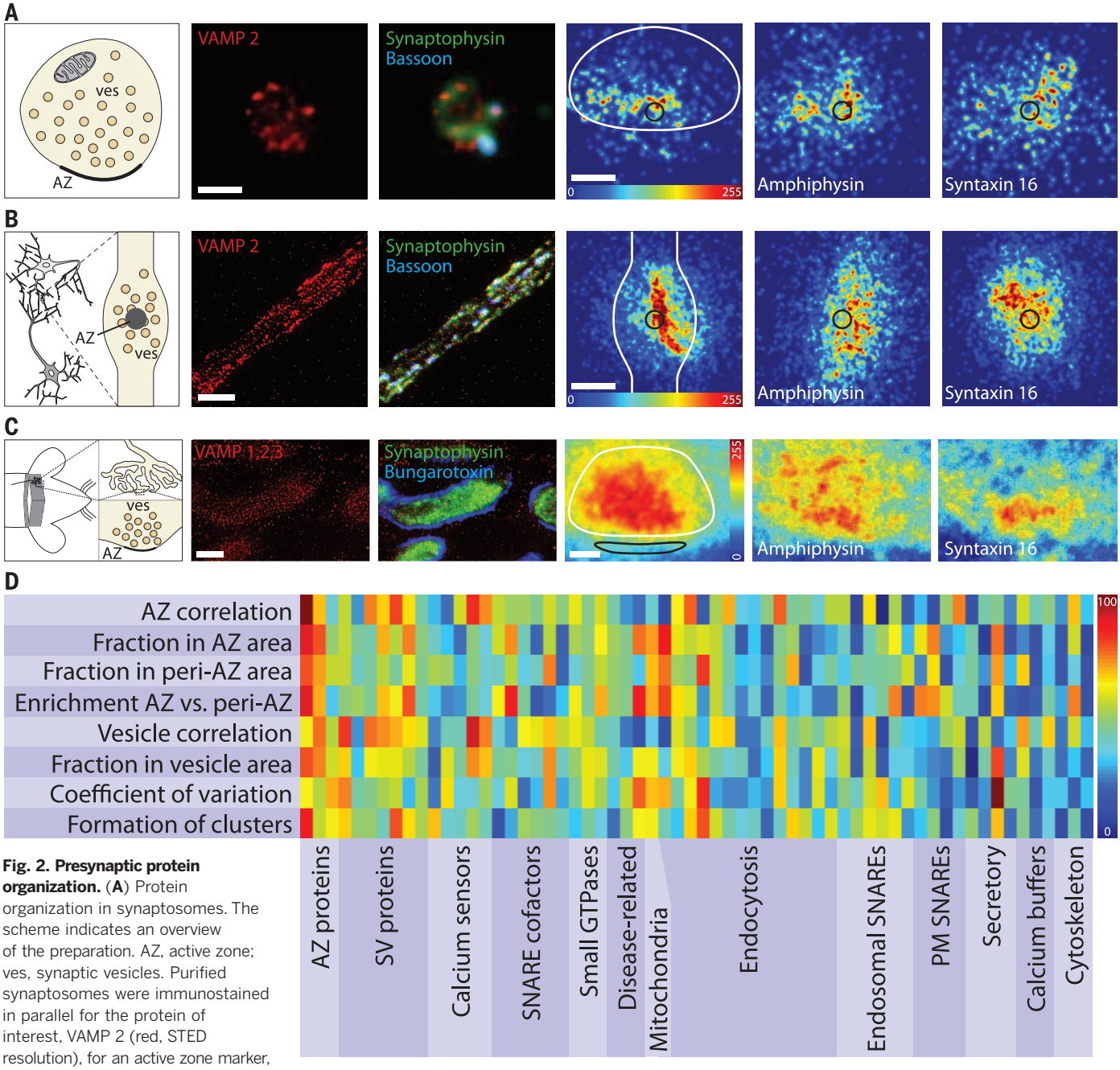


Fig. 2. Presynaptic protein organization. (**A**) Protein organization in synaptosomes. The scheme indicates an overview of the preparation. AZ, active zone; ves, synaptic vesicles. Purified synaptosomes were immunostained in parallel for the protein of interest, VAMP 2 (red, STED resolution), for an active zone marker, bassoon (blue, confocal resolution), and for a vesicle marker, synaptophysin (green, confocal resolution). The fourth panel shows the relative spatial distribution of VAMP 2 as obtained from average images (several hundred synapses from two independent experiments; see the supplementary materials for further details). The putative outline of the synapse is indicated by the white line, the active zone by the black circle; the relative spatial abundance is color-coded (see color bar). Scale bars are 500 nm (image panels) and 200 nm (fourth panel). The last two panels on the right are density distributions for two additional presynaptic proteins, amphiphysin and syntaxin 16. Scale bar is 200 nm. (**B**) Protein organization in hippocampal cultures. Details as in (A). Scale bars are 2 μm and 200 nm, respectively. (**C**) Protein organization in the mouse neuromuscular junction. Instead of immunostaining for bassoon, the active zone position was obtained by labeling postsynaptic acetylcholine receptors with bungarotoxin. All other details as in (A). Scale bars are 2 μm and 500 nm, respectively. Imaging data for all the other proteins are provided in fig. S6. (**D**) Different spatial parameters were measured for each of the 62 proteins we imaged, as indicated by the labeling of the rows. Parameter values were normalized to the maximum (100%). All values are indicated according to the color scale (right). The proteins are grouped according to functional categories: active zone proteins (bassoon, piccolo, and RIM1), synaptic vesicle proteins (synaptophysin, VGlut 1/2, VAMP 2, VAMP 1, SV2 A/B, synapsin I/II, and synaptogyrin 1), calcium sensor proteins (synaptotagmin 2, synaptotagmin 1, synaptotagmin 7, doc 2A/B, and calmodulin), SNARE cofactors (CSP, Munc13a, Munc18a, NSF, α-SNAP, and complexin 1/2), small guanosine triphosphatases (GTPases) (Rab3, Rab5, and Rab7), disease-related proteins (α/β-synuclein, APP, and β-secretase), mitochondrial proteins (VDAC), endocytosis proteins (AP-2 mu2, SGIP1, synaptojanin, epsin 1, clathrin heavy chain, clathrin light chain, dynamin 1,2,3, endophilin I,II,III, amphiphysin, Hsc70, intersectin 1, PIPK Iγ, AP 180, and syndapin 1), endosomal SNAREs (syntaxin 13, syntaxin 16, syntaxin 7, syntaxin 6, Vti1a, and VAMP4), plasma membrane SNAREs (syntaxin 1, SNAP 23, SNAP 25, and SNAP 29), general secretory proteins (CAPS, SCAMP 1, SGTα, and vATPase a1), calcium buffer proteins (calbindin, calretinin, and parvalbumin), and cytoskeletal proteins (actin, septin 5, and tubulin).

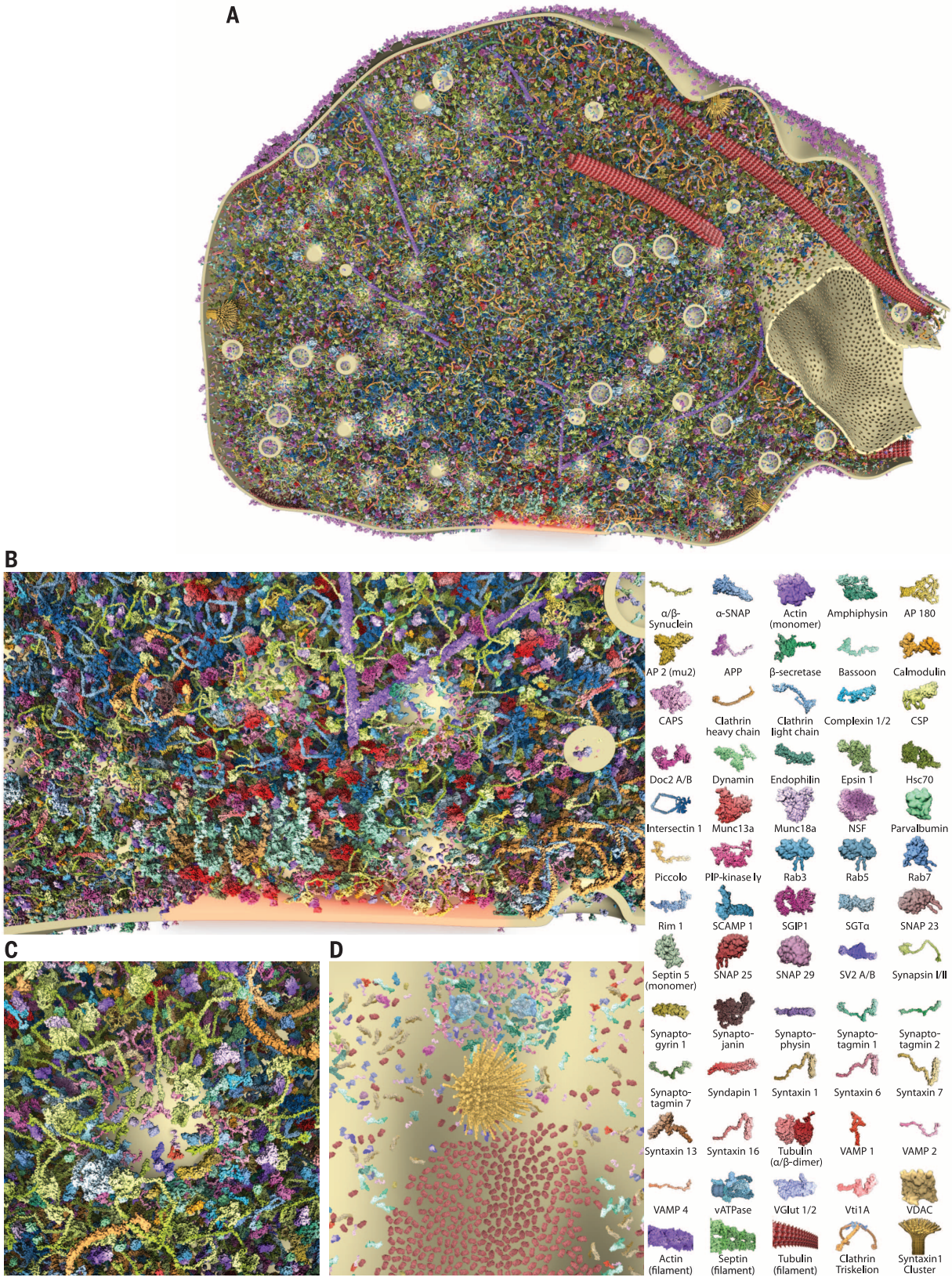


Fig. 3. A 3D model of synaptic architecture. (**A**) A section through the synaptic bouton, indicating 60 proteins. The proteins are shown in the copy numbers indicated in tables S1 and S2 and in positions determined according to the imaging data (Fig. 2 and fig. S6) and to the literature (see fig. S6 for details). (**B**) High-zoom view of the active zone area. (**C**) High-zoom view of one vesicle within the vesicle cluster. (**D**) High-zoom view of a section of the plasma membrane in the vicinity of the active zone. Clusters of syntaxin (yellow) and SNAP 25 (red) are visible, as well as a recently fused synaptic vesicle (top). The graphical legend indicates the different proteins (right). Displayed synaptic vesicles have a diameter of 42 nm.

by summing the percentages indicated in tables S1 to S3).

The members of heteromultimeric complexes, such as the vesicular adenosine triphosphatase (vATPase), were present in the correct (expected) stoichiometries (Fig. 1F), verifying the accuracy of our quantification procedure. The copy numbers of proteins known to be involved in a particular step of synaptic vesicle recycling correlated remarkably well. This observation applied to the exocytotic fusion proteins [SNAREs (fig. S5B), whose abundance was only matched by actin and tubulin (fig. S5M)], to proteins involved in fusion regulation [SNARE-binding or priming proteins (fig. S5C)], to proteins of the clathrin-mediated endocytosis pathway (fig. S5E), to endosomal or constitutive fusion proteins (fig. S5D), to structural vesicle cluster proteins (fig. S5F), to active zone proteins (fig. S5G), to major synaptic vesicle constituents (fig. S5H), or to adhesion proteins (fig. S5I). Proteins involved in membrane trafficking pathways unrelated to synaptic vesicle recycling, such as the exocyst pathway (fig. S5J), were not abundant. There was no correlation between structurally similar proteins, such as those of the Rab or septin families (fig. S5, K and L). Protein copy numbers are high in some steps of the vesicle recycling pathway but much lower in other steps. For example, the exocytotic SNAREs were present in 20,100 to 26,000 copies, despite the fact that one vesicle fusion event requires the formation of only one to three SNARE complexes, which contain one copy of each of the three SNAREs (*15*–*17*). SNARE-interacting proteins were found at copy numbers of one to several thousands (Munc13a, Munc18a, complexin I, and complexin II) (fig. S5C). In contrast, only ~4000 clathrin molecules and 2300 dynamin molecules were present in the average synapse. Because at least 150 to 180 copies of clathrin are needed for one recycling vesicle (*18*, *19*), the entire clathrin complement of the synapse would be sufficient for the simultaneous endocytosis of only 7% of all vesicles. The dynamin complement of the synapse was only sufficient for 11% of the vesicles, taking into account that at least 52 copies, corresponding to two adjacent dynamin rings, are needed for one pinch-off event (*20*). Finally, the endosomal SNAREs, which form tetrameric complexes containing one copy of each SNARE (*4*, *6*), were even less abundant (50 to 150 copies) than the endocytotic cofactors.

For some proteins, a strong enrichment in the location where they function may compensate for their low copy numbers. Conversely, abundant proteins may be scattered throughout the synaptic space, which would render their concentrations fairly low at individual sites. To estimate the influence of protein localization, we selected 62 proteins and analyzed them by immunostaining and fluorescence microscopy. We used stimulated emission depletion (STED) (*21*), a diffraction-unlimited technique, to investigate protein positions with a resolution of ~40 nm (Fig. 2A). To avoid bias owing to possible artifacts connected to the brain homogenization procedure required for generating synaptosomes, we also studied two additional preparations: cultured hippocampal neurons (Fig. 2B) and the levator auris longus neuromuscular junction (Fig. 2C), acutely dissected from adult animals (*22*).

We analyzed the proteins of interest in relation to the positions of the release site (identified by marking active zone proteins) and of the vesicle cluster (visualized by staining for the protein that is most strongly enriched in purified synaptic vesicles, synaptophysin) (*8*). We averaged single synapses by overlapping their active zones and rotating the images until reaching the best possible alignment of the vesicle cluster and of the protein of interest. This procedure provided an overview of the relative spatial distribution of each protein. Overall, many of the protein distributions were similar (Fig. 2, A to C, and fig. S6). Active zone proteins were mostly confined to the active zone areas. Most of the other proteins could be found throughout the synaptic boutons [albeit they were enriched to different levels in areas such as the active zone or the vesicle cluster (Fig. 2D); see fig. S7, A to H, for a more detailed analysis of differences between the proteins]. These observations are consistent with the presence of most of the proteins on purified synaptic vesicles (*8*) and with the fact that the synaptic vesicle cluster occupies much of the synaptic bouton volume (Fig. 1B). Thus, for the majority of proteins, localization does not appear to compensate for low copy numbers.

Although the imaging parameters measured above did not pinpoint actual positions within the synapse, they allowed us to make broad estimates for the organization of each protein (fig. S7I). We used the data to generate a three-dimensional (3D) model containing 60 proteins placed within a typical synaptic volume (obtained from an individual electron microscopy reconstruction whose parameters were close to synaptosome averages) (Fig. 3). The proteins were modeled in atomic detail, according to their known molecular structures, and were placed in the synaptic space according to the information provided by the STED images and the literature (Fig. 2 and fig. S6). For example, the SNARE molecules syntaxin 1 and SNAP 25 are shown in clusters with a specific organization (*23*–*25*). The hippocampal culture images (Fig. 2B) were used to obtain an additional set of data, the correlation of protein amounts with synapse size [judged from the amount of vesicles (*26*) (fig. S6)]. The copy numbers of some proteins increase linearly with synapse size; others, including most endocytotic proteins, follow an exponential curve, which implies that small synapses contain proportionally larger amounts of these proteins than large synapses.

We used the modeled volumes of the proteins to calculate the fraction of the synaptic volume that they occupy. This value, ~7% of the synaptosome volume (excluding mitochondria), is comparable to the space occupied by the synaptic vesicles (~6%, derived from the electron microscopy measurements). These low values could lead to the impression that the synaptic volume is not densely populated by proteinaceous structures. However, the 3D model suggests that the synaptic space is rather crowded, especially inside the vesicle cluster and at the active zone (Fig. 3, A to C, and movie S1). This probably places constraints on both organelle and protein diffusion. The high copy numbers of exocytosis-related proteins may have evolved as a mechanism to cope with these constraints, to ensure the high speed of neurotransmitter release. In contrast, endocytosis can take place for many tens of seconds after exocytosis. This allows endocytosis to proceed with proportionally lower numbers of cofactor proteins. In principle, the synaptic boutons could increase the speed of endocytosis by accumulating larger amounts of endocytotic proteins. This, however, would result in an even greater congestion of the synaptic space, which presumably might perturb synaptic function. A simpler solution for the problem of balancing rapid release with slow vesicle retrieval appears to have been to maintain a large enough reservoir of vesicles (*22*, *27*, *28*).

Our data reveal a correlation between the copy numbers of proteins involved in the same steps of synaptic vesicle recycling. The mechanisms behind this correlation are unclear. A simple hypothesis would be that such proteins either are produced together or are transported to the synapse together. However, these proteins have different lifetimes (*29*) and are transported from the neuronal cell body on different precursors (*30*). One possible explanation, at least for the soluble cofactor proteins, is that the synaptic vesicle cluster regulates their number. The vesicles are known to bind to and buffer such proteins (*22*, *31*–*33*), thereby retaining in the synapse only a defined number of cofactors. Such mechanisms do not apply, however, to transmembrane proteins, whose regulation remains to be determined.

REFERENCES AND NOTES

1. V. Haucke, E. Neher, S. J. Sigrist, *Nat. Rev. Neurosci.* **12**, 127–138 (2011).
2. R. Jahn, D. Fasshauer, *Nature* **490**, 201–207 (2012).
3. T. C. Südhof, *Annu. Rev. Neurosci.* **27**, 509–547 (2004).
4. P. Hoopmann *et al.*, *Proc. Natl. Acad. Sci. U.S.A.* **107**, 19055–19060 (2010).
5. V. Uytterhoeven, S. Kuenen, J. Kasprowicz, K. Miskiewicz, P. Verstreken, *Cell* **145**, 117–132 (2011).
6. S. O. Rizzoli *et al.*, *Traffic* **7**, 1163–1176 (2006).
7. D. G. Nicholls, T. S. Sihra, *Nature* **321**, 772–773 (1986).
8. S. Takamori *et al.*, *Cell* **127**, 831–846 (2006).
9. F. Opazo *et al.*, *Traffic* **11**, 800–812 (2010).
10. M. Darna *et al.*, *J. Biol. Chem.* **284**, 4300–4307 (2009).
11. S. A. Mutch *et al.*, *J. Neurosci.* **31**, 1461–1470 (2011).
12. B. Schwanhäusser *et al.*, *Nature* **473**, 337–342 (2011).
13. J. Cox, M. Mann, *Nat. Biotechnol.* **26**, 1367–1372 (2008).
14. J. Cox *et al.*, *J. Proteome Res.* **10**, 1794–1805 (2011).
15. R. Mohrmann, H. de Wit, M. Verhage, E. Neher, J. B. Sørensen, *Science* **330**, 502–505 (2010).
16. R. Sinha, S. Ahmed, R. Jahn, J. Klingauf, *Proc. Natl. Acad. Sci. U.S.A.* **108**, 14318–14323 (2011).
17. G. van den Bogaart *et al.*, *Nat. Struct. Mol. Biol.* **17**, 358–364 (2010).

18. Y. Cheng, W. Boll, T. Kirchhausen, S. C. Harrison, T. Walz, *J. Mol. Biol.* **365**, 892–899 (2007).
19. H. T. McMahon, E. Boucrot, *Nat. Rev. Mol. Cell Biol.* **12**, 517–533 (2011).
20. A. V. Shnyrova *et al.*, *Science* **339**, 1433–1436 (2013).
21. K. I. Willig, S. O. Rizzoli, V. Westphal, R. Jahn, S. W. Hell, *Nature* **440**, 935–939 (2006).
22. A. Denker *et al.*, *Proc. Natl. Acad. Sci. U.S.A.* **108**, 17177–17182 (2011).
23. D. Bar-On *et al.*, *J. Biol. Chem.* **287**, 27158–27167 (2012).
24. J. J. Sieber, K. I. Willig, R. Heintzmann, S. W. Hell, T. Lang, *Biophys. J.* **90**, 2843–2851 (2006).
25. J. J. Sieber *et al.*, *Science* **317**, 1072–1076 (2007).
26. V. N. Murthy, T. Schikorski, C. F. Stevens, Y. Zhu, *Neuron* **32**, 673–682 (2001).
27. V. Marra *et al.*, *Neuron* **76**, 579–589 (2012).
28. T. Rose, P. Schoenenberger, K. Jezek, T. G. Oertner, *Neuron* **77**, 1109–1121 (2013).
29. L. D. Cohen *et al.*, *PLOS ONE* **8**, e63191 (2013).
30. D. Bonanomi, F. Benfenati, F. Valtorta, *Prog. Neurobiol.* **80**, 177–217 (2006).
31. A. Denker, K. Kröhnert, J. Bückers, E. Neher, S. O. Rizzoli, *Proc. Natl. Acad. Sci. U.S.A.* **108**, 17183–17188 (2011).
32. O. Shupliakov, *Neuroscience* **158**, 204–210 (2009).
33. S. O. Rizzoli, *EMBO J.* **33**, 788–822 (2014).
34. N. Kitagawa, H. Mazon, A. J. R. Heck, S. Wilkens, *J. Biol. Chem.* **283**, 3329–3337 (2008).

ACKNOWLEDGMENTS

We thank the following collaborators for providing purified proteins and antibodies: R. Jahn, C. Griesinger, B. Shwaller, and A. Roux. We thank H. Martens for technical help and support, B. Rizzoli for helpful comments on the manuscript, and T. Sargeant for providing the carve source code for creation of the voltage-dependent anion channel (VDAC)-based mitochondrial membrane cut-outs. B.G.W. was supported by a Boehringer Ingelheim Fonds PhD Fellowship. S.T. was supported by an Excellence Stipend of the Göttingen Graduate School for Neurosciences, Biophysics, and Molecular Biosciences (GGNB). The work was supported by grants to S.O.R. from the European Research Council (FP7 NANOMAP and ERC-2013-CoG NeuroMolAnatomy) and from the Deutsche Forschungsgemeinschaft (DFG) Cluster of Excellence Nanoscale Microscopy and Molecular Physiology of the Brain, as well as from DFG grants RI 1967 2/1, RI 1967 3/1, and SFB 889/A5. We acknowledge support by the DFG to V.H. (Exc-257-Neurocure and SFB 958/A01), H.U. (SFB 889), and M.K. (SFB 958/A11). Author contributions: B.G.W. prepared the synaptosomes and performed all immunoblotting experiments. K.K. performed the electron microscopy imaging and all neuromuscular junction imaging. C.S. performed the hippocampal culture imaging. S.T. performed the synaptosome imaging. B.R. generated the synapse model. S.J.K., G.A.C., and M.K. participated in the biochemistry experiments. S.M. and H.U. designed and performed all mass spectrometry experiments. S.O.R., B.G.W., and V.H. designed the experiments. All authors analyzed the data and contributed to writing the manuscript.

SUPPLEMENTARY MATERIALS

www.sciencemag.org/content/344/6187/1023/suppl/DC1
Materials and Methods
Figs. S1 to S7
Tables S1 to S3
Movie S1
References (*35*–*46*)

3 March 2014; accepted 6 May 2014
10.1126/science.1252884

CONSERVATION ECOLOGY

Optimal approaches for balancing invasive species eradication and endangered species management

Adam Lampert,[1]* Alan Hastings,[1] Edwin D. Grosholz,[1] Sunny L. Jardine,[2] James N. Sanchirico[1,3]

Resolving conflicting ecosystem management goals—such as maintaining fisheries while conserving marine species or harvesting timber while preserving habitat—is a widely recognized challenge. Even more challenging may be conflicts between two conservation goals that are typically considered complementary. Here, we model a case where eradication of an invasive plant, hybrid *Spartina*, threatens the recovery of an endangered bird that uses *Spartina* for nesting. Achieving both goals requires restoration of native *Spartina*. We show that the optimal management entails less intensive treatment over longer time scales to fit with the time scale of natural processes. In contrast, both eradication and restoration, when considered separately, would optimally proceed as fast as possible. Thus, managers should simultaneously consider multiple, potentially conflicting goals, which may require flexibility in the timing of expenditures.

Ecosystem-based management recognizes that managing individual species does not account for trade-offs and interactions with natural and human communities (*1*, *2*). Yet, the development of this approach has been limited by an absence of attempts to address conflicting goals and interactions. Conflicting goals may occur when two or more species or entities are being manipulated, such as when harvest of commercial fishes threatens endangered marine species via by-catch (*3*–*7*), when timber harvest destroys habitats of endangered wildlife species (*8*, *9*), and when supplying water at a high quantity reduces water quality at the source reservoir (*10*). Here, we focus on a particularly instructive example, where eradication of an invasive species (*11*–*13*) threatens the recovery of an endangered species (*14*–*16*). By modeling this case study, we suggest a general framework for managing conservation conflicts where actions for reaching one management goal have negative impacts on another goal. We begin with a description of the specific system and the conflicting management efforts directed at the two species.

Species of cordgrass in the genus *Spartina* have invaded many salt marshes around the world, which has resulted in changes to physical, biogeochemical, and biological processes that support benthic food webs and ecosystem productivity (*17*, *18*). *Spartina* invasions have also had an impact on human economies by altering shoreline geomorphology, affecting aquaculture, and reducing property values (*19*). Consequently, efforts to eradicate invasive *Spartina* have occurred worldwide (*19*). In San Francisco Bay, California, *S. alterniflora* was introduced from the eastern United States in the mid-1970s (*20*). It then hybridized with native *S. foliosa* and ultimately invaded ~800 acres (*21*) (Fig. 1A). Eradication of hybrid invasive *Spartina* began in 2005 and, to date, ~92% has been removed (Fig. 1B) (*22*). However, native *Spartina* has been slow to recover after eradication of the invader.

During the invasive *Spartina* eradication period, between 2005 and 2011, populations of the federally endangered California clapper rail (*Rallus longirostris obsoletus*) in San Francisco Bay declined by nearly 50% (*23*), presumably because of the overall decline in cover of *Spartina* in which clapper rail nests and forages. Thus, the U.S. Fish and Wildlife Service prohibited further eradication of invasive *Spartina* in the remaining untreated infested areas, which cover ~8% of the originally infested area. To allow completion of invasive *Spartina* eradication within the areas currently off limits without further losses of clapper rail habitat, restoration of native *Spartina* using nursery plants began in 2012.

To determine whether restoring native *Spartina* is cost-effective, and if so, how to best allocate efforts and a budget over time to combine native *Spartina* restoration with invasive *Spartina* eradication, we developed a theoretical model of *Spartina* management and estimated parameters for the model based on field data that was collected over several years (Fig. 2) (*24*). In addition to the distinction between native and invasive *Spartina*, we used a density-structured model (*25*) and further distinguished between two types of each *Spartina* species, "isolates" and "meadows." For invasive *Spartina*, isolates include individual plants that remain after treatment and new seedlings produced by remaining plants, whereas meadows are dense mature stands of untreated invasive *Spartina* that cover large areas. For native *Spartina*, isolates include naturally produced seedlings and restored individual plants, whereas meadows are dense mature stands covering larger areas. This distinction is important because clapper rails prefer larger meadows and are less willing to use individual plants as their habitat (*21*). Therefore, constraining the total amount of meadows (of either invasive or native *Spartina*) to remain above a certain limit is a plausible approach to promote the recovery of clapper rail while still allowing cost-effective management planning for the eradication program.

[1]University of California, Davis, One Shield Avenue, Davis, CA 95616, USA. [2]University of Delaware, Newark, DE 19716, USA. [3]Resources for the Future, Washington, DC 20036, USA.
*Corresponding author. E-mail: alampert@ucdavis.edu

To model the dynamics, we considered a spatially implicit model with four state variables that characterize the relative area covered by each type (Fig. 2). In our main analysis (*24*), we assumed that the area required for clapper rail recovery is a small portion of the entire area that could support *Spartina*, and we neglected density-dependent effects (*25*, *26*). In other words, for both native and invasive *Spartina*, we considered constant annual growth rates at which isolates and meadows increase and at which isolates turn into meadows and vice versa (*24*). Next, we simultaneously considered three possible management actions (Fig. 2): (i) eradication of invasive *Spartina* isolates; (ii) eradication of invasive *Spartina* meadows; and (iii) restoration of native *Spartina* isolates. To find the optimal management strategy, allowing any combination of these three actions, we sought to minimize the net cost over time, taking into account: (i) costs of eradication; (ii) costs of restoration; and (iii) damages caused by infestation of invasive *Spartina*. Using linear programming (*24*), we found the most cost-effective, optimal management subject to (i) the maximal annual budget, B, constraining the annual costs of eradication plus restoration; (ii) the maximal time horizon, T, after which eradication and restoration are not allowed; and (iii) the minimal total amount of meadows of either invasive or native *Spartina* necessary for the recovery of clapper rail, below which eradication is not allowed. Finally, we verified that our results are valid in two ways. First, we checked the robustness of the results from our linear, discrete-time model by comparing them to a continuous time-optimal control model with both linear and nonlinear cost of eradication and restoration functions (*24*). Second, we verified that the results are robust and insensitive to density-dependent effects and noise, using dynamic programming (*24*).

We used field-based population data together with economic data detailing the costs of eradication, restoration, and direct damages from invasive *Spartina* over the past 9 years for model parameterization (*24*) (table S1). We found that the optimal management comprises three stages (Fig. 3). First, the manager eradicates invasive *Spartina* until the clapper rail's habitat constraint is limiting (at which point further removal is prohibited). To avoid further spread of invasive *Spartina* that would make the treatment more costly, the manager uses the entire annual budget each year during this stage. Second, the manager replants native *Spartina* isolates in fully eradicated areas until they cover some fraction of what is ultimately needed to support clapper rail. Initially, the isolates are insufficient to provide adequate habitat, but these plants initiate native *Spartina*'s population dynamics and eventually grow into meadows that support clapper rail. During this stage, the manager again uses the entire annual budget each year. Third, the manager slowly removes the remaining invasive *Spartina*, while native *Spartina* isolates grow into meadows. Once the native *Spartina* meadows are sufficiently abundant to support the clapper rail population, the manager completes the eradication

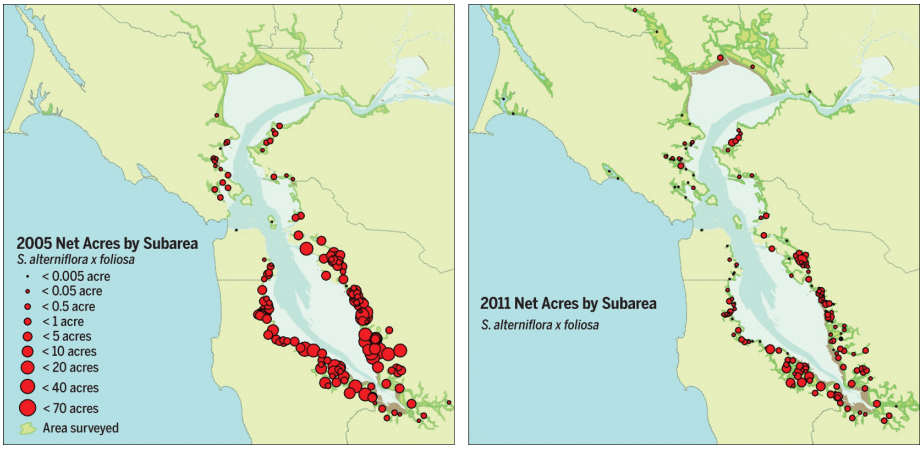


Fig. 1. Changing abundance of invasive *Spartina*. (**Left**) Abundance of invasive hybrid *Spartina* before the eradication program (2005–2011). (**Right**) Abundance of invasive *Spartina* showing greatly reduced distribution in 2011. Eradication is not permitted in the remaining untreated areas, totaling ~8% of the area covered by invasive *Spartina* in 2005.

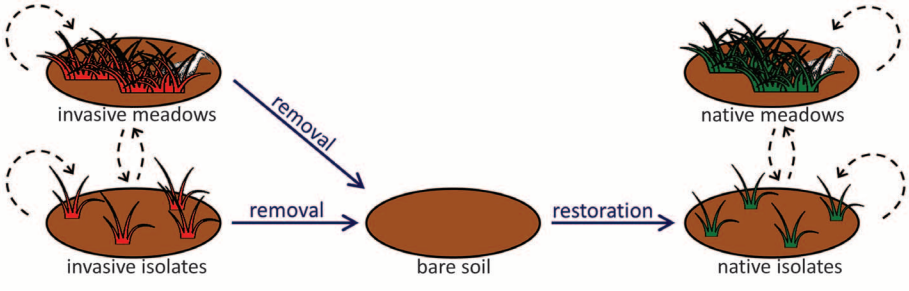


Fig. 2. Invasive species eradication concurrent with endangered species recovery. Both invasive *Spartina* and native *Spartina* are stage-structured and comprise isolates, which include any form of *Spartina* in which clapper rail cannot nest (isolated plants, seedlings), and meadows, which include any form of *Spartina* in which clapper rail can nest (large areas covered by mature stands of *Spartina*). Bare soil represents area that was eradicated but where native *Spartina* is still absent. Each *Spartina* species has its own natural growth rates (dashed arrows). The goal of management is to remove invasive *Spartina*, while maintaining sufficient clapper rail habitat composed of either invasive or native *Spartina* meadows (or both) at any given time. We examine how to optimally combine the three management actions (solid arrows: invasive meadows removal; invasive isolates removal; native replanting) over time to achieve the goals in the most cost-effective manner.

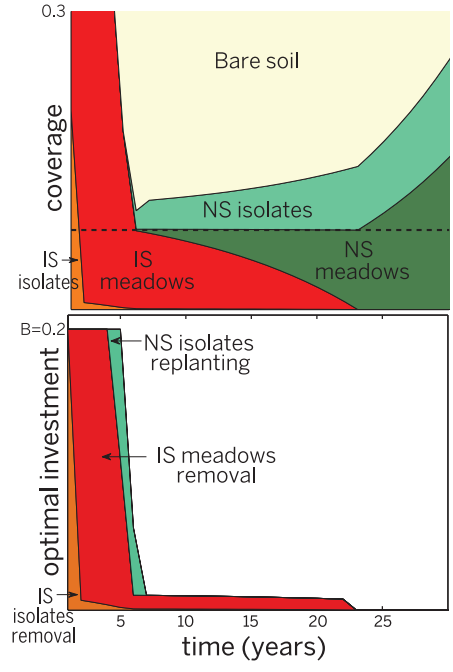


Fig. 3. Optimal synthesis between invasive species eradication and endangered species recovery. (**Top**) The fraction covered (unitless) by invasive *Spartina* (IS) and by native *Spartina* (NS), when we assume optimal management. (**Bottom**) Optimal investment levels in eradication and restoration over time given a fixed annual budget (B): First, remove IS as quickly as possible but not below the minimum habitat needed for the clapper rail (dashed line in top panel); next, replant some NS isolates; and finally, use only the necessary amount of budget to remove the remaining IS while keeping enough meadows to provide nesting habitat for clapper rail. The progress continues until there are enough NS meadows to allow complete eradication of IS. The parameters used here are based on field data (table S1).

of invasive *Spartina*. During this last stage, the manager uses only a small fraction of the available annual budget because eradication is constrained by the minimal amount of meadows needed for clapper rail recovery, and the manager has to wait for more native *Spartina* meadows to grow naturally (Figs. 3 and 4). This management scheme, particularly the last stage, stands in contrast to optimal eradication in the absence of endangered species, which would include a single stage and proceed as fast as possible with the entire annual budget being used each year until eradication is completed (*27*).

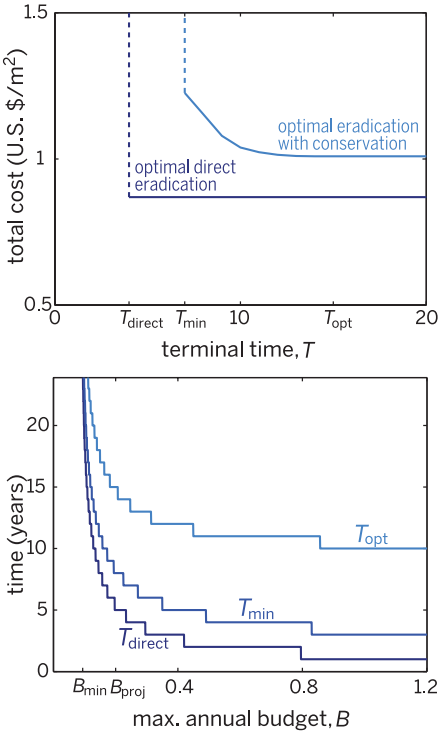


Fig. 4. Importance of long-term restoration and conservation. (**Top**) Plotted is the present value of the total net costs over the years, including both direct costs due to damages caused by invasive *Spartina* and costs of treatment. If the manager eradicates invasive *Spartina* without considering the endangered clapper rail, then eradication could be completed within T_{direct} years (dark line). Optimally, the manager would eradicate as fast as possible until eradication is completed within T_{direct} years, and therefore, additional years would not make any difference. However, achieving both eradication of invasive *Spartina* and recovery of clapper rail, using the same annual budget, requires at least T_{min} years (light line). Moreover, it would be more cost-effective to divide the budget over several more years, using a smaller fraction of the annual budget each year. Particularly, approaching the minimal net cost is possible if the manager can carry the budget over more years until year T_{opt} (*24*). (**Bottom**) Plotted are T_{direct}, T_{min}, and T_{opt} for various maximal annual budgets, B. The actual annual budget used in the project is B_{proj}. Parameters are the same as used in Fig. 3 (table S1).

Our robustness analysis shows that the need for long-term management is insensitive to parameter changes: Optimal management dictates rapid eradication of invasive *Spartina* until further eradication is prohibited, followed by slower eradication that is constrained by the recovery process of native *Spartina* (figs. S1 to S6). This analysis also shows that (i) the first eradication stage and the restoration stage may overlap (fig. S1), and (ii) ultimate eradication may occur with a delay after restoration, either if more years are needed for native *Spartina* isolates to grow into meadows and provide habitat for clapper rail (fig. S2) or if *Spartina* growth is stochastic (fig. S6), which implies that the manager should carry over the unused budget to the following years. Alternatively, if eradication is restricted to a shorter time frame, then it may still be possible to complete the eradication by accelerating the process using the remaining budget for further active restoration of native *Spartina* (fig. S1), but this implies a greater net cost (Fig. 4). Thus, restricting eradication to shorter time frames is suboptimal and decreases cost-efficiency. Moreover, an inadequate budget and/or an even shorter time frame may ultimately preclude complete eradication (Fig. 4), which may require abandoning the program.

As invasive species are becoming increasingly abundant, more threatened and endangered species are becoming dependent on invasive species for habitat or food resources (*28*–*30*). Examples include (i) camphor laurel (*Cinnamomum camphora*), a damaging invasive tree that also provides habitat for wildlife in Australia, including endangered fruit doves (*28*), and (ii) tamarisk (*Tamarix* spp.), an invasive tree that has colonized riparian zones in the southwestern United States and, in the absence of native trees, provides nesting habitat for southwestern willow flycatcher (*Empidonax traillii extimus*) (*29*). This conflict has led to cancellation of an eradication program for tamarisk. The management principles we developed also apply to these examples, and therefore, estimation of the relevant parameters would readily enable planning of optimal management based on our approach.

Considering multiple objectives simultaneously is needed more generally when a management action for one goal has unintended negative impacts on another, conflicting goal. Examples include managed relocation to conserve species while minimizing damage to native species (*31*), introduction of trees for restoration and forestry while actively preventing their invasion to neighboring regions (*32*), harvesting commercial species in marine systems that involve by-catch of sensitive species (*3*–*7*), and timber production or land use while maintaining habitat for wildlife (*8*–*10*, *30*). Management is even more challenging if each goal is evaluated differently by different agencies with overlapping or competing authority. Our framework balances between the conflicting objectives by constraining the negative impacts during the entire management period. Reaching the first goal cost-effectively without violating the constraint may require additional management actions (e.g., restoration) to prevent or compensate for its negative impacts. The general conclusion is that optimal management, which considers multiple goals simultaneously, entails less-intensive investment over extended periods and may require carrying unused budget over to the following years, even if each action, when considered separately, should proceed as fast as possible.

REFERENCES AND NOTES

1. C. Folke, T. Hahn, P. Olsson, J. Norberg, *Annu. Rev. Environ. Resour.* **30**, 441–473 (2005).
2. H. M. Leslie, K. L. McLeod, *Front. Ecol. Environ* **5**, 540–548 (2007).
3. D. L. Alverson, M. H. Freeberg, S. A. Murawski, J. G. Pope, "A global assessment of fisheries bycatch and discards" (Fisheries Technical Paper no. 339, Food and Agriculture Organization, Rome, 1994).
4. L. B. Crowder, S. A. Murawski, *Fisheries (Bethesda, Md.)* **23**, 8–17 (1998).
5. A. Hastings, L. W. Botsford, *Ecol. Appl.* **13** (suppl.), S65–S70 (2003).
6. T. P. Hughes, D. R. Bellwood, C. Folke, R. S. Steneck, J. Wilson, *Trends Ecol. Evol.* **20**, 380–386 (2005).
7. B. Worm *et al*., *Science* **314**, 787–790 (2006).
8. D. J. Nalle, C. A. Montgomery, J. L. Arthur, S. Polasky, N. H. Schumaker, *J. Environ. Econ. Manage.* **48**, 997–1017 (2004).
9. F. J. Swanson, J. F. Franklin, *Ecol. Appl.* **2**, 262–274 (1992).
10. K. D. Hambright, A. Parparov, T. Berman, *Aquat. Conserv.* **10**, 393–406 (2000).
11. Y. M. Buckley, *J. Appl. Ecol.* **45**, 397–402 (2008).
12. R. N. Mack *et al*., *Ecol. Appl.* **10**, 689–710 (2000).
13. D. Simberloff *et al*., *Trends Ecol. Evol.* **28**, 58–66 (2013).
14. M. J. Groom, G. K. Meffe, C. R. Carroll, *Principles of Conservation Biology* (Sinauer Associates, Sunderland, MA, 2006).
15. M. E. Soule, B. A. Wilcox, *Conservation Biology: An Evolutionary-Ecological Perspective* (Sinauer Associates, Sunderland, MA, 1980).
16. A. Ando, J. Camm, S. Polasky, A. Solow, *Science* **279**, 2126–2128 (1998).
17. E. D. Grosholz, L. A. Levin, A. C. Tyler, C. Neira, in *Human Impacts on Salt Marshes: A Global Perspective* (Univ. of California Press, Berkeley and Los Angeles, 2009), pp. 23–40.
18. L. A. Levin, C. Neira, E. D. Grosholz, *Ecology* **87**, 419–432 (2006).
19. D. R. Strong, D. R. Ayres, *Annu. Rev. Ecol. Evol.* **44**, 389–410 (2013).
20. P. M. Faber, *California Coast Ocean* **16**, 14–17 (2000).
21. D. R. Ayres, D. L. Smith, K. Zaremba, S. Klohr, D. R. Strong, *Biol. Invasions* **6**, 221–231 (2004).
22. I. Holge, Olofson Environmental, Inc., "San Francisco Estuary Invasive *Spartina* Project monitoring report for 2011" (San Francisco Estuary Invasive *Spartina* Project, California State Coastal Conservancy, Oakland, CA, 2012).
23. J. McBroom, "2010 California clapper rail surveys for the San Francisco Estuary Invasive *Spartina* Project" (San Francisco Estuary Invasive *Spartina* Project, California State Coastal Conservancy, Oakland, CA, 2011).
24. Materials and methods are available as supplementary materials on *Science* Online.
25. C. M. Taylor, A. Hastings, *J. Appl. Ecol.* **41**, 1049–1057 (2004).
26. A. Hastings, R. J. Hall, C. M. Taylor, *Theor. Popul. Biol.* **70**, 431–435 (2006).
27. C. W. Clark, *Mathematical Bioeconomics: The Optimal Management of Renewable Resources* (Wiley Interscience, New York, 1990).
28. W. Neilan, C. P. Catterall, J. Kanowski, S. McKenna, *Biol. Conserv.* **129**, 393–407 (2006).
29. M. K. Sogge, S. J. Sferra, E. H. Paxton, *Restor. Ecol.* **16**, 146–154 (2008).

30. T. G. Martin, S. McIntyre, C. P. Catterall, H. P. Possingham, *Biol. Conserv.* **127**, 201–214 (2006).
31. O. Hoegh-Guldberg *et al.*, *Science* **321**, 345–346 (2008).
32. H. Yokomizo, H. P. Possingham, P. E. Hulme, A. C. Grice, Y. M. Buckley, *Biol. Invasions* **14**, 839–849 (2012).

ACKNOWLEDGMENTS

We thank the personnel of the Invasive *Spartina* Project, including P. Olofson, E. Grijalva, D. Kerr, I. Hogle, W. Thornton, M. Latta, and others, who provided data on *Spartina* distributions, clapper rail populations, and costs of eradication and restoration efforts. We thank D. Kling for research assistance and P. Reynolds for comments on the manuscript. We thank the California State Coastal Conservancy and the California State Wildlife Conservation Board for use of their data. The data used for this paper are summarized in table S1 (*24*) and are given in more detail in (*24*). This research was supported by NSF grant no. DEB 1009957 to A.H., E.D.G., J.N.S., A.L., and S.L.J.

SUPPLEMENTARY MATERIALS

www.sciencemag.org/content/344/6187/1028/suppl/DC1
Materials and Methods
Supplementary Text
Figs. S1 to S6
Tables S1 to S4
References (*33*–*46*)

13 January 2014; accepted 23 April 2014
10.1126/science.1250763

CELLULAR DYNAMICS

High-resolution mapping of intracellular fluctuations using carbon nanotubes

Nikta Fakhri,[1] Alok D. Wessel,[1] Charlotte Willms,[1] Matteo Pasquali,[2] Dieter R. Klopfenstein,[1] Frederick C. MacKintosh,[3]* Christoph F. Schmidt[1]*

Cells are active systems with molecular force generation that drives complex dynamics at the supramolecular scale. We present a quantitative study of molecular motions in cells over times from milliseconds to hours. Noninvasive tracking was accomplished by imaging highly stable near-infrared luminescence of single-walled carbon nanotubes targeted to kinesin-1 motor proteins in COS-7 cells. We observed a regime of active random "stirring" that constitutes an intermediate mode of transport, different from both thermal diffusion and directed motor activity. High-frequency motion was found to be thermally driven. At times greater than 100 milliseconds, nonequilibrium dynamics dominated. In addition to directed transport along microtubules, we observed strong random dynamics driven by myosins that result in enhanced nonspecific transport. We present a quantitative model connecting molecular mechanisms to mesoscopic fluctuations.

The cytoplasm of eukaryotic cells is a highly dynamic composite polymer material. Its mechanical properties are dominated by protein polymers: microtubules (MTs), F-actin, and intermediate filaments (*1*–*4*). Metabolism maintains a chemical nonequilibrium that energizes this mechanical framework of cells. Dominant driving forces stem from the polymerization of actin and tubulin and from motor proteins, both deriving energy from nucleotide triphosphate hydrolysis (*5*, *6*). Molecules self-organize into complex machineries on all scales to drive functions as various as intracellular transport, cell locomotion, and muscle contraction. Understanding these machineries requires observing intracellular dynamics from molecular to macroscopic scales. Fluorescence microscopy allows labeling of specific targets, but it has been impossible to achieve long-term tracking of single molecules because of the fluorescent background in cells and fluorophore instabilities. Observations of intramolecular dynamics have often used mesoscopic endogenous particles or ingested beads (*7*, *8*) instead of molecular tracers.

Generally, dynamics in cells are scale-dependent. At short times (microseconds to milliseconds), thermal motions should dominate. Between milliseconds and seconds, thermal diffusion might still be relevant, but there is mounting evidence, both in vitro and in vivo, that the motion of larger objects couples to myosin-driven stress fluctuations in the cytoskeleton (*9*, *10*). Here, temporal fluctuations, reminiscent of thermal diffusion in liquids, can arise from nonequilibrium dynamics in the viscoelastic cytoskeleton (*11*). On longer time scales, from minutes to hours, directed transport and larger-scale collective motions typically dominate. The motion of probe particles tracked inside cells has been classified as subdiffusive, diffusive, or superdiffusive. Such classifications, however, obscure the distinction between thermally driven and nonequilibrium fluctuations and are inadequate to identify intracellular material properties.

Motor proteins are good reporters of dynamics from the molecular scale upward because they drive many cellular motions. Kinesins and myosins have been extensively studied in vitro (*12*, *13*), but the dynamics of motors in cells remain largely unexplored (*14*). Following motor motion in cells by fluorescence microscopy requires (i) stable, nonbleaching fluorescent probes, (ii) high signal-to-noise ratio in imaging, and (iii) efficient targeting of probes to specific molecules. Modern optical equipment in conjunction with optimized fluorescent dyes can resolve and track single molecules with high temporal and spatial resolution in vitro (*15*). In living cells, however, molecular imaging has been limited to short times (~1 s)—for example, in superresolution microscopy (*16*). Moreover, signal-to-noise ratios tend to be marginal because of cellular background fluorescence.

Here, we used single-walled carbon nanotubes (SWNTs) as a tool for high-bandwidth intracellular tracking. SWNTs are stiff quasi–one-dimensional tubular all-carbon nanostructures with diameters of ~1 nm and persistence lengths above 10 μm (*17*). Individual semiconducting SWNTs luminesce with large Stokes shifts in the near-infrared (900 to 1400 nm) (*18*). This window is virtually free of autofluorescence in biological tissues. Fluorescence emission is highly stable with no blinking and negligible photobleaching (*19*, *20*) (fig. S1), allowing for long-term tracking (*21*). The fluorescence lifetime is short [~100 ps (*22*)] so that high excitation intensities allow millisecond time resolution.

To track the dynamics of the cytoskeleton without introducing invasive probes, we specifically targeted short SWNTs (~100 to 300 nm; fig. S2) to the endogenous kinesin-1 motor Kif5c in cultured COS-7 cells (see supplementary materials). Kif5c functions as a cargo transporter in cells (*23*). We dispersed SWNTs by wrapping with short DNA oligonucleotides and used HaloTag (*24*) to covalently attach SWNTs specifically to full-length kinesins expressed in the cells (Fig. 1, A and B). We used an additional green fluorescent protein label to confirm localization and motility of the motors on MTs (figs. S3 and S4 and movie S1). Tracking motor proteins makes it possible to observe several types of dynamics. Besides observing directed kinesin-driven transport on MTs, it is possible to directly observe fluctuations of the MT network because a moving kinesin must be bound to a MT. The MT tracks are embedded in the viscoelastic actin cytoskeleton, which in turn fluctuates as a result of stresses generated by cytoplasmic myosins (Fig. 1C) (*25*, *26*).

The high photostability of SWNTs made it possible to introduce only a small number, around 100 per cell, and still track individual SWNTs

[1]Drittes Physikalisches Institut–Biophysik, Georg-August-Universität, 37077 Göttingen, Germany. [2]Department of Chemical and Biomolecular Engineering, Department of Chemistry, Smalley Institute for Nanoscale Science and Technology, Rice University, Houston, TX 77005, USA. [3]Department of Physics and Astronomy, Vrije Universiteit, 1081 HV Amsterdam, Netherlands.
*Corresponding author. E-mail: christoph.schmidt@phys.uni-goettingen.de (C.F.S.); fcmack@gmail.com (F.C.M.)

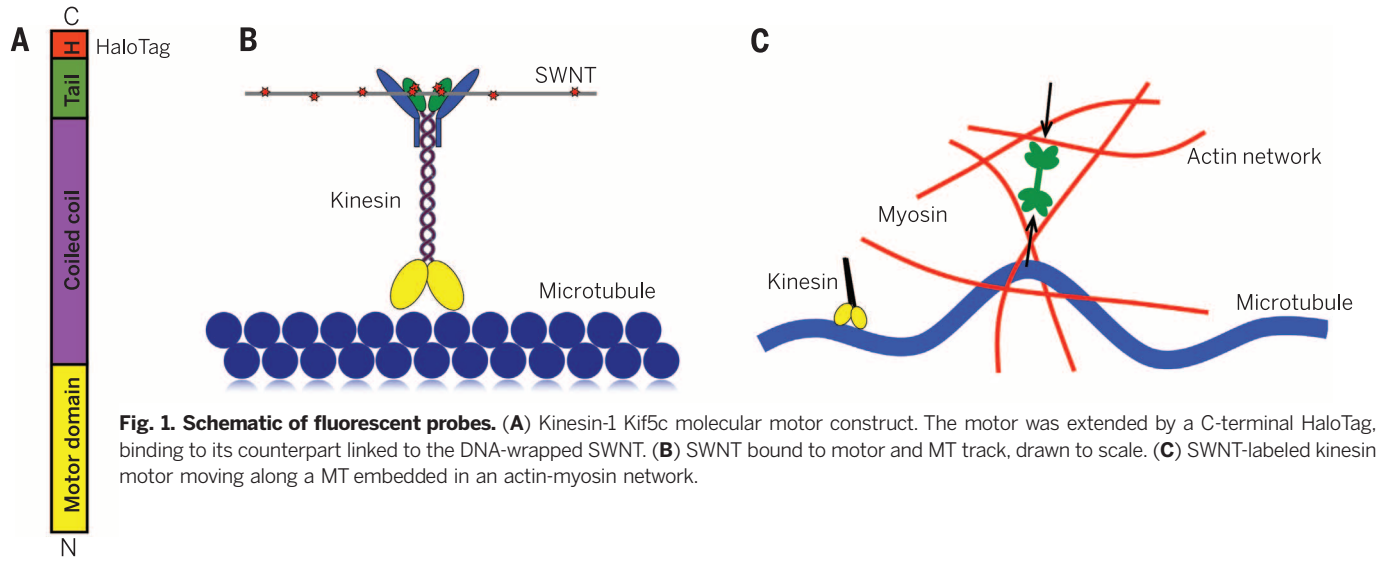
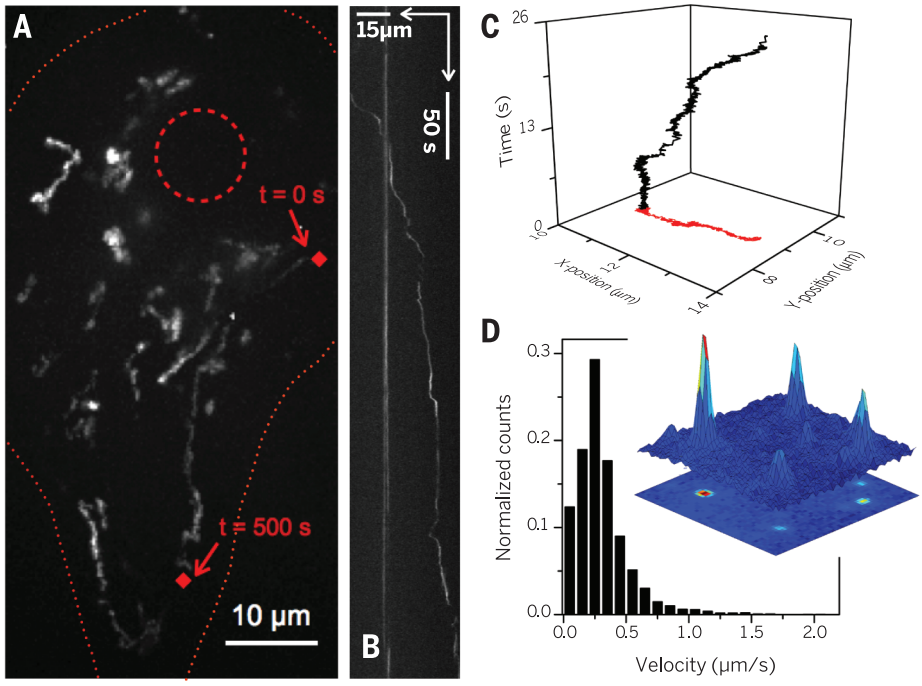


Fig. 1. Schematic of fluorescent probes. (**A**) Kinesin-1 Kif5c molecular motor construct. The motor was extended by a C-terminal HaloTag, binding to its counterpart linked to the DNA-wrapped SWNT. (**B**) SWNT bound to motor and MT track, drawn to scale. (**C**) SWNT-labeled kinesin motor moving along a MT embedded in an actin-myosin network.

Fig. 2. Tracking SWNT-labeled kinesins in COS-7 cells. (**A**) Tracks of SWNT-labeled kinesin-1 motors (Kif5c) in a COS-7 cell shown as 2D maximum-intensity projection (movie S2). Nucleus and cell periphery are outlined with red dashed and dotted lines, respectively. Red diamonds mark beginning and end of the 8.3-min trajectory of a particular SWNT-kinesin. (**B**) Kymograph of a single SWNT-labeled kinesin tracked over ~40 μm [track marked by red diamonds in (A)]. (**C**) Track of a SWNT-labeled kinesin in a cell; frame time, 5 ms (movie S4). (**D**) Histogram of the magnitude of velocity of SWNT-labeled kinesins, averaged over 2-s segments (N = 367 in 30 cells). The inset is a single frame of individual SWNT-labeled kinesins showing high image contrast. Heat map color code indicates relative intensity.



for up to 1.5 hours. We used a single-molecule tracking algorithm (*27*) and determined the centroid position of SWNTs in the focal plane to a precision of 20 to 50 nm. Fluorescent spots were detected with a signal-to-noise ratio of about 20 (for integration times of 60 to 250 ms; Fig. 2D, inset, and fig. S5). In typical recordings, we observed up to 30% of SWNTs moving in a directed manner, with the rest moving randomly but remaining locally constrained. Occasionally, random motion turned into directed motion and vice versa. These cases confirm that the label was attached to a motor, which in turn was attached to a MT. Tracks of the moving SWNTs (Fig. 2A) showed long and relatively straight unidirectional runs, typical for kinesin-1. The average velocity of straight runs, low-pass filtered over segments of 2 s, was 300 ± 210 nm/s (mean ± SD), consistent with previous reports (*28*, *29*) (Fig. 2D), confirming largely unimpeded motility. Several SWNT-labeled kinesins could be tracked across the whole cell, much farther than the average run length (~1 μm) of a single kinesin-1 in vitro (*30*) (Fig. 2A and fig. S6). This suggests that the labeled motors were attached to cargo vesicles with other motors. Motors generally moved in a stop-and-go fashion (Fig. 2B). Pauses might reflect temporary detachment or mechanical obstacles (*31*). During phases of movement, kinesin velocity varied in magnitude and direction, predominantly pointing toward the cell periphery (Fig. 2A).

The photostability of SWNTs also made it possible to increase the time resolution by increasing illumination intensity without sacrificing overall recording time. To capture short-time dynamics, we imaged with a time resolution of 5 ms per frame (Fig. 2C and movie S4). With this resolution, we analyzed the randomly moving population (Fig. 3A, inset) by computing the mean squared displacement (MSD) of trajectories, $\langle \Delta r^2(\tau) \rangle$, where τ is the lag time and $\Delta r(\tau) = r(t + \tau) - r(t)$ is the distance traveled in the focal plane in time τ. The MSD grows with lag time, typically exhibiting approximate power-law behavior $\langle \Delta r^2(\tau) \rangle \propto \tau^{\alpha}$. The MSD exponent α, which may vary from one to another time regime, provides an important characteristic of the motion. For observation times between 5 ms and 2.5 s, we found an averaged MSD transitioning from $\alpha \approx 0.25$ to $\alpha \approx 1$ (Fig. 3B).

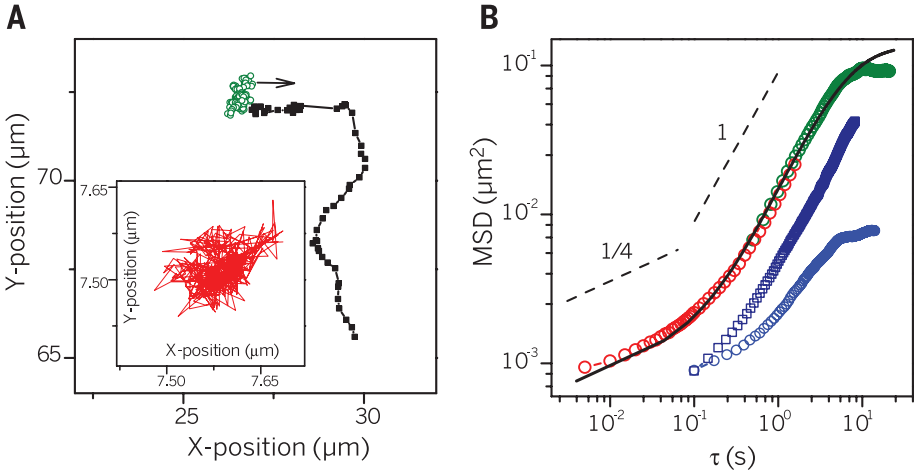


Fig. 3. Nonequilibrium stirring of the cytoplasm. (**A**) 2D projection of a SWNT-labeled kinesin trajectory initially moving randomly (stationary phase, green circles) and then moving on MTs; frame time, 250 ms (black squares). The inset shows the trajectory of a SWNT-labeled kinesin with frame time of 5 ms. (**B**) Average 2D MSD of the motor during the stationary phase at frame times of 250 ms (green circles, $N = 10$) and 5 ms (red circles, $N = 10$). A noise floor is subtracted (fig. S12 and supplementary materials). Approximate power-law slopes of 0.25 and 1 are indicated. Same after treatment with blebbistatin (dark blue squares, 10 μM blebbistatin, $N = 5$; blue circles, 50 μM blebbistatin, $N = 5$). The black line is the model curve, the weighted sum of Eqs. 3 and 4. The following values for the parameters (in addition to weights) have been chosen to best approximate the data: $\beta = 0.2$, $\tau_c = 5$ s.

Next we analyzed longer trajectories recorded with a 250-ms frame time. When random motion turned into directed motion (Fig. 3A), we could be sure that we were observing SWNTs attached to motors. We separately analyzed the stationary and directed segments of those trajectories. The MSDs from stationary segments showed a scaling exponent $\alpha = 1.1 \pm 0.2$ (Fig. 3B) for intermediate times, connecting in slope and amplitude to the short-time MSDs, and then leveling off for $\tau > 5$ to 10 s. Motors might have been unbound from MTs during the stationary segments. To exclude ambiguity, we also analyzed the directed-motion segments of the tracks. The fact that MTs are locally straight allowed us to distinguish track fluctuations by decomposing trajectories into longitudinal (on-axis) and transverse (off-axis) components (Fig. 4A). Longitudinal motion showed a MSD with $\alpha \approx 2$ at long times, confirming processive motor motion (Fig. 4, B and D), while the transverse MSD again showed an exponent $\alpha \approx 1$ for intermediate times. The transverse MSD also leveled off for times longer than 5 to 10 s, just as the MSD from the stationary segments (Fig. 4, B to D). To test whether there was a mutual dependency between the speed of directed transport and the off-axis fluctuations, we correlated on-axis velocity and off-axis displacement variance in time windows of 0.5 s (fig. S7). There was no apparent correlation, except for a slight decrease in variance at the highest velocities measured (>750 nm/s), which is likely to be an artifact. As a control, we also introduced functionalized SWNTs into COS-7 cells that did not express HaloTag kinesins (fig. S8 and movie S3). In those cells, we did not observe MSDs with $\alpha \approx 2$, but for roughly half of the tracked SWNTs, we did observe the active exponent of $\alpha \approx 1.2$ while the remainder of SWNTs were less mobile (fig. S9).

Thus, the active transverse MT fluctuations are not due to kinesin motors, but instead reflect the dynamics of the cytoskeleton. The way the relatively rigid MTs report these dynamics depends on two restoring forces: the elastic force of bent MTs and the force exerted by the strained cytoskeletal matrix in which the MTs are embedded. Because it is hard to bend an elastic rod on short length scales, the surrounding matrix yields to the MT when it is deformed on short length scales. By contrast, the MT yields to matrix forces for deflections of wavelength larger than ~1 μm (*32*). The shorter-wavelength MT deflections relax faster than our 5-ms frame rate (*5*). Therefore, we assume that the transverse MT motion we observe reflects the (active or passive) strain fluctuations of the surrounding matrix.

The MSD power-law exponent α generally reflects the randomness of motion. More precisely, in any medium, the MSD of an embedded probe particle is governed both by the material properties of the medium and the temporal characteristics of the forces driving the particle. For thermally driven Brownian motion in simple liquids, the MSD exponent $\alpha = 1$. For thermal motion in viscoelastic media, which exhibit time- and frequency-dependent viscosity and elasticity, $\alpha < 1$ strictly holds. For viscoelastic materials, the stiffness $G(\omega)$ typically increases with a power of frequency ω: $G(\omega) \propto \omega^{\beta}$. This is observed in polymer solutions, where the viscoelastic exponent $\beta \approx 0.5$ to 0.8 (*33*), as well as in cells, where $\beta \approx 0.1$ to 0.2 on time scales on the order of seconds (*34*). This value of the exponent is close to what is expected for purely elastic materials, where $\beta = 0$. The nearly elastic behavior of cells can be understood as a consequence of strong cross-linking in the cytoskeleton. Knowing the driving forces, it is possible to construct a relation between MSD exponent α and viscoelastic exponent β. For thermal driving forces, the MSD exponent $\alpha = \beta$ (*9*). Thermal fluctuations can therefore never appear as "superdiffusive" motion with $\alpha > 1$. Nonthermal driving, by contrast, can result in superdiffusive motion. Theory provides a specific prediction for motion in nearly elastic solids driven by random stress fluctuations with long correlation times and sudden transitions: $\alpha = 1 + 2\beta$ (*11*, *35*, *36*). This prediction is expected to apply for cytoskeletal stress fluctuations caused by randomly distributed cytoplasmic myosin minifilaments. Myosin locally contracts the actin network with an attachment time of several seconds, followed by sudden release. Some hints of this predicted scaling have been reported for cells and reconstituted acto-myosin model systems (*9*–*11*, *35*). When $\beta = 0$ (i.e., in the elastic limit), the resulting MSDs can look deceptively like Brownian motion in a simple liquid, although the physical reason is entirely different. For observation times τ longer than the correlation time of the driving forces, the MSD is predicted to level off (*11*), as we observed. In our experiments, the stress correlation time should correspond to typical cytoplasmic myosin motor engagement times, which are indeed reported to be ~10 s in cells.

We modeled the entire expected MSD curves to match asymptotic power-law segments and to also capture the transitions between the different regimes we observed. For a medium with shear stiffness $G(\omega)$, the frequency-dependent displacement $r(\omega)$ is proportional to applied force $f(\omega)$ and inversely proportional to $G(\omega)$. Thus, the power spectral density (PSD) of r is given by

$$\langle r^2\rangle_\omega = \int \langle r(t+\tau)r(t)\rangle \exp(i\omega\tau)d\tau \propto \frac{\langle f^2\rangle_\omega}{|G(\omega)|^2} \quad (1)$$

For active forces governed by a correlation time τ_c, the force spectrum is predicted to be

$$\langle f^2\rangle_\omega = \int \langle f(t)f(0)\rangle \exp(i\omega\tau)dt \propto \frac{1}{1+(\omega\tau_c)^2} \quad (2)$$

(*11*, *35*). This spectrum corresponds, in the time domain, to a net force due to randomly distributed myosins that grows as a random walk in time $\langle \Delta f^2(\tau)\rangle \propto \tau$ for times less than τ_c, and looks like white, uncorrelated noise at longer times (*37*). Thus, the active MSD is

$$\langle \Delta r^2(\tau)\rangle_{\text{active}} \propto \int [1 - \exp(-i\omega\tau)] \frac{1}{[1+(\omega\tau_c)^2]|G(\omega)|^2} \frac{d\omega}{2\pi} \quad (3)$$

(see supplementary materials). By contrast, the passive MSD is given by

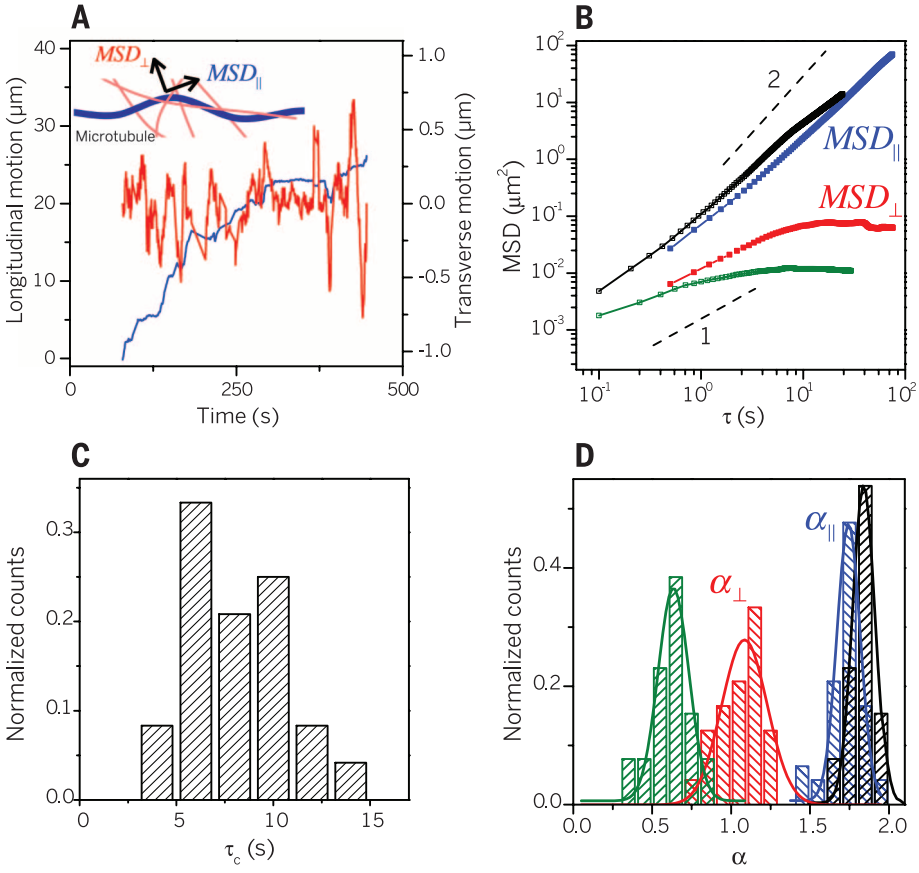


Fig. 4. Kinesin tracking on MTs buffeted by myosin. (**A**) Decomposition of a motor trajectory into longitudinal (blue) and transverse (red) components relative to the MT tangent. (**B**) Average MSD of longitudinal (blue squares, N = 5) and transverse (red squares, N = 5) components of a run. Same after treatment with 50 μM blebbistatin, transverse (green open squares, N = 7) and longitudinal (black open squares, N = 7). Power-law slopes are indicated. (**C**) Histogram of characteristic leveling-off times τ_c of the transverse MSDs, representing myosin correlation time (N = 30). (**D**) Histogram of MSD scaling exponents at intermediate times for longitudinal (blue) and transverse (red) components for motors moving processively along MTs (N = 30). After treatment with 50 μM blebbistatin: transverse scaling exponent (green) and longitudinal scaling exponent (black) (N = 20).

$$\langle \Delta r^2(\tau)\rangle_{\text{passive}} \propto kT\int[1-\exp(-i\omega\tau)]\frac{G''(\omega)}{\omega|G(\omega)|^2}\frac{d\omega}{2\pi} \quad (4)$$

where T is temperature and k is Boltzmann's constant. In Fig. 3B, we plot the sum of active and passive fluctuations (Eqs. 3 and 4) for comparison with our data. We found $\beta = 0.2$ and $\tau_c = 5$ s to result in a good fit of the data after adjusting the amplitudes of both passive and active fluctuations. The motor proteins thus served as multi-timescale probes of cytoskeletal fluctuations. We observed a transition between thermal dynamics in the dominantly elastic cytoskeleton at short times to strongly nonequilibrium power-law dynamics, likely driven by myosin activity, at intermediate times. When the time exceeded the correlation time of the random stress generators, the intermediate regime was followed by a saturation to a maximum MSD, nearly constant over time. Note that in this regime, the MSD amplitude corresponds to a root mean square displacement of ~500 nm (fig. S10), which is larger than the estimated mesh size of the actin network, and thus larger than the expected spacing of obstacles in the crowded cytoplasm.

To investigate whether the transverse nonequilibrium kinesin motor fluctuations were indeed indirectly driven by myosin, we incubated transfected COS-7 cells with blebbistatin and again tracked SWNTs attached to Kif5c kinesin. Blebbistatin is a small-molecule inhibitor of nonmuscle myosin II, blocking myosin in an actin-detached state (*38*, *39*). We used two concentrations, 10 μM and 50 μM blebbistatin, for about 50% and 95% inhibition of myosin (*40*). We again tracked both stationary kinesins and those that moved in a directed manner. MSD analysis showed convergence in the short-time thermal fluctuations as expected, as well as a dose-dependent response in the nonequilibrium section of the MSDs (Fig. 3B). At 10 μM blebbistatin, the amplitude of active stirring was reduced by a factor of ~2, but the exponent $\alpha \approx 1$ was still evident. At 50 μM blebbistatin, the stirring amplitude was suppressed by a further factor of 2, and the MSD exponent decreased, consistent with a substantial suppression of the active stress fluctuations. Tracking of moving motors and separate analysis of on-axis and off-axis MSDs confirmed the suppression of off-axis fluctuations. The exponent decreased to $\alpha \approx 0.6$, whereas on-axis kinesin motility remained largely unaffected (Fig. 4, B and D). There was a slight increase in on-axis motility and a broadening of the velocity distribution (fig. S11), which we speculate might be due to softening of the actin network in the absence of tension (*10*). These results establish nonmuscle myosin II as the dominant driving factor for random cytoskeletal stirring.

Our recordings of kinesin-1 motility in cells over five orders of magnitude in time provide a wide window on intracellular dynamics. We can explain the regimes we observe by a quantitative model of cytoskeletal fluctuations and directed motor motion that describes the transition from thermal motion to nonequilibrium stirring dynamics driven by myosin, as well as the transition from stirring dynamics to directed transport driven by kinesin. Our observations were made possible by the use of SWNT labels for broadband molecular tracking in cells. Many questions concerning motor transport in cells will now be addressable using this approach. We have focused here on the stirring dynamics, which constitute an important mode of active intracellular transport between the limits of random thermal diffusion and directed transport, accelerating nonspecific transport through the nanoporous cytoskeleton.

REFERENCES AND NOTES

1. P. A. Janmey, C. A. McCulloch, *Annu. Rev. Biomed. Eng.* **9**, 1–34 (2007).
2. D. A. Fletcher, R. D. Mullins, *Nature* **463**, 485–492 (2010).
3. F. Huber *et al.*, *Adv. Phys.* **62**, 1–112 (2013).
4. J. Stricker, T. Falzone, M. L. Gardel, *J. Biomech.* **43**, 9–14 (2010).
5. J. Howard, *Mechanics of Motor Proteins and the Cytoskeleton* (Sinauer Associates, Sunderland, MA, 2001).
6. A. Basu, J. F. Joanny, F. Jülicher, J. Prost, *Eur. Phys. J. E* **27**, 149–160 (2008).
7. Y. Tseng, T. P. Kole, D. Wirtz, *Biophys. J.* **83**, 3162–3176 (2002).
8. J. C. Crocker, B. D. Hoffman, *Methods Cell Biol.* **83**, 141–178 (2007).
9. C. P. Brangwynne, G. H. Koenderink, F. C. MacKintosh, D. A. Weitz, *J. Cell Biol.* **183**, 583–587 (2008).
10. D. Mizuno, C. Tardin, C. F. Schmidt, F. C. Mackintosh, *Science* **315**, 370–373 (2007).
11. F. C. MacKintosh, A. J. Levine, *Phys. Rev. Lett.* **100**, 018104 (2008).
12. W. J. Greenleaf, M. T. Woodside, S. M. Block, *Annu. Rev. Biophys. Biomol. Struct.* **36**, 171–190 (2007).

13. C. Leduc, F. Ruhnow, J. Howard, S. Diez, *Proc. Natl. Acad. Sci. U.S.A.* **104**, 10847–10852 (2007).
14. K. J. Verhey, N. Kaul, V. Soppina, *Annu. Rev. Biophys.* **40**, 267–288 (2011).
15. H. Kim, T. Ha, *Rep. Prog. Phys.* **76**, 016601 (2013).
16. B. Huang, H. Babcock, X. Zhuang, *Cell* **143**, 1047–1058 (2010).
17. N. Fakhri, D. A. Tsyboulski, L. Cognet, R. B. Weisman, M. Pasquali, *Proc. Natl. Acad. Sci. U.S.A.* **106**, 14219–14223 (2009).
18. S. M. Bachilo *et al.*, *Science* **298**, 2361–2366 (2002).
19. D. A. Tsyboulski, S. M. Bachilo, R. B. Weisman, *Nano Lett.* **5**, 975–979 (2005).
20. R. B. Weisman, *Anal. Bioanal. Chem.* **396**, 1015–1023 (2010).
21. N. Fakhri, F. C. MacKintosh, B. Lounis, L. Cognet, M. Pasquali, *Science* **330**, 1804–1807 (2010).
22. S. Berciaud, L. Cognet, B. Lounis, *Phys. Rev. Lett.* **101**, 077402 (2008).
23. N. Hirokawa, Y. Noda, Y. Tanaka, S. Niwa, *Nat. Rev. Mol. Cell Biol.* **10**, 682–696 (2009).
24. G. V. Los *et al.*, *ACS Chem. Biol.* **3**, 373–382 (2008).
25. C. P. Brangwynne, G. H. Koenderink, F. C. Mackintosh, D. A. Weitz, *Phys. Rev. Lett.* **100**, 118104 (2008).
26. I. M. Kulic *et al.*, *Proc. Natl. Acad. Sci. U.S.A.* **105**, 10011–10016 (2008).
27. K. Jaqaman *et al.*, *Nat. Methods* **5**, 695–702 (2008).
28. D. Cai, D. P. McEwen, J. R. Martens, E. Meyhofer, K. J. Verhey, *PLOS Biol.* **7**, e1000216 (2009).
29. S. Courty, C. Luccardini, Y. Bellaiche, G. Cappello, M. Dahan, *Nano Lett.* **6**, 1491–1495 (2006).
30. S. Dunn *et al.*, *J. Cell Sci.* **121**, 1085–1095 (2008).
31. Š. Bálint, I. Verdeny Vilanova, Á. Sandoval Álvarez, M. Lakadamyali, *Proc. Natl. Acad. Sci. U.S.A.* **110**, 3375–3380 (2013).
32. C. P. Brangwynne *et al.*, *J. Cell Biol.* **173**, 733–741 (2006).
33. M. Rubinstein, R. Colby, *Polymer Physics (Chemistry)* (Oxford Univ. Press, New York, 2003).
34. B. Fabry *et al.*, *Phys. Rev. Lett.* **87**, 148102 (2001).
35. A. W. C. Lau, B. D. Hoffman, A. Davies, J. C. Crocker, T. C. Lubensky, *Phys. Rev. Lett.* **91**, 198101 (2003).
36. A. J. Levine, F. C. MacKintosh, *J. Phys. Chem. B* **113**, 3820–3830 (2009).
37. This behavior can be understood as follows: The low-frequency behavior, corresponding to times longer than τ_c, is white noise that is independent of frequency, characteristic of uncorrelated fluctuations. For times shorter than τ_c, by contrast, the binding of myosins, subsequent force generation, and eventual release combine to result in a random walk of the net force due to multiple motors in time, with $\langle \Delta f^2(\tau) \rangle \propto \tau$, the Fourier transform of which is $\langle f^2 \rangle_\omega \propto 1/\omega^2$.
38. B. Ramamurthy, C. M. Yengo, A. F. Straight, T. J. Mitchison, H. L. Sweeney, *Biochemistry* **43**, 14832–14839 (2004).
39. A. F. Straight *et al.*, *Science* **299**, 1743–1747 (2003).
40. M. Kovács, J. Tóth, C. Hetényi, A. Málnási-Csizmadia, J. R. Sellers, *J. Biol. Chem.* **279**, 35557–35563 (2004).

ACKNOWLEDGMENTS

We thank L. Cognet, J. Enderlein, M. Guo, J. Lippincott-Schwartz, and D. A. Weitz for helpful discussions; I. Schaap and M. Platen for atomic force microscopy measurements; and the Kavli Institute for Theoretical Physics (University of California, Santa Barbara) for hospitality and useful discussions. Supported by the Center for Nanoscale Microscopy and Molecular Physiology of the Brain and the Collaborative Research Center SFB 937 (Project A2), both funded by the Deutsche Forschungsgemeinschaft, as well as by the Foundation for Fundamental Research on Matter of the Netherlands Organization for Scientific Research, Welch Foundation grant C-1668, and NSF grant NSF PHY11-25915. N.F. was supported by a Human Frontier Science Program Fellowship. N.F. and C.F.S. are inventors on a provisional U.S. patent application on the method used in the paper, filed by Georg-August-Universität. The single-walled carbon nanotubes are available from M.P. under a material transfer agreement with Rice University.

SUPPLEMENTARY MATERIALS

www.sciencemag.org/content/344/6187/1031/suppl/DC1
Materials and Methods
Figs. S1 to S14
Movies S1 to S4
References (*41*–*45*)

24 December 2013; accepted 2 May 2014
10.1126/science.1250170

STRUCTURAL BIOLOGY

Structures of PI4KIIIβ complexes show simultaneous recruitment of Rab11 and its effectors

John E. Burke,[1]*† Alison J. Inglis,[1] Olga Perisic,[1] Glenn R. Masson,[1] Stephen H. McLaughlin,[1] Florentine Rutaganira,[2] Kevan M. Shokat,[2] Roger L. Williams[1]*

Phosphatidylinositol 4-kinases (PI4Ks) and small guanosine triphosphatases (GTPases) are essential for processes that require expansion and remodeling of phosphatidylinositol 4-phosphate (PI4P)–containing membranes, including cytokinesis, intracellular development of malarial pathogens, and replication of a wide range of RNA viruses. However, the structural basis for coordination of PI4K, GTPases, and their effectors is unknown. Here, we describe structures of PI4Kβ (PI4KIIIβ) bound to the small GTPase Rab11a without and with the Rab11 effector protein FIP3. The Rab11-PI4KIIIβ interface is distinct compared with known structures of Rab complexes and does not involve switch regions used by GTPase effectors. Our data provide a mechanism for how PI4KIIIβ coordinates Rab11 and its effectors on PI4P-enriched membranes and also provide strategies for the design of specific inhibitors that could potentially target plasmodial PI4KIIIβ to combat malaria.

Intracellular compartments are essential to eukaryotic cell biology, and both small guanosine triphosphatases (GTPases) and lipids such as phosphoinositides are key components of compartment identity (*1*, *2*). The phosphatidylinositol 4-kinases (PI4Ks) and the small G-protein Rab11 play prominent roles in compartment identity. PI4KIIIβ is one of four mammalian PI4K enzymes that phosphorylate phosphatidylinositol to generate phosphatidylinositol 4-phosphate (PI4P). PI4KIIIβ localizes primarily at the Golgi and is essential for Golgi formation and function (*3*–*5*). PI4P is recognized by protein modules, including the PH domains of oxysterol-binding protein, ceramide transfer protein, and four-phosphate-adaptor protein, that are important for intra-Golgi transport (*6*–*8*). However, typically, lipid recognition alone is not sufficient for Golgi localization, which requires both PI4P and specific small GTPases. In addition to its catalytic role in synthesizing PI4P, PI4KIIIβ also has noncatalytic roles that rely on the interactions with other proteins such as the small GTPase Rab11 (*9*). Rab11 is predominately located on recycling endosomes (*10*). However, Rab11 is also found associated with Golgi membranes, which requires an interaction with PI4KIIIβ (*9*).

PI4KIIIβ activity is essential for replication of a range of RNA viruses, including enteroviruses, SARS coronavirus, and hepatitis C virus (*11*, *12*). These RNA viruses hijack the activity of host cell PI4KIIIβ to generate replication organelles enriched in PI4P. There is no approved antiviral therapy for enteroviruses. However, several compounds inhibit enteroviral replication by targeting cellular PI4KIIIβ (*13*, *14*). PI4KIIIβ is also important in malaria, and inhibitors of *Plasmodium falciparum* PI4KIIIβ are potent antimalarial agents. However, mutations in both PI4KIIIβ and Rab11 confer resistance to these compounds (*15*). Inhibition of *P. falciparum* PI4KIIIβ prevents the membrane ingression that occurs during completion of the asexual erythrocytic stage of the plasmodial life cycle. The role of *Plasmodium* Rab11 and PI4KIIIβ in membrane remodeling is similar to the role of Rab11 and PI4KIIIβ in cytokinesis in *Drosophila* spermatocytes (*16*). In *Drosophila*, PI4KIIIβ is required for the recruitment of both Rab11 and its downstream effectors.

To understand how PI4KIIIβ can both recruit Rab11 and enable its interactions with Rab11 effectors, we used hydrogen-deuterium exchange mass spectrometry (HDX-MS) to facilitate the x-ray crystal structure of human PI4KIIIβ in complex with Rab11a–GTPγS [GTPγS, guanosine 5′-*O*-(3′-thiotriphosphate)] at 2.9 Å resolution (see supplementary materials and methods). To form crystals, highly flexible regions of PI4KIIIβ identified by HDX-MS were truncated (residues 1 to 120, 408 to 507, and 785 to 801) (Fig. 1A). This included a C-terminal region necessary for catalytic activity (fig. S2A). The PI4KIIIβ structure consists of two domains, a right-handed helical solenoid (residues 128 to 243) and a kinase domain (residues 306 to 801) (Fig. 1B), that are related to the PI3Ks (fig. S3). The kinase domain has two lobes, an N-terminal lobe dominated by a five-stranded antiparallel β sheet and a C-terminal lobe that is largely helical, with the adenosine triphosphate (ATP)–binding site located in a cleft between the lobes. The N lobe of PI4KIIIβ has a PI4KIIIβ-distinct, large insertion (residues 391 to 539) (Fig. 1B).

[1]Medical Research Council (MRC) Laboratory of Molecular Biology, Cambridge CB2 0QH, UK. [2]Howard Hughes Medical Institute and Department of Cellular and Molecular Pharmacology, University of California, San Francisco (UCSF), San Francisco, CA 94158, USA.
***Corresponding author. E-mail: jeburke@uvic.ca (J.E.B.); rlw@mrc-lmb.cam.ac.uk (R.L.W.)** †Present address: Department of Biochemistry and Microbiology, University of Victoria, Victoria, British Columbia, Canada.

PI4KIIIβ makes a distinct interaction with Rab11a that is not characteristic of any Rab or Arf effector (*17*). This interaction involves primarily helix α3 of the PI4KIIIβ helical domain (Figs. 1B and 2A). Because a previous study of human PI4KIIIβ mapped the epitope interacting with Rab11a to the insertion in the N lobe of the kinase domain (*9*), we also used HDX-MS to determine the Rab11 binding site on full-length PI4KIIIβ in solution (figs. S4 and S5). The HDX-MS measurements confirmed the interaction between the N-terminal part of the PI4KIIIβ helical domain and Rab11a (fig. S5). Soluble Rab11 had no effect on PI4KIIIβ activity (fig. S2B).

The PI4KIIIβ-Rab11 interface is predominantly hydrophobic, with no hydrogen bonds or salt links (Fig. 2A). Surprisingly, PI4KIIIβ makes only a single, peripheral contact with the Rab11 switch I (only with the edge residues 38-LES-40 of switch I) and no contact with switch II (Fig. 2, A and B). The switch regions change conformation depending on whether Rab11 is bound to GTP or guanosine diphosphate (GDP). Consistent with the structure, PI4KIIIβ bound both GTP- and GDP-loaded Rab11, with a slight preference for GTP (Fig. 2D and fig. S6). Within the PI4KIIIβ-Rab11 interface, G155 (*18*) of PI4KIIIβ makes a direct contact with the ribose moiety of GTPγS bound to the Rab11 (Fig. 2A). The small residue at position 155 is completely conserved among PI4KIIIβ homologs, from yeast to mammals, and might be required to maintain the contact with Rab11. Indeed, a PI4KIIIβ-G155D mutation (where G155D denotes Gly^{155}→Asp^{155}) decreased binding to Rab11 (Fig. 2, C and D). Consistent with PI4KIIIβ directly contacting the nucleotide, PI4KIIIβ decreased the rate of EDTA-mediated Rab11 nucleotide exchange (fig. S2C). PI4KIIIβ residues Y159, N162, and F165 also form prominent contacts with the Rab11. The mutants PI4KIIIβ-Y159A, N162A, and F165A and the double mutant Y159A/N162A all eliminated measurable binding to Rab11 (Fig. 2, C and D). The Rab11 residues interacting with PI4KIIIβ are all conserved among Rab11a and Rab11b, but not among other Rabs that do not bind PI4KIIIβ (Fig. 2B). The PI4KIIIβ residues interacting with Rab11 are also strongly conserved among PI4KIIIβ orthologs (Fig. 2B and fig. S3).

The structure of the PI4KIIIβ-Rab11a complex shows that the Rab11a switch regions remained available to contact Rab11a effectors. Among the Rab11 effectors is a family of related proteins known as the Rab11 family-interacting proteins, or FIPs (*19*). In *Drosophila*, both catalytic and noncatalytic functions of Four wheel drive (PI4KIIIβ ortholog in *Drosophila*) are required for the proper localization of both Rab11a and its downstream effector Nuf (ortholog of human FIP3) at the cleavage furrow, which is essential for cytokinesis in spermatocytes (*16*). During interphase, FIP3 is required for the structural integrity of the pericentriolar recycling endosome compartment (*20*), whereas during cytokinesis, it is involved in delivering material from recycling endosomes to the cleavage furrow (*21*). The FIP proteins interact with Rab11 using a conserved C-terminal region known as the Rab-binding domain (RBD). Two FIPs form a parallel coiled-coil dimer with two Rab11 binding sites (*22*–*24*) that engage both switch I and switch II of Rab11.

The structure of Rab11a bound to the RBD domain of FIP3 (*22*–*24*) and our structure of the PI4KIIIβ-Rab11a complex suggest that a ternary complex might be formed. Glutathione *S*-transferase (GST) pulldowns carried out with the GST-tagged RBD domain from FIP3 (residues 713 to 756) revealed that the complex of the FIP3-RBD with GTPγS-loaded Rab11a (Q70L) was able to bind PI4KIIIβ (Fig. 3A). To understand how this occurs, we crystallized a ternary PI4KIIIβ/Rab11a/FIP3-RBD complex. Although this is a low-resolution (6 Å) structure with a very large asymmetric unit (~1 MD, containing 12 ternary complexes), both FIP3 and PI4KIIIβ were bound simultaneously to Rab11a–GTPγS (Fig. 3B and fig. S7). The ability of PI4KIIIβ to recruit both Rab11a and its downstream effectors is unlikely to be limited to only the FIP family of proteins. The production of PI4P by Pik1, the yeast ortholog of PI4KIIIβ, is required for the Ypt32 (yeast ortholog of Rab11)–dependent recruitment of the Rab guanine nucleotide exchange factor Sec2p (*25*), in a phosphoinositide-dependent regulation of Rab activation cascade. The conservation of the PI4KIIIβ-Rab11a interface in Pik1 and Ypt32 indicates the possibility of a ternary Pik1-Ypt32-Sec2 complex. Furthermore, the switch-independent interaction of PI4KIIIβ with Rab11 suggests that ternary PI4KIIIβ/Rab11/RabGAP and PI4KIIIβ/Rab11/Rab Escort complexes could also be formed (fig. S8).

The inhibitor PIK93 shows a clear selectivity for PI4KIIIβ over PI4KIIIα, with partial selectivity over PI3Ks (*26*). This inhibitor has been used to decipher PI4K-specific functions (*27*), for example, in demonstrating the role of PI4KIIIβ in viral replication (*11*). PIK93 bound in the ATP-binding pocket, using its thiazol and acetamide moieties to make a pair of hydrogen bonds with the backbone of V598 in the hinge between the N and C lobes (Fig. 4A and fig. S9A). The PI4KIIIβ ATP-binding pocket and those of PI3Ks and

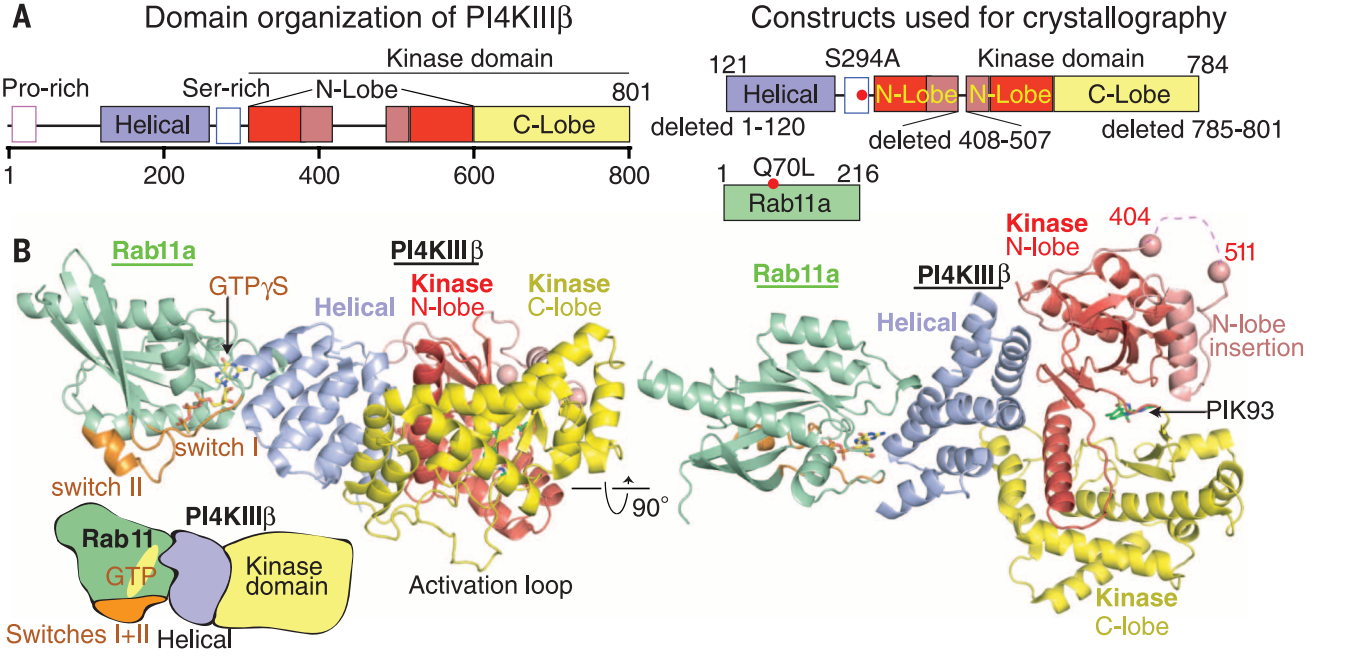


Fig. 1. Crystal structure of the human PI4KIIIβ complex with Rab11a (Q70L)–GTPγS. (**A**) Full-length PI4KIIIβ (isoform 2) (left) and constructs of PI4KIIIβ and Rab11a (Q70L) used for crystallization (right). The PI4KIIIβ crystallization construct contained three deletions, as well as an S294A mutation. (**B**) Overall architecture of the complex. The PI4K-specific insertion (residues 391 to 540) in the N lobe is salmon colored. The large spheres mark a disordered region within which residues 408 to 507 are deleted. The switch I and switch II regions of Rab11a (Q70L) are represented in orange.

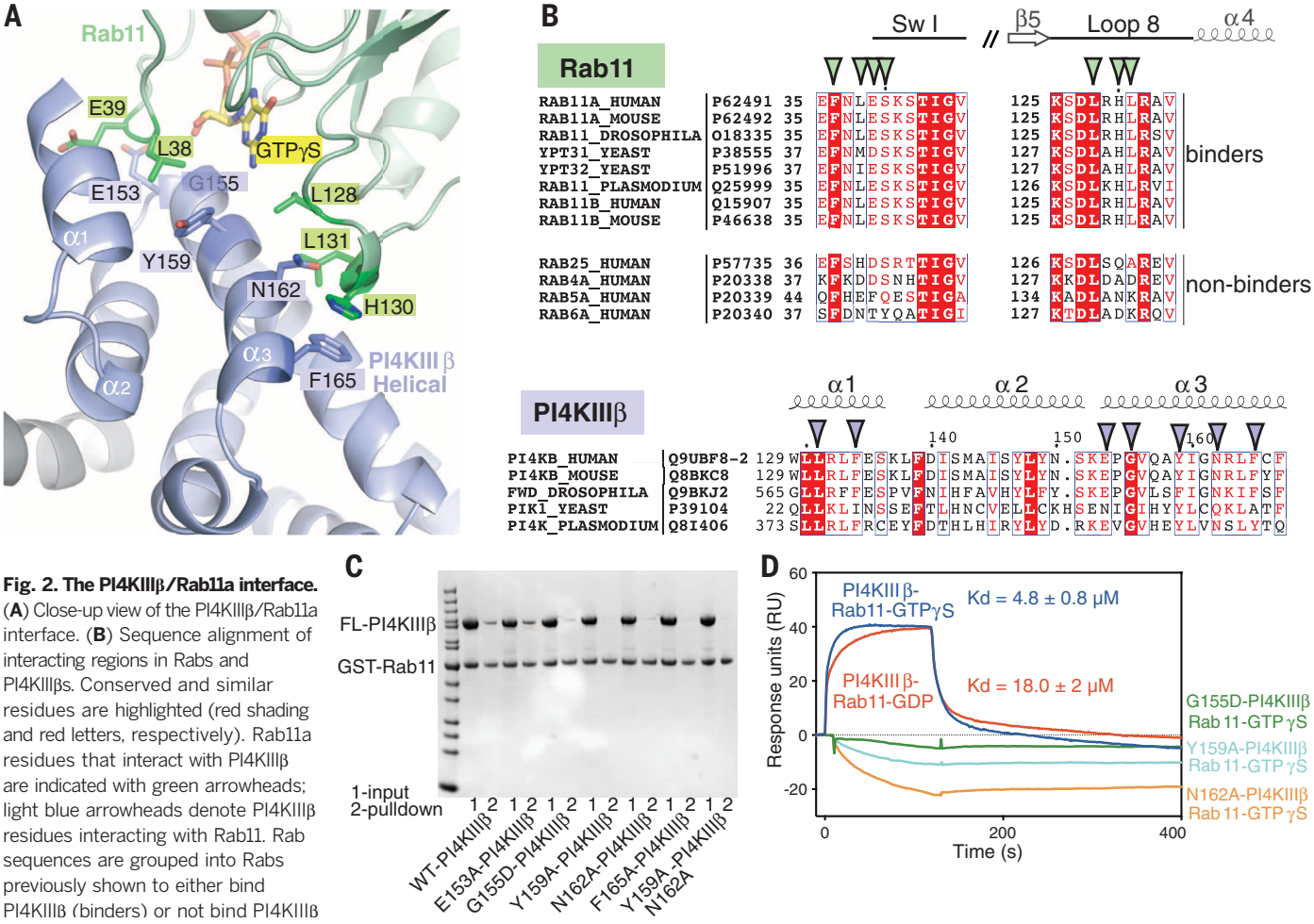


Fig. 2. The PI4KIIIβ/Rab11a interface. (**A**) Close-up view of the PI4KIIIβ/Rab11a interface. (**B**) Sequence alignment of interacting regions in Rabs and PI4KIIIβs. Conserved and similar residues are highlighted (red shading and red letters, respectively). Rab11a residues that interact with PI4KIIIβ are indicated with green arrowheads; light blue arrowheads denote PI4KIIIβ residues interacting with Rab11. Rab sequences are grouped into Rabs previously shown to either bind PI4KIIIβ (binders) or not bind PI4KIIIβ (nonbinders). (**C**) Pull-down assays with GST-tagged Rab11A (Q70L)–GTPγS and either wild-type or mutant full-length PI4KIIIβ. The inputs and the bound proteins (lanes 1 and 2, respectively) were analyzed on SDS gels stained with InstantBlue. (**D**) Surface plasmon resonance (SPR) analysis of the full-length wild-type PI4KIIIβ binding to the immobilized GST-tagged Rab11a (Q70L) loaded with either GDP (red sensogram) or GTPγS (blue). The affinity of PI4KIIIβ for GST-Rab11a is indicated next to the graphs (data are mean ± SEM based on five independent experiments). Full details are shown in fig. S6. Also shown are the sensograms for several PI4KIIIβ mutants binding to Rab11a (Q70L)–GTPγS.

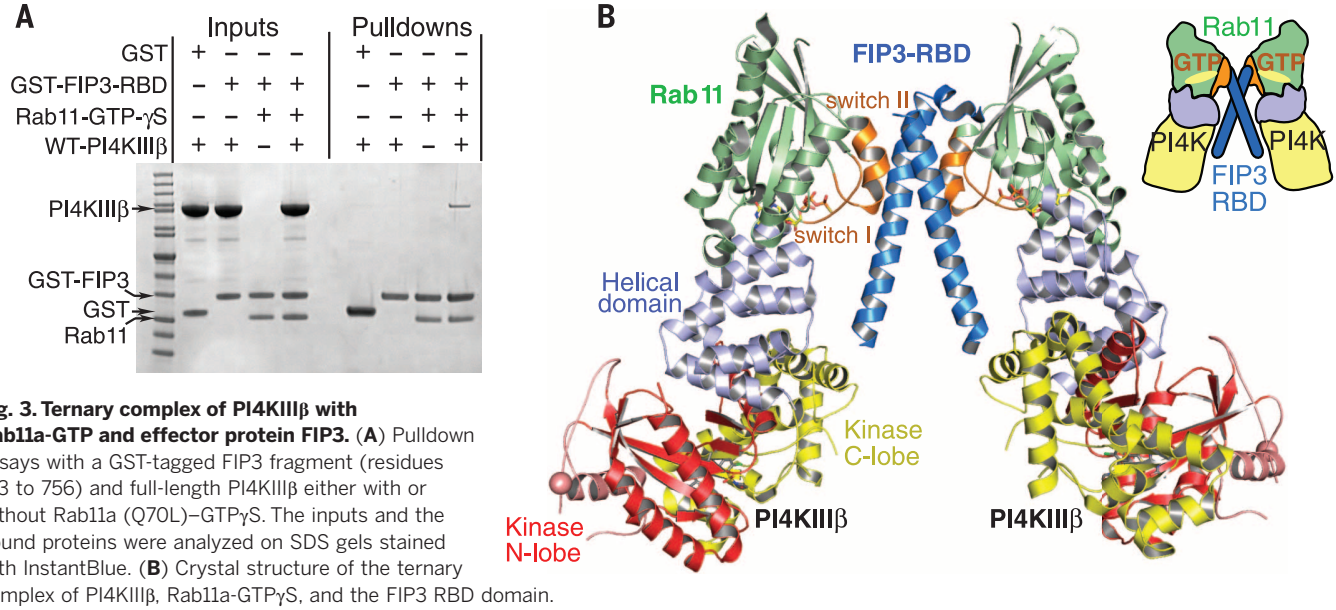


Fig. 3. Ternary complex of PI4KIIIβ with Rab11a-GTP and effector protein FIP3. (**A**) Pulldown assays with a GST-tagged FIP3 fragment (residues 713 to 756) and full-length PI4KIIIβ either with or without Rab11a (Q70L)–GTPγS. The inputs and the bound proteins were analyzed on SDS gels stained with InstantBlue. (**B**) Crystal structure of the ternary complex of PI4KIIIβ, Rab11a-GTPγS, and the FIP3 RBD domain.

phosphatidylinositol 3-kinase–related kinases show considerable consistency. Most of the contacts that PIK93 makes with PI4KIIIβ involve residues that are conserved among both the PI3Ks and PI4Ks (Fig. 4, A and C). The PIK93 sulfamoyl moiety makes a hydrogen bond with K549 of PI4KIIIβ. Although this lysine is conserved in the PI3Ks, its conformation is variable, and in the structures of PIK93 in complex with either p110γ (*26*) or Vps34 (*28*), the equivalent lysine does not make this hydrogen bond (fig. S9B). There is more sequence divergence in the residues near the hinge. Though the class III PI3K Vps34 is more closely related to PI4KIIIβ than other PI3Ks, PIK93 is a poor inhibitor of Vps34. The PI4KIIIβ has a great deal of space near the hinge that allows PIK93 to form hydrogen bonds with the hinge and simultaneously optimize contacts elsewhere (fig. S9B). Y583 packs against the hinge to form one wall of the pocket contacting both the Cl substituent of the thiazole and the phenyl moiety. The structure helps rationalize why a Y583M mutation makes PI4KIIIβ insensitive to wortmannin and PIK93 (*29*) (fig. S9C).

Inhibitors specific against plasmodial PI4KIIIβ are potent antimalarial agents, and resistance mutations in either Rab11a or PI4KIIIβ can evade the antimalarial activity of these compounds (*15*). The plasmodial Y1356F resistance mutation involves the hinge residue, which is equivalent to human P597. It may be that Y1356 makes an additional interaction with the inhibitor (Fig. 4, B and D). The S1320L resistance mutation corresponds to F561 in human PI4KIIIβ. This residue packs against Y583 (Y1342 in *P. falciparum*), which forms one wall of the inhibitor-binding pocket, and the mutation may alter the conformation of the pocket. The third mutation, H1484Y, is in a bend between kα8 and kα9 and is equivalent to H728 in human PI4KIIIβ. Several somatic mutations associated with cancer have been detected for human p110α PI3K in the equivalent bend, and the most common of these mutations increases enzymatic activity and membrane binding (*30*). It is plausible that the H1484Y resistance mutation is making PI4KIIIβ more active.

The structures of a binary complex of PI4KIIIβ with Rab11a and a ternary complex of PI4KIIIβ with Rab11a and Rab11-effector FIP3 revealed a Rab11 interface that is compatible with the PI4KIIIβ-driven recruitment of Rab11 and its effectors to PI4P-enriched membranes. PI4KIIIβ plays key roles in regulating Rab11a in cytokinesis of spermatocytes, recruitment of Rab guanine nucleotide exchange factors in yeast, and membrane remodeling in *Plasmodium* development. The PI4KIIIβ-Rab11 interface is conserved and demonstrates that PI4K, in addition to its kinase activity, plays key kinase-independent roles in mediating these membrane-trafficking events. This structure opens up exciting prospects for the development of highly specific inhibitors, which may act as potent antimalarial and antiviral therapeutics.

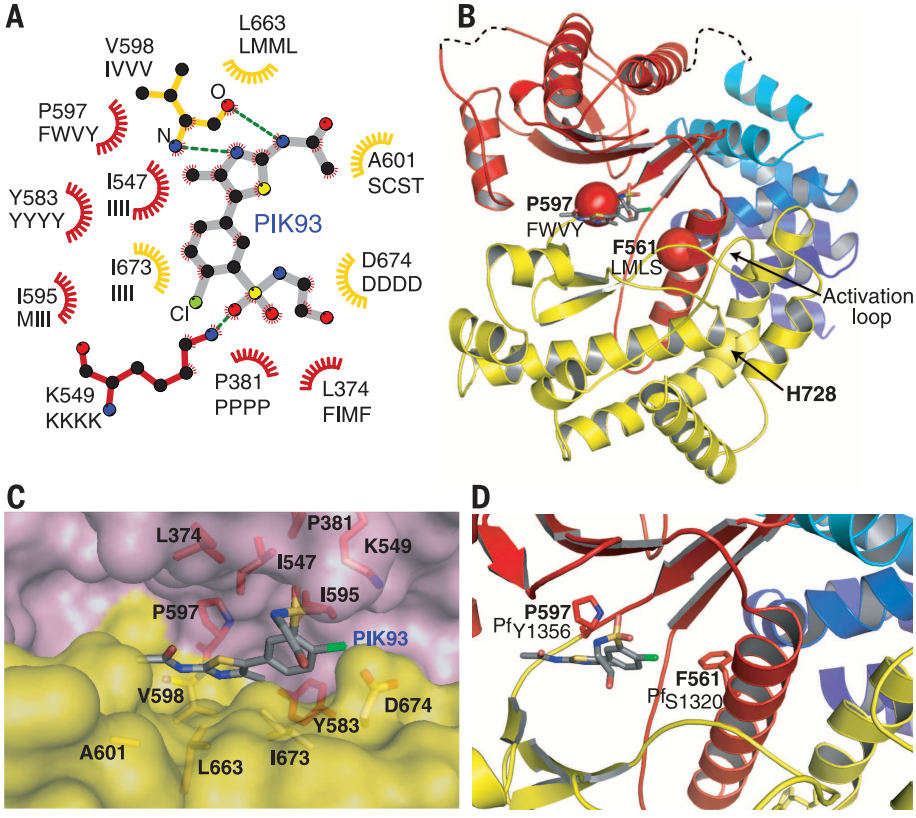


Fig. 4. Inhibitor binding to PI4KIIIβ. (**A**) Interactions of PI4KIIIβ with PIK93. Dotted lines represent putative hydrogen bonds [prepared by LIGPLOT (*31*)]. For each PI4KIIIβ residue, the equivalent residues are shown below for human Vps34, human mTOR, human p110α, and *P. falciparum* PI4KIIIβ (left to right). (**B**) Ribbon diagram of PI4KIIIβ, illustrating sites of *P. falciparum* resistance mutations (spheres). The helical domain is colored from dark to light blue from N terminus to the C terminus. (**C**) PIK93 bound to PI4KIIIβ. (**D**) Close-up of the active site, illustrating positions of *P. falciparum* resistance mutations.

REFERENCES AND NOTES

1. S. Jean, A. A. Kiger, *Nat. Rev. Mol. Cell Biol.* **13**, 463–470 (2012).
2. F. H. Santiago-Tirado, A. Bretscher, *Trends Cell Biol.* **21**, 515–525 (2011).
3. A. Godi *et al.*, *Nat. Cell Biol.* **1**, 280–287 (1999).
4. A. Audhya, M. Foti, S. D. Emr, *Mol. Biol. Cell* **11**, 2673–2689 (2000).
5. V. A. Sciorra *et al.*, *Mol. Biol. Cell* **16**, 776–793 (2005).
6. T. P. Levine, S. Munro, *Curr. Biol.* **12**, 695–704 (2002).
7. S. Dowler *et al.*, *Biochem. J.* **351**, 19–31 (2000).
8. G. D'Angelo *et al.*, *Nature* **501**, 116–120 (2013).
9. P. de Graaf *et al.*, *Mol. Biol. Cell* **15**, 2038–2047 (2004).
10. O. Ullrich, S. Reinsch, S. Urbé, M. Zerial, R. G. Parton, *J. Cell Biol.* **135**, 913–924 (1996).
11. N.-Y. Hsu *et al.*, *Cell* **141**, 799–811 (2010).
12. N. Altan-Bonnet, T. Balla, *Trends Biochem. Sci.* **37**, 293–302 (2012).
13. H. M. van der Schaar *et al.*, *Antimicrob. Agents Chemother.* **57**, 4971–4981 (2013).
14. M. Arita *et al.*, *J. Virol.* **85**, 2364–2372 (2011).
15. C. W. McNamara *et al.*, *Nature* **504**, 248–253 (2013).
16. G. Polevoy *et al.*, *J. Cell Biol.* **187**, 847–858 (2009).
17. A. R. Khan, J. Ménétrey, *Structure* **21**, 1284–1297 (2013).
18. Single-letter abbreviations for the amino acid residues are as follows: A, Ala; C, Cys; D, Asp; E, Glu; F, Phe; G, Gly; H, His; I, Ile; K, Lys; L, Leu; M, Met; N, Asn; P, Pro; Q, Gln; R, Arg; S, Ser; T, Thr; V, Val; W, Trp; and Y, Tyr.
19. E. E. Kelly, C. P. Horgan, M. W. McCaffrey, *Biochem. Soc. Trans.* **40**, 1360–1367 (2012).
20. C. P. Horgan *et al.*, *Traffic* **8**, 414–430 (2007).
21. G. M. Wilson *et al.*, *Mol. Biol. Cell* **16**, 849–860 (2005).
22. S. Eathiraj, A. Mishra, R. Prekeris, D. G. Lambright, *J. Mol. Biol.* **364**, 121–135 (2006).
23. W. N. Jagoe *et al.*, *Structure* **14**, 1273–1283 (2006).
24. T. Shiba *et al.*, *Proc. Natl. Acad. Sci. U.S.A.* **103**, 15416–15421 (2006).
25. E. Mizuno-Yamasaki, M. Medkova, J. Coleman, P. Novick, *Dev. Cell* **18**, 828–840 (2010).
26. Z. A. Knight *et al.*, *Cell* **125**, 733–747 (2006).
27. B. Tóth *et al.*, *J. Biol. Chem.* **281**, 36369–36377 (2006).
28. S. Miller *et al.*, *Science* **327**, 1638–1642 (2010).
29. A. Balla *et al.*, *Biochemistry* **47**, 1599–1607 (2008).
30. J. E. Burke, O. Perisic, G. R. Masson, O. Vadas, R. L. Williams, *Proc. Natl. Acad. Sci. U.S.A.* **109**, 15259–15264 (2012).
31. R. A. Laskowski, M. B. Swindells, *J. Chem. Inf. Model.* **51**, 2778–2786 (2011).

ACKNOWLEDGMENTS

We thank C. Mueller-Dieckmann and D. De Sanctis at the European Synchrotron Radiation Facility and C. Lobley at Diamond Light Source for assistance with beamlines ID23-EH2, ID29, and I04-1; S. Maslen, M. Skehel, and S. Y. Peak-Chew for help with HDX-MS setup; and M. Yu for help with x-ray data collection. J.E.B. was supported by a grant from the British Heart Foundation (PG11/109/29247) and F. Rutaganira by an NSF predoctoral fellowship. This work was funded by the NIH (RO1AI099245 to K.M.S.) and the UK MRC (MC_U105184308 to R.L.W). K.M.S. has filed for patent protection on PIK93 analogs in the following application between UCSF and Stanford University: PCT/US2012/059023. Coordinates and structure factors have been deposited in the Protein Data Bank with accession numbers 4D0L and 4D0M, for PI4KIIIβ/Rab11a and PI4KIIIβ/Rab11a/FIP3 complexes, respectively. Author contributions: J.E.B., O.P., and R.L.W. initiated the project and designed the experiments; J.E.B., A.J.I., G.R.M., and O.P. performed the experiments; J.E.B. and R.L.W. carried out the structure determination and analysis; S.H.M. performed SPR analysis; F.R. and K.M.S. synthesized PI4K inhibitors; and J.E.B., O.P., and R.L.W. wrote the manuscript.

SUPPLEMENTARY MATERIALS

www.sciencemag.org/content/344/6187/1035/suppl/DC1
Materials and Methods
Figs. S1 to S9
Table S1
References (*32*–*42*)

14 March 2014; accepted 30 April 2014
10.1126/science.1253397

SUBSURFACE MICROBES

Sulfur-mediated electron shuttling during bacterial iron reduction

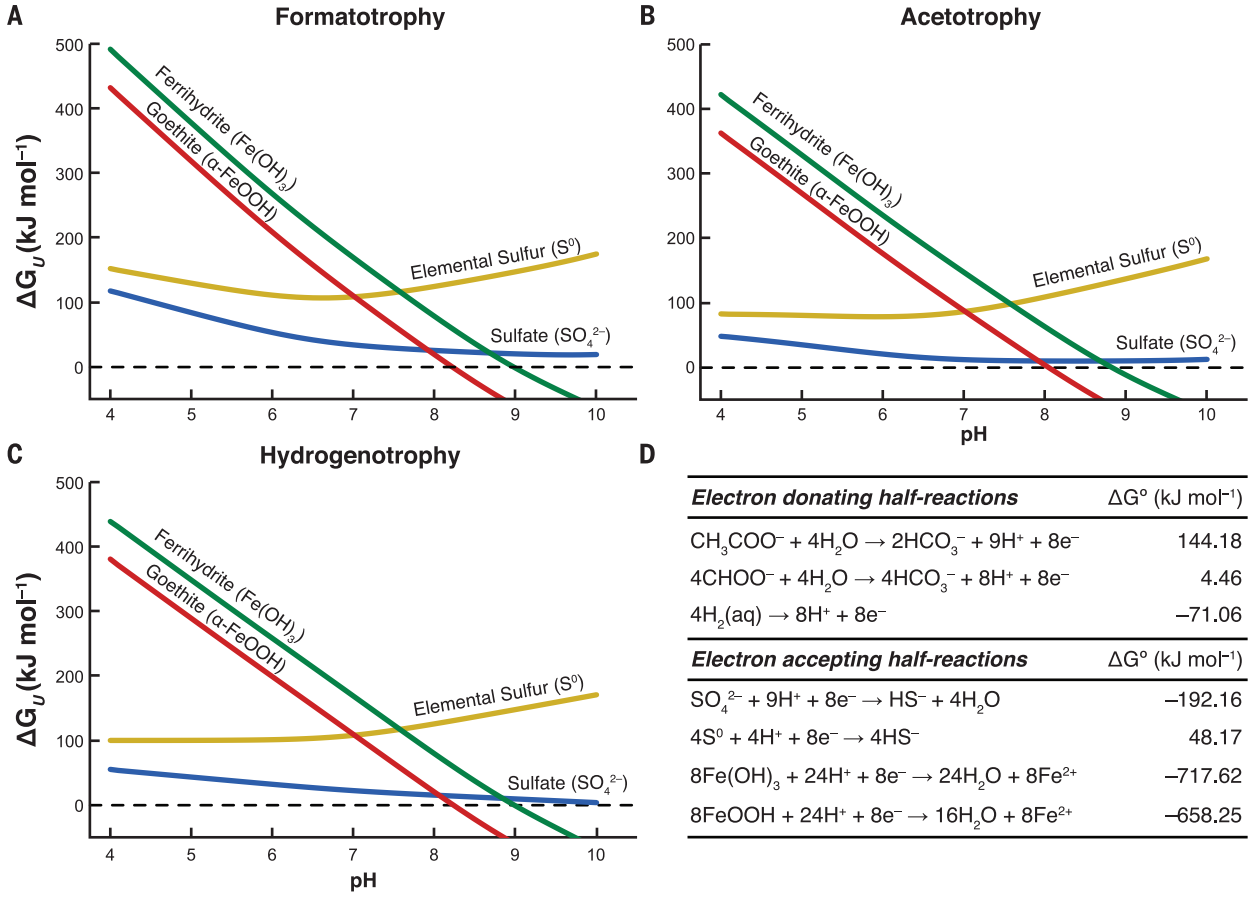
Theodore M. Flynn,[1,2] Edward J. O'Loughlin,[1] Bhoopesh Mishra,[1,3] Thomas J. DiChristina,[4] Kenneth M. Kemner[1]*

Microbial reduction of ferric iron [Fe(III)] is an important biogeochemical process in anoxic aquifers. Depending on groundwater pH, dissimilatory metal-reducing bacteria can also respire alternative electron acceptors to survive, including elemental sulfur (S^0). To understand the interplay of Fe/S cycling under alkaline conditions, we combined thermodynamic geochemical modeling with bioreactor experiments using *Shewanella oneidensis* MR-1. Under these conditions, *S. oneidensis* can enzymatically reduce S^0 but not goethite (α-FeOOH). The HS^- produced subsequently reduces goethite abiotically. Because of the prevalence of alkaline conditions in many aquifers, Fe(III) reduction may thus proceed via S^0-mediated electron-shuttling pathways.

Dissimilatory metal-reducing bacteria (DMRB) are diverse microorganisms that can use insoluble, extracellular substrates as electron acceptors for respiration (*1*, *2*). Although DMRB can reduce a variety of chemical compounds, their ability to reduce ferric iron [Fe(III)] is their most studied trait. Fe(III) is common in the environment as insoluble (oxyhydr)oxide minerals, such as ferrihydrite [$Fe(OH)_3$] or goethite (α-FeOOH). The reductive dissolution of these minerals by DMRB produces highly reactive ferrous ions (Fe^{2+}), making Fe(III) reduction important to water quality (*3*), contaminant fate and transport (*4*), biogeochemical cycling of carbon (*5*), and geochemical evolution of early Earth (*6*).

In addition to Fe(III), many DMRB strains can use elemental sulfur (S^0) as an electron acceptor. The ecological importance of S^0 reduction in aquifers, however, is poorly understood. Although Fe(III) minerals are abundant in these environments, the steady-state concentration of S^0 is frequently below detection (*7*). Nevertheless, S^0 may still serve as a transient but important electron sink (*8*, *9*). S^0 is also abundant in marine sediments where steep redox gradients allow the direct mixing of sulfidic waters with dissolved O_2, but it can be created in anoxic freshwater systems by the reaction of dissolved sulfide with Fe(III) minerals such as goethite (*10*). Many common DMRB in these environments (e.g., several *Shewanella*, *Desulfuromonas*, and *Geobacter* spp.) can respire S^0 directly. Genetic evidence suggests that this ability is derived from an enzymatic mechanism distinct from the pathway

[1]Biosciences Division, Argonne National Laboratory, 9700 South Cass Avenue, Argonne, IL 60439, USA. [2]Computation Institute, University of Chicago, Chicago, IL 60637, USA. [3]Physics Department, Illinois Institute of Technology, Chicago, IL 60616, USA. [4]School of Biology, Georgia Institute of Technology, Atlanta, GA 30332, USA.
*Corresponding author. E-mail: kemner@anl.gov



D

Electron donating half-reactions	ΔG° (kJ mol⁻¹)
$CH_3COO^- + 4H_2O \rightarrow 2HCO_3^- + 9H^+ + 8e^-$	144.18
$4CHOO^- + 4H_2O \rightarrow 4HCO_3^- + 8H^+ + 8e^-$	4.46
$4H_2(aq) \rightarrow 8H^+ + 8e^-$	–71.06
Electron accepting half-reactions	**ΔG° (kJ mol⁻¹)**
$SO_4^{2-} + 9H^+ + 8e^- \rightarrow HS^- + 4H_2O$	–192.16
$4S^0 + 4H^+ + 8e^- \rightarrow 4HS^-$	48.17
$8Fe(OH)_3 + 24H^+ + 8e^- \rightarrow 24H_2O + 8Fe^{2+}$	–717.62
$8FeOOH + 24H^+ + 8e^- \rightarrow 16H_2O + 8Fe^{2+}$	–658.25

Fig. 1. Free energy change of microbial metabolisms in a hypothetical pristine aquifer. The amount of usable energy (ΔG_U) available to microorganisms from the reduction of S^0, Fe(III) minerals (ferrihydrite and goethite), and sulfate with either (**A**) formate, (**B**) acetate, or (**C**) hydrogen as an electron donor changes with pH. The dotted line at ΔG_U = 0 kJ mol^{-1} represents the theoretical minimum energy required to support microbial respiration (*14*). (**D**) Modeled electron-donating and -accepting processes.

used to reduce Fe(III) (*11*) and is therefore unlikely to be simply an incidental consequence of these microorganisms' ability to reduce transition metals. Rather, the common co-occurrence in metal reducers of the ability to reduce Fe(III) and S^0 suggests an evolutionary explanation linked to the ecology of the terrestrial subsurface, where DMRB are frequently abundant (*2*).

Most microorganisms can respire using a variety of substrates, but their ability to use any one respiratory pathway depends on the amount of thermodynamic energy available from that reaction (*12*). The available energy can be calculated directly from the chemical activity of reactants and products in the metabolic reaction being catalyzed (*13*). For example, some metabolic reactions such as Fe(III) reduction are strongly proton-consuming and therefore much less energetically favorable in alkaline environments (*14*). Alkaline aquifers are common and serve as critical water resources—especially in arid regions, where water-rock interactions can drive the pH up to 8 to 10 (*15*). Furthermore, alkaline groundwater is often associated with high levels of arsenic (*16*), a toxic metal whose mobility in groundwater has been tied to the activity of Fe(III) and sulfate-reducing bacteria (SRB) (*17*).

To better understand the biogeochemistry of Fe and S in alkaline environments, we calculated the energy available to microorganisms from the reduction of Fe(III) and S^0 versus sulfate by creating a thermodynamic model of a pristine, anoxic, electron-donor-limited aquifer (table S1). To test the model predictions regarding the effect of pH on the microbial reduction of Fe(III) and S^0, we inoculated pH-buffered suspensions of Fe(III)- and S^0-bearing minerals (goethite and rhombic S^0) with *Shewanella oneidensis* MR-1, a DMRB capable of reducing both. We chose strain MR-1 because a genetic mutant, PSRA1, contains an in-frame deletion of the gene *psrA* and is unable to respire S^0 (*11*). Additional information on methodology is available as supplementary materials.

Our thermodynamic models show that, under these hypothetical groundwater conditions, the reduction of Fe(III)-containing minerals is favored much more strongly at acidic pH than alkaline (Fig. 1). With all three electron donors tested, goethite reduction yields as much energy as sulfate reduction at pH ~ 8 but considerably less than S^0 reduction above pH = 7. The reduction of ferrihydrite provides more energy per mole of substrate than reduction of goethite (table S1), but even this pathway ceases to provide sufficient energy for respiration at roughly pH = 9 for the conditions tested. Although the amount of energy available from these reactions also depends on the concentration of the electron donor being used, the strong correlation of pH with the amount of energy available from reducing Fe(III) minerals shows that these means

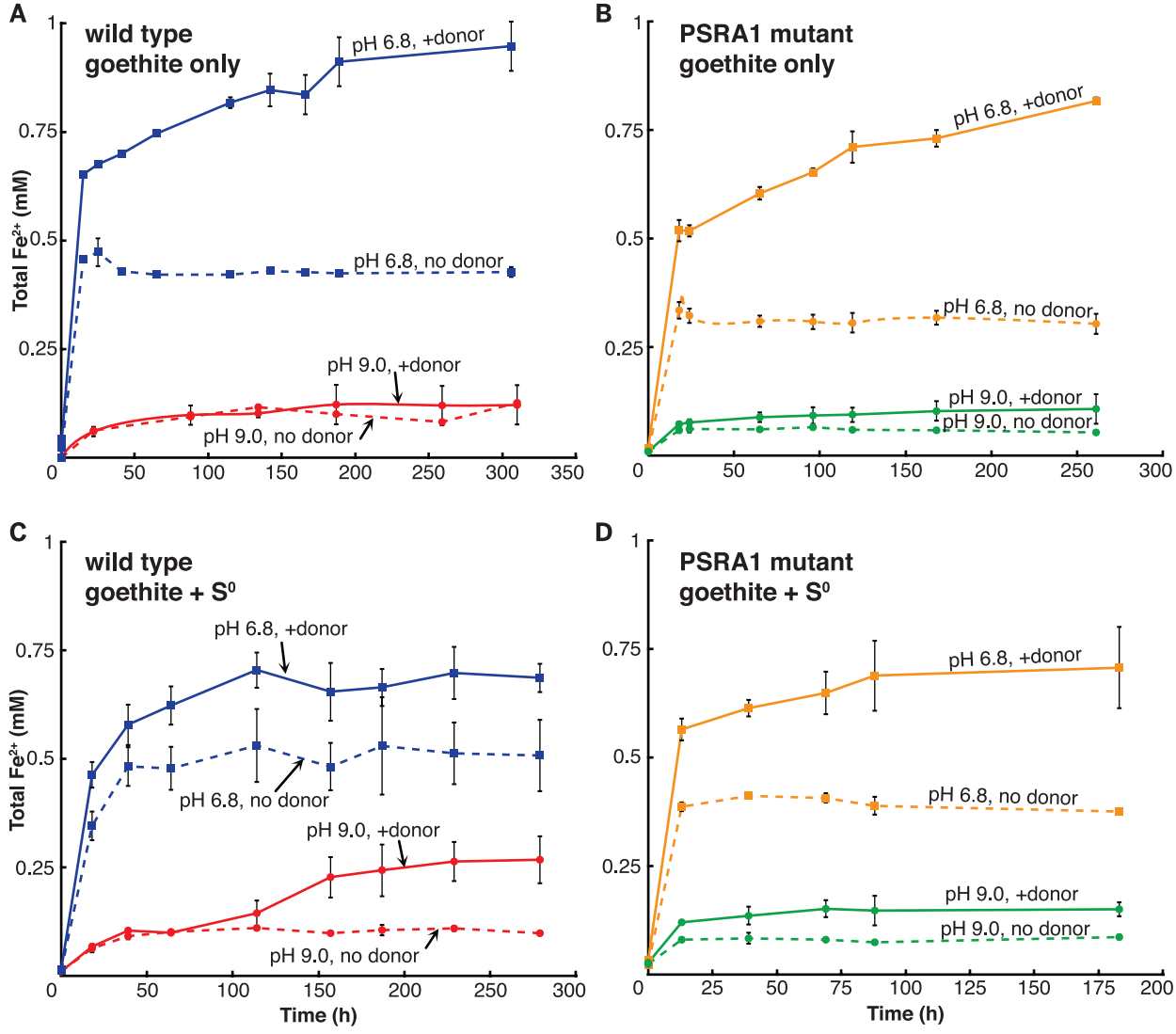


Fig. 2. Total Fe^{2+} production in bioreactor experiments. Experiments were conducted at pH = 6.8 and 9.0 using *S. oneidensis* MR-1 wild type (**A** and **C**) and *psrA*-deficient mutant PSRA1 (**B** and **D**) as an inoculum. Bioreactors contained either 10 mM goethite alone [(A) and (B)] or 10 mM each of goethite and S^0 [(C) and (D)]. Data points represent the average of triplicate bioreactors; error bars, ±SD.

of respiration are likely to be much less favorable at the near-neutral to basic pH of aquifers like the Columbia River Basalt Group (*18*) or the Continental Intercalaire aquifer (*15*). The reduction of S^0, in contrast, is energetically favorable at any pH and becomes more favorable as pH increases.

Under the modeled conditions, the reduction of Fe(III) provides insufficient thermodynamic energy to support the respiration of DMRB at alkaline pH. Still, DMRB might respire and grow under these conditions. Indeed, under laboratory conditions with abundant nutrients and large concentrations of electron donor and acceptor, microbial reduction of Fe(III) has been shown to occur at pH > 11 (*19*) via microorganisms such as *Geoalkalibacter* and *Anaerobranca* (*20*). However, these idealized conditions differ markedly from those found in most aquifers, where concentrations of organic acids such as acetate and formate are typically found in micromolar concentrations or less and the thermodynamic driving force is small (*21*).

In goethite-only bioreactors inoculated with wild-type *S. oneidensis*, considerably more Fe^{2+} was produced at pH = 6.8 than pH = 9.0 (Fig. 2A). We attribute some reduction without added donor to the accumulation of residual reducing power in *S. oneidensis* cells during their initial growth in rich medium (supplementary materials). At pH = 6.8, however, more than twice as much Fe^{2+} was produced when formate was added versus the no-donor control; at pH = 9.0, Fe^{2+} production was the same in control and donor-containing experiments. This result suggests that, under the alkaline conditions tested, no respiratory reduction of goethite coupled to formate oxidation occurred, which is where our model predicts it to be thermodynamically unfavorable (Fig. 1 and fig. S1). As previously reported (*11*), the production of Fe^{2+} via goethite reduction did not differ between the PSRA1 mutant or the wild type (Fig. 2, A and B).

In bioreactors containing both goethite and S^0, the overall production of Fe^{2+} at pH = 6.8 was nearly equivalent to that of goethite-only experiments at pH = 6.8 for both wild type and PSRA1 (Fig. 2, C and D). At pH = 9.0, however, the wild type produced nearly three times more Fe^{2+} when given formate compared with no-donor controls (Fig. 2C). The rate at which Fe^{2+} accumulated was slower at pH = 9.0 than 6.8, which is likely due to the slower reaction kinetics between sulfide and goethite at alkaline pH (*22*). In contrast, the amount of Fe^{2+} produced by PSRA1 at pH = 9.0 differs little with or without S^0 (Fig. 2, B and D). Synchrotron-based measurement of sulfur speciation by x-ray absorption near-edge structure (XANES) spectroscopy confirmed that, at pH = 9.0, S^0 was reduced to sulfide by wild type but not by PSRA1 (Fig. 3), leading to the formation of mackinawite (FeS). Sulfide was detected in S^0-containing bioreactors of both wild-type and PSRA1 cells at pH = 6.8, although for the mutant this likely resulted from the abiotic reaction of Fe^{2+} with S^0 to form mackinawite through a polysulfide intermediate (*23*). Our results indicate that, as predicted by the model (Fig. 1 and fig. S1), under alkaline conditions *S. oneidensis* can enzymatically reduce S^0 but not goethite. The production of Fe^{2+} at pH = 9.0 is instead due to the abiotic reduction of goethite by sulfide produced through the enzymatic reduction of S^0, suggesting that Fe(III) reduction at alkaline pH proceeds via an indirect, sulfur-dependent electron shuttling pathway similar to those known to occur via flavins or humic substances (*20*).

The primary source of dissolved sulfide in the subsurface is microbial sulfate reduction (*24*), a process where the available energy is affected little by changes in pH (Fig. 1). By reducing sulfate to HS^- in the presence of Fe(III) minerals in an alkaline aquifer, the respiration of SRB would create S^0 and allow DMRB like *Shewanella* spp. to respire (Fig. 4). Many studies indicate that Fe(III) reduction and sulfate reduction co-occur frequently in the subsurface (*25*). Therefore, under alkaline conditions DMRB would depend on the activity of SRB to respire in a commensal or even mutualistic relationship (*26*). In addition to modern aquifers, such an interaction could have been important on early Earth, where alkaline conditions are thought to have predominated in large areas of the ocean (*27*), and may have contributed to the formation of sedimentary pyrite during the Archean and early Proterozoic (*28*). The extreme alkalinity of the early oceans (pH > 10) makes the direct enzymatic reduction of Fe(III) even less likely to have been energetically favorable, and dissimilatory iron reduction alone probably would not be responsible for the production of Fe^{2+} there.

This ecological connection explains why many DMRB maintain separate genetic pathways to respire Fe(III) and S^0. In the presence of active sulfate reduction and faced with an inability to respire Fe(III) because of energetic limitations, a microorganism able to respire both S^0 and Fe(III) would have a competitive advantage. For example, the microbial reduction of the Fe(III) minerals ferrihydrite and goethite coupled to formate or acetate oxidation results in substantial increases in pH because of H^+ consumption during the corresponding catabolic reactions (table S1). The ability to transition from enzymatic reduction of Fe(III) minerals at circumneutral pH to a S^0-reducing pathway at alkaline pH, where Fe(III) minerals are thermodynamically unavailable for use as electron acceptors, thus provides DMRB with a mechanism to sustain energy-generating electron transport processes over a much wider pH range than direct enzymatic Fe(III) reduction alone. Furthermore, at alkaline pH, Fe^{2+} ions are thought to adsorb more strongly to the surfaces of iron oxides and thereby inhibit direct enzymatic reduction (*29*). Sulfide produced through the reduction of sulfate and S^0 would strip these adsorbed ions away and thereby circumvent the passivation of Fe(III) oxide surfaces, providing further evidence for the importance of sulfate and S^0 reduction for the reduction of Fe(III) oxides in alkaline environments. Because alkaline aquifers are primary targets for carbon capture and sequestration (*30*) and the production of Fe^{2+} via the reductive dissolution of Fe(III) minerals is a critical step in the formation of the mineral siderite, this process may be particularly relevant in the mineralization and retention of carbon in the deep subsurface.

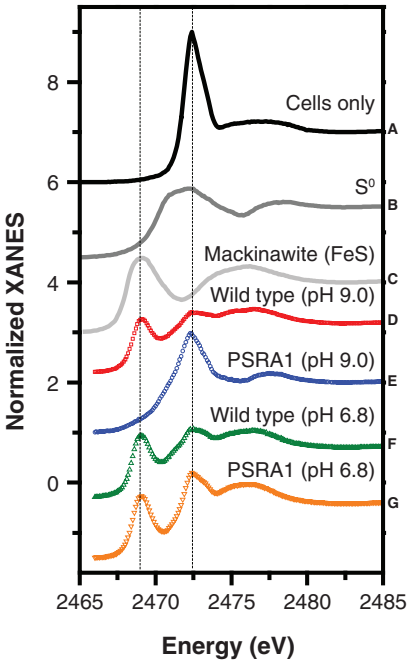


Fig. 3. Sulfur K-edge XANES spectra of S-containing bioreactors. Standards shown are (A) unreacted *S. oneidensis* MR-1 cells, (B) rhombic S^0, and (C) mackinawite (FeS). Samples are shown from bioreactors containing both goethite and S^0 at pH = 9.0 (D and E) or pH = 6.8 (F and G) that were inoculated with cells of either wild type (D and F) or PSRA1 mutant (E and G).

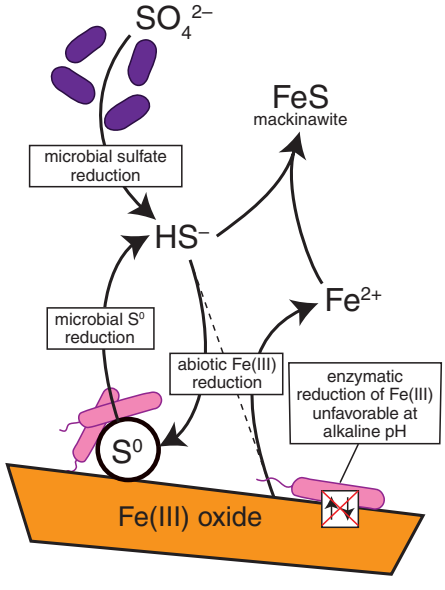


Fig. 4. Illustration of S^0-mediated Fe(III) reduction under alkaline conditions.

REFERENCES AND NOTES

1. K. H. Nealson, A. Belz, B. McKee, *Antonie van Leeuwenhoek* **81**, 215–222 (2002).
2. D. R. Lovley, in *The Prokaryotes*, E. Rosenberg, E. F. DeLong, S. Lory, E. Stackebrandt, F. Thompson, Eds. (Springer, Berlin, 2013), pp. 287–308.
3. M. F. Kirk, L. J. Crossey, C. Takacs-Vesbach, D. L. Newell, R. S. Bowman, *Appl. Geochem.* **24**, 426–437 (2009).
4. T. Borch *et al.*, *Environ. Sci. Technol.* **44**, 15–23 (2010).
5. K. J. Edwards, K. Becker, F. Colwell, *Annu. Rev. Earth Planet. Sci.* **40**, 551–568 (2012).
6. A. Heimann *et al.*, *Earth Planet. Sci. Lett.* **294**, 8–18 (2010).
7. K. H. Nealson, *Annu. Rev. Earth Planet. Sci.* **25**, 403–434 (1997).
8. K. L. Straub, B. Schink, *Appl. Environ. Microbiol.* **70**, 5744–5749 (2004).
9. S. A. Haveman *et al.*, *Appl. Environ. Microbiol.* **74**, 4277–4284 (2008).
10. S. W. Poulton, M. D. Krom, R. Raiswell, *Geochim. Cosmochim. Acta* **68**, 3703–3715 (2004).
11. J. L. Burns, T. J. DiChristina, *Appl. Environ. Microbiol.* **75**, 5209–5217 (2009).
12. Q. Jin, C. M. Bethke, *Am. J. Sci.* **307**, 643–677 (2007).
13. T. M. Hoehler, B. B. Jørgensen, *Nat. Rev. Microbiol.* **11**, 83–94 (2013).
14. C. M. Bethke, R. A. Sanford, M. F. Kirk, Q. Jin, T. M. Flynn, *Am. J. Sci.* **311**, 183–210 (2011).
15. J. N. Andrews *et al.*, *Water Resour. Res.* **30**, 45–61 (1994).
16. A. H. Welch, D. B. Westjohn, D. R. Helsel, R. B. Wanty, *Ground Water* **38**, 589–604 (2000).
17. M. F. Kirk *et al.*, *Geology* **32**, 953 (2004).
18. B. P. McGrail *et al.*, *J. Geophys. Res. Solid Earth* **111**, B12201 (2006).
19. A. J. Williamson *et al.*, *Appl. Environ. Microbiol.* **79**, 3320–3326 (2013).
20. S. J. Fuller *et al.*, *Appl. Environ. Microbiol.* **80**, 128–137 (2014).
21. P. B. McMahon, F. H. Chapelle, *Nature* **349**, 233–235 (1991).
22. S. W. Poulton, *Chem. Geol.* **202**, 79–94 (2003).
23. K. Hellige, K. Pollok, P. Larese-Casanova, T. Behrends, S. Peiffer, *Geochim. Cosmochim. Acta* **81**, 69–81 (2012).
24. M. Ledin, K. Pedersen, *Earth Sci. Rev.* **41**, 67–108 (1996).
25. R. Jakobsen, D. Postma, *Geochim. Cosmochim. Acta* **63**, 137–151 (1999).
26. T. M. Flynn *et al.*, *BMC Microbiol.* **13**, 146 (2013).
27. S. Kempe, E. T. Degens, *Chem. Geol.* **53**, 95–108 (1985).
28. C. M. Johnson, B. L. Beard, E. E. Roden, *Annu. Rev. Earth Planet. Sci.* **36**, 457–493 (2008).
29. L. Wu, B. L. Beard, E. E. Roden, C. M. Johnson, *Geochim. Cosmochim. Acta* **73**, 5584–5599 (2009).
30. M. J. Bickle, *Nat. Geosci.* **2**, 815–818 (2009).

ACKNOWLEDGMENTS

This research is part of the Subsurface Science Scientific Focus Area at Argonne National Laboratory supported by the Subsurface Biogeochemical Research Program, U.S. Department of Energy (DOE) Office of Science, Office of Biological and Environmental Research, under DOE contract DE-AC02-06CH11357. We appreciate the technical assistance of M. Newville, and A. Lanzirotti. K. Nealson, J. Fredrickson, and K. Haugen provided helpful comments that improved the manuscript. X-ray analyses were conducted at Argonne National Laboratory's Advanced Photon Source (APS), GeoSoilEnviroCARS (Sector 13), supported by NSF–Earth Sciences (EAR-1128799) and DOE–GeoSciences (DE-FG02-94ER14466). Use of the APS was supported by the DOE Office of Science, Office of Basic Energy Sciences. T.F. was supported in part by an Argonne Director's Fellowship and the National Institute of Allergy and Infectious Diseases, NIH, Department of Health and Human Service (contract no. HHSN272200900040C). T.D. was supported by NSF (Molecular and Cellular Biosciences grant no. 1021735). All additional data have been archived in the supplementary materials.

SUPPLEMENTARY MATERIALS

www.sciencemag.org/content/344/6187/1039/suppl/DC1
Materials and Methods
Supplementary Text
Figs. S1 and S2
Tables S1 and S2
References (*31*–*45*)

11 February 2014; accepted 18 April 2014
Published online 1 May 2014;
10.1126/science.1252066

TRANSCRIPTION

A pause sequence enriched at translation start sites drives transcription dynamics in vivo

Matthew H. Larson,[1] Rachel A. Mooney,[2] Jason M. Peters,[3] Tricia Windgassen,[2] Dhananjaya Nayak,[2] Carol A. Gross,[3] Steven M. Block,[4,5] William J. Greenleaf,[6]* Robert Landick,[2,7]* Jonathan S. Weissman[1]*

Transcription by RNA polymerase (RNAP) is interrupted by pauses that play diverse regulatory roles. Although individual pauses have been studied in vitro, the determinants of pauses in vivo and their distribution throughout the bacterial genome remain unknown. Using nascent transcript sequencing, we identified a 16-nucleotide consensus pause sequence in *Escherichia coli* that accounts for known regulatory pause sites as well as ~20,000 new in vivo pause sites. In vitro single-molecule and ensemble analyses demonstrate that these pauses result from RNAP–nucleic acid interactions that inhibit next-nucleotide addition. The consensus sequence also leads to pausing by RNAPs from diverse lineages and is enriched at translation start sites in both *E. coli* and *Bacillus subtilis*. Our results thus reveal a conserved mechanism unifying known and newly identified pause events.

Transcriptional pausing by RNA polymerase (RNAP) is an important feature of gene regulation that facilitates RNA folding (*1*), factor recruitment (*2*), transcription termination (*3*), and synchronization with translation in prokaryotes (*4*, *5*). Previously characterized regulatory pauses (*6*) represent a very small and biased fraction of potential pause sites in the bacterial genome. Furthermore, it remains unknown whether most pauses identified by in vitro studies affect transcription in vivo. To study transcriptional pausing in vivo, we adapted a high-throughput approach to isolate and sequence nascent elongating transcripts (NET-seq) (*7*). *Escherichia coli* nascent transcripts were captured by immunoprecipitating FLAG-tagged RNAP molecules, converted to DNA, and sequenced to a depth of ~30 million reads per sample (figs. S1 to S3 and tables S1 and S2). Each sequencing read was mapped to a single site corresponding to the 3′ end of the nascent transcript (Fig. 1A), allowing us to define RNAP locations along ~2000 genes with single-nucleotide resolution (table S2).

[1]Department of Cellular and Molecular Pharmacology, Howard Hughes Medical Institute, California Institute for Quantitative Biosciences, Center for RNA Systems Biology, University of California, San Francisco, San Francisco, CA 94158, USA. [2]Department of Biochemistry, University of Wisconsin, Madison, WI 53706, USA. [3]Department of Microbiology and Immunology, University of California, San Francisco, San Francisco, CA 94158, USA. [4]Department of Biological Sciences, Stanford University, Stanford, CA 94025, USA. [5]Department of Applied Physics; Stanford University, Stanford, CA 94025, USA. [6]Department of Genetics, Stanford University, Stanford, CA 94025, USA. [7]Department of Bacteriology, University of Wisconsin, Madison, WI 53706, USA.
***Corresponding author. E-mail: wjg@stanford.edu (W.J.G.); landick@biochem.wisc.edu (R.L.); weissman@cmp.ucsf.edu (J.S.W.)**

The number of mapped reads at each genomic position is proportional to the number of RNAP molecules at that position. We observed well-defined single-nucleotide peaks within transcribed regions at known regulatory pause sites, including sites that synchronize transcription with translation, mediate RNA folding, or recruit transcription factors (Fig. 1B and fig. S4, A to E). NET-seq profiles also revealed a large number of other highly reproducible peaks in RNAP density throughout the genome (example gene in Fig. 1C). In total, we identified ~20,000 previously undocumented pause sites across well-transcribed genes, representing an average frequency of 1 per 100 base pairs (bp) (Fig. 1D). Thus, known regulatory pause sites represent a tiny fraction of actual pause positions.

We found that in vivo pause propensity depended strongly on the sequence identity at the 3′ end of the transcript (87% of paused transcripts end with either cytosine or uracil), as well as on the identity of the incoming nucleoside triphosphate (NTP) substrate [70% of pause sites occur before addition of guanosine 5′-triphosphate (GTP)] (Fig. 2A). Sequence dependence extends outside the RNAP active site to 11 nucleotides (nt) upstream and 5 nt downstream of the pause position, consistent with the extent of core nucleic-acid contacts made within the elongation complex (*8*). To determine the contribution of each base to pause duration, we used the density of reads in the NET-seq profile to calculate the relative dwell time of RNAP at each well-transcribed position in the genome. Modeling the addition of the next nucleotide as a process with a single activation barrier, we calculated the effective energetic barrier to nucleotide addition as the logarithm of the RNAP occupancy signal (supplementary materials). We used these values to determine the sequence dependence of this

barrier for all positions within 15 bases of the transcript 3′ end. The resulting plot provides an energetic view of sequence-dependent pausing, in which peaks indicate bases that increase the relative RNAP dwell time (Fig. 2B). These observations implicate a 16-nt consensus pause sequence whose prominent features include GG at the upstream edge of RNA:DNA hybrid and TG or CG at the location of the 3′ end of the nascent transcript and incoming NTP (Fig. 2A).

We used the energetic profile as a metric to determine whether most in vivo pauses could be explained by the consensus pause sequence. The energetics of nucleotide addition (Fig. 2B) allowed us to compute the propensity for pausing at every well-transcribed position by summing the energetic contribution of each base from position −1 to −11. The predicted energies were grouped into two categories: sequences for which pausing was observed, and sequences for which pausing was undetectable. A cumulative histogram of the energetics for the two populations shows that pause-associated sequences were well separated in sequence space from nonpause sequences (Fig. 2C). Using a receiver-operating characteristic analysis, we determined the optimal threshold for distinguishing these two populations (fig. S5) and found that most pause sequences lay above the threshold (Fig. 2C). Furthermore, the same threshold correctly classified the group of "canonical" regulatory pauses previously identified in *E. coli*, suggesting that this seemingly disparate group of pause sequences derive from a single consensus sequence. Intriguingly, the HIV-1 TAR pause element, which affects mammalian RNAPII (*9*), resembles our consensus sequence (Fig. 2C).

To understand the minimal requirements for pausing, we modified a high-resolution optical-trapping technique to measure sequence-resolved nucleotide addition by individual RNAP molecules in vitro (*10*, *11*). By limiting the concentration of GTP, which is the nucleotide most frequently associated with pausing in vivo, its addition became rate limiting for elongation, allowing us to determine the absolute alignment of single-molecule records with the transcribed sequence. In this fashion, we measured the nucleotide addition rate for *E. coli* RNAP at more than 300 unique positions in a segment of the *E. coli rpoB* gene (Fig. 2D). These position-specific rates, which ranged over two to three orders of magnitude, yielded activation-energy barriers well correlated to those computed from NET-seq (Fig. 2, E and F). Moreover, they are qualitatively consistent with an in vitro consensus proposed previously from a small set of pause-inducing elements (*12*). This agreement suggests that interactions of RNAP with the DNA template and nascent transcript are sufficient for pausing in vivo and that these interactions largely dictate genome-wide pause patterns.

To probe individual elements of the consensus pause sequence, we reconstituted transcription complexes on a series of short, artificial nucleic-acid scaffolds. These scaffolds encoded either the consensus pause or an anti-consensus pause, in which the nucleotide at each position from −11 to +5 (excepting the highly conserved −1/+1 active-site positions) was altered to be the nucleotide predicted to cause the shortest dwell time (Fig. 3A). Strong pausing was observed at the expected position on the short consensus scaffold (Fig. 3A), and also on a template with the same consensus sequence embedded in a long DNA template (fig. S6). The consensus pause was roughly five times as long as the *his* pause (τ = 2 s at saturating GTP, Fig. 3B), even though the *his* pause is stabilized by a nascent RNA hairpin. Pausing was undetectable at the equivalent position on the anti-consensus scaffold (Fig. 3A). Thus, sequence elements upstream and downstream of the RNAP active site, although less enriched in our analysis, are essential for generating a pause signal. Consistent with prior proposals that discrete pause elements act together to form a multipartite pause signal (*13*), substitutions that disrupt RNA:DNA base-pairing at the −11 or −10 positions, remove the +1 nontemplate strand base, or alter the downstream DNA at positions +2 to +4 were found to reduce pause strength significantly (Fig. 3C; see fig. S7 for additional analysis of sequence dependence).

RNAP has the ability to "backtrack," shifting the transcript 3′ end downstream from the −1/+1 positions of the active site into the NTP-entry pore. Backtracking is resolved by cleavage of two or more nucleotides from the RNA, generating a

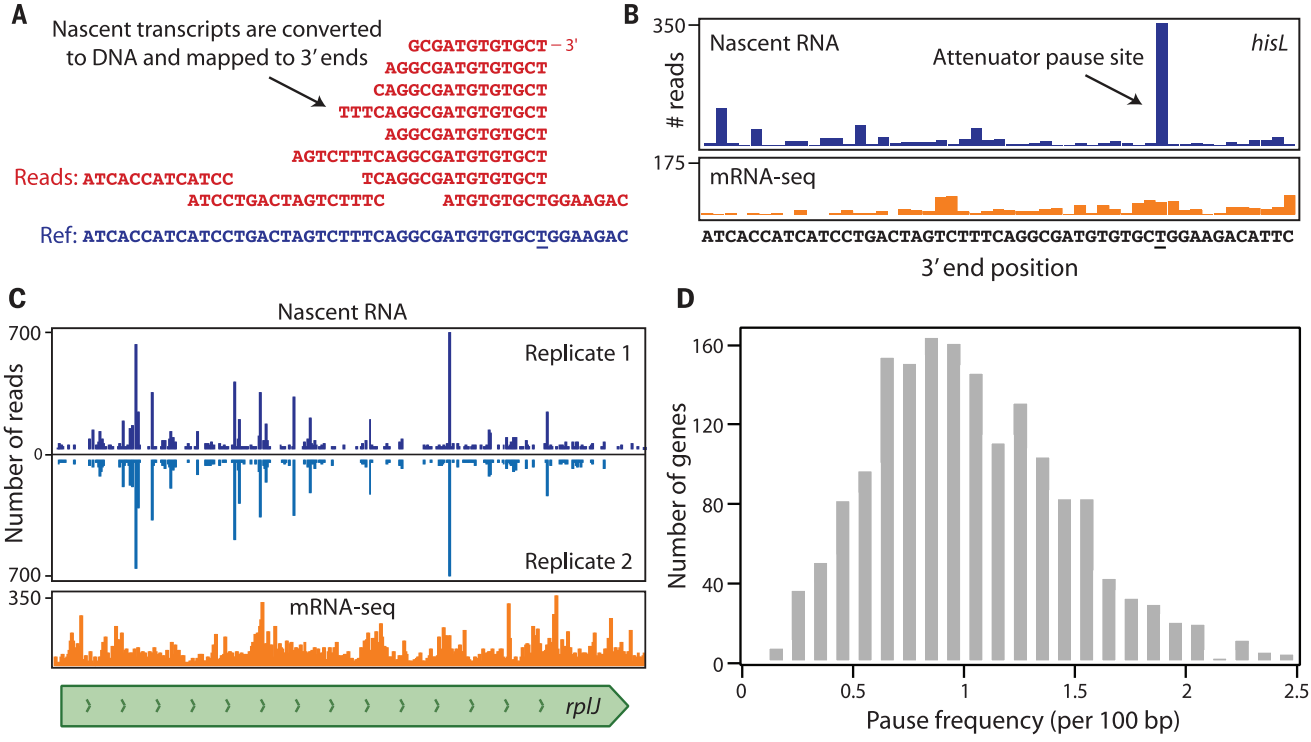


Fig. 1. Bacterial NET-seq provides a genome-wide view of transcription dynamics. (**A**) Nascent RNA is isolated from bacteria and converted to a DNA library sequenced with deep coverage. Reads are aligned to the reference genome and mapped according to their 3′ end, which corresponds to the RNAP active site. (**B**) An example of RNAP density in the *his* leader region (*hisL*) shows a peak at a single site that matches the previously mapped regulatory pause position (underlined). (**C**) Biological replicates along the ribosomal L10 protein subunit (*rplJ*). (**D**) Histogram of pause frequency for highly transcribed genes (n = 1984, gene average >1 read/bp) within the protein-coding sequence.

new 3′ end in the active site. To determine whether RNAP backtracked at the consensus pause, we tested for transcript cleavage at the active site. Pause complexes reconstituted on the consensus scaffold cleaved only a single nucleotide, consistent with no backtracking, clearly different from the 2-nt cleavage observed with complexes prepared with an obligately backtracked scaffold, and also from complexes prepared with an anti-consensus scaffold (Fig. 3D). GreA, a cleavage factor in *E. coli* known to relieve backtracking, stimulated a 2-nt cleavage of the RNA at the consensus pause, but failed to reduce the pause dwell time (Fig. 3C and fig. S8), suggesting that the consensus pause sequence leads to a predominantly pretranslocated register that may be poised to backtrack, but that such backtracking does not principally determine the barrier to pause escape. It is likely that variations of the consensus sequence may lead to pauses that backtrack more readily. The observed pause profiles in vivo were unaffected by the deletion of GreA and GreB (Fig. 3E), suggesting that most transcriptional pauses in *E. coli* lead to an elemental non-backtracked pause state (*12*, *14*).

Pausing at the consensus sequence is conserved across diverse lineages, as demonstrated

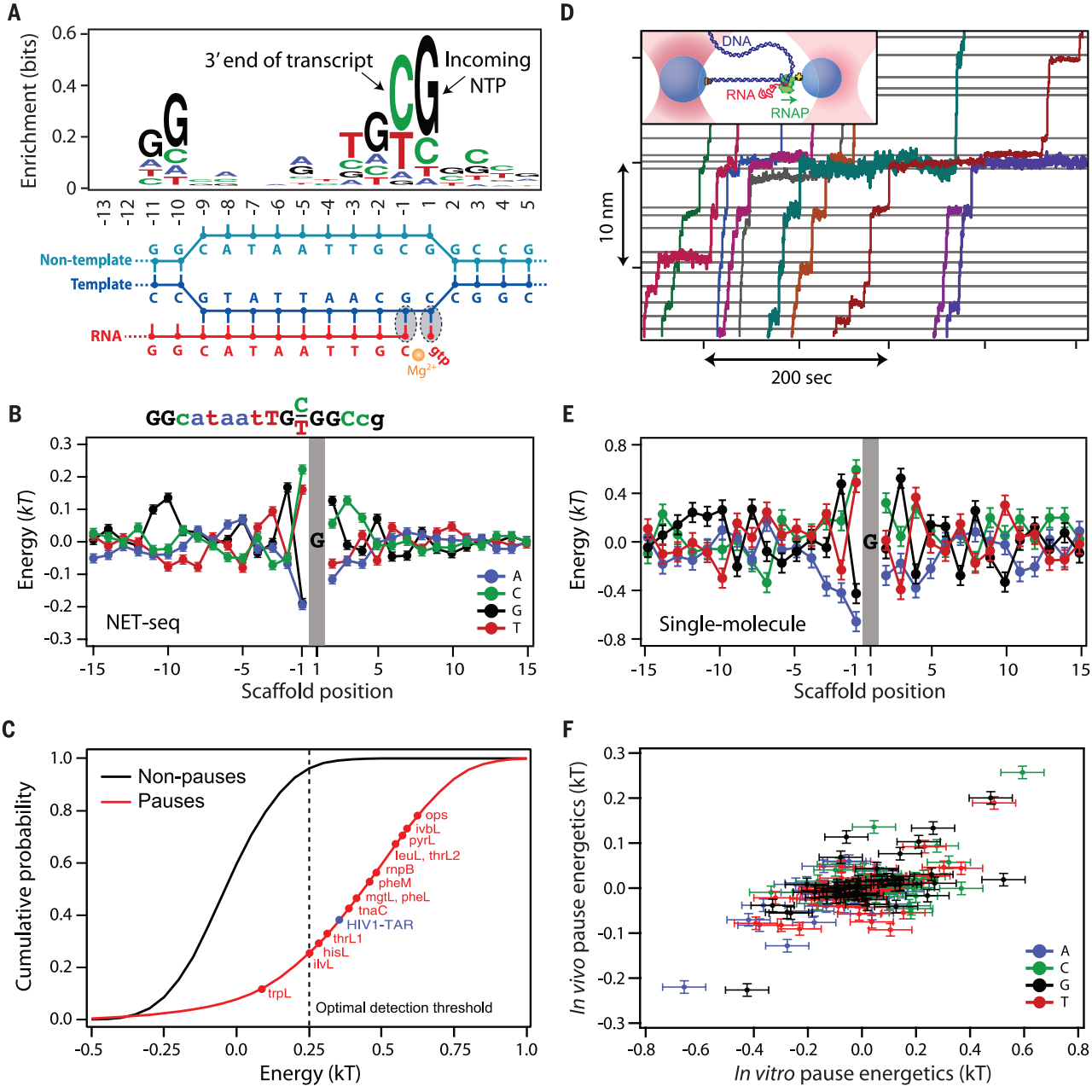


Fig. 2. Transcriptional pauses are driven by RNAP–nucleic acid interactions. (**A**) Sequences corresponding to peaks in RNAP density were aligned at their 3′ end to generate a consensus pause sequence, the length of which matches the size of the transcription bubble (shown below). (**B**) Relative energetic contribution of neighboring bases as they affect in vivo pause dynamics (mean ± SD). The 16-nt consensus pause sequence, represented by peaks in energy, is shown above. (**C**) Cumulative distribution function for the energetics of both pause and nonpause sequences. (**D**) Experimental geometry for the single-molecule pausing assay and representative records of transcription by individual RNAP molecules in GTP-limiting conditions. Long pauses at GTP-coding positions (gray lines) provide register with the template DNA. (**E**) In vitro pause energetics calculated from the single-molecule data (mean ± SD, see supplementary methods for SD estimation). (**F**) In vitro pause energetics are well correlated with in vivo pause energetics determined by NET-seq (Pearson $r = 0.6$, two-tailed $P = 9.8 \times 10^{-17}$). Each point corresponds to a given nucleotide at a specific scaffold position (unlabeled).

in vitro with RNAPs derived from *Rhodobacter sphaeroides* (*Rsp*), *Mycobacteria bovis* (*Mbo*), and *Thermus thermophilus* (*Tth*), which paused on the consensus template, but not on the anti-consensus template (Fig. 3C and figs. S9 and S10). Mammalian RNAPII (*B. taurus*, *Bta*) also responded to the consensus sequence (Fig. 3C), but exhibited a somewhat different pattern, involving pausing at the consensus position and even stronger pausing 1 nt downstream (fig. S11). Addition of the cleavage factor TFIIS converted the downstream pause to a strong pause at the consensus position, suggesting that the consensus pause leads to backtracking by RNAPII. This result is consistent with other evidence indicating a greater proclivity for eukaryotic RNAPII to backtrack as compared to bacterial RNAP (*15*).

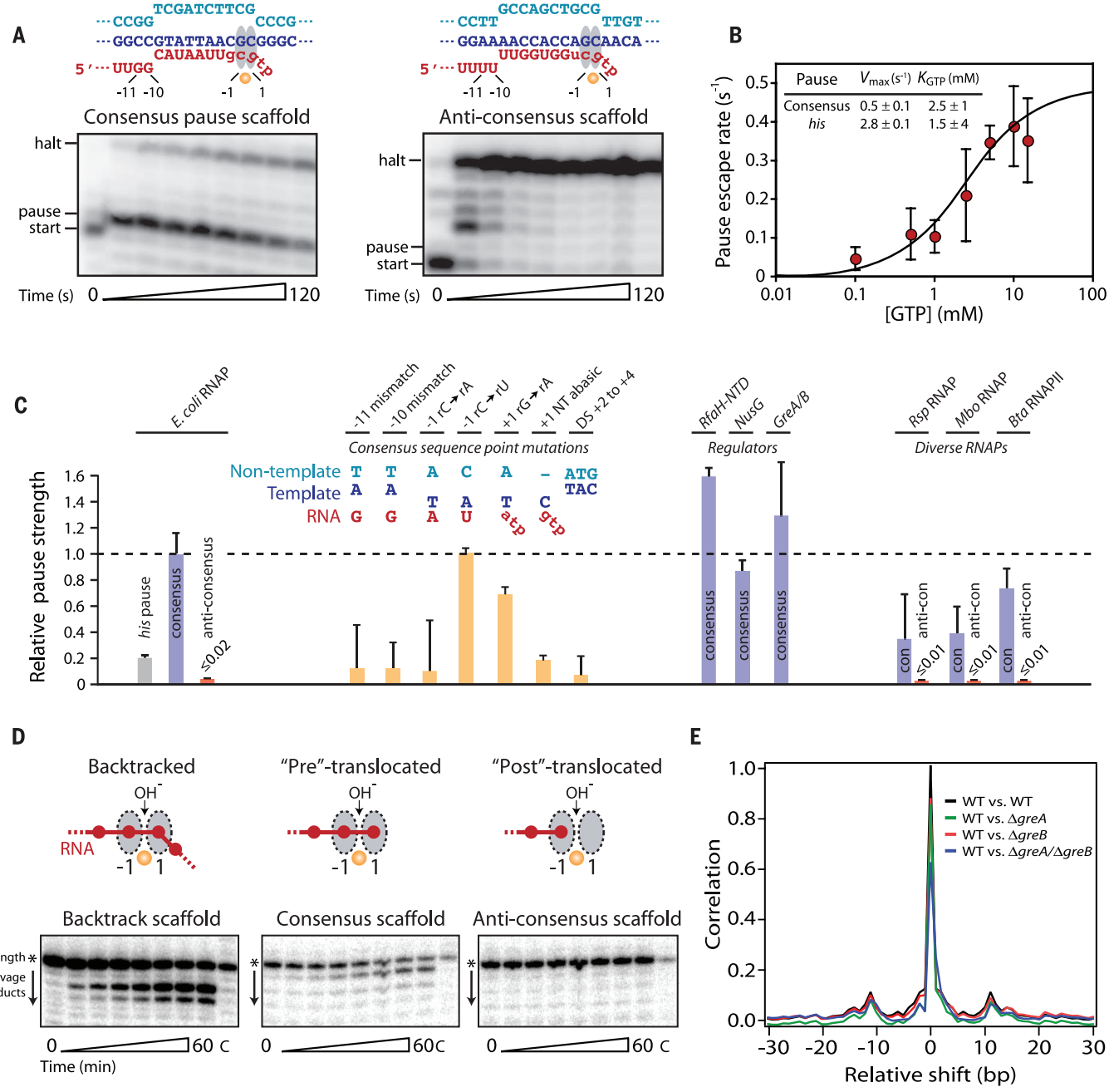


Fig. 3. Pause consensus sequence leads to a long-lived, non-backtracked pause in vitro. (**A**) Purified *E. coli* RNAP was reconstituted on a nucleic-acid scaffold containing either the consensus pause sequence or an anti-consensus sequence. RNA nucleotides in lowercase were added after initial reconstitution by extension with α-^{32}P–labeled or unlabeled NTPs. Full sequences are shown in fig. S7. A strong pause is observed at the predicted position on the consensus pause scaffold, but does not occur on the anti-consensus scaffold. (**B**) Consensus pause escape rate (SD of ≥3 replicates) as a function of GTP concentration reveals a maximal escape rate about one-fifth of that for the *his* pause. (**C**) Relative pause strengths for variants of the consensus pause (yellow), in the presence of transcription regulators, or with diverse RNAPs (SD of ≥3 replicates). (**D**) RNAP active site–catalyzed hydrolytic cleavage of nascent RNA in complexes reconstituted with a 3′ mismatch forcing a backtracked register (left), at the pause site on the consensus pause scaffold (middle), and at the equivalent position on the anti-consensus scaffold (right). (**E**) Mean cross-correlation between NET-seq profiles for wild-type (WT) *E. coli* and Δ*greA* (green), Δ*greB* (red), or Δ*greA*/Δ*greB* (blue) strains for well-transcribed genes (n = 1240, gene average >1 read/bp for each sample). The mean autocorrelation for the WT strain is shown for comparison (black).

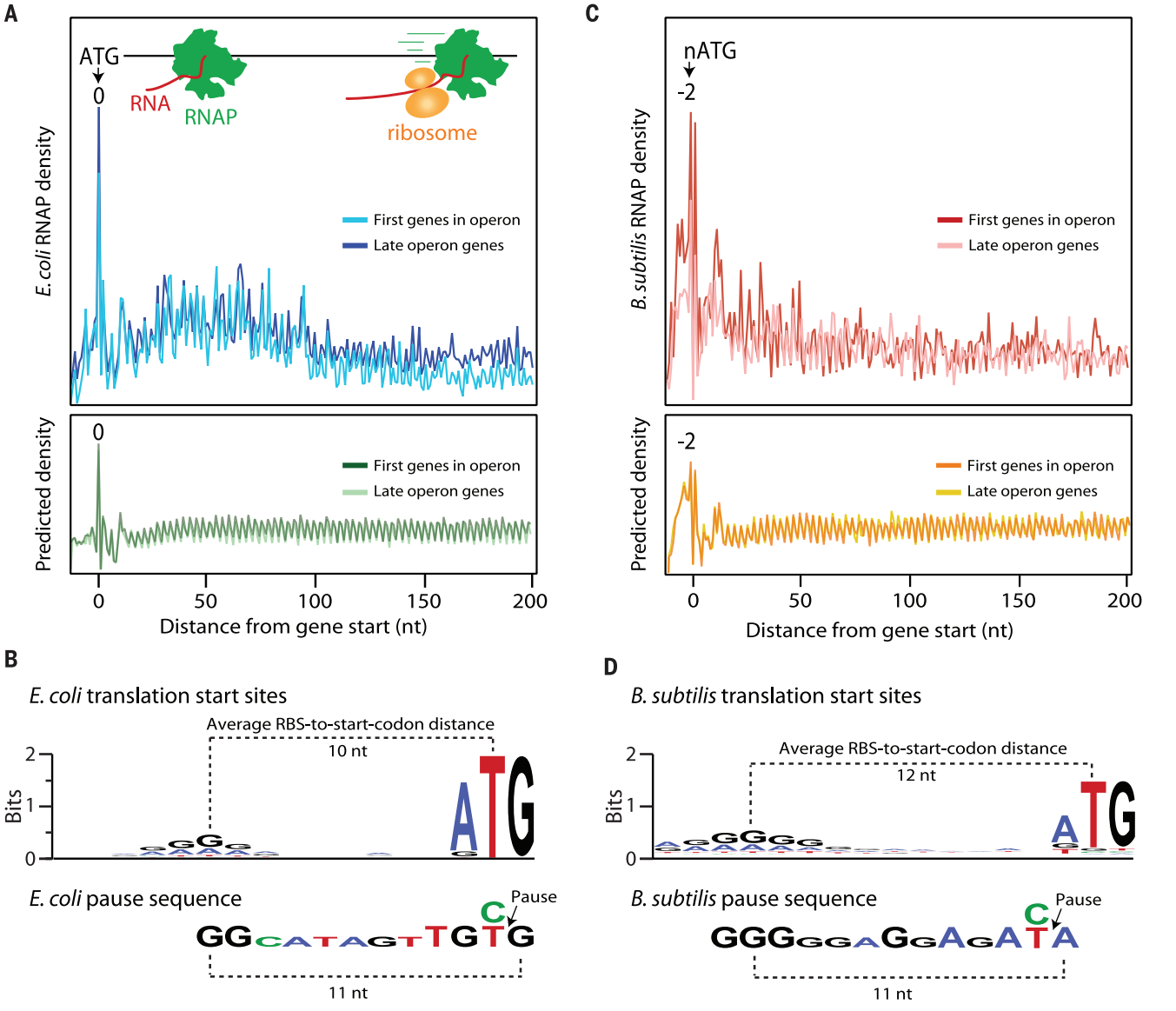


Fig. 4. Consensus pause sequence is enriched at translation start sites. (**A**) Average RNAP density for well-transcribed genes in *E. coli*. The predicted RNAP density calculated by using pause energetics (Fig. 2B) shows a peak at the same position in the start codon. (**B**) Alignment of sequences surrounding translation start sites in *E. coli* reveals a sequence that resembles the pause consensus. (**C**) Average RNAP density for well-transcribed genes in *B. subtilis* shows a peak 2 nt before the center of the start codon. This peak is predicted by the in vivo pause energetics (fig. S13B). (**D**) Alignment of sequences surrounding translation start sites in *B. subtilis* shows a 2 nt increase in the average RBS-to-start codon separation compared to *E. coli*, whereas the separation between consensus pause features remains unchanged.

The average RNAP density across all genes exhibited a sharp peak within the start codon (Fig. 4A), at the juxtaposition of the ribosome-binding sequence (RBS; AGGAGG) and the ATG start codon, which are separated by an average spacing of 10 nt in *E. coli* (*16*) and consequently define the ends of a consensus pause sequence (Fig. 4B). Indeed, RBS substitutions abolished the start-codon pause for the *lacZ* gene in vivo (fig. S12). Similar to *E. coli*, we observed frequent pausing throughout the genome of the Gram-positive bacterium *B. subtilis*, with a consensus pause sequence characterized by –11G/–10G and a –1 pyrimidine, but with A rather than G as the preferred +1 nt (fig. S13, A and B). Start-codon pausing also occurred in *B. subtilis*, just before the A of the ATG codon, placing it 2 nt earlier than the *E. coli* start-codon pause (Fig. 4C). The *B. subtilis* RBS, which generates the –11G/–10G of the start-codon consensus pause, is, on average, 2 nt further upstream from the ATG codon than in *E. coli* (Fig. 4D) (*16*). Thus, the change in the consensus pause sequence in *B. subtilis* may reflect an evolved alteration that compensates for the 2-nt upstream shift of the RBS relative to the start codon (Fig. 4D).

In addition to start-codon pausing, RNAP also exhibits a pronounced tendency to pause within the first 100 nt of expressed genes, even though consensus pause sequences are not statistically overrepresented within these regions (Fig. 4A, compare RNAP density to predicted density). This 5′-proximal RNAP pausing may be increased until a ribosome can initiate translation and inhibit pausing during coupled transcription-translation (*4*, *5*) (Fig. 4A), which likely explains the promoter-proximal buildup of *E. coli* RNAP previously observed by chromatin immunoprecipitation (*17*).

We have defined a consensus pause sequence that temporarily halts transcription at more than 20,000 unique sites in *E. coli*. Pauses are overrepresented at ATG translation start codons, and this could direct folding of the 5′–untranslated region into structures that preserve accessibility of the RBS once transcription resumes (fig.

S14), consistent with the known ability of paused RNAP to influence nascent RNA folding (*1*) and the correlation between RBS accessibility and the rate of translation initiation (*18*, *19*). The enhanced pausing downstream of the start codon (in the first 100 nt of genes) may also help preserve the unstructured RBS by limiting synthesis of additional RNA until translation starts. More generally, the conservation of pause sequences across diverse lineages suggests that consensus-sequence pausing may have evolved early in primitive organisms and was subsequently co-opted to control transcription in a variety of regulatory contexts, accounting for the diverse functions of transcriptional pausing observed today.

REFERENCES AND NOTES

1. T. Pan, T. Sosnick, *Annu. Rev. Biophys. Biomol. Struct.* **35**, 161–175 (2006).
2. I. Artsimovitch, R. Landick, *Cell* **109**, 193–203 (2002).
3. I. Gusarov, E. Nudler, *Mol. Cell* **3**, 495–504 (1999).
4. R. Landick, J. Carey, C. Yanofsky, *Proc. Natl. Acad. Sci. U.S.A.* **84**, 1507–1511 (1987).
5. S. Proshkin, A. R. Rahmouni, A. Mironov, E. Nudler, *Science* **328**, 504–508 (2010).
6. R. Landick, *Biochem. Soc. Trans.* **34**, 1062–1066 (2006).
7. L. S. Churchman, J. S. Weissman, *Nature* **469**, 368–373 (2011).
8. D. G. Vassylyev, M. N. Vassylyeva, A. Perederina, T. H. Tahirov, I. Artsimovitch, *Nature* **448**, 157–162 (2007).
9. M. Palangat, T. I. Meier, R. G. Keene, R. Landick, *Mol. Cell* **1**, 1033–1042 (1998).
10. E. A. Abbondanzieri, W. J. Greenleaf, J. W. Shaevitz, R. Landick, S. M. Block, *Nature* **438**, 460–465 (2005).
11. W. J. Greenleaf, S. M. Block, *Science* **313**, 801 (2006).
12. K. M. Herbert *et al.*, *Cell* **125**, 1083–1094 (2006).
13. C. L. Chan, D. Wang, R. Landick, *J. Mol. Biol.* **268**, 54–68 (1997).
14. A. Weixlbaumer, K. Leon, R. Landick, S. A. Darst, *Cell* **152**, 431–441 (2013).
15. M. L. Kireeva, M. Kashlev, *Proc. Natl. Acad. Sci. U.S.A.* **106**, 8900–8905 (2009).
16. J. Starmer, A. Stomp, M. Vouk, D. Bitzer, *PLOS Comput. Biol.* **2**, e57 (2006).
17. R. A. Mooney *et al.*, *Mol. Cell* **33**, 97–108 (2009).
18. D. B. Goodman, G. M. Church, S. Kosuri, *Science* **342**, 475–479 (2013).
19. G. Kudla, A. W. Murray, D. Tollervey, J. B. Plotkin, *Science* **324**, 255–258 (2009).

ACKNOWLEDGMENTS

We thank O. Brandman, V. Chu, D. Larson, G. Li, C. McLean, and E. Simmons for critical reading of the manuscript and J. Lund and E. Chow for assistance with sequencing. This research was supported by the Center for RNA Systems Biology (J.S.W.), the Howard Hughes Medical Institute (J.S.W.), a Ruth L. Kirschstein National Research Service Award (M.H.L., J.M.P.), and grants from the NIH to C.A.G., S.M.B., W.J.G., and R.L. All data are deposited in Gene Expression Omnibus (accession number GSE56720). Jonathan Weissman and Stirling Churchman have submitted a patent on the NET-seq technology.

SUPPLEMENTARY MATERIALS

www.sciencemag.org/content/344/6187/1042/suppl/DC1
Materials and Methods
Supplementary Text
Figs. S1 to S14
Tables S1 to S4
References (*20*–*57*)

6 February 2014; accepted 18 April 2014
Published online 1 May 2014;
10.1126/science.1251871

Liquid Chromatography Columns

The new GlycanPac AXR-1 columns help users achieve greater resolution of glycans using HPLC, providing easier profile characterization. This is useful for characterizing glycans from monoclonal antibodies being developed for therapeutics. The columns are designed for excellent resolution of labeled and unlabeled glycans, and are compatible with fluorescence and mass spectrometry detection methods. Mass spectrometry has emerged as a powerful tool for determining the structures of glycans, and this new column is designed to enable researchers to harness the power of high-resolution accurate-mass mass spectrometry at high throughput rates. This column is designed to separate both labeled and native glycans based on the availability of samples. Native glycan separation allows researchers to eliminate the fluorescent labeling step and increase throughput without eroding performance.
Thermo Fisher Scientific
For info: 800-532-4752
www.thermoscientific.com/glycanpac

Ultralow Flow Electrospray Ionization Instrument

CESI marks a novel combination of capillary electrophoresis and electrospray ionization technologies to create an integrated workflow solution. The CESI-Mass Spectrometry (MS) workflow includes the industry's first commercially available ultralow-flow separation and ESI module for biologics, along with a high-performance, high-resolution, accurate mass instrument. The new CESI 8000 System for Biologics Characterization is an innovative, high-performance separation-electrospray ionization system for mass spectrometry (MS). This new frontend CESI technology can be integrated with the well-established AB Sciex TripleTOF 5600+ mass spectrometry system into a seamless solution. With a single approach that increases efficiency and productivity, the CESI 8000 provides orthogonal and/or superior results compared to dual-method liquid chromatography/mass spectrometry-based approaches. From a single digest and run, users of CESI-MS gain the following: (a) identity and purity information with 100% coverage in a peptide map; (b) heterogeneity information with ultrasensitive glycopeptide quantitation; and (c) stability information identifying, deamidation, cyclization, and oxidation.
AB Sciex
For info: 877-740-2129
www.sciex.com/cesi



Inductively Coupled Plasma Mass Spectrometer

The NexION 350 Inductively Coupled Plasma Mass Spectrometer (ICP-MS) is designed to empower laboratory professionals with greater efficiency in elemental analyses, specifically delivering the most accurate characterization of nanoparticles in the market. Syngistix for ICP-MS Software is a proprietary workflow-based platform with an intuitive interface and new, automated method setup tools for faster, more efficient implementation. The NexION 350 delivers enhanced instrument uptime and productivity through several technical innovations designed to reduce background and interferences, optimize signal stability, and to minimize maintenance requirements and downtime. The combination of these features can enable lab professionals to run more samples per unit of time. The NexION 350's data acquisition rates of 100,000 data points per second (10 times faster than any other ICP-MS currently on the market) are ideal for applications that require fast, transient signal analysis, such as nanoparticle characterization, speciation and laser ablation ensuring that critical events are not missed.
PerkinElmer
For info: 877-754-6973
www.perkinelmer.com/atomicspectroscopy

Microfluidic UPLC Separation Device

Intended for use with Waters ACQUITY UPLC M-Class System and Xevo TQ-S Mass Spectrometer, the ionKey/MS System physically integrates a UPLC separation into the mass spectrometer producing a significant improvement in sensitivity, enabling unparalleled separation and detection of compounds. With the ionKey/MS, scientists can reduce solvent and sample sizes and no longer have to contend with delicate fittings and columns or concern themselves with extra column dispersion and the inevitable variability and band broadening that comes with it. The iKey Microfluidic Separation Device, which is about the size of a smart phone, contains the fluidic connections, electronics, ESI interface, column heater, eCord Intelligent Chip Technology, and the 1.7 µm UPLC grade particles packed inside a 150 µm I.D. channel to perform hundreds upon hundreds of UPLC separations reproducibly and reliably without a degradation in performance. Additionally, it can be inserted into the source of the mass spectrometer in just a few seconds.
Waters
For info: 800-252-4752
www.waters.com/ionkey

MALDI-TOF(/TOF) Mass Spectrometers

Autoflex speed, the new member of the Flex series of MALDI-TOF(/TOF) mass spectrometers, delivers superior performance by incorporating numerous innovative technology advancements which provide further enhanced data quality, acquisition speed, class-leading mass and dynamic range, and general robust and efficient performance. The new autoflex speed is designed to dramatically enhance the productivity of laboratories involved in protein sequencing, biomarker discovery, polymer analysis, lipid and glycan analysis, molecular imaging, drug and metabolite tissue distribution, as well as high throughput MALDI Biotyper microbiological molecular identification. System configurations can be optimized for a number of different analytical operations and environments utilizing both TOF and TOF/TOF modes in combination with dedicated hardware and software tools for a variety of applications. The new autoflex speed system incorporates a smartbeam-II laser, now with up to 2 kHz repetition rate with true-pixel image resolution at 20 µm for proteins and has a self-cleaning ion source, which cleans the instrument source in minutes.
Bruker
For info: 510-683-4300
www.bruker.com/autoflexspeed

Electronically submit your new product description or product literature information! Go to www.sciencemag.org/products/newproducts.dtl for more information.

Newly offered instrumentation, apparatus, and laboratory materials of interest to researchers in all disciplines in academic, industrial, and governmental organizations are featured in this space. Emphasis is given to purpose, chief characteristics, and availability of products and materials. Endorsement by *Science* or AAAS of any products or materials mentioned is not implied. Additional information may be obtained from the manufacturer or supplier.

Downloaded from www.sciencemag.org on May 30, 2014

By **Christina Reed**

Winter is coming

In Antarctica this week, the daylight is dimming as the polar night approaches. "The weather is pretty changing at the moment. There are a lot of low-pressure systems coming from the Weddell Sea, leading to high wind speeds up to 55 knots and a lot of snowdrift," says meteorologist Elena Stautzebach. She is part of a small team of early-career scientists overwintering at the German research base Neumayer-Station III. "In between, we have periods of sunny weather and temperatures around –10°C." But the darkness will be continuous starting on 28 May. It will last 56 days.

Located 450 kilometers from its closest neighbor, the station has a proud meteorological history: Scientists have conducted measurements and observations there every 3 hours for more than 30 years. Many measurements run on a programmed schedule. But visual observations—cloud and weather conditions, air pressure, dew-point temperature, wind speed and direction, and visibility, for example—must be made by people, rather, a person. "We have just one meteorologist, who has to sleep now and then," says the team's lead off-continent contact, Gert König-Langlo of the Alfred Wegener Institute for Polar and Marine Research in Germany. This winter, that meteorologist is Stautzebach. The team operates on Coordinated Universal Time. At 9 a.m., noon, 3 p.m., 6 p.m., 9 p.m., and midnight, she is outside collecting data, whatever the weather.



"Overwintering and being in charge of a scientific observatory in Antarctica is a challenge."

"As it gets darker, it is getting more difficult to distinguish between different cloud layers and types. Observations are therefore taking a lot longer without daylight, as you have to stay outside longer in order to adapt your eyes to the darkness. But this also means that you have time to watch the beautiful stars of the Southern Hemisphere and that you have higher chances of seeing polar lights," she says.

To ensure that her measurements are accurate, Stautzebach must do daily rounds, dusting snow and breaking off ice crystals from 10 radiation sensors, two ventilated temperature sensors, two wind anemometers (one of them 10 meters above the ground), three humidity sensors, and snow depth and air pressure sensors—all located 200 meters from the station to avoid wind and shadow influences. Stautzebach also climbs up on the station's roof to check the visibility sensor and the ceilometer, which detects cloud height.

As the temperature drops, Stautzebach will start to travel 20 kilometers by snowmobile every 3 weeks to Atka Bay, where she will measure the first growth of sea ice and platelet ice. As winter digs in, the ice will become strong enough to support an automated meteorological station equipped with radiation sensors.

"Overwintering and being in charge of a scientific observatory in Antarctica is a challenge," Stautzebach says. "During the winter season, we have to deal with all sorts of situations on our own. Our team includes one engineer who is responsible for the functioning of the entire station, one IT-specialist who has to maintain the communication with the world outside Antarctica, and one doctor. Additionally, in case of a fire, we have to turn into our own firefighters."

Winter for the team officially started at the end of February "when the last plane left Antarctica," Stautzebach says. "We are now on our own until November." The nine-person team will then continue its work through the following Antarctic summer, helping the next overwintering team prepare for what is coming.

"Now that I am in Antarctica, the continent with the harshest weather conditions in the world, I can't wait to experience probably the most extreme weather in my life. Even more exciting than cold temperatures are storm events with snowdrift and whiteouts. As soon as the highest wind speeds of a storm event are reached, I often go outside with one of my colleagues (and a radio and GPS of course) in order to experience the strength of the wind.

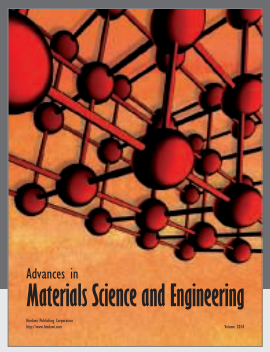
"This winter I will simply enjoy the harsh weather conditions in Antarctica, and as soon as I am back in Europe, I'll think back to storm events that I had the chance to experience down here."

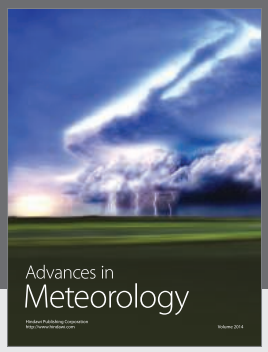
Christina Reed is a nomadic freelance science journalist.

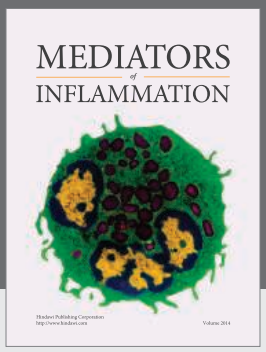
ILLUSTRATION: MARC ROSENTHAL

Downloaded from www.sciencemag.org on May 30, 2014

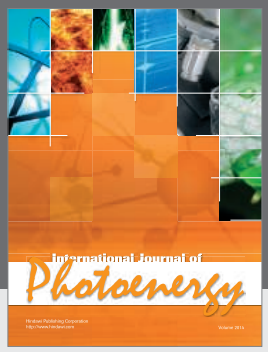
Published by AAAS

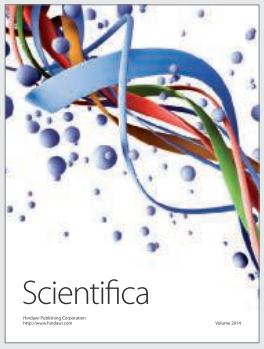


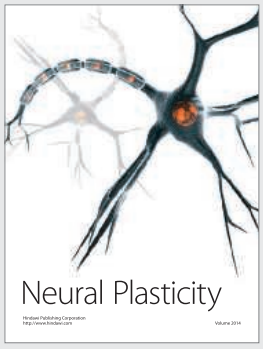










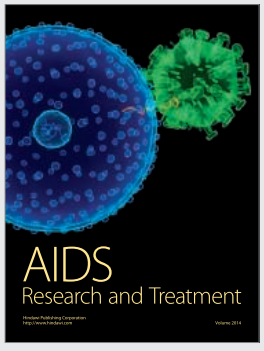


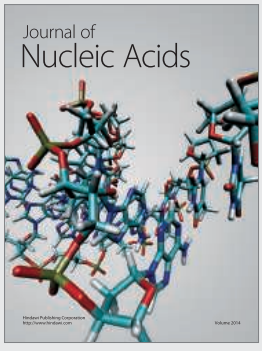
Hindawi

Submit your manuscripts at
http://www.hindawi.com





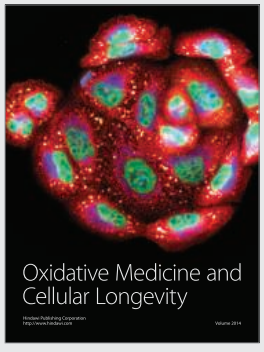


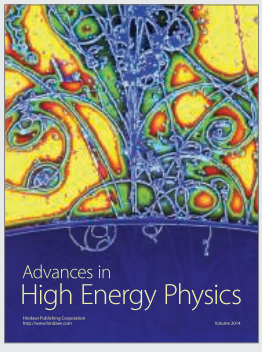






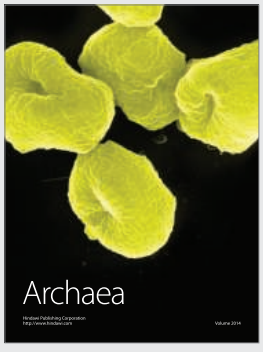












Applied Biosystems®

For when every step needs to be precise



Applied Biosystems® thermal cyclers enable consistent, precise results no matter the challenge



- Engineered with your highest standards in mind
- Consistently deliver the highest performance
- Accuracy you need to advance your research

Request an in-lab demo at **lifetechnologies.com/consistent**

life technologies

A Thermo Fisher Scientific Brand

For Research Use Only. Not for use in diagnostic procedures. © 2014 Thermo Fisher Scientific Inc. All rights reserved.
All trademarks are the property of Thermo Fisher Scientific and its subsidiaries unless otherwise specified. **CO09233 0414**

Verifi(Ab)le Antibodies

Lot to lot. Experiment to experiment. Our Anti-Fail testing guidelines meet your most demanding expectations.

Our antibodies are among the most thoroughly verified in our industry. We have developed internal criteria that far exceeds the industry standards. Our validation processes are centered around the principle that a tested antibody has more value to our customers. If our antibodies fail to meet our strictest specifications, they are discarded without question, even if they have hit initial targets. Our stringent, multi-step validation process offers you the highest quality, most well-validated antibodies on the market today.

Put the most verifiable antibodies to work for you.
www.emdmillipore.com/Ab



EMD Millipore is a division of
Merck KGaA, Darmstadt, Germany

EMD Millipore and the M logo are trademarks of Merck KGaA, Darmstadt, Germany.
03/2014 © 2014 EMD Millipore Corporation, Billerica, MA USA.
All rights reserved.

BS-GEN-13-09105

Western weary



Western wonderful!



Novex®

A hands-free western blotting innovation that's changing the face of westerns

The first-of-its kind iBind™ Western System offers:

- Automated western processing
- Highly reproducible results
- Increased sensitivity and western quality
- Speed—only 2.5 hours to process
- No electricity or battery required

With the iBind™ Western System, you can set it and get on with your life.



WESTERN WORKFLOW

SEPARATE TRANSFER DETECT

Watch how automated blotting works at
lifetechnologies.com/western

life technologies

A Thermo Fisher Scientific Brand

For Research Use Only. Not for use in diagnostic procedures. © 2014 Thermo Fisher Scientific Inc. All rights reserved.
All trademarks are the property of Thermo Fisher Scientific and its subsidiaries unless otherwise specified. **CO09143 0414**

PROVEN PERFORMANCE

Real-time PCR assays that go beyond a guarantee





Our PrimePCR™ assays take the uncertainty out of real-time PCR — each assay is expertly designed, wet-lab validated, and specificity-verified using next-generation sequencing (NGS) for proven assay performance. Assays are available as individual assays, custom plates, and predesigned pathway and disease panels.

Learn more at **bio-rad.com/PrimePCRreagents**

BIO-RAD

Caris Life Sciences: The World's Most Comprehensive Molecular Profiling Service.

There is a reason why more physicians choose Caris Life Sciences.® We provide drug associations that are **Evidenced Based and Clinically Actionable.** No other company can provide you with more potential treatment options for your patients:

- ✓ **51** clinically actionable FDA approved drug associations vs. 19 from Foundation Medicine®
- ✓ **96%** drug to biomarker associations are based upon Level 1 or Level 2 clinical evidence (human clinical trials)
- ✓ **600+** NGS genes analyzed** vs. 236 NGS genes from Foundation Medicine
- ✓ **Multi-technology platform** profiles biomarkers in DNA, RNA and proteins vs. DNA alone from Foundation Medicine
- ✓ **60,000+** tumor profiles performed
- ✓ **6,000** oncologists have ordered from 60 countries

CARIS® LIFE SCIENCES

To learn more, please visit www.CarisLifeSciences.com.

©2014 Caris Life Sciences and affiliates. All rights reserved. Other trademarks are the property of their respective owners. ***CLIA & ISO launch Q3 2014.* TN0204

CARIS MOLECULAR INTELLIGENCE™

Technologies Used:

- Next-Generation Sequencing *(NGS)* - DNA
- Fluorescence *in situ* Hybridization *(FISH)* - DNA
- Chromogenic *in situ* Hybridization *(CISH)* - DNA
- Immunohistochemistry *(IHC)* - Protein
- Sanger Sequencing - DNA
- PyroSequencing - DNA
- Fragment Analysis - DNA & RNA
- Quantitative Polymerase Chain Reaction *(qPCR - cobas®)* - DNA

51 Actionable Drug/Target Associations††

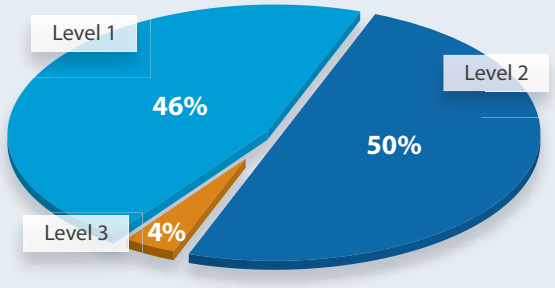
abarelix	carboplatin†	degarelix	everolimus†	gemcitabine	leuprolide	panitumumab†	temozolomide†	triptorelin
abiraterone	cetuximab†	docetaxel	exemestane	goserelin	liposomal-doxorubicin†	pemetrexed	temsirolimus†	vandetanib
afatinib	cisplatin†	doxorubicin†	fluorouracil	imatinib	megestrol acetate	pertuzumab†	topotecan	vemurafenib
anastrozole	crizotinib	enzalutamide	flutamide	irinotecan	nab-paclitaxel	sunitinib	toremifene	
bicalutamide	dabrafenib	epirubicin†	fulvestrant	lapatinib†	oxaliplatin	tamoxifen	trametinib	
capecitabine	dacarbazine†	erlotinib†	gefitinib†	letrozole	paclitaxel	T-DM1†	trastuzumab†	

† *Associations driven by profiling multiple analytes.*

96% of *Caris Molecular Intelligence* actionable drug/target associations are based on Level 1or Level 2 evidence

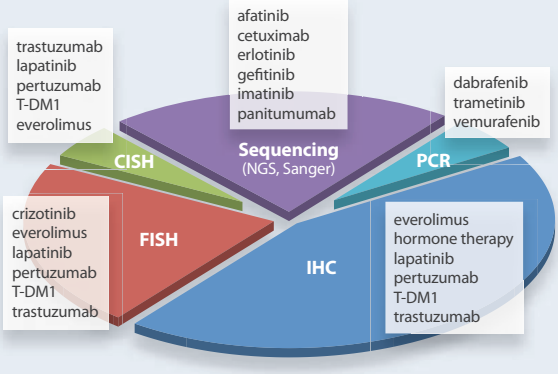
Evidence Level:

- **Level 1:** Randomized, controlled trials; meta-analyses
- **Level 2:** Non-randomized controlled trials, single arm, cohort/case-control studies
- **Level 3:** Expert committee opinion, case reports or series



Caris Molecular Intelligence incorporates multiple technologies to profile actionable targets.

More than 25 therapies associated with companion markers and NCCN-Guidelines®



FoundationOne™ from Foundation Medicine*

Technologies Used:

Next-Generation Sequencing *(NGS)* - DNA

19 Actionable Drug/Target Associations††

afatinib	everolimus	temsirolimus
carboplatin	gefitinib	trametinib
cetuximab	imatinib	trastuzumab
cisplatin	oxaliplatin	vandetanib
dabrafenib	panitumumab	vemurafenib
dacarbazine	sunitinib	
erlotinib	temozolomide	

The same 19 drug/target associations are included in the 51 drug/target associations for *Caris Molecular Intelligence.*

* *Based on information found at www.foundationone.com.* †† *Drug/target associations supported by Levels 1, 2 or 3 evidence.*

CARIS MOLECULAR INTELLIGENCE™

600+ NGS Genes**

FoundationOne™

236 NGS Genes

** *CLIA & ISO launch Q3 2014.* The same 236 NGS genes are included in the 600+ NGS profile for *Caris Molecular Intelligence.*

eppendorf & Science

PRIZE FOR NEURO BIOLOGY



2013 Winner
Dr. Michael Yartsev
CV Starr Research Fellow
Princeton Neuroscience Institute

Application Deadline
June 15, 2014

Call for Entries

Eppendorf & Science Prize for Neurobiology
The annual Eppendorf & Science Prize for Neurobiology, an international award, honors young scientists for their outstanding contributions to neurobiological research based on methods of molecular and cell biology.
The winner and finalists are selected by a committee of independent scientists, chaired by Science's Senior Editor, Dr. Peter Stern. To be eligible, you must be 35 years of age or younger.

You could be next to win this prize and to receive
> Prize money of US$25,000
> Publication of your work in Science
> Full support to attend the Prize Ceremony held in conjunction with the Annual Meeting of the Society for Neuroscience in the USA
> An invitation to visit Eppendorf in Hamburg, Germany

It's easy to apply!

Learn more at: www.eppendorf.com/prize

eppendorf

Science AAAS

AAAS® and Science® are registered trademarks of the American Society for the Advancement of Science, USA. Eppendorf® and the Eppendorf logo are registered trademarks of Eppendorf AG.
All rights reserved, including graphics and images. Copyright © 2014 by Eppendorf AG. Kurstin Roe Photography.

Sequencing power for every scale.



The HiSeq X Ten contains 10 sequencing systems.

NEW
HiSeq X™ Ten

Population power.
$1000 human genome and extreme throughput for population-scale sequencing.

HiSeq® 2500

Production power.
Power and efficiency for large-scale genomics.

NEW
NextSeq™ 500

Flexible power.
Speed and simplicity for whole-genome, exome, and transcriptome sequencing.

MiSeq®

Focused power.
Speed and simplicity for targeted and small-genome sequencing.

MiSeqDx™

Focused Dx power.
The first and only FDA-cleared *in vitro* diagnostic next-generation sequencing system.

Find the right sequencer to fit your every need. www.illumina.com/power

illumina®

©2014 Illumina, Inc. All rights reserved.

22% of the Total Citations in Chemistry





Out of 152 journals in the category of multidisciplinary chemistry, ***JACS*** **is #1 with 431,286 total citations**, representing **22% of the citations** in the category. With a **10.677 Impact Factor**, ***JACS*** is the world's preeminent journal for all of chemistry and the interfacing areas of science.

ACS Publications
Most Trusted. Most Cited. Most Read.

Visit **pubs.acs.org/JACS** for more information.

Follow *JACS* on Twitter **@JACS**

Follow *JACS* at **facebook.com/JAmChemSoc**

Join the Conversation!

Twitter is a great way to connect with AAAS members and staff about the issues that matter to you most. Be a part of the discussion while staying up-to-date on the latest news and information about your personal member benefits.

Follow us @AAASmember

and join the conversation

with #AAAS

AAAS MEMBERCENTRAL

MemberCentral.aaas.org

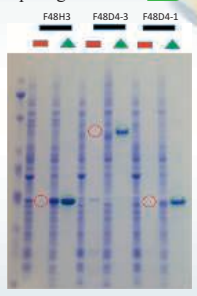
APERTO

Protein Extraction Buffer for *E.coli*

Solubilizes proteins that the top 3 lysis buffers do not!

Gentle Rapid Active Enzymes

Competing Product Aperto



Note missing bands indicated by red circles

4 lanes per protein:
Competitor soluble fraction, Comp. His-Tag, Aperto soluble, Aperto His-Tag

F48H3 (UniProt ID D0AAZ6, 28 kDa)
F48D4-3 (UniProt ID E6YHI3, 65 kDa)
F48D4-1 (UniProt ID E6YFV4, 28 kDa)

phone: 1-855-242-0011
www.TEKnova.com

enfold by TEKnova

AAAS *Travels*

ANTARCTICA

Christmas in Antarctica



Save $800 per person!
December 17-29, 2014

Scientists consider Antarctica one of the last pristine regions and most inhospitable habitats on earth, offering the world's most magnificent wilderness with concentrations of wildlife, icebergs sculptured by the sea, and extraordinary scenery. Once we reach the Antarctic Convergence, we will begin to see a profusion of wildlife, which thrives on the nutrient rich waters. Travel is on the excellent *M/V Corinthian*. From $9,990 pp

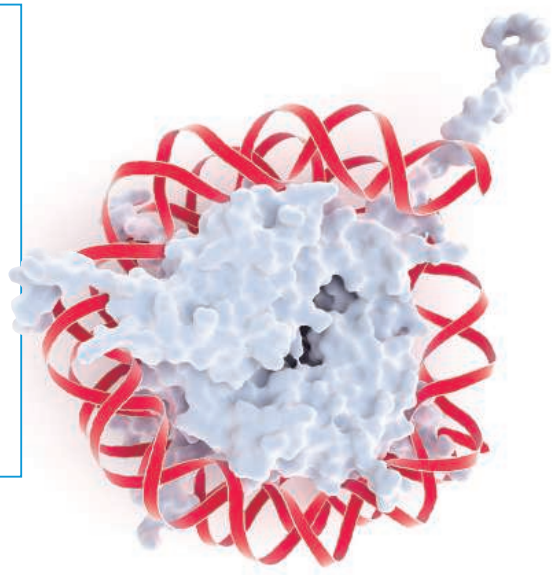
For a detailed brochure, please call (800) 252-4910
All prices are per person twin share + air

BETCHART EXPEDITIONS Inc.
17050 Montebello Rd, Cupertino, CA 95014
Email: AAASInfo@betchartexpeditions.com
www.betchartexpeditions.com

New Tools, New Targets

Novel Approaches for Identifying and Characterizing Epigenetic Modifications

Webinar



Wednesday, June 25, 2014

12 noon Eastern, 9 a.m. Pacific, 5 p.m. UK, 6 p.m. Central Europe

In this webinar, viewers will:

- Obtain an overview of epigenetic modifications and their role in disease
- Hear about the latest technologies for identifying and characterizing histone modifications
- Gain insight into some of the latest advances in epigenetics research
- Have their questions answered live by our expert panel!

Since the successful sequencing of the human genome, interest in the group of genes encoding proteins responsible for DNA remodeling has grown exponentially. Included in this group are enzymes that methylate and demethylate DNA as well as those that modify histones by adding chemical groups through acetylation, methylation, and sumoylation reactions, amongst others. Epigenetic enzymes are now among the most important pharmaceutical targets due to their involvement in numerous key cellular processes and in the etiology of many devastating diseases including cancer, neurodegenerative disease, and developmental disorders. Significant efforts are under way in both academic and industrial laboratories to identify and validate new so-called reader, writer, and eraser enzymes as well as their histone substrates. Understanding the functions of these proteins may lead to a new generation of therapeutics. While various molecular biology techniques were initially used to identify and validate epigenetics enzymes and their substrates, novel approaches are now available to perform pharmacological characterization of histone-modifying enzymes. During this webinar, our expert panelists will describe these methods and present breakthrough research data obtained using novel experimental approaches, including immunoassays, microfluidics-based techniques, and high-content screening immunophenotypic assays.

Speakers



Yan-Ling Zhang, Ph.D.
Broad Institute of MIT and Harvard
Cambridge, MA



William P. Janzen
University of North Carolina
Chapel Hill, NC

REGISTER NOW! webinar.sciencemag.org

Webinar sponsored by

PerkinElmer
For the Better

Brought to you by the *Science*/AAAS Custom Publishing Office

Science
AAAS

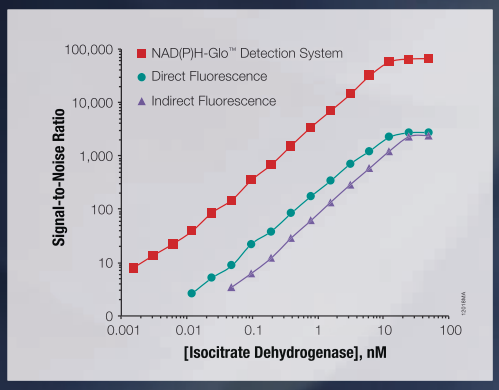
@SciMagWebinars

Promega

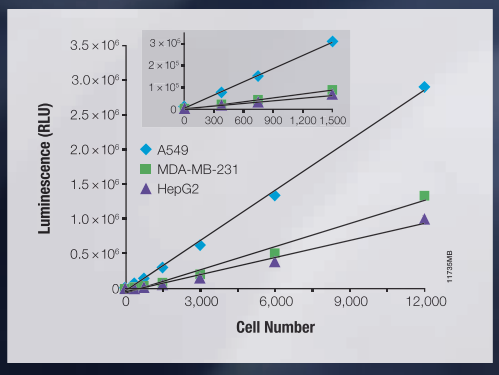
Better Biology, Less Work

NAD(P)/NAD(P)H-Glo Assays

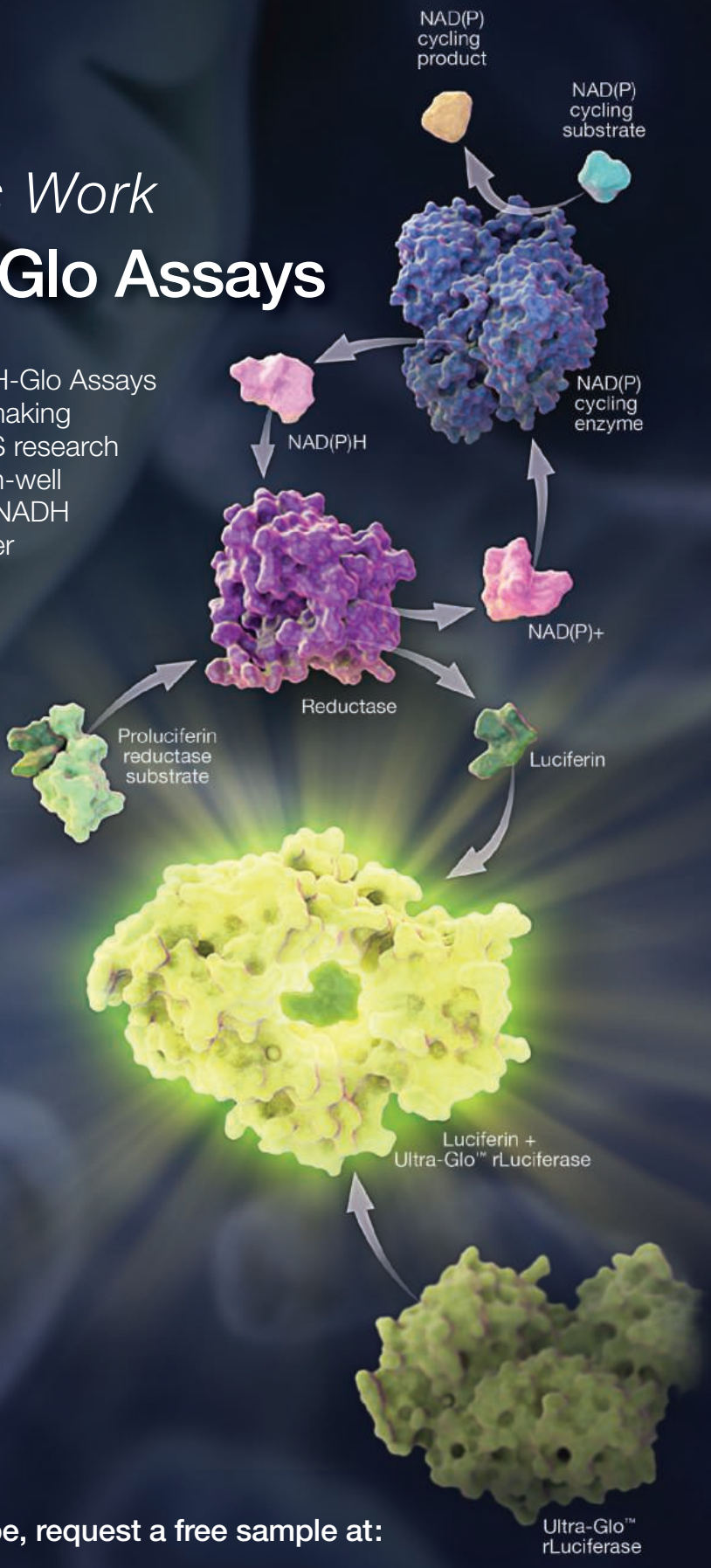
The simple add-and-read NAD(P)/NAD(P)H-Glo Assays have unparalleled sensitivity and linearity making them ideal for metabolic research and HTS research applications. These assays enable direct in-well measurement of total and individual NAD/NADH or NADP/NADPH and can be used in either biochemical or cell-based applications.



Superior sensitivity compared to fluorescent methods (Total NADH + NADPH measured).



Directly measure total dinucleotide concentrations in multiwell plates using low cell numbers (Total NADP + NADPH measured).



To see how easy better biology can be, request a free sample at:

www.promega.com/NADassays

©2014 Promega Corporation. All rights reserved. 13977644

Max-Planck-Institute for Solid State Research

The Max-Planck-Institute for Solid State Research invites applications for the position as

Leader of a Max Planck Research Group on "Ab initio Computation of Novel Materials"

The applicant is assumed to be a recognized researcher with excellent knowledge of condensed-matter theory and working experience with ab initio computation of the structure, dynamics, and electronic properties of novel materials. Of particular interest are systems with strongly correlated electrons and nanostructured materials.

The appointment will be for 5 years. An extension is possible after a successful evaluation. Remuneration will be paid at the associate professor level (W2) with all fringe benefits of the German public sector. The position includes an independent budget for personnel, running costs, and investment, office space for students and postdocs, and use of the research infrastructure of the institute.

The Max Planck Gesellschaft seeks to increase the number of women in those areas where they are underrepresented and therefore explicitly encourages women to apply.

The Max Planck Gesellschaft is committed to employing more disabled individuals and especially encourages them to apply.

Your application should include a CV, a list of publications and invited talks, a summary of scientific achievements, and references. For further inquiries, please contact Dr. Michael Eppard (m.eppard@fkf.mpg.de).

Please send your application by July 30, 2014 to:

Max Planck Institute for Solid State Research
Managing Director
Heisenbergstr. 1
D-70569 Stuttgart, Germany

Zertifikat seit 2006 audit berufundfamilie



AAAS is here – helping scientists achieve career success.

Every month, over 400,000 students and scientists visit ScienceCareers.org in search of the information, advice, and opportunities they need to take the next step in their careers.

A complete career resource, free to the public, *Science* Careers offers a suite of tools and services developed specifically for scientists. With hundreds of career development articles, webinars and downloadable booklets filled with practical advice, a community forum providing answers to career questions, and thousands of job listings in academia, government, and industry, *Science* Careers has helped countless individuals prepare themselves for successful careers.

As a AAAS member, your dues help AAAS make this service freely available to the scientific community. If you're not a member, join us. Together we can make a difference.

To learn more, visit
aaas.org/plusyou/sciencecareers

AAAS + U = Δ



Science Careers Advertising

For full advertising details, go to ScienceCareers.org and click For Employers, or call one of our representatives.

Tracy Holmes
Worldwide Associate Director
Science Careers
Phone: +44 (0) 1223 326525

THE AMERICAS

E-mail: advertise@sciencecareers.org
Fax: 202-289-6742

Tina Burks
Phone: 202-326-6577

Nancy Toema
Phone: 202-326-6578

Marci Gallun
Sales Administrator
Phone: 202-326-6582

Online Job Posting Questions
Phone: 202-312-6375

EUROPE / INDIA / AUSTRALIA / NEW ZEALAND / REST OF WORLD

E-mail: ads@science-int.co.uk
Fax: +44 (0) 1223 326532

Axel Gesatzki
Phone: +44 (0)1223 326529

Sarah Lelarge
Phone: +44 (0) 1223 326527

Kelly Grace
Phone: +44 (0) 1223 326528

JAPAN

Yuri Kobayashi
Phone: +81-(0)90-9110-1719
E-mail: ykobayas@aaas.org

CHINA / KOREA / SINGAPORE / TAIWAN / THAILAND

Ruolei Wu
Phone: +86-1367-1015-294
E-mail: rwu@aaas.org

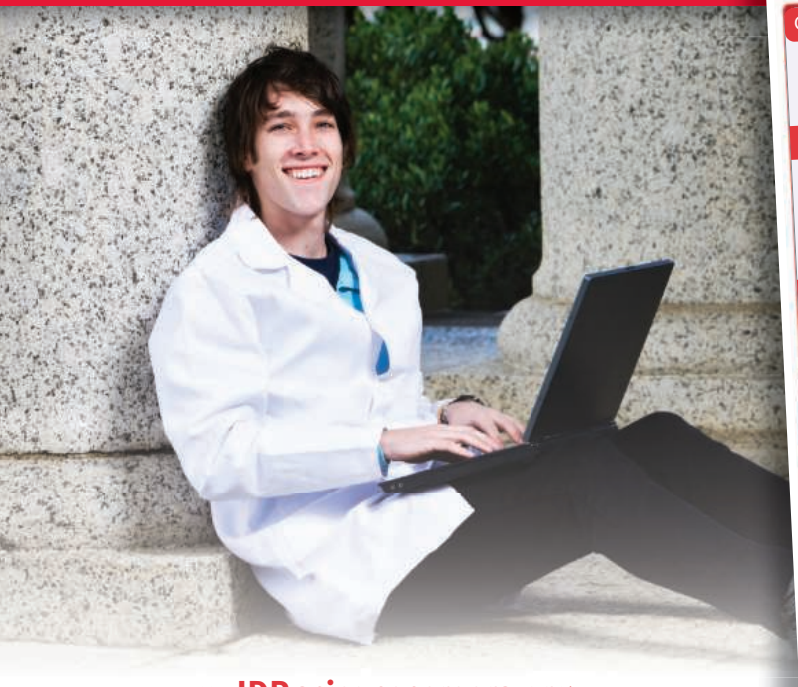
All ads submitted for publication must comply with applicable U.S. and non-U.S. laws. *Science* reserves the right to refuse any advertisement at its sole discretion for any reason, including without limitation for offensive language or inappropriate content, and all advertising is subject to publisher approval. *Science* encourages our readers to alert us to any ads that they feel may be discriminatory or offensive.

Science Careers
From the journal *Science* AAAS

ScienceCareers.org

For your career in science, there's only one Science

A career plan customized *for* you, *by* you.



myIDP.sciencecareers.org



Recommended by leading professional societies and endorsed by the National Institutes of Health, an individual development plan will help you prepare for a successful and satisfying scientific career.

my IDP Science Careers

In collaboration with FASEB, UCSF, and the Medical College of Wisconsin and with support from the Burroughs Wellcome Fund, AAAS and *Science* Careers present the first and only online app that helps scientists prepare their very own individual development plan.

Visit the website and start planning today!
myIDP.sciencecareers.org

In partnership with:

advancing the life sciences 1912-2012 FASEB Federation of American Societies for Experimental Biology

UCSF University of California San Francisco

Medical College of Wisconsin

Burroughs Wellcome Fund

DIRECTOR
OKLAHOMA GEOLOGICAL SURVEY
UNIVERSITY OF OKLAHOMA

Applications are being solicited for the position of Director, Oklahoma Geological Survey (OGS). The OGS is located on the University of Oklahoma campus in Norman, Oklahoma, and is under the direction and supervision of the Board of Regents of the University of Oklahoma. Organizationally, the OGS is located within the Mewbourne College of Earth & Energy, which also includes the ConocoPhillips School of Geology & Geophysics and the Mewbourne School of Petroleum & Geological Engineering. The Director of the OGS reports administratively to the Dean, Mewbourne College of Earth & Energy. If appropriate, the successful candidate may hold a dual appointment as a faculty member within the College as an Associate or Full Professor, renewable term or tenured. Candidates should hold a doctorate in geology, geophysics or a closely related field. Prior experience with a public agency would be beneficial.

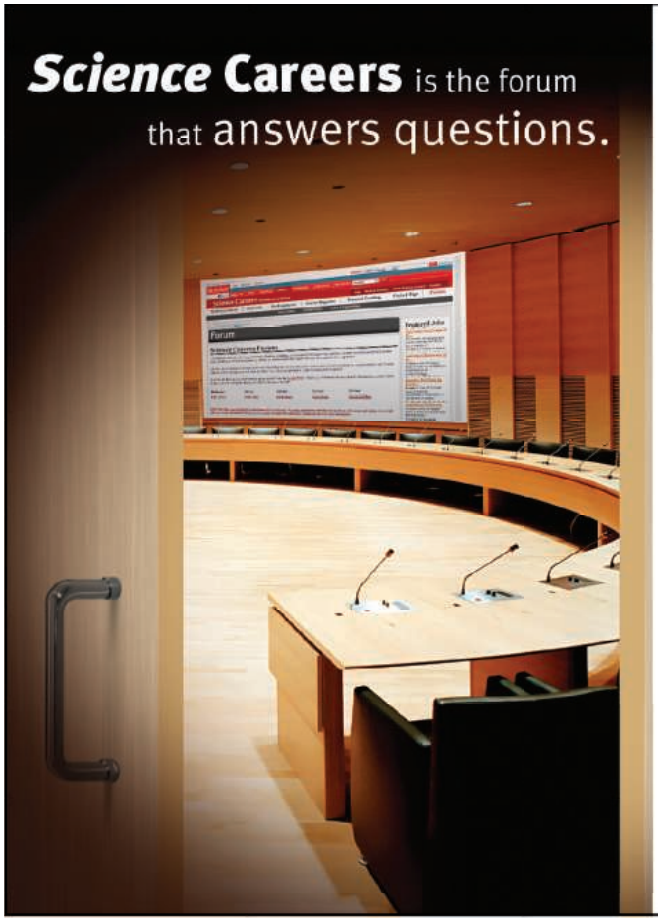
The objectives and duties of the Oklahoma Geological Survey include the following:

(a) A study of the geological formations of the state with special reference to its natural resources, including coal, oil, gas, asphalt, gypsum, salt, cement, stone, clay, lead, zinc, iron, sand, road building material, water resources and all other mineral resources.
(b) Management of the Oklahoma seismic recording network, and the reporting and analysis of earthquake activity in the state.
(c) The preparation and publication of bulletins and reports, accompanied with necessary illustrations and maps, including both general and detailed descriptions of the geological structure and mineral resources of the state.
(d) The consideration of such other related scientific and economic questions that shall be deemed of value to the people of Oklahoma.

The Director of the OGS has the responsibility of overseeing activities related to geological and geophysical studies of Oklahoma and adjacent areas, preparation of reports documenting the findings of these studies, and communication of these results to individuals, agencies and the general public as appropriate and/or required. The position requires supervision and administration of an organization of approximately 50 staff and associated facilities including offices, labs and the Oklahoma Petroleum Information Center (OPIC), which contains an extensive collection of rock cores and samples, other well information and selected facilities for the examination of these cores and samples. It is anticipated that the Director of the OGS will work with Oklahoma universities, state and federal agencies, industry and other entities to conduct research in areas of public interest, as well as providing advice and service in the areas of geology, geophysics and natural resources. One particular area of current high interest is the recent, significant increase in Oklahoma earthquake activity. The successful candidate will have the demonstrated experience and ability to oversee these activities, while acting as the State Geologist of Oklahoma. Areas of experience that could be considered include an appropriate background with state or national surveys, administration in academia, experience in industry or research, or other related areas.

Review of candidates will begin **June 1, 2014** and continue until the position is filled. The anticipated starting date is January 1, 2015. Applicants are requested to submit a complete resume, statement of relevant experience and a list of five references who can be contacted, including names, phone numbers, e-mail addresses and complete mailing addresses. Questions or requests for additional information may be addressed to **Larry R. Grillot, Dean of the Mewbourne College of Earth & Energy, and Chair of the OGS Director Search Committee, at (405) 325-3821, or lrgrillot@ou.edu**. Applications and nominations should be addressed to **OGS Director Search Committee, University of Oklahoma, Sarkeys Energy Center, 100 East Boyd Street, Room 1510, Norman, OK 73019-1008**.

The University of Oklahoma is an Affirmative Action, Equal Opportunity Employer.
Women, minorities, protected veterans and individuals with disabilities are encouraged to apply.



Science Careers is dedicated to opening new doors and answering questions on career topics that matter to you. With timely feedback and a community atmosphere, our careers forum allows you to connect with colleagues and experts to get the advice and guidance you seek as you pursue your career goals.

Science Careers Forum:

» Relevant Career Topics
» Timely Advice and Answers
» Community, Connections, and More!

Visit the forum and join the conversation today!



Your Future Awaits.

Science Careers
From the journal *Science* AAAS
ScienceCareers.org



Nontraditional Careers: Opportunities Away From the Bench Webinar

Want to learn more about exciting and rewarding careers outside of academic/industrial research? View a roundtable discussion that looks at the various career options open to scientists and strategies you can use to pursue a nonresearch career.

Now Available On Demand
www.sciencecareers.org/webinar

Produced by the *Science*/AAAS Business Office.

Science Careers
From the journal *Science* AAAS

POSITIONS OPEN

UNIVERSITY of WASHINGTON

WRF-IPD INNOVATION FELLOWS PROGRAM
Postdoctoral Fellowship Opportunities at Seattle Research Institutions

The WRF-IPD Innovation Fellows Program supports postdoctoral researchers between the Institute for Protein Design and other Seattle-area research institutes or UW departments. We are recruiting exceptionally talented researchers who have just finished their Ph.D. to join expert laboratories at local institutions to apply protein design methods to current health, energy, and materials related research problems.

To Apply: Submit application materials via website: http://apply.interfolio.com/24848.

Details: WRF-IPD Innovation Fellows have an annual salary of $53,000 for two to three years plus $25,000 for supplies.

Full application details can be found at website: http://www.ipd.uw.edu/wrf-ipd-innovation-fellows-program.

RESEARCH POSITION, in the Department of Obstetrics and Gynecology, Georgia Regents University (GRU), Augusta, Georgia is available immediately to participate in a study on stem cell/epigenetics and female reproduction. Primary responsibilities for the position include, but not limited to: (1) Isolation and Characterization of stem cells, (2) characterization of the epigenetic signals involved in stem cell differentiation particularly in relation to histone modifications, (3) in vivo reconstruction and characterization of appropriate murine models, and (4) translation/correlation of murine observations to the human systems. Applicants should have a Ph.D. degree and experience in molecular biology and cell biology. Experience in stem cell/epigenetics is a must. Competitive salaries will be commensurate with experience. Application review begins immediately and will continue until the positions are filled. Please send curriculum vitae including names and contact info of three references to **Ayman Al-Hendy**, MD, Ph.D., **e-mail: aalhendy@gru.edu**. Georgia Regents University is an exciting intellectual environment with many opportunities for collaboration and career development. *Georgia Regents University is an Equal Opportunity/Affirmative Action Employer.*

POSTDOCTORAL FELLOW

We are seeking enthusiastic postdoctoral fellows to study the vascular smooth muscle biology. The current focus of the laboratory is on the Hippo-YAP signaling pathway in smooth muscle phenotypic modulation (Arteriosclerosis, Thrombosis, and Vascular Biology, 2012; Journal of Biological Chemistry, 2013, "paper of the week") and development (Circulation Research, 2014, cover article). The candidate must hold a Ph.D. degree in biomedical sciences with basic training in molecular biology and histology. Experience with rodents is a plus. Salary will be commensurate with level of experience and skills. Interested individuals should electronically send cover letter and curriculum vitae to **Dr. Jiliang Zhou** at **e-mail: jizhou@gru.edu**, Department of Pharmacology & Toxicology, Medical College of Georgia, Georgia Regents University. *Georgia Regents University of Augusta is an Equal Employment, Equal Access, and Equal Educational Opportunity and Affirmative Action Institution.*

PLANT MICROBE ECOLOGIST OR EPIDEMIOLOGIST

The Department of Plant Pathology at the University of Wisconsin-Madison seeks a researcher at the **ASSISTANT PROFESSOR** level who studies the ecology or epidemiology of plant-associated microbes through the use of emerging and novel quantitative methods. For details and application instructions, see the links at **website: http://www.plantpath.wisc.edu**.

POSITIONS OPEN

UNIVERSITY OF SOUTH CAROLINA School of Medicine

TENURE-TRACK FACULTY POSITION in Virology

The Department of Pathology, Microbiology, and Immunology at the University of South Carolina's School of Medicine invites applications for a tenure-track **ASSISTANT PROFESSOR** position in Virology. The successful candidate is expected to develop a strong extramurally funded research program, and must participate in the teaching mission of the department. Outstanding applicants working in an area complementing our existing faculty research interests (**website: http://pmi.med.sc.edu/**) will be considered. Candidates must have a Ph.D. or equivalent, and at least three years of postdoctoral research experience. Preference will be given to a candidate who has shown evidence of independence with currently active grant funding. Competitive salary and startup funds are available. Please submit curriculum vitae, teaching philosophy, and statement of research plans to: **Dr. Mitzi Nagarkatti, Chair, Department of Pathology, Microbiology, and Immunology, University of South Carolina School of Medicine, Columbia, SC 29208** or **e-mail: virology@uscmed.sc.edu**. Kindly arrange to submit three letters of recommendation upon request. The search will start immediately and will continue until the position is filled. *University of South Carolina Columbia is an Equal Opportunity/Affirmative Action Employer and encourages applications from women and minorities and is responsive to the needs of dual career couples.*

Find your future here.

Science Careers
From the journal *Science* AAAS
www.ScienceCareers.org

☑ More scientists agree —we are the most useful website.
www.ScienceCareers.org

MARKET PLACE

PREMIUM REFURBISHED
GC/MS and LC/MS Systems
Save up to 50%
agilent.com/chem/refurbished
Agilent Technologies

Cleveland Clinic

Faculty Positions in Cancer Research
Department of Cancer Biology
Lerner Research Institute (LRI)

The Department of Cancer Biology is seeking multiple cancer researchers at all levels (Assistant/Associate/Full Professor) with a focus in hematological/lymphoid malignancies, kidney cancer, or breast cancer and strong translational interests. The positions provide an exceptional opportunity to translate basic discoveries to the clinic through collaborative interactions with outstanding clinical programs.

The Department of Cancer Biology currently has 9 primary Faculty actively involved in basic and translational research programs investigating cancers of the brain, colon/rectum, kidney, and prostate, as well as hematologic malignancies. Research foci include cell signaling, DNA damage and repair, tumor suppressor genes, new targets, histone modification, cell cycle control, developmental therapeutics, drug resistance, invasion, metastasis, angiogenesis, tumor microenvironment, and the innate defense against viruses and cancer. The LRI offers over 20 Cleveland Clinic-subsidized Core services, including an Animal Tumor Core, Mass Spectrometry, Imaging and Confocal Microscopy, Genomics, and Small Molecule Screening Cores, allowing access to the latest state-of-the-art equipment.

To be considered, applicants must have an M.D., M.D./Ph.D., or Ph.D. degree and must have ongoing grant support and an accomplished research program in any of the above-mentioned cancers. The successful applicants will be supported by generous start-up funds and joint appointment in Cleveland Clinic's Taussig Cancer Institute (part of the NCI-designated Case Comprehensive Cancer Center) and the Lerner College of Medicine.

Candidates should submit a curriculum vitae, summary of research interests, and three references, via e-mail to: **Colleen Corrigan (corrigc3@ccf.org)**.

For further information see: **http://www.lerner.ccf.org/cancerbio/**

Cleveland Clinic is an Equal Opportunity/Affirmative Action Employer.

UNLV

Director, School of Life Sciences

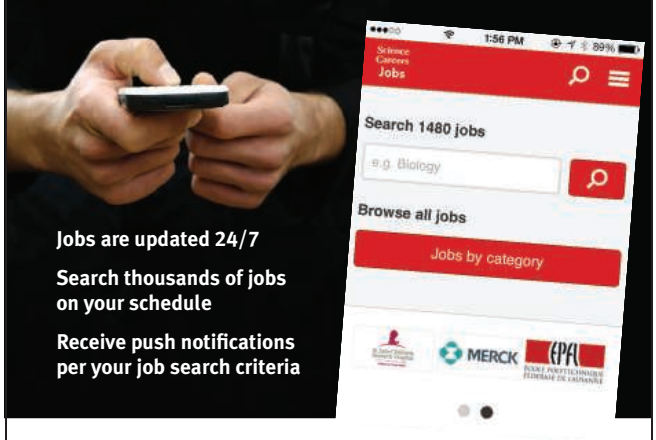
The University of Nevada, Las Vegas seeks an individual with outstanding academic credentials in any field of Biology to serve as Director of the School of Life Sciences. The successful candidate must have proven management and leadership skills, as well as a strong track record of extramurally funded, internationally recognized research commensurate with appointment at the level of Professor and a demonstrated commitment to excellence in teaching and mentoring. Applicants should present a clear vision to build upon Life Sciences' recent growth and strengths in diverse areas of biology. The new director will lead an active and productive school comprised of 27 tenure-track faculty, 6 full-time lecturers and 10 staff. With over 2000 undergraduate majors and over 40 M.S. and Ph.D. students, Life Sciences has the largest enrollment in the College of Sciences.

UNLV is an urban campus in a growing, vibrant, culturally diverse city, set in the Mojave Desert with easy access to numerous national parks, wilderness, and recreational areas. It is the largest research university in the Nevada System of Higher Education, offering more than 200 degree programs to over 27,000 students, and is a Title III and Title V Minority Serving Institution (MSI). The School of Life Sciences has taken advantage of UNLV's location in an EPSCoR and IDeA-eligible state to attract substantial program funding and will continue to play a significant role in advancing UNLV's goal of Carnegie Foundation - Tier 1 designation within the next decade (**http://www.unlv.edu/tier1**).

For more information and application details, visit **http://hr.unlv.edu/jobs** or call (702) 895-2894.

UNLV is an Equal Opportunity/Affirmative Action Educator and Employer Committed to Achieving Excellence Through Diversity.

Introducing the new
***Science* Careers Jobs app from Science**



Jobs are updated 24/7

Search thousands of jobs on your schedule

Receive push notifications per your job search criteria

Get a job on the go.
Search worldwide for thousands of scientific jobs in academia, industry, and government. Keep your finger on the pulse of your field—set up an alert for the type of job you are looking for and receive push notifications when jobs are posted that meet your criteria. The application process is seamless, linking you directly to job postings from your customized push notifications.

Scan this code to download app or visit **apps.sciencemag.org** for information.

Science Careers
From the journal *Science* AAAS

ScienceCareers.org

nature

Nature Neuroscience has a position available for an Assistant Editor. The journal publishes high-quality papers in all areas of neuroscience and provides a highly visible forum for communicating important advances to a broad readership. For more information about the journal, see our website (**http://www.nature.com/natureneuroscience**).

Applicants should have a PhD, a strong research background (in any area of neuroscience but preferably in systems neuroscience), broad interest in neuroscience, excellent literary skills, commitment to the communication of scientific ideas, and willingness and ability to learn new fields.

The successful candidate will participate in all aspects of the editorial process, including manuscript selection, commissioning and editing News and Views and Reviews, and writing for the journal. The job also involves attending meetings in the US and abroad to maintain contact with the international scientific community.

The new editor will join our team in the Manhattan office of the larger publishing group that also produces *Nature Genetics, Nature Medicine, Nature Biotechnology, Nature Structural and Molecular Biology, Nature Methods* and *Nature Immunology*.

To apply, please go to **https://home.eease.adp.com/recruit/?id=9357471**. You can also apply online through our job advertisement found at **www.naturejobs.com**. Applications will be reviewed upon receipt and should arrive no later than **June 15, 2014**.

To learn more about Nature Publishing Group, please visit our web site at www.nature.com.

Nature Publishing Group is an Equal Opportunity Employer.